Department of Radio Science and Engineering

Low-noise monolithic millimeter-wave integrated circuits and a radiometric imaging system

Mikko Kantanen

Aalto University

DOCTORAL DISSERTATIONS

Aalto University publication series
DOCTORAL DISSERTATIONS 270/2016
VTT SCIENCE 145

Low-noise monolithic millimeter-wave integrated circuits and a radiometric imaging system

Mikko Kantanen

A doctoral dissertation completed for the degree of Doctor of Science (Technology) to be defended, with the permission of the Aalto University School of Electrical Engineering, at a public examination held at the lecture hall AS1, TUAS building, Maarintie 8 on 27th January 2017 at 12.

Aalto University
School of Electrical Engineering
Department of Radio Science and Engineering

Supervising professor
Prof. Antti Räisänen, Aalto University, Finland

Thesis advisors
Dr. Jussi Tuovinen, MilliLab, VTT, Finland (2000-05), now with JoyHaptics, Finland
Dr. Arttu Luukanen, MilliLab, VTT, Finland (2005-13), now with Asqella, Finland

Preliminary examiners
Prof. Colombo R. Bolognesi, Swiss Federal Institute of Technology, ETH Zürich, Switzerland
Dr. Pekka Kangaslahti, Jet Propulsion Laboratory, California Institute of Technology, USA

Opponent
Prof. Herbert Zirath, Chalmers University of Technology, Sweden

Aalto University publication series
DOCTORAL DISSERTATIONS 270/2016

VTT SCIENCE 145

ISBN 978-952-60-7207-4 (printed)
ISBN 978-952-60-7206-7 (pdf)
ISSN-L 1799-4934
ISSN 1799-4934 (printed)
ISSN 1799-4942 (pdf)
http://urn.fi/URN:ISBN:978-952-60-7206-7

ISBN 978-951-38-8486-4 (printed)
ISBN 978-951-38-8485-7 (pdf)
ISSN-L 2242-119X
ISSN 2242-119X (printed)
ISSN 2242-1203 (pdf)
http://urn.fi/URN:ISBN:978-951-38-8485-7

Unigrafia Oy
Helsinki 2016

Finland

NORDIC ECOLABEL
441 697
Printed matter

Aalto University

Abstract

Aalto University, P.O. Box 11000, FI-00076 Aalto www.aalto.fi

Author
Mikko Kantanen

Name of the doctoral dissertation
Low-noise monolithic millimeter-wave integrated circuits and a radiometric imaging system

Publisher School of Electrical Engineering

Unit Department of Radio Science and Engineering

Series Aalto University publication series DOCTORAL DISSERTATIONS 270/2016

Field of research Radio engineering

Manuscript submitted 6 June 2016 **Date of the defence** 27 January 2017

Permission to publish granted (date) 30 November 2016 **Language** English

☐ **Monograph** ☒ **Article dissertation** ☐ **Essay dissertation**

Abstract

This thesis focuses on design and characterization of low-noise millimeter-wave devices and circuits, especially for radiometers. In addition, a millimeter-wave imaging system based on a radiometer is presented. The thesis is based on seven scientific articles and an overview of the research area including a summary of the main results of the work.

An automated measurement system for wideband on-wafer noise parameter determination of transistors has been developed for 50-75 GHz. The system can be utilized to develop and verify noise models of integrated transistors regardless the manufacturing technology. Noise parameters of a passive and an active circuit are presented. Noise parameters F_{min} = 2.65 dB, r_n = 0.25, and $\Gamma_{opt} = 0.57\angle 121°$ have been measured for an indium phosphide high electron mobility transistor.

Active cold loads based on monolithic millimeter-wave integrated circuits have been developed for millimeter-wave frequencies. The active cold loads have been realized using MHEMT technology and their suitability for radiometer calibration have been demonstrated. Noise temperatures of 75 K and 141 K are achieved at 31.4 GHz and 50-54 GHz, respectively.

Monolithic millimeter-wave integrated circuit low-noise amplifiers for millimeter-wave operation have been designed and characterized. The amplifiers have been manufactured using the metamorphic high electron mobility transistor technology and they cover specific frequency bands within 75-200 GHz. Noise figures of 3.0-3.5 dB, 5.2 dB, and 7.5 dB are achieved with the 100 nm process at 94 GHz, 153 GHz, and 183 GHz, respectively. With the 50 nm process, the noise figure of 5.2 dB is achieved at 165 GHz. All amplifiers have more than 18 dB of gain.

A millimeter-wave imaging system has been designed and realized. The system is capable to produce images of noise temperature variation using a single radiometer and a mechanically scanned antenna. The feasibility of millimeter-wave imaging for security and surveillance applications is demonstrated by millimeter-wave images taken with the system.

Keywords Millimeter-waves, millimeter-wave imaging, monolithic micro-/millimeter-wave integrated circuits, low-noise amplifiers, active cold loads, noise parameter measurements

ISBN (printed) 978-952-60-7207-4 **ISBN (pdf)** 978-952-60-7206-7

ISSN-L 1799-4934 **ISSN (printed)** 1799-4934 **ISSN (pdf)** 1799-4942

Location of publisher Helsinki **Location of printing** Helsinki **Year** 2016

Pages 174 **urn** http://urn.fi/URN:ISBN:978-952-60-7206-7

Tekijä
Mikko Kantanen

Väitöskirjan nimi
Millimetriaaltoalueen vähäkohinaiset integroidut piirit sekä millimetriaaltoalueen kuvausjärjestelmä

Julkaisija Sähkötekniikan korkeakoulu

Yksikkö Radiotieteen ja -tekniikan laitos

Sarja Aalto University publication series DOCTORAL DISSERTATIONS 270/2016

Tutkimusala Radiotekniikka

Käsikirjoituksen pvm 06.06.2016 **Väitöspäivä** 27.01.2017

Julkaisuluvan myöntämispäivä 30.11.2016 **Kieli** Englanti

☐ **Monografia** ☒ **Artikkeliväitöskirja** ☐ **Esseeväitöskirja**

Tiivistelmä

Tämä väitöskirja keskittyy millimetriaaltoalueen radiometreihin soveltuvien vähäkohinaisten piirien ja komponenttien suunnitteluun ja karakterisointiin. Lisäksi työssä esitetään radiometriin perustuva millimetriaaltokuvausjärjestelmä. Väitöskirja koostuu seitsemästä tieteellisestä artikkelista sekä tutkimuksen päätulokset sisältävästä tutkimusaiheen yhteenvedosta.

Työssä on kehitetty automatisoitu laajakaistainen mittausjärjestelmä transistorien kohinaparametrien määrittämiseen suoraan puolijohdekiekolta tai -sirulta 50-75 GHz taajuusalueelle. Mittausjärjestelmää voidaan hyödyntää integroitujen transistorien kohinamallien kehittämiseen ja verifiointiin transistorien valmistusteknologiasta riippumatta. Työssä esitetään aktiiviselle ja passiiviselle piirille mitatut kohinaparametrit. Indiumfosfidi-pohjaiselle HEMT-transistorille mitattiin kohinaparametrit F_{min} = 2.65 dB, r_n = 0.25, and $\Gamma_{opt} = 0.57\angle 121°$.

Työssä on kehitetty MMIC-tekniikalla valmistettuja aktiivisia kylmäkuormia millimetriaaltotaajuuksille. Kylmäkuormat toteutettiin metamorfisella HEMT-teknologialla ja työssä osoitettiin niiden sopivuus radiometrin kalibrointiin. Kylmäkuormille mitatut kohinalämpötilat olivat 75 K 31.4 GHz:n taajuudella ja 141 K 50-54 GHz:n kaistalla.

Työssä suunniteltiin ja karakterisoitiin MMIC-tekniikalla toteutettuja vähäkohinaisia vahvistimia millimetriaaltoalueelle. Vahvistimet valmistettiin MHEMT-teknologialla ja ne suunniteltiin toimimaan valituille taajuuskaistoille 75-200 GHz:n taajuusalueella. Saavutetut kohinaluvut 100 nm:n prosessilla ovat 3.0-3.5 dB 94 GHz:n taajuudella, 5.2 dB 153 GHz:n taajuudella sekä 7.2 dB 183 GHz:n taajuudella. 50 nm:n prosessilla saavutettiin 5.2 dB:n kohinaluku 165 GHz:n taajuudella. Kaikkien vahvistimien vahvistus on yli 18 dB.

Työssä suunniteltiin ja toteutettiin millimetriaaltokuvausjärjestelmä. Järjestelmä tuottaa kuvan kohinalämpötilan vaihtelusta yhtä radiometriä käyttäen mekaanisesti keilaamalla. Järjestelmällä otetut kuvat osoittavat millimetriaaltokuvauksen soveltuvuuden turvatarkastukseen tai aluevalvontaan.

Avainsanat Millimetriaallot, millimetriaaltokuvaus, monoliittiset mikro- tai millimetriaaltoalueen integroidut piirit, vähäkohinaiset vahvistimet, aktiiviset kylmäkuormat, kohinaparametrimittaukset

ISBN (painettu) 978-952-60-7207-4 **ISBN (pdf)** 978-952-60-7206-7

ISSN-L 1799-4934 **ISSN (painettu)** 1799-4934 **ISSN (pdf)** 1799-4942

Julkaisupaikka Helsinki **Painopaikka** Helsinki **Vuosi** 2016

Sivumäärä 174 **urn** http://urn.fi/URN:ISBN:978-952-60-7206-7

Preface

This thesis ties up the results of multiple projects related to low-noise radiometers I have been involved in during my (first) 17 years of working at VTT Technical Research Centre of Finland. VTT has given me a chance to work with challenging projects in the intriguing field of millimeter-wave technology. Although our team's name has changed multiple times during the years the actual work has remained the same. In addition to radiometer related projects, I have had an opportunity to study millimeter-wave communications in several projects.

The work presented in this thesis has been funded mainly by the European Space Research and Technology Centre (ESTEC) of the European Space Agency (ESA). Financial support for the millimeter-wave imager was received from the Finnish Defence Forces Technical Research Center.

Writing this preface gives me a great opportunity to look back at past years and remember those who have contributed in my work. First, I want to thank my former and current colleagues who have worked with circuits, antennas, systems, and measurements regardless of the frequency range. It has always been easy to knock on the door and ask for support. I thank Manu Lahdes, Tauno Vähä-Heikkilä, Jussi Tuovinen, Jussi Varis, Mikko Varonen, and Timo Karttaavi for their participation in research projects and writing the publications presented in this thesis. Jan Holmberg, Tero Kiuru, Pekka Rantakari, Jussi Säily, Antti Lamminen, Mervi Hirvonen, Pekka Pursula, Arttu Luukkanen, and Hannu Hakojärvi deserve thanks for their support.

Secondly, most of this work could not have been completed without international collaboration. Special thanks go to Tapani Närhi from ESA, who originally initiated the collaboration between our groups. He also kept pushing us towards ever better results. Mikko Kärkkäinen needs to be acknowledged for his participation in the design work in multiple projects as part of the MilliLab team. Great part of our collaboration has been the work performed at Fraunhofer IAF in Freiburg, Germany. I wish to thank Michael Schlechtweg, Matthias Seelmann-Eggebert, Rainer Weber, Arnulf Leuther, Markus Rösch, Ernst Weissbrodt, and Axel Tessmann for their efforts. I have always enjoyed my visits to Freiburg, hopefully I will see you soon again. A part of the work presented in the publications has been performed by DA-Design. I thank Petri Jukkala and others for the participation in the projects. The

work with millimeter-wave low-noise amplifiers has continued with reliability studies and hopefully we will see the results of our work operating in space in the 2020s.

Finally, I thank my father and late mother for their support over the years. Terhi and Ilpo also deserve thanks for the fun times we have together and the support for each other. I thank Eva-Lisa for the help with English grammar, and also for the support and patience during the finalisation of my thesis. I also thank my former and current volleyball teammates for providing me a chance to forget everything else and focus on the game as well as all the fun times in and out of the court.

Helsinki, November 2016

Mikko Kantanen

Contents

List of publications

This thesis is based on the following original publications which are referred to in the text as [I]–[VII]. The publications are reproduced in appendices with kind permission from the publishers.

I Kantanen, M., Lahdes, M., Vähä-Heikkilä, T., Tuovinen, J., "A wide-band on-wafer noise parameter measurement system at 50-75 GHz," *IEEE Transactions on Microwave Theory and Techniques*, vol. 51, no. 5, pp. 1489-1495, May 2003.

II Kantanen, M., Weissbrodt, E., Varis, J., Leuther, A., Seelmann-Eggebert, M., Rösch, M., Schlecthweg, M., Poutanen, T., Sundberg, I., Kaisti, M., Altti, M., Jukkala, P., Piironen, P., "Active cold load MMICs for Ka-, V-, and W-bands," *IET Microwaves, Antennas & Propagation*, vol. 9, no. 8, pp. 742-747, May 2015.

III Varonen, M., Kärkkäinen, M., Kantanen, M., Laaninen, M., Karttaavi, T., Weber, R., Leuther, A., Seelmann-Eggebert, M., Närhi, T., Lahtinen, J., Halonen, K.A.I, "W-band low noise amplifiers," *Proceedings of the European Microwave Association*, vol. 3, no. 4, pp. 358-366, Dec. 2007.

IV Kantanen, M., Kärkkäinen, M., Varonen, M., Laaninen, M., Karttaavi, T., Weber, R., Leuther, A., Seelmann-Eggebert, M., Närhi, T., Lahtinen, J., Halonen, K.A.I, "Low noise amplifiers for D-band," *Proceedings of the European Microwave Association*, vol. 4, no. 4, pp. 268-275, Dec. 2008.

V Kärkkäinen, M., Kantanen, M., Caujolle-Bert, S., Varonen, M., Weber, R., Leuther, A., Seelmann-Eggebert, M., Alanne, A., Jukkala, P., Närhi, T., Halonen, K.A.I., "MHEMT G-band low-noise amplifiers," *IEEE Transactions on Terahertz Science and Technology*, vol. 4, no. 4, pp. 459-468, July 2014.

VI Kantanen, M., Kärkkäinen, M., Caujolle-Bert, S., Varonen, M., Weber, R., Seelmann-Eggebert, M., Leuther, A., Jukkala, P., Närhi, T., Halonen, K.A.I., "Low noise amplifiers for G-band radiometers," in *Proceedings of joint 6th ESA Workshop on Millimetre-Wave Technology and Applications and the 4 Global Symposium on Millimeter Waves (GSMM)*, Espoo, Finland, 2011, pp. 1-4.

VII Kantanen, M., Lahdes, M., Tuovinen, J., “Passive millimeter-wave imager,” in *Proceedings of International Joint Conference of the Seventh Topical Symposium on Millimeter Waves and the Sixth MINT Millimeter-wave International Symposium,* Seoul, South Korea, 2005, pp. 240-243.

Author's contributions

[I] "A wide-band on-wafer noise parameter measurement system at 50-75 GHz"

This publication was the result of collaborative work. The author was responsible of developing and setting up the measurement system, as well as developing the measurement control software and the software routine to calculate noise parameters from noise figure and calibration data. The author performed the measurements for passive and active devices presented in the publication. The author also performed the Monte Carlo analysis for uncertainty estimation under guidance from Manu Lahdes. The author had the main responsibility of writing the publication.

[II] "Active cold load MMICs for Ka-, V-, and W-bands"

This publication was the result of collaborative work. The author designed the Ka- and V-band active cold loads presented in the publication. The author performed the wideband S-parameter measurements and noise temperature measurements at all three bands. The author had the main responsibility of writing the publication.

[III] "W-band low noise amplifiers"

This publication was the result of collaborative work. The author designed the LNA3 and LNA4 presented in the publication. The author performed the reported S-parameter and noise figure measurements both on-wafer and in-package. The author performed the cryogenic noise figure measurement. The author contributed to writing the publication.

[IV] "Low noise amplifiers for D-band"

This publication was the result of collaborative work. The author designed the LNA3 and LNA4 presented in the publication. The author performed the reported S-parameter and noise figure measurements both on-wafer and in-package. The author had the main responsibility writing the publication.

[V] "MHEMT G-band low-noise amplifiers"

This publication was the result of collaborative work. The author designed the LNA2 presented in the publication. The author designed the G-band noise figure

measurement system and performed the reported S-parameter and noise figure measurements. The author contributed to writing the publication.

[VI] “Low noise amplifiers for G-band radiometers”

This publication was the result of collaborative work. The author designed the LNA2 and LNA5 presented in the publication. The author performed the reported S-parameter and noise figure measurements. The author had the main responsibility of writing the publication.

[VII] “Passive millimeter-wave imager”

This publication was the result of collaborative work. The author designed the radiometer used in the imager together with Manu Lahdes. The author designed the close range focusing lens for the antenna. The author developed the control and measurement software for the imager. The author took the millimeter-wave images presented in the publication with Manu Lahdes. The author had the main responsibility of writing the publication.

List of abbreviations

ABCS	Antimony based compound semiconductor
ACL	Active cold load
AD	Analog to digital
AlGaAs	Aluminum gallium arsenide
ALMA	Atacama large millimeter-wave array
CMOS	Complementary metal oxide semiconductor
CPW	Coplanar waveguide
DC	Direct current
DUT	Device under test
ESA	European space agency
EUMETSAT	European organisation for the exploitation of meteorological satellites
FET	Field effect transistor
GaAs	Gallium arsenide
HDPE	High density polyethylene
HEMT	High electron mobility transistor
InP	Indium phosphide
LNA	Low-noise amplifier
MetOp-SG	Meteorological operational satellite - second generation
MHEMT	Metamorphic high electron mobility transistor
MilliLab	Millimeter-wave laboratory of Finland
MIM	Metal-insulator-metal
MIMIC	Monolithic millimeter-wave integrated circuit

MMIC	Monolithic microwave integrated circuit, Monolithic millimeter-wave integrated circuit
MMID	Millimeter-wave identification
MTTF	Mean time to failure
MWS	Microwave sounder
NiCr	Nickel chromium
PHEMT	Pseudomorphic high electron mobility transistor
PIN	P-type, intrinsic, N-type material stack
R&D	Research and development
RF	Radio frequency
RFID	Radio frequency identification
SiGe	Silicon germanium
SPDT	Single pole double throw
VTT	Technical research centre of Finland
WMAP	Wilkinson microwave anisotropy probe
2-DEG	Two-dimensional electron gas

List of symbols

B	Bandwidth
B_{bb}	Black body surface brightness
B_{opt}	Optimum source susceptance
C_l	Center point of load stability circle
C_{PDS}	Drain-source pad capacitance
C_{PGD}	Gate-drain pad capacitance
C_{PGS}	Gate-source pad capacitance
C_s	Center point of source stability circle
c	Speed of light
c_{ds}	Drain-source capacitance
c_{gd}	Gate-drain capacitance
c_{gs}	Gate-source capacitance
F	Noise figure
F_{DUT}	Noise figure of the device under test
F_i	Noise figure
F_{min}	Minimum noise figure
F_{RCV}	Noise figure of the receiver
F_{TOT}	Total noise figure of cascaded system
f	Frequency
f_{max}	Maximum oscillation frequency
f_t	Transit frequency
G	Gain
G_{av}	Available power gain

G_{avi}	Available power gain
$G_{av,max}$	Maximum available power gain
$G_{av,AD}$	Available power gain of network AD
G_{DUT}	Gain of the device under test
G_i	Gain
G_{opt}	Optimum source conductance
G_{sys}	System power gain
$G_{sys,max}$	Maximum system power gain
G_t	Transducer power gain
$G_{t,max}$	Maximum transducer power gain
$G_{t,RCV}$	Transducer gain of the receiver
$G_{t,RCV,50}$	Transducer gain of the receiver with 50 Ω source impedance
$G_{t,TOT}$	Total transducer gain
$G_{xy,ti}$	Terminal invariant power gain
g_{ds}	Drain-source conductance
g_m	Transconductance
$g_{m,max}$	Maximum transconductance
h	Planck's constant
I_d	Drain current
$I_{d,max}$	Maximum drain current
K	Stability parameter
k	Boltzmann's constant
L	Loss
L_d	Drain inductance
L_g	Gate inductance
L_s	Source inductance
M	Noise measure
$P_{av,N}$	Power available from two-port
$P_{av,S}$	Power available from source
P_C	Cold noise power

P_{Ci}	Cold noise power
P_{det}	Detected power
P_e	Emitted power
P_H	Hot noise power
P_L	Power delivered to load
P_n	Noise power
P_{ni}	Input noise power
P_{no}	Output noise power
P_{si}	Input signal power
P_{so}	Output signal power
p	Pressure
R_d	Drain resistance
R_g	Gate resistance
R_n	Noise resistance
R_s	Source resistance
r_{gd}	Gate-drain resistance
r_{gs}	Gate-source resistance
r_l	Radius of load stability circle
r_n	Normalized noise resistance
r_s	Radius of source stability circle
S_{ij}	S-parameters
$S_{ij,AD}$	S-parameters of the network AD
$S_{ij,DUT}$	S-parameters of the device under test
$S_{ij,PRB}$	S-parameters of the probe
$S_{ij,RCV}$	S-parameters of the receiver
T	Temperature
T_a	Alternate noise temperature
T_{acl}	Noise temperature of active cold load
T_{ant}	Antenna temperature
T_b	Alternate noise temperature

T_{body}	Noise temperature of a natural object
T_{br}	Brightness temperature
T_C	Cold noise temperature
T_{DUT}	Noise temperature of the device under
$T_{e,min}$	Minimum noise temperature
T_H	Hot noise temperature
T_k	Noise temperature parameter
T_n	Noise temperature
T_{ni}	Noise temperature
T_n'	Translated noise temperature
T_p	Physical temperature
T_{phys}	Physical temperature
T_{RCV}	Receiver noise temperature
T_{rec}	Receiver noise temperature
T_{ref}	Reference noise temperature
T_{refl}	Noise temperature of reflected radiation
T_{sys}	System noise temperature
T_{s1}	Noise temperature incident at two-port input
T_{s2}	Noise temperature incident at two-port output
T_{TOT}	Total noise temperature of cascaded system
T_0	Standard temperature
T_1	System noise temperature
T_2	Load noise temperature
V_{bd}	Breakdown voltage
V_d	Drain voltage
V_{ds}	Drain-to-source voltage
Y	Y-factor, ratio between hot and cold noise powers
Y_{opt}	Optimum source admittance

Δ	Stability parameter
ΔG_{sys}	Root mean square of radiometers' system gain variation
ΔT	Radiometric sensitivity
Γ_{in}	Input source reflection coefficient
Γ_{l}	Load reflection coefficient
Γ_{LRCV}	Receiver's load reflection coefficient
Γ_{L2}	Load reflection coefficient
Γ_{opt}	Optimum source reflection coefficient
Γ'_{opt}	Alternate optimum source reflection coefficient
Γ_{out}	Output source reflection coefficient
Γ_{s}	Source reflection coefficient
Γ_{SDUT}	Source reflection coefficient of device under test
Γ_{SDUTi}	Source reflection coefficient of device under test
Γ_{SRCV}	Receiver's source reflection coefficient
Γ_{SRCVi}	Receiver's source reflection coefficient
Γ_1	Reflection coefficient at two-port input
Γ_2	Reflection coefficient at two-port output
ε	Emissivity
μ	Load stability parameter
μ'	Source stability parameter
ρ	Reflectivity
ρ_{water}	Water vapor density
σ	Standard deviation
τ	Delay
τ_i	Integration time
ω	Angular frequency

1. Introduction

The frequency range of 30-300 GHz is called the millimeter-wave range due to the corresponding wavelength range of 10-1 mm. Traditionally the use of millimeter-wave frequencies has been limited to scientific purposes, especially astronomy. Examples of astronomy missions are the Wilkinson microwave anisotropy probe (WMAP) [1], the Planck-mission [2], [3], and the Atacama large millimeter-wave array (ALMA) [4]. Millimeter-wave radars are used for collision avoidance in cars at around 77 GHz and there are missile seeker heads operating at 94 GHz [5], [6]. More recently, an increasing demand for data transfer is pushing the communications systems towards higher frequencies. The frequency ranges 39-44 GHz, 59-66 GHz, 71-76 GHz, 81-86 GHz, 92-95 GHz, 140 GHz, and 220 GHz are reserved or considered for communication systems [7]-[11]. Millimeter-wave identification (MMID) systems have been proposed as an extension of radio frequency identification (RFID) systems [12]. Radiometers operating at specific ranges between 31 and 243 GHz are used to gather meteorological data for weather forecasting [13], [14].

1.1 Background

This thesis focuses on millimeter-wave low-noise circuits for sensitive radiometers and related devices, systems and measurements. In the following, a general background of radio receivers, millimeter-wave radiometers, and transistor technologies as well as essential two-port parameter definitions are introduced.

1.1.1 Receiver topologies

Radio receivers can be divided into two main categories, direct detection (or homodyne) and heterodyne receivers. Simplified schematics with optional amplification are presented in Figure 1.1. In the direct detection receiver, the signal captured by an antenna is detected without frequency conversion. Most receiver systems use low-noise amplifiers (LNAs) to improve the sensitivity of the receiver. The detection can involve power measurement of the incoming signal or demodulation of amplitude, frequency or phase. In a heterodyne receiver, the incoming signal is converted to a different frequency for the detection. In general, detection electronics are easier to design at lower frequencies, thus the signal is

usually downconverted. Main figures of merit for the receivers are sensitivity, linearity, selectivity, and stability. In the millimeter-wave region, the low-noise receivers are essential for most applications.

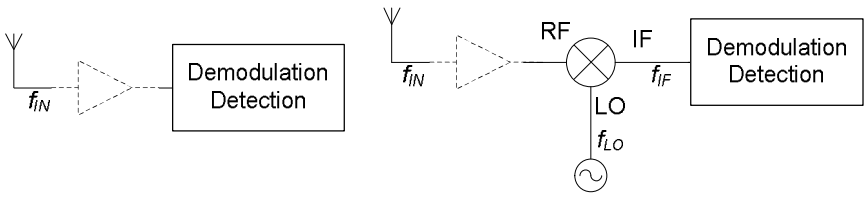

a) b)

Figure 1.1. Simplified schematics of main receiver categories. a) Direct detection, b) heterodyne receiver.

Noise of a radio receiver can be calculated using noise temperature. The output noise power of any resistive load

$$P_n = kT_nB \tag{1.1}$$

where the noise temperature T_n is defined as a physical temperature where the resistive load should be in order to produce output noise power P_n, k is Boltzmann's constant, and B is the measurement bandwidth. Noise of a two-port can be modeled using a matched load with effective noise temperature T_n at the input of a noiseless two-port as shown in Figure 1.2.

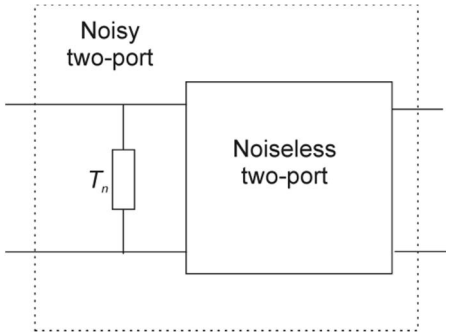

Figure 1.2. Presentation of noise in two-port by noise temperature.

When two-ports with available power gains of G_{avi} and noise temperatures T_{ni} are cascaded, the resulting total noise temperature at the input

$$T_{TOT} = T_{n1} + \frac{T_{n2}-1}{G_{av1}} + \frac{T_{n3}-1}{G_{av1}G_{av2}} + \cdots. \tag{1.2}$$

This is commonly known as the Friis formula [15]. A noise figure F describes the deterioration of signal-to-noise ratio in a circuit

$$F = \frac{P_{si}/P_{ni}}{P_{so}/P_{no}} \tag{1.3}$$

where P_{si}/P_{ni} and P_{so}/P_{no} are signal-to-noise available power ratios at input and output, respectively. The noise figure can be calculated from noise temperature using

$$F = 1 + \frac{T_n}{T_0} \tag{1.4}$$

where T_0 is standard temperature 290 K [16]. The Friis formula expressed using noise figures is

$$F_{TOT} = F_1 + \frac{F_2 - 1}{G_{av1}} + \frac{F_3 - 1}{G_{av1} G_{av2}} + \cdots. \tag{1.5}$$

1.1.2 Millimeter-wave radiometers and atmospheric measurements

Radiation of all objects can be characterized using Planck's black body radiation law for surface brightness

$$B_{bb} = \frac{2hf^3}{c^2}\left(\frac{1}{e^{hf/kT_p} - 1}\right) \tag{1.6}$$

where h is Planck's constant, c is the speed of light, f is the frequency of radiation, and T_p is the physical temperature of the object [17]. At microwave and millimeter-wave frequencies $hf << kT_p$; therefore the brightness of a black body can be approximated using the Rayleigh-Jeans law [17]

$$B_{bb} = \frac{2f^2 kT_p}{c^2}. \tag{1.7}$$

According to the Rayleigh-Jeans law, the brightness of an object is proportional to its physical temperature. Natural objects are not perfect black bodies. The detected radiation is partly due to the object itself and partly to reflected radiation from the surroundings. The emissivity ε defines the ratio of the radiation emitted by the object itself

$$B_{bb} = \varepsilon \frac{2f^2 kT_p}{c^2}. \tag{1.8}$$

Commonly, instead of brightness B_{bb}, the brightness temperature

$$T_{br} = \varepsilon T_p \tag{1.9}$$

is defined [17]. An object with a physical temperature T_p and an emissivity ε radiates as a black body with a brightness temperature T_{br} as long as the Rayleigh-Jeans law applies. The reflectivity ρ describes how much an object reflects radiation from its surroundings. For an object that radiation cannot penetrate

$$\varepsilon + \rho = 1. \tag{1.10}$$

Emissivity and reflectivity depend on the frequency. Power emitted by a black body, measured on a single polarization and over the bandwidth B is

$$P_e = kT_{br}B. \tag{1.11}$$

The brightness temperature is an equivalent quantity to the noise temperature. The noise temperature of the radiation emanating from a natural object is

$$T_{body} = T_{br} + \rho T_{refl} = \varepsilon T_p + \rho T_{refl} \tag{1.12}$$

where T_{refl} is the noise temperature of the incident radiation reflected by the object.

Radiometers are sensitive receivers that are used to measure the power of the incident radiation [17]. Simplified schematic of a radiometer is presented in Figure 1.3. Detected power at the radiometer output

$$P_{det} = kBG_{sys}T_{sys} \tag{1.13}$$

where G_{sys} is the average power gain of the radiometer system and T_{sys} is the system noise temperature. The bandwidth can be derived by integrating the gain over frequency

$$B = \frac{1}{G_{sys,max}} \int_0^\infty G_{sys}(f)\mathrm{d}f \tag{1.14}$$

where $G_{sys,max}$ is the maximum system gain [18]. Commonly, B is approximated with the 3 dB bandwidth of system gain. The system noise temperature

$$T_{sys} = T_{ant} + T_{rec} \tag{1.15}$$

where T_{ant} is the antenna noise temperature and T_{rec} is the total noise temperature of the receiver. The antenna noise temperature describes the power of the received noise signal. Minimum detectable noise temperature difference of an ideal radiometer or radiometric sensitivity is given by

$$\Delta T = \frac{T_{sys}}{\sqrt{Bt_i}} \tag{1.16}$$

where τ_i is the integration time; *i.e.* the time spent observing the target. If non-idealities, such as gain variation, are considered, ΔT will change to

$$\Delta T = T_{sys}\sqrt{\frac{1}{B\tau_i} + \left(\frac{\Delta G_{sys}}{G_{sys}}\right)^2} \tag{1.17}$$

where ΔG_{sys} is the root mean square value of the detected power gain variation.

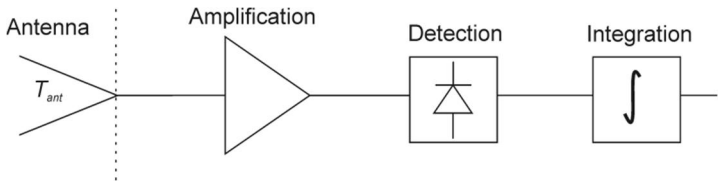

Figure 1.3. Simplified schematic of a radiometer.

Radiometers have high gain and wide bandwidth to increase the power level above the threshold for detection because the input power level is typically very low. As other radio receivers, the radiometers can be realized as direct detection or heterodyne radiometers. Heterodyne radiometers are utilized when good frequency selectivity is needed. Direct detection radiometers typically utilize wide bandwidth to increase the received noise signal power. Both types of radiometers can be further divided to total power radiometers, Dicke-radiometers, noise injection radiometers, continuous comparison radiometers, and other more complex radiometers [17]. Some radiometers utilize a reference load with known noise temperature to reduce the effects of gain variation. For example, the Dicke-radiometer [19] utilizes a switch to connect either the antenna or the reference load to the radiometer. Simplified schematic of the Dicke-radiometer is presented in Figure 1.4. If equal time is spent measuring the target and the reference,

$$\Delta T = \sqrt{\frac{2T_{sys}^2 + 2(T_{ref} + T_{rec})^2}{B\tau_i} + \left(\frac{\Delta G_{sys}}{G_{sys}}\right)^2 (T_{ant} - T_{ref})^2} \tag{1.18}$$

where T_{ref} is the noise temperature of the reference load [17]. It is apparent from (1.17) that if T_{ref} is equal to T_{ant} the effects of gain variation are cancelled and ΔT is doubled compared to the ideal radiometer.

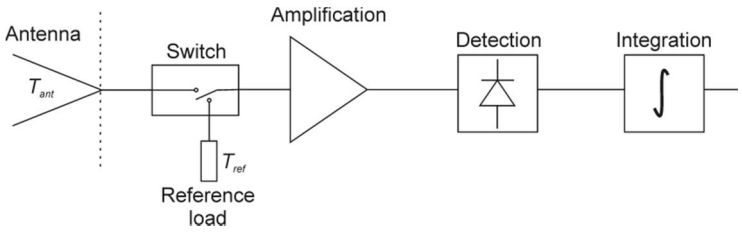

Figure 1.4. Simplified schematic of the Dicke-radiometer.

For accurate measurements of the target temperature the radiometers need to be calibrated. Radiometers are calibrated by measuring at least two loads with known noise temperature [17], [20]. For the best accuracy, noise temperatures of the loads should be outside the expected noise temperature of the target, *i.e.*, a 'hot' and 'cold' load.

One of the main applications of millimeter-wave radiometers is the remote sensing of the Earth's atmosphere from space. The attenuation of the atmosphere at microwave and millimeter-wave frequencies is presented in Figure 1.5. Local maxima in attenuation are caused by molecular absorption of oxygen and water molecules. In the microwave and millimeter-wave regions, there are absorption peaks caused by oxygen around 60 GHz and 118 GHz and peaks caused by water vapor around 23.8 GHz and 183 GHz. Local minima between the absorption frequencies are called window frequencies.

The attenuation and the shape of the peaks depend on the temperature, humidity and pressure. Shapes of the 183 GHz water vapor peak with different meteorological values are shown in Figure 1.6. Water vapor density ρ_{water} has a large effect to the peak attenuation value while temperature changes have moderate effect to the attenuation. By performing measurements at several frequencies, different parameters for meteorological models and weather forecasting can be determined. For example, MetOp-SG satellites to be launched after 2022 by EUMETSAT and ESA will have on-board an instrument called microwave sounder (MWS) that has multiple radiometers operating at different channels [13]. The channels and their use are listed in Table 1.1.

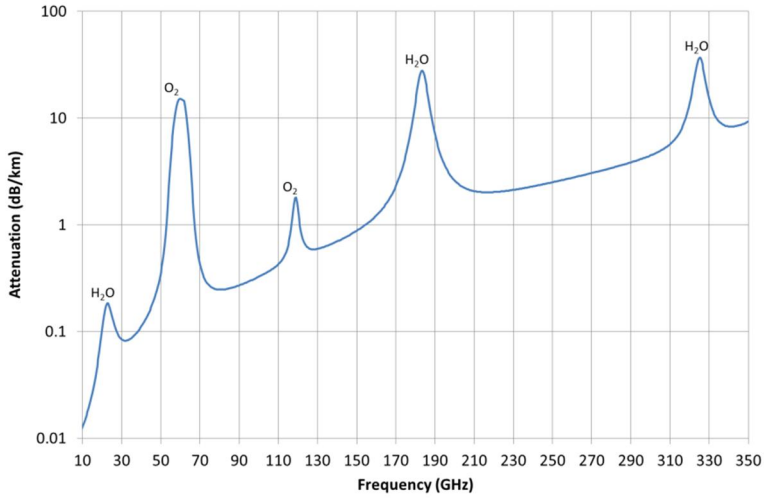

Figure 1.5. Attenuation of the atmosphere at sea level [21]. T = 15 °C, p = 1013 mbar, ρ_{water} = 7.5 g/m^3.

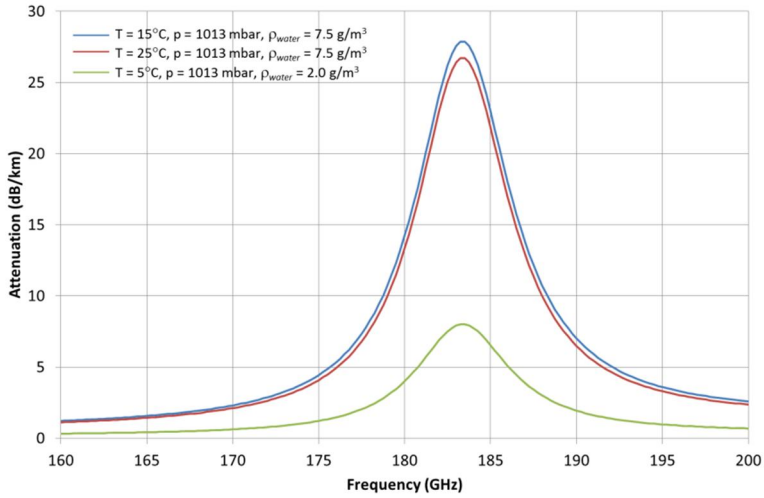

Figure 1.6. Shapes of the 183 GHz water vapor absorption peak with different meteorological values [21]. Water vapor density ρ_{water} has a large effect to the peak attenuation value.

Table 1.1. Microwave channels and their utilization in the microwave sounder instrument for the MetOp-SG satellite [13].

Channel	Frequency (GHz)	Utilisation
MWS-1	23.8	Water-vapour column
MWS-2	31.4	Window, water-vapour column
MWS-3	50.3	Quasi-window, surface emissivity
MWS-4	52.8	Temperature profile
MWS-5	53.246±0.08	Temperature profile
MWS-6	53.596±0.115	Temperature profile
MWS-7	53.948±0.081	Temperature profile
MWS-8	54.4	Temperature profile
MWS-9	54.94	Temperature profile
MWS-10	55.5	Temperature profile
MWS-11	57.290344	Temperature profile
MWS-12	57.290344±0.217	Temperature profile
MWS-13	57.290344±0.3222±0.048	Temperature profile
MWS-14	57.290344±0.3222±0.022	Temperature profile
MWS-15	57.290344±0.3222±0.010	Temperature profile
MWS-16	57.290344±0.3222±0.0045	Temperature profile
MWS-17	89	Window
MWS-18	165.5±0.725	Quasi-window, water vapour profile
MWS-19	183.311±7.0	Water vapour profile, precipitation
MWS-20	183.311±4.5	Water vapour profile
MWS-21	183.311±3.0	Water vapour profile
MWS-22	183.311±1.8	Water vapour profile
MWS-23	183.311±1.0	Water vapour profile
MWS-24	229	Quasi-window, water vapour profile

1.1.3 Transistor technologies for millimeter-wave frequencies

Traditionally millimeter-wave low-noise amplifiers have been realized by using III-V compound semiconductor technologies such as gallium arsenide (GaAs) or indium phosphide (InP) [22]. During the past few years developments in silicon based technologies, CMOS and silicon germanium (SiGe), have allowed the use of these technologies at millimeter-wave frequencies [22]. While gain and noise properties of III-V compound semiconductor based technologies are superior to their silicon based counterparts, the possibility to integrate more functions on a single chip makes silicon based circuits attractive for mass production applications.

The most common III-V compound semiconductor transistor type utilized in the millimeter-wave region is the high electron mobility transistor (HEMT). HEMT is a special type of the field effect transistor (FET) where a so called two dimensional electron gas is formed on a thin layer in the structure. In FETs, the amount of the available carrier electrons between the source and drain terminals is controlled by applied voltage at the gate terminal.

Cross sections of a conventional GaAs HEMT structure and metamorphic HEMT structure are presented in Figure 1.7 [23], [25]. In a conventional GaAs HEMT, an undoped GaAs buffer layer and an undoped aluminum gallium arsenide (AlGaAs) spacer layer are grown on a semi-insulating GaAs substrate. Due to a higher band gap of AlGaAs compared to GaAs, free electrons diffuse into GaAs and form a thin two-dimensional electron gas (2-DEG) at the interface. Electrons in the 2-DEG channel exhibit high mobility and velocity due to lack of donor atoms in the undoped GaAs layer. The amount of charge in 2-DEG is controlled by the gate to source voltage. The main advantages of the HEMT structure are high electron mobility, small source resistance, high transit frequency f_t due to high electron velocity, high transconductance, and high output resistance [23].

When comparing different HEMT technologies, InP HEMTs have enhanced noise and gain properties compared to GaAs HEMTs. However, pure InP is very fragile and very expensive to manufacture. This has led to the development of pseudomorphic and metamorphic HEMT technologies. In the pseudomorphic HEMT (PHEMT) technology, devices with an indium channel are manufactured on a GaAs wafer. InP and GaAs have different lattice constants which results in lattice mismatch. The lattice mismatch causes structural strain and dislocations which reduce electron mobility in the device. In metamorphic HEMT (MHEMT) technology, a buffer layer is processed between the GaAs wafer and the In channel. Indium content is adjusted linearly in the buffer layer which allows matching the lattice constants [23], [24].

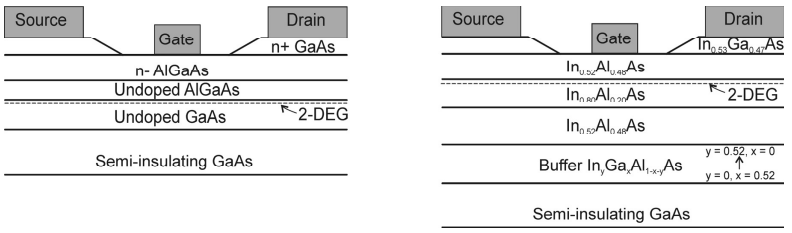

a) b)

Figure 1.7. Cross-sections of a) conventional GaAs HEMT and b) metamorphic HEMT devices. Adapted from [23], [25].

The high frequency small signal equivalent circuit of a HEMT device is presented in Figure 1.8. The equivalent circuit consists of intrinsic and extrinsic components. The intrinsic components (c_{gs}, r_{gs}, c_{gd}, r_{gd}, g_m, τ, g_{ds}, and c_{ds}) describe the behavior inside the device while the extrinsic components (L_g, R_g, R_s, L_s, R_d, L_d, C_{PGS}, C_{PGD}, and C_{PDS}) describe the effects of connections to circuit components [23], [26], [27]. The noise of a HEMT device can be modeled by assigning the temperatures T_d and T_g on resistors g_{ds} and r_{gs}, respectively [28]. Together with the small signal model the temperatures T_d and T_g determine the complex noise parameters of the device.

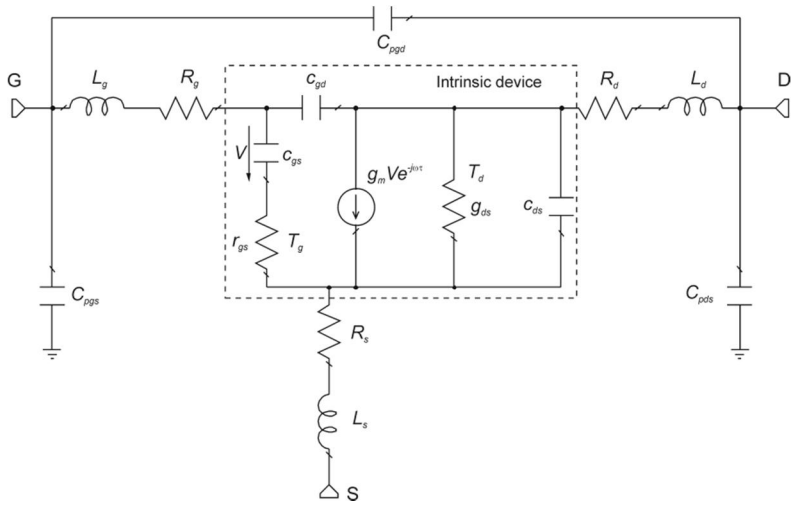

Figure 1.8. High frequency small signal equivalent circuit of a HEMT device. Adapted from [26].

Transconductance as a function of the gate voltage with different drain voltage values of a HEMT device is presented in Figure 1.9. For each drain voltage value there is a gate voltage value maximizing the transconductance. Maximum transconductance biasing is utilized in circuit design to maximize the gain of the transistor.

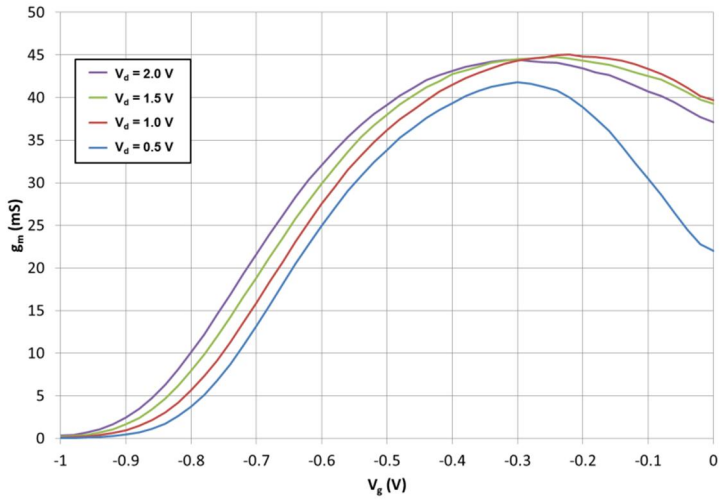

Figure 1.9. Measured transconductance of a HEMT device as a function of gate voltage.

1.1.4 Parameter definitions for two-ports

During the circuit design work, most of the electrical components are considered to be one-ports, two-ports or multiports. In the following, definitions of the parameters used in this thesis are given. A two-port characterized with S-parameters and related reflection coefficients is presented in Figure 1.10.

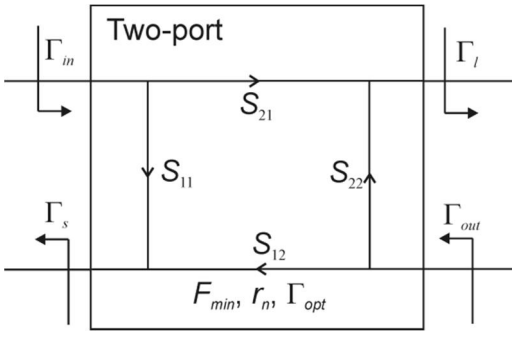

Figure 1.10. Two-port characterized with S-parameters and reflection coefficients.

The noise figure F of any two-port varies as a function of the source reflection coefficient Γ_s as [29]

$$F = F_{min} + 4r_n \frac{|\Gamma_s - \Gamma_{opt}|^2}{(1-|\Gamma_s|^2)|1+\Gamma_{opt}|^2} \tag{1.19}$$

where F_{min} is the minimum noise figure of the two-port, r_n is the normalized noise resistance, and Γ_{opt} is the optimum source reflection coefficient, with which the minimum noise figure is achieved. The parameters F_{min}, r_n, and Γ_{opt} are called noise parameters. As a three dimensional representation, equation (2.1) defines a paraboloid over the Smith chart. When the noise figure values are projected on the Smith chart they form noise circles. These circles aid in optimizing the input matching of low-noise amplifiers. Both the noise paraboloid and the noise circles with a Smith chart are presented in Figure 1.11.

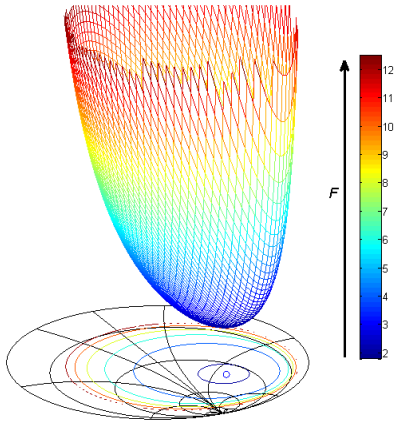

Figure 1.11. Noise paraboloid over the Smith chart with projected noise circles. Colors of the noise circles correspond to the noise figure values at the paraboloid surface. Optimum source reflection coefficient value is marked with an o.

Stability is a very important consideration in the design of amplifiers. Conventional requirement [30] for unconditional stability is $K > 1$ and $|\Delta| > 1$ where

$$K = \frac{1-|S_{11}|^2-|S_{22}|^2+|\Delta|^2}{2|S_{12}S_{21}|} \tag{1.20}$$

and

$$\Delta = S_{11}S_{22} - S_{12}S_{21}. \tag{1.21}$$

If both requirements are not met amplifier is conditionally stable. Stability can be examined on the Smith chart by using stability circles as shown in Figure 1.12 [31]. The radii $r_{l,s}$ and center points of the circles $C_{l,s}$ are

$$r_l = \left|\frac{S_{12}S_{21}}{|S_{22}|^2-|\Delta|^2}\right|, \tag{1.22}$$

$$C_l = \frac{\left(S_{22}-S_{11}^*\Delta\right)^*}{|S_{22}|^2-|\Delta|^2}, \tag{1.23}$$

$$r_s = \left|\frac{S_{12}S_{21}}{|S_{22}|^2-|\Delta|^2}\right|, \tag{1.24}$$

and

$$C_s = \frac{\left(S_{11}-S_{22}^*\Delta\right)^*}{|S_{11}|^2-|\Delta|^2}, \tag{1.25}$$

for load and source, respectively. If $|S_{11}|< 1$, then the area outside the load stability circle is the stable area and stability of the two-port is maintained using any impedance from that area as load impedance. The same applies for $|S_{22}|$ and source stability [31]. Alternatively to K and $|\Delta|$, two-port is unconditionally stable if stability circles lie outside of the Smith chart and the stable area is outside the stability circles. This can be characterized by stability factors μ and μ' which define the shortest distance to the edge of stability circle from the center of the Smith chart for load and source, respectively [32]. These stability factors can be calculated using

$$\mu = \frac{1-|S_{11}|^2}{\left|S_{22}-S_{11}^*\Delta\right|+|S_{12}S_{21}|} \tag{1.26}$$

and

$$\mu' = \frac{1-|S_{22}|^2}{\left|S_{11}-S_{22}^*\Delta\right|+|S_{12}S_{21}|}. \tag{1.27}$$

Conditions for unconditional stability are $\mu > 1$ and $\mu' > 1$.

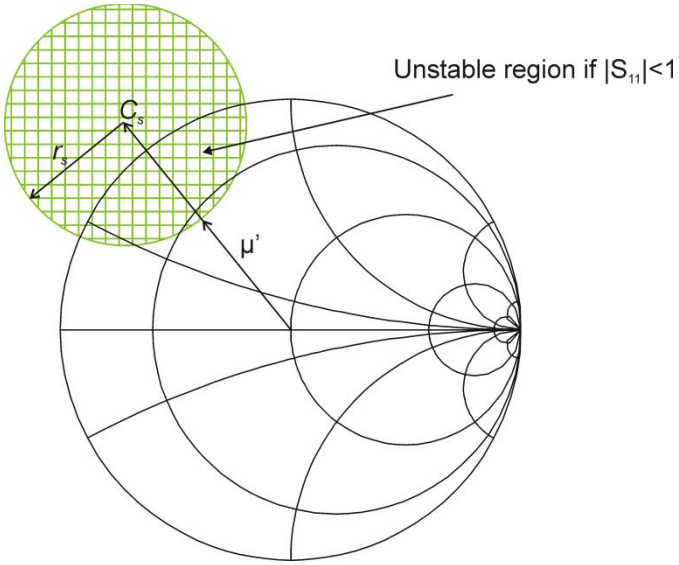

Figure 1.12. Source stability circle on the Smith chart. Similar figure can be drawn using C_l, r_l and μ.

The available power gain of a two-port is defined as the ratio between the power available from the two-port $P_{av,N}$ to the power available from the source $P_{av,S}$

$$G_{av} = \frac{P_{av,N}}{P_{av,S}} = \frac{1-|\Gamma_s|^2}{|1-S_{11}\Gamma_s|^2}|S_{21}|^2\frac{1}{1-|\Gamma_{out}|^2} \tag{1.28}$$

where Γ_s is source reflection coefficient and Γ_{out} is the output source reflection coefficient. Values of Γ_s that produce constant G_{av} can be shown to form circles known as constant available power gain circles on a Smith chart [31]. Another power gain definition is the transducer power gain defined as the ratio between the power delivered to the load P_L to the power available from the source

$$G_t = \frac{P_L}{P_{av,S}} = \frac{1-|\Gamma_s|^2}{|1-S_{11}\Gamma_s|^2}|S_{21}|^2\frac{1-|\Gamma_l|^2}{|1-\Gamma_{out}\Gamma_l|^2} \tag{1.29}$$

where Γ_l is load reflection coefficient. The transducer power gain is maximized when both input and output are conjugate matched ($\Gamma_s = \Gamma^*_{in}$, $\Gamma_l = \Gamma^*_{out}$). Under these conditions also $G_{av} = G_t$. If stability factor $K > 1$, then maximum available or transducer power gain can be calculated from [31]

$$G_{av,max} = G_{t,max} = K - \sqrt{K^2-1}\frac{|S_{21}|}{|S_{12}|}. \tag{1.30}$$

1.2 Objectives and content of this thesis

The research work done in the frame of this thesis has been motivated by several R&D projects that VTT and MilliLab have carried out for the space and other industries. Industries need new measurement techniques and new high performance solutions for sensing with lower cost circuits and systems at ever higher frequencies.

The objectives of the work described in this thesis are:

1. To develop a measurement system for transistor noise characterization at millimeter-wave frequencies.
2. To develop novel calibration sources for radiometers.
3. To develop low-noise amplifiers for sensitive radiometers.
4. To develop a radiometer for imaging purposes.

The first part of the thesis gives an introduction to the research area and summarizes the results presented in the scientific articles.

The second part of the thesis presents seven scientific articles where theoretical and experimental results of the work have been reported.

2. Millimeter-wave on-wafer measurement techniques

In general, radio frequency (RF), microwave, and millimeter-wave measurements can be divided into small signal and large signal measurements. Small signal measurements, such as S-parameter and noise measurements, describe the linear behavior of the device under test (DUT); *i.e.*, in the cases where the operation of the DUT is not affected by the test signals. Large signal measurements, such as compression point and intercept point measurements, characterize the non-linear operation of the DUT.

On-wafer measurements require on-wafer probes, which are used to connect measurement system to the DUT. Probes with coaxial cable interface are available up to 140 GHz and probes with waveguide interface are offered up to 1100 GHz [33]-[35].

2.1 S-parameter and noise figure measurements

Scattering parameters (or S-parameters) are commonly used to describe operation of linear circuits at microwave and millimeter-wave frequencies. An s-parameter presentation of a two-port is shown in Figure 2.1. The S-parameters describe how incoming (a_1, a_2) and outgoing (b_1, b_2) signal waves are reflected (S_{11}, S_{22}) or travelled through (S_{21}, S_{12}) the two-port. Noise of the two-port can be modeled with correlated noise waves (c_1, c_2).

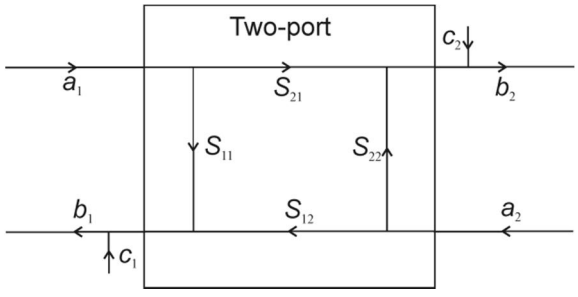

Figure 2.1. S-parameter presentation of a two-port.

Presently, vector network analyzers for S-parameter measurements are commercially available up to 140 GHz with coaxial cable interface. Extension units are available with waveguide interfaces from 50 GHz up to 1100 GHz covering a single waveguide band at a time [36], [37].

For on-wafer measurements, the vector network analyzer needs to be calibrated with on-wafer calibration standards. The most commonly used calibration methods at millimeter-wave frequencies are TRL and LRRM [40]-[42].

A simplified schematic of a noise figure measurement system is presented in Figure 2.2. The main functional blocks are a noise source and a noise receiver. The noise source is a component producing noise at controlled power level, for example a temperature controllable termination or a noise diode. The output power of the noise source is characterized as noise temperature. The noise receiver is essentially a radiometer measuring noise power and can be realized as a direct detection or heterodyne receiver. Commercially available measurement equipment, noise figure analyzers, can be used as a basis of the noise receiver. If needed, an additional noise downconverter is utilized to convert high frequency noise to frequency which is suitable for the noise figure analyzer. By delivering two different known noise power levels to the noise receiver and using (1.13), the receiver's noise temperature can be determined using the commonly known Y-factor method [20]

$$T_{RCV} = \frac{T_H - YT_C}{Y-1} \tag{2.1}$$

where T_H and T_C are the hot and cold noise temperatures, respectively, corresponding to two known noise power levels generated by noise sources. Factor $Y = P_H/P_C$, the ratio between the measured power levels P_H and P_C for load noise temperatures T_H and T_C, respectively. Commonly, noise sources with noise temperatures T_H and T_C are referred to as a hot and a cold source, respectively.

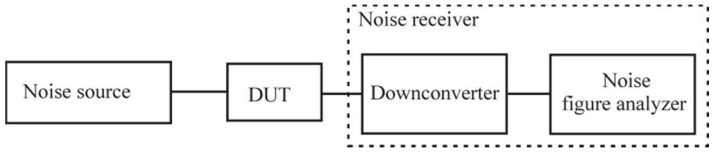

Figure 2.2. Simplified noise figure measurement system.

After receiver calibration, the DUT is connected to the measurement system and total noise temperature of cascaded DUT and receiver (T_{TOT}) is determined using (2.2). Finally, the noise temperature of the DUT is calculated using (1.2)

$$T_{DUT} = T_{TOT} - \frac{T_{RCV}-1}{G_{DUT}}\,. \tag{2.2}$$

Noise figure and noise parameter measurement systems and software solutions are commercially available up to 110 GHz [38]. For higher frequencies, noise diodes based on avalanche diodes can be purchased up to roughly 200 GHz [39]. Above that, the parasitic capacitance of avalanche diodes reduces their usability. Terminations, either as waveguide component or black body radiators, are available at higher frequencies [43], [44]. Fully assembled receivers or their components can be purchased up to 1100 GHz [36].

2.2 Millimeter-wave on-wafer measurement system for noise parameter determination

For efficient design work of low-noise amplifiers, it is essential to have accurate small signal models for the passive and active components utilized in the designs. While passive components can be modeled with a combination of electromagnetic simulations and measurements, the small signal models of active components are typically derived from measured data only. S-parameter measurements provide data that partially describe the operation of an active component. To completely characterize an active component, additional measurements, such as noise figure or noise parameters, are needed. Usually, the models used to describe noise behavior in the millimeter-wave region are extrapolated from noise parameter determination in the microwave region or are based only on noise figure measurements [45]-[50]. Determination of noise parameters at millimeter-wave frequencies are needed to refine the low frequency models to accurately characterize noise behavior in the millimeter-wave region.

The noise parameters are not directly measurable quantities; instead they are determined by measuring the noise figure with different source reflection coefficient values. Because the optimum source reflection coefficient is a complex quantity, at least four noise figure measurements with different source impedances are needed to solve the noise parameters in (1.16). To reduce the effect of measurement uncertainty, more than four measurements are usually made and noise parameters are solved using mathematical fitting routines. For passive two-ports, the noise parameters can be directly calculated from the measured S-parameters, as presented in [51].

In order to measure the noise figure as a function of source impedance an impedance tuner can be inserted between the noise source and the DUT to the noise figure measurement system. The schematic of a general noise figure measurement system with a tuner is presented in Figure 2.3. The tuner losses change the noise temperature generated by the noise source. The noise temperature after a lossy passive two-port can be expressed as

$$T_n' = \left(1 - \tfrac{1}{L}\right) T_{phys} + \tfrac{1}{L} T_n \tag{2.3}$$

where T_{phys} is the physical temperature of the two-port, L is the loss of the two-port, and T_n is the noise temperature delivered to the lossy passive two-port [16].

When the input reflection coefficient seen by the DUT is changed, the losses introduced by the tuner will also change and very careful characterization of tuner losses is needed in order to preserve good accuracy for the noise figure measurements. It can be seen in (2.3) that if the noise temperature T_n equals the physical temperature of the two-port, also the noise temperature after the two-port is equal to the physical temperature. Thus, for any impedance created by a lossy passive network at an ambient temperature, the noise temperature equals the ambient temperature. This has led to a development of a so called cold-source measurement technique [52]. With the cold-source measurement technique, most of the noise figure measurements are performed with a passive source at ambient temperature, only one measurement with a noise source with higher noise temperature is needed. This measurement should be performed in a low-loss state of the tuner and close to a 50 Ω impedance to reduce measurement uncertainty.

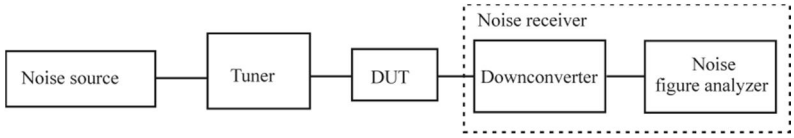

Figure 2.3. Simplified noise parameter measurement system.

Several mathematical approaches to determine noise parameters have been reported [53]-[58]. Most of the methods rely on least square fitting of (2.1) to the measurement data minimizing an error between measured and calculated noise figure for each source impedance [53]-[55]. Possible measurement errors in both noise figures and source impedances are taken into account in [56] and [57]. In [58], a direct method to calculate noise parameters as an average of each four measurement point groups from measurement data is presented.

The on-wafer noise parameter measurement setup used in this work is presented in Figure 2.4. The measurement setup is based on WR-15 waveguide components and operates over the frequency range of 50-75 GHz. The measurements are based on the cold-source method [52]. A solid state noise diode is used to provide hot ($T_H \approx 10000$ K) and cold (T_C = 295 K) noise temperatures during the noise receiver calibration. During measurements with a DUT, the noise diode is used only as an ambient temperature load. The noise receiver consists of a waveguide probe, an isolator, an LNA, a mixer, a signal generator, and a noise figure meter. A commercially available waveguide tuner controls the source reflection coefficient seen by the DUT with a moveable needle or probe inside a straight waveguide. The magnitude of the source reflection coefficient is controlled by changing the probe's insertion into the waveguide and the phase is controlled by moving the probe along the waveguide. The probe motion is controlled by two stepper motors. Probe's placement inside the waveguide can be characterized by step counts of the stepper motors. The DUT is placed in an on-wafer probing station and is connected to the measurement system with on-wafer probes with waveguide interfaces. Bias for active devices

can be fed through the probes or a separate biasing probe may be used. A vector network analyzer can be used to perform S-parameter measurements by utilizing two waveguide switches.

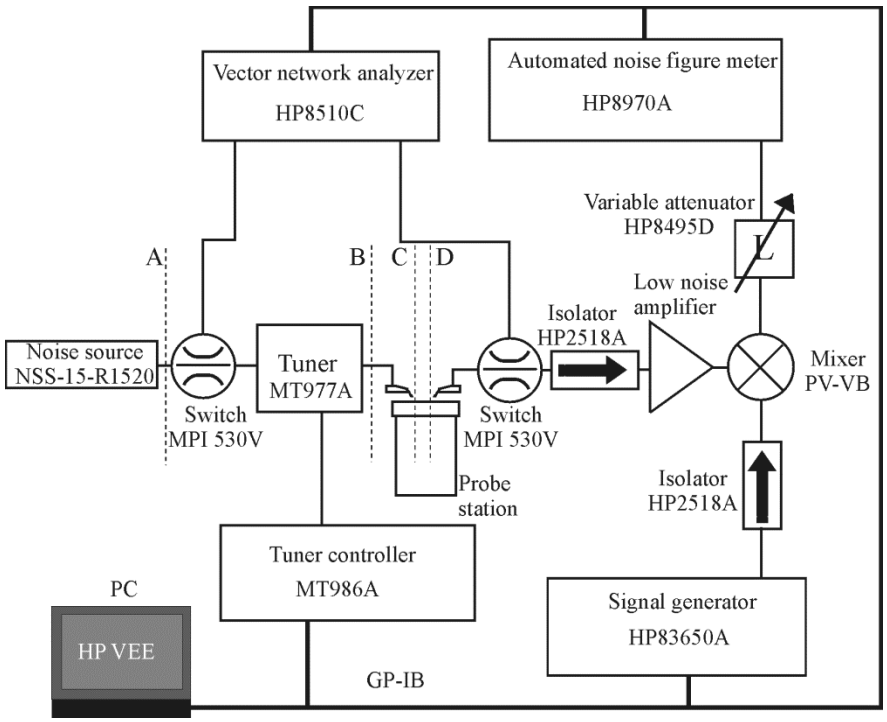

Figure 2.4. Automated noise parameter measurement setup [I].

From an operational point of view, the measurement system can be divided into five functional blocks which are presented in Figure 2.5 with notations for noise figure calculations. The calibration measurements include two port S-parameter measurements of the tuner, the input probe, the DUT, and a thru calibration standard. One port S-parameter measurements of the noise source, the receiver and the source reflection coefficients are also needed.

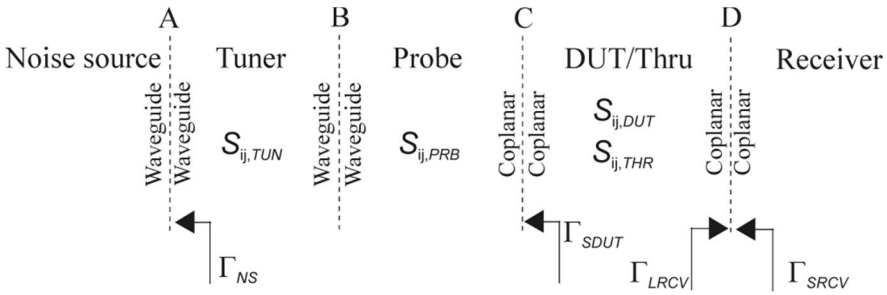

Figure 2.5. Functional blocks of the noise parameter measurement system with notation for noise figure calculations [I].

The noise receiver is calibrated by placing an on-wafer thru calibration standard between the probes. In order to subtract the receiver's noise contribution, its *kBG*-factor and noise parameters are required. The *kBG*-factor, normalized to perfectly matched load (Γ_{LRCV} = 0), is determined by measuring one hot and one cold noise power measurement and is calculated using

$$kBG = \frac{P_H - P_C}{T_H - T_C} |1 - \Gamma_{LRCV}\Gamma_{SRCV}|^2 \frac{|1 - S_{11,AD}\Gamma_{NS}|^2}{(1 - |\Gamma_{NS}|^2)|S_{21,AD}|^2} \tag{2.4}$$

where P_H and P_C are the noise powers measured with a hot and a cold noise source, respectively. T_H is the noise temperature of the hot noise source transferred to the receiver input plane, T_C is the physical temperature of the measurement system, Γ_{SRCV} is the source reflection coefficient of the input network at the receiver input, Γ_{LRCV} is the reflection coefficient of the receiver, and $S_{ij,AD}$ are the overall S-parameters of the cascaded tuner, probe, and thru. The derivation of formula (2.4) is presented in Appendix A.

The noise figure of the receiver with different source reflection coefficient values can be determined from cold noise source measurements using

$$F_i = \frac{P_{Ci}}{T_0 kBG} \frac{|1 - \Gamma_{LRCV}\Gamma_{SRCVi}|^2}{1 - |\Gamma_{SRCVi}|^2} - \frac{T_C}{T_0} + 1 \tag{2.5}$$

where P_{Ci} is the measured noise power with the ith source reflection coefficient Γ_{SRCVi}, and T_0 is the standard temperature 290 K. By measuring the noise power for at least four source reflection coefficient values, the noise parameters of the receiver can be calculated. The method in [58] with the modifications suggested in [59] is used in this work.

After the calibrations, the DUT is placed in the probe station and power measurements with the cold noise source are performed. For each source reflection coefficient value Γ_{SDUTi} the total noise figure of the cascade of the DUT and the noise receiver

$$F_{TOTi} = \frac{P_{Ci}}{T_0 kBG} \frac{|1-S_{11,DUT}\Gamma_{SDUTi}|^2 |1-\Gamma_{LRCV}\Gamma_{SRCVi}|^2}{(1-|\Gamma_{SDUTi}|^2)|S_{21,DUT}|^2} - \frac{T_C}{T_0} + 1 \quad (2.6)$$

where P_{Ci} is the measured noise power for the ith source reflection coefficient Γ_{SDUTi}, and Γ_{SRCVi} is the reflection coefficient of the network connected to the input of the receiver. The noise figure of the DUT can be calculated by the Friis noise formula (1.5)

$$F_{DUTi} = F_{TOTi} - \frac{F_{RCVi}-1}{G_{DUTi}} \quad (2.7)$$

where F_{RCVi} is the noise figure of the receiver and G_{DUTi} the available power gain of the DUT for the ith source reflection coefficient. Noise parameters of the DUT are calculated similarly as for the receiver.

Almost 40 measured quantities affect to the final values of the noise parameters. These include S-parameters, reflection coefficients, power measurements, ENR calibration of the noise source and room temperature. To get an estimation of measurement accuracy, a Monte Carlo analysis [60] was carried out. In the analysis, random errors are added to the initial measured values and the noise parameters are calculated, for example 1000 times. Statistical analysis is then performed to the obtained noise parameter sets. To get values for random error distributions, uncertainties were divided into A- and B-type uncertainties as suggested in [61]. A-type uncertainties are determined through statistical analysis and B-type uncertainties by other means (e.g. from literature). Prior work with manual on-wafer measurement system provided most of the information [62]. Uncertainties used in the error analysis are listed in Table 2.1. Rectangular distribution was used for S-parameter, reflection coefficient, and power measurement errors. Triangular distribution was used for ambient temperature.

Deviation of the minimum noise figure of an InP HEMT device is presented in Figure 2.6. S-parameters of the DUT and the source reflection coefficient measurement (Γ_{SDUTi}) were found to be the main sources of errors [I]. Confidence boundaries depend heavily on the test device. As an example the measured values for the HEMT device at 57 GHz with the corresponding 2σ confidence boundaries are given in Table 2.2. Obtained boundaries correspond to observed ripple well when clearly erroneous values are discarded.

Table 2.1. Uncertainties of the measured parameters. Data from [I].

Parameter	Standard uncertainty	Uncertainty type
$S_{11,TUN}$, $S_{22,TUN}$	0.005	A, B
$S_{12,TUN}$, $S_{21,TUN}$	0.006	A, B
$S_{11,PRB}$, $S_{22,PRB}$	0.036	B
$S_{12,PRB}$, $S_{21,PRB}$	0.005	B
$S_{11,DUT}$, $S_{22,DUT}$	0.036	B
$S_{12,DUT}$, $S_{21,DUT}$	0.05	B
Γ_{LRCV}	0.036	B
Γ_{SDUTi}	0.036	A, B
Γ_{NS}	0.005	B
ENR (dB)	0.06	B
P_H, P_C (dB)	0.04	B
T_C (K)	0.82	B

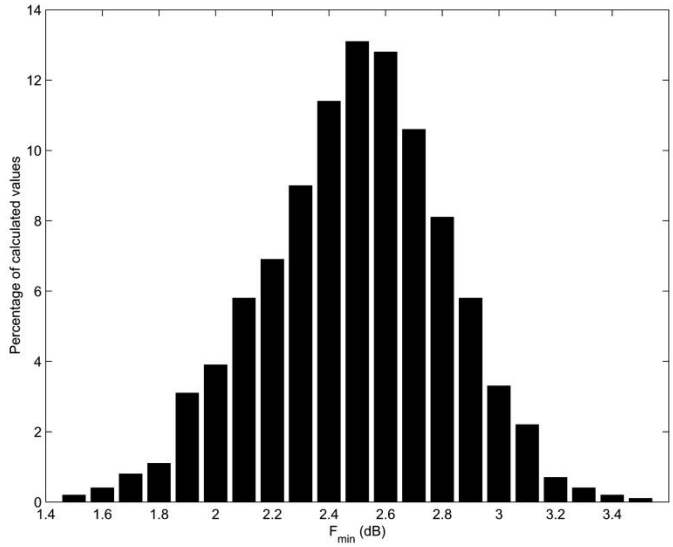

Figure 2.6. Deviation of F_{min} obtained in the Monte Carlo analysis with 1000 runs at 57 GHz. Data from [I].

Table 2.2. Measured noise parameters and corresponding confidence boundaries for a HEMT device at 57 GHz. Data from [I].

Parameter	Measured value	2σ (95.5 %) confidence boundary
F_{min}	2.65 dB	± 0.6 dB
r_n	0.25	± 0.06
$\lvert\Gamma_{opt}\rvert$	0.57	± 0.1
$\angle\Gamma_{opt}$	121°	± 9°

2.3 Experimental results

The noise parameters of a passive and active test device were presented in [I]. For passive devices, the noise parameters can be calculated from S-parameters [51] and they can be utilized to verify the operation of the test system. For both devices, the noise parameters were determined by measuring the noise figure with nine source reflection coefficient values. The noise parameters of an InP HEMT device are presented in Figure 2.7. The measurements show minimum noise figures in the range of 2.0-3.0 dB and normalized noise resistances in the range of 0.1-0.2. A similar transistor has also been measured at W-band using a similar measurement system [63] and comparison between the bands has been presented in [64].

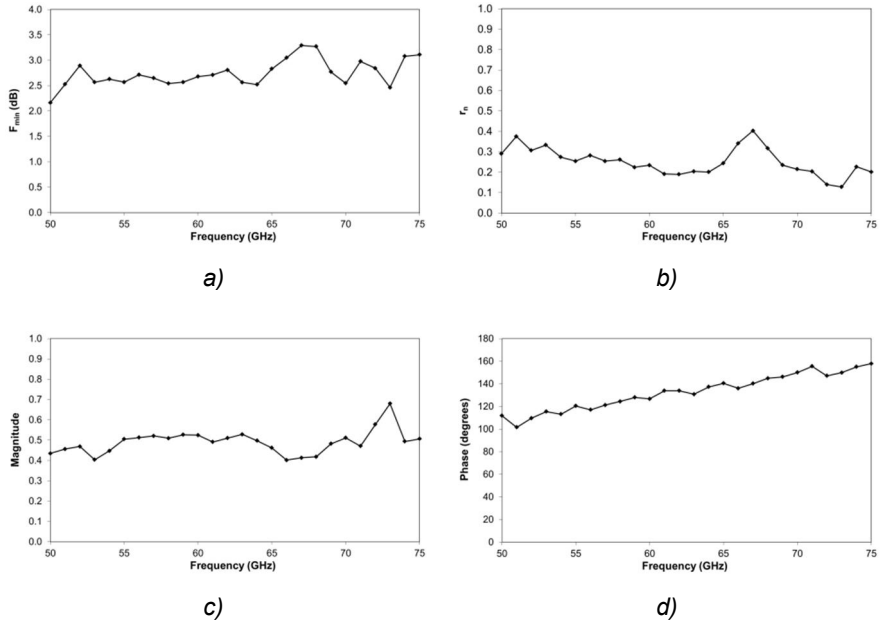

Figure 2.7. Noise parameters measured for an InP HEMT device. a) Minimum noise figure, b) normalized noise resistance, c) magnitude of optimum source reflection coefficient, and d) phase of optimum source reflection coefficient, Data from [I].

In addition to the data presented in this work, the on-wafer noise parameter measurement system presented here has been utilized to verify and develop noise models for HEMT and CMOS devices [65]-[68].

Besides the wideband measurements with a low number of source reflection coefficient values per frequency, the test system can be used to measure the noise figures with large number of source reflection coefficient values at a single frequency. Noise figure values and noise circles calculated using fitted noise

parameters for a CMOS device with 80 reflection coefficients are presented in Figure 2.8.

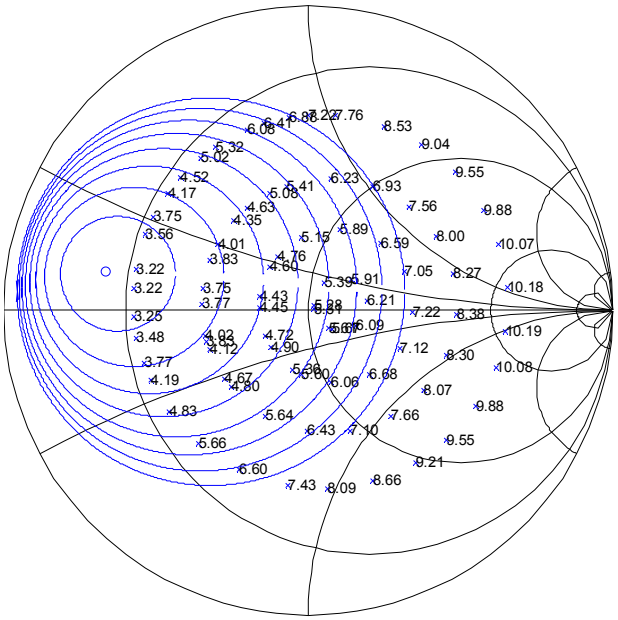

Figure 2.8. Noise figure values (in dB) measured using 80 reflection coefficient values (x) and constant noise circles from 3.5 dB to 7 dB with 0.5 dB step calculated from fitted noise parameters of a CMOS transistor at 60 GHz.

Only a small number of noise parameter measurement results has been published in the millimeter-wave region. Researchers from MilliLab have published results on V- and W-bands with waveguide based systems utilizing manual tuners [62], [63], [69], [70]. Noise parameter results using a measurement system based on a coaxial cable environment have been published up to 40 GHz and 60 GHz, in [71] and [72], respectively. At W-band, noise parameters of a passive device have been published in [73], [74]. Integrating a tuner as a part of a DUT with noise parameter results have been reported in [75]-[79].

3. Millimeter-wave active cold loads

Loads with known noise temperature are utilized as reference or calibration loads for the radiometers. The radiometer calibration loads can be either external or internal. External calibration loads are viewed by the entire radiometer system, including a target-pointed antenna. This way the antenna and the associated feed network are also calibrated [80]. An external calibration load can be a cold sky, *i.e.* measurement of cosmic microwave background noise, or a temperature controlled microwave absorber. Internal calibration loads are connected between the antenna and the radiometer front-end. Thus, only the radiometer itself is calibrated by the internal calibration loads. The antenna and the feed network need to be calibrated by other means. Examples of internal calibration loads are noise diodes, matched loads, and active cold loads (ACLs).

An active cold load is a one port circuit with noise temperature below the physical ambient temperature. It was shown in [81] that a FET based circuit can have a noise temperature below the ambient by a proper feedback network design. Low noise temperatures make ACLs attractive calibration loads especially in Earth-observing radiometers. For Earth-observing radiometers the hot calibration load has typically noise temperature of 300 K. It is beneficial to have the cold calibration load with around 100 K noise temperature that an ACL can provide. Most of the reported ACLs are based on FETs [81]-[89]. It is also possible to achieve a noise temperature lower than the ambient temperature with a Schottky diode where shot noise is the dominant noise source [90].

3.1 Design of active cold loads

A noise wave based analysis and general design flow of active cold loads have been presented by Weatherspoon and Dunleavy [91]. A notation for the two-port noise analysis is presented in Figure 3.1. The noise temperature incident at the input plane of the system

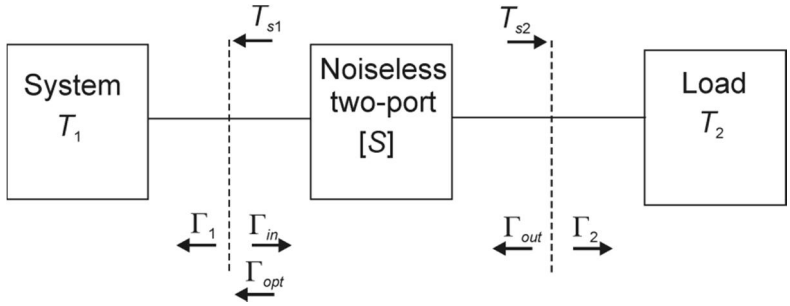

Figure 3.1. Noise wave based notation for active cold load design. Adapted from [91].

$$T_{s1} = T_b + \left[\left(T_1\left(1-|\Gamma_1|^2\right)+T_a\right)G_{21,ti}|\Gamma_2|^2 + T_2\left(1-|\Gamma_2|^2\right)\right]G_{21,ti} \tag{3.1}$$

where T_a and T_b are alternate noise parameters [92], [93], which are derived from the traditional noise parameters ($T_{e,min}$, R_n, $Y_{opt} = G_{opt}+jB_{opt}$) by

$$T_a = T_{e,min} + \frac{T_k|\Gamma'_{opt}|^2}{1-|\Gamma'_{opt}|^2} \tag{3.2}$$

and

$$T_b = \frac{T_k}{1-|\Gamma'_{opt}|^2} - T_{e,min}. \tag{3.3}$$

T_k is given by

$$T_k = 4T_0R_nG_{opt} \tag{3.4}$$

and

$$\Gamma'_{opt} = \frac{\Gamma^*_{in}-\Gamma_{opt}}{\Gamma_{opt}\Gamma_{in}-1} \tag{3.5}$$

where the T_0 is the standard temperature of 290 K. The terminal invariant gains are derived from the circuit S-parameters and are given by

$$G_{12,ti} = \frac{|S_{12}|^2}{1-|S_{11}|^2} \tag{3.6}$$

and

$$G_{21,ti} = \frac{|S_{21}|^2}{1-|S_{22}|^2}. \tag{3.7}$$

T_{s1} is minimized when $\Gamma_{in} = \Gamma^*_{opt}$. Input noise and power matching can be obtained simultaneously when

$$\Gamma_2 = \frac{\Gamma^*_{opt} - S_{11}}{S_{12}S_{21} + S_{22}(\Gamma^*_{opt} - S_{11})}. \quad (3.8)$$

A single transistor can have the magnitude of Γ_2 greater than unity, which would not be possible to realize by a purely passive network. In this case a feedback network has to be designed to obtain a realizable value $|\Gamma_2| < 1$. In principle ACL design has three steps [91]:

1. The design of a feedback network to obtain a realizable value for the drain matching circuit reflection coefficient $\Gamma_L = \Gamma_2$.
2. The design of a drain matching circuit for Γ_L.
3. The design of a gate matching circuit for Γ^*_{opt}.

The ACL design process is quite close to the low-noise amplifier design process. Main differences are that the gain of the resulting circuit when designed for an ACL operation is typically low and the output and input matching networks can be designed independently for the ACL due to low reverse gain. In an LNA design process, design iterations of the input and output matching networks are usually needed.

3.2 Experimental results

Two ACL circuits were designed for millimeter-wave frequencies using the 100 nm MHEMT process from Fraunhofer IAF, Freiburg, Germany [II]. The schematic of the realized ACL designs is presented in Figure 3.2.

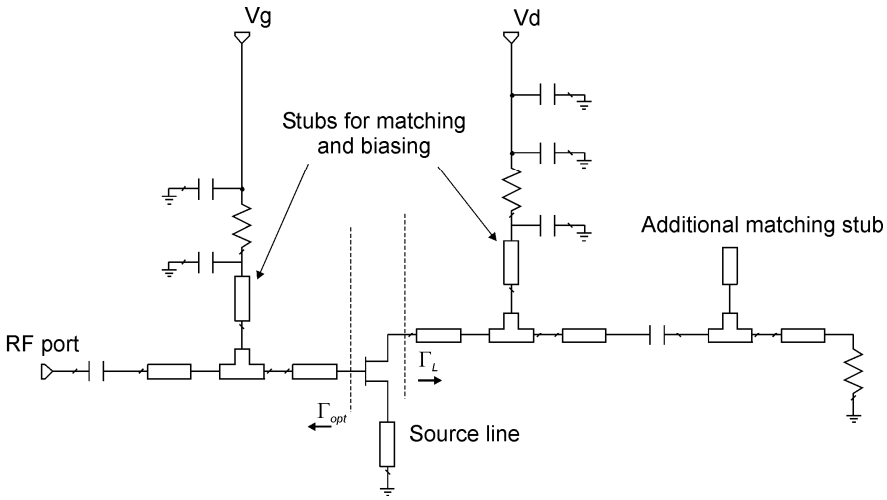

Figure 3.2. Schematic of the realized active cold loads [II].

An inductive source feedback was utilized to obtain $|\Gamma_L| < 1$ for the drain matching network. Additional constraints for the length of the inductive source transmission line arose from stability considerations [II]. The drain matching network consists of an open ended shunt stub, an RF short circuited shunt stub, a 50 ohm termination, and a DC blocking capacitor. Wideband matching of the RF port can be improved by using two stubs in the drain matching network.

The gate matching network provides simultaneous noise and conjugate impedance match for the transistor. The gate matching network is realized using an RF shorted stub, a series transmission line and a DC blocking capacitor. The losses of the gate matching network have a large effect on the overall noise temperature of the ACL as is apparent from (2.3). Micrographs of the two realized ACL monolithic millimeter-wave integrated circuits (MMICs) for 31.4 GHz and 52 GHz are presented in Figure 3.3.

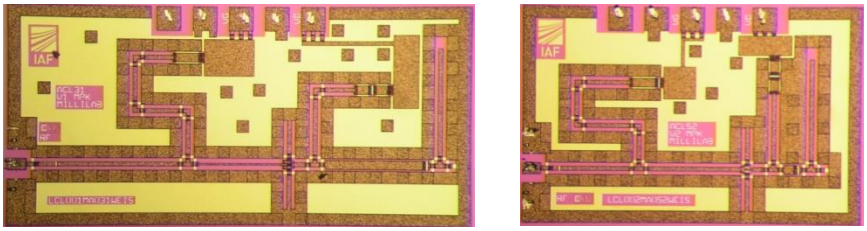

a) *b)*

Figure 3.3. Micrographs of the realized ACLs. a) 31.4 GHz, chip size 2.0 mm x 1.0 mm, b) 50-54 GHz, chip size 1.5 mm x 1.0 mm [II].

Two test setups are used to characterize the noise temperatures of the realized ACLs. The setups are based on waveguide components at Ka- and V-bands. Both measurement setups have similar functional blocks and a generic block diagram is shown in Figure 3.4. At Ka-band, the probe block includes a coaxial on-wafer probe and a short section of coaxial cable. Stainless steel waveguide is not used at Ka-band, but it is included in the V-band setup. The noise calibration plane is at the coaxial port of the coaxial to waveguide transition connected to a waveguide full-band isolator input. A commercially available waveguide LNA and a fundamental mixer are used to amplify and downconvert the noise signal to fixed IF frequency band. The isolator provides constant source impedance to the LNA. A microwave signal generator provides the LO signal to the mixer. A noise figure analyzer is utilized for noise power measurements.

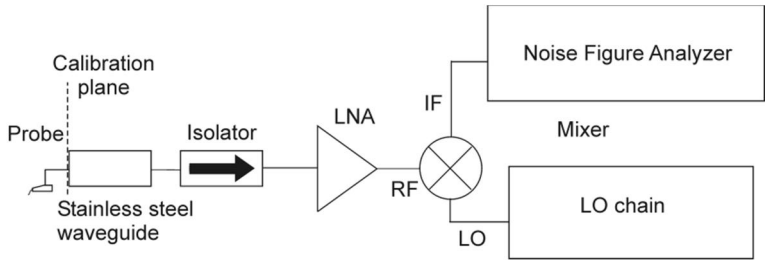

Figure 3.4. An ACL noise temperature measurement system [II].

The Ka-band setup is calibrated by a noise diode with a nominal excess noise ratio (ENR) of 12 dB. The calibration method is not optimal for the ACL measurement because the expected noise temperature is lower than the cold noise temperature used for the calibration. Extrapolation of the calibration line increases the measurement uncertainty because the setup behavior is assumed to be linear, which may not always be the case. Also, the hot calibration noise temperature is very high compared to the expected ACL noise temperature.

In the V-band setup, the waveguide on-wafer probe is followed by a section of stainless steel waveguide. Again, an isolator is utilized to provide constant source impedance for the LNA. The LNA has been developed in-house and is housed in a split-block waveguide package. A fundamental mixer is used and the LO-chain includes a microwave signal generator and a quadrupler. The noise calibration is performed using a heatable waveguide load. Noise powers are measured with load temperatures of 298 K and 373 K. The stainless steel waveguide prevents heat flow from the load to the rest of the measurement setup. A temperature controller keeps the load temperature within ±1.5 K during the frequency sweep. Again, the expected ACL noise temperature is below the calibration points and the extrapolation of the calibration line is required.

Comparisons of the simulated noise performance and RF port reflection coefficients are shown in Figure 3.5 and Figure 3.6. The simulations agree quite well with the measured values, the difference is 10-20 K over the 26-40 GHz band and 10-30 K over the 50-75 GHz band. The measured noise temperatures are 75 K at 31.4 GHz and 141 K over the 50-54 GHz range. The RF port reflection coefficients are below a -24 dB level for both designs. Variations of noise temperatures over bias conditions at 31.4 GHz and 52 GHz are presented in Figure 3.7. Both circuits are rather insensitive to small bias variations. The noise temperatures of the realized ACLs are compared to those of the other reported FET based ACLs in Table 3.1. In order to assess the usefulness of the ACLs in a real radiometer, careful system level calculations are needed for the specific radiometer and application. Especially the 1/*f* performance, which relates to integration time, is important to take into account.

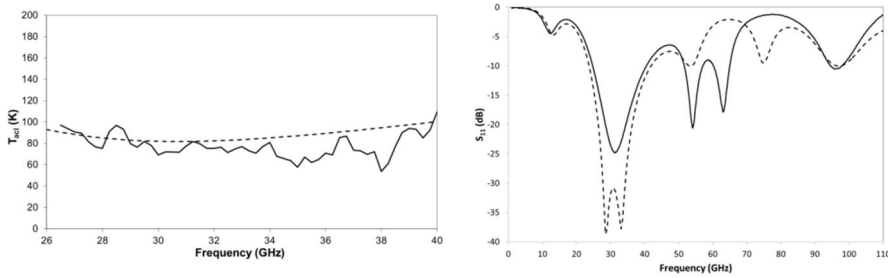

a) *b)*

Figure 3.5. Comparison between simulated (dashed) and measured performance (solid) of 31.4 GHz ACL. a) Noise temperature, b) Input reflection coefficient. Data from [II].

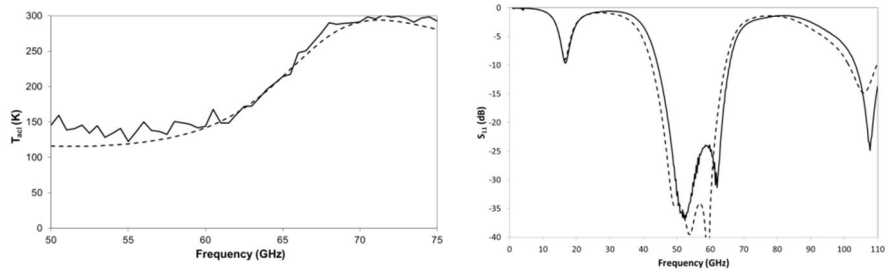

a) *b)*

Figure 3.6. Comparison between simulated (dashed) and measured performance (solid) of 50-54 GHz ACL. a) Noise temperature, b) Input reflection coefficient. Data from [II].

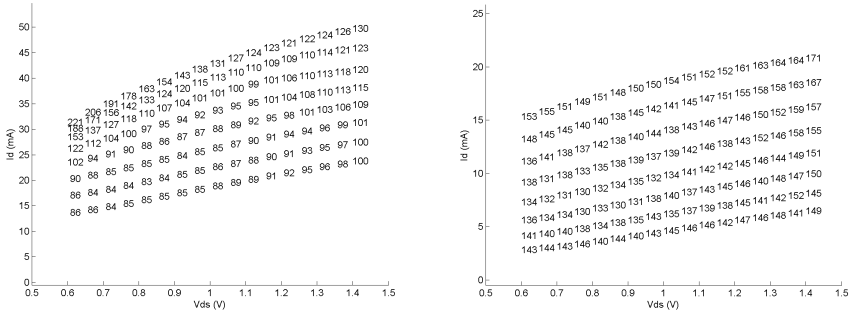

a) *b)*

Figure 3.7. Noise temperature variation over bias conditions at a single frequency. a) 31.4 GHz, b) 52 GHz. The lowest noise temperature values are achieved around V_{ds} = 0.8 V, I_d = 18 mA at 31.4 GHz and around V_{ds} = 0.8 V, I_d = 8 mA at 52 GHz. Data from [II].

Table 3.1. Comparison of reported FET based ACLs. Data from [II].

Frequency (GHz)	Noise temperature (K)	Technology, integration level	Reference
1.4	50	GaAs MESFET, hybrid	[81]
18	105	InP HEMT, hybrid	[82]
2-10	90	GaAs MHEMT, MMIC	[83]
10-26	125	GaAs MHEMT, MMIC	[83]
4-8	100	GaAs PHEMT, MMIC	[84]
10.69	56	GaAs PHEMT, hybrid	[85]
23.8	72	GaAs MHEMT, hybrid	[86]
1.4	65	GaAs PHEMT, MMIC	[87]
94	155	GaAs MHEMT, MMIC	[88]
94	190	GaAs MHEMT, MMIC	[89]
31.4	75	GaAs MHEMT, MMIC	[II]
50-54	141	GaAs MHEMT, MMIC	[II]

4. Millimeter-wave low-noise amplifiers

Sensitivity is the key figure of merit for millimeter-wave radiometers and many other receivers. According to (1.5) the first component of a receiver should have low noise figure and high gain in order to minimize the total noise figure. Low noise and high gain are the main design parameters for LNA. A good figure of merit when comparing amplifiers is the noise measure

$$M = \frac{F-1}{1-\frac{1}{G_{av}}} \tag{4.1}$$

where F is the noise figure and G_{av} is the available power gain of the amplifier [94]. An amplifier with the lowest noise measure is the best choice as the first amplifier in a chain of amplifiers. In the millimeter-wave region, MMIC technology is the most frequently used way to realize low-noise amplifiers. Presently, MMIC LNAs can be manufactured up to 850 GHz [95], [96]. The first low-gain amplifiers have even been reported at 1 THz [97].

4.1 Design of monolithic low-noise amplifiers

With sufficient gain, the noise temperature of a receiver is determined entirely by the first low-noise amplifier in the receiver chain, as seen in (1.5). Typically, low-noise amplifiers have multiple stages in order to obtain sufficient gain. The designer's goal is to design input, output, and inter-stage matching networks to provide low-noise, sufficient gain and specified input and output matching performance simultaneously.

Figure 4.1 shows constant noise and available power gain circles at a single frequency calculated using a small signal model for a HEMT device on a Smith chart. Also, part of the input stability circle is presented. Typically, the optimum source reflection coefficients in terms of noise Γ_{opt} and conjugate matching S^*_{11} are not the same. Feedback networks can be utilized to change values of Γ_{opt} and S^*_{11}. The change is seen more easily in S^*_{11}. Inductive feedback can be realized by adding sections of transmission lines to the source terminals of the transistor in the common source configuration. For the optimum noise performance, a matching network should present a source reflection coefficient of Γ_{opt} to a

transistor, whereas for the best gain performance, conjugate matching S^*_{11} should be used.

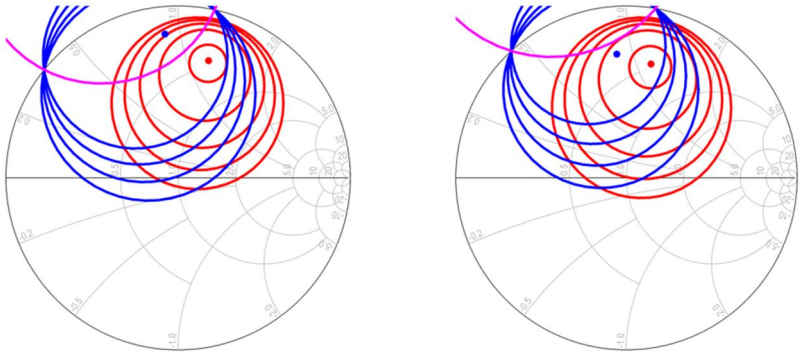

a) *b)*

Figure 4.1. Simulated noise circles with minimum noise reflection coefficient (red), available power gain circles with conjugate matching impedance (blue), and source stability circle (purple) for an integrated MHEMT device. a) Without inductive source feedback, b) with inductive source feedback. The stable impedance region is outside the stability circle.

The gain of a single transistor is moderate (5-10 dB) at millimeter-wave frequencies. The overall noise performance is mainly set by the first couple of stages of the amplifier. The gain of different stages play an important role, and the designer is bound to make trade-offs between noise and gain of individual stages in order to obtain an optimal performance for the amplifier. Moreover, matching networks need to be designed with additional care in order to maintain the stability of the amplifier also outside the desired frequency range.

4.2 Experimental results

A number of MMIC LNAs has been designed and manufactured using GaAs based MHEMT processes developed by Fraunhofer IAF, Freiburg, Germany [III]-[VI]. Their two processes differ by the gate length (50 or 100 nm) of the MHEMT device [98], [99]. The processes are suitable for coplanar waveguide (CPW) designs and feature nickel chromium (NiCr) thin film resistors, metal-insulator-metal (MIM) capacitors and backside metallization. Unwanted substrate modes are suppressed using ground via holes through the GaAs substrate [98]. As a result of extensive modeling work, Fraunhofer IAF provides reliable models for CPW components and transistors. The characteristics of the two processes are presented in Table 4.1.

Table 4.1. Characteristics of 100 nm and 50 nm MHEMT processes of Fraunhofer IAF [98], [99].

Parameter	100 nm MHEMT	50 nm MHEMT
Indium content	65 %	80 %
$I_{d,max}$ (mA/mm)	900	1200
V_{bd} (V)	4.3	2.2
$g_{m,max}$ (mS/mm)	1200	1800
f_t (GHz)	220	400
f_{max} (GHz)	300	420
MTTF (h)	3×10^7	2.7×10^6

The LNAs were designed to demonstrate the suitability of GaAs MHEMT technology for Earth observation radiometers. Specifications for gain, noise, center frequency and bandwidth have been given by the European Space Agency.

Radiometric measurements around 89 GHz are utilized for path loss, precipitation, and snowfall characterization [13]. Two LNAs were designed and manufactured with the 100 nm MHEMT process [98], [100] for use in spaceborne W-band radiometers. A micrograph and a simplified schematic of the LNA are presented in Figure 4.2 and Figure 4.3, respectively. The on-wafer measured S-parameters and noise figure are shown in Figure 4.4. The design was optimized for a low noise performance and wide bandwidth. The first stage of the four stage design was biased to low noise bias, while the maximum transconductance bias was used for the latter stages. Inductive source feedback transmission lines are added to transistors to improve stability and further improvements are achieved by not matching to maximum gain. The input and output matching networks have open stubs as a matching element and quarter wavelength shorted stubs are used for biasing. The interstage matching networks consist of short-circuited shunt stubs and a DC decoupling capacitor in series. The RF-short is realized by small capacitance. Additional resistors and capacitors are used to improve stability at frequencies well below the operating range [101].

The amplifier MMIC was packaged in an E-plane split-block module and the performance of the LNA in the module was compared to on-wafer measurement results. Performance improvement at cryogenic temperatures was also demonstrated [III]. A comparison of published MMIC LNAs around 94 GHz is presented in Table 4.2.

The LNAs designed in this work have 5.7-6.0 dB of gain per stage and noise measures of 1.0-1.3 which are similar or better performance values than those of the most of the LNAs realized with GaAs PHEMT, GaAs MHEMT or InP HEMT devices with 100 nm gate length. With the demonstrated 3.0 dB noise figure of the LNAs, the MHEMT technology was found useful for W-band Earth observing radiometers.

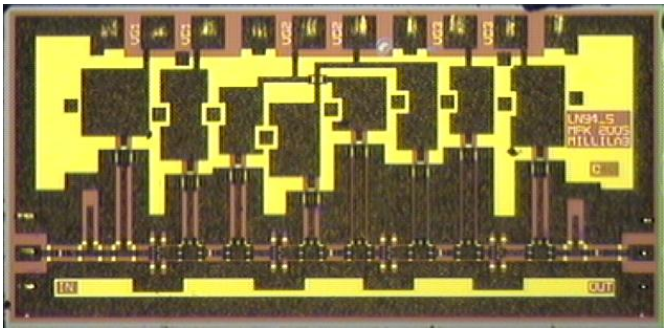

Figure 4.2. Micrograph of a low-noise amplifier [III].

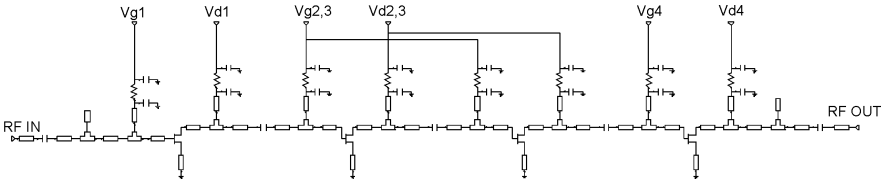

Figure 4.3. Simplified schematic of a four stage low-noise amplifier [III].

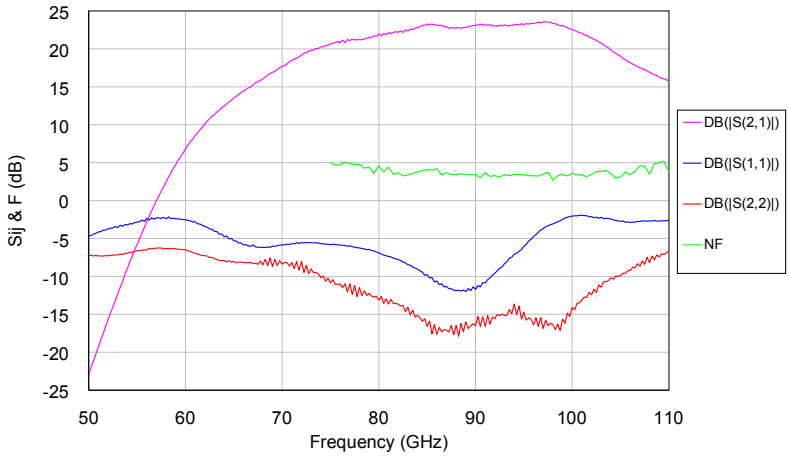

Figure 4.4. S-parameters and noise figure of a four stage W-band amplifier measured on-wafer. Data from [III].

Table 4.2. Comparison to other reported HEMT based MMIC low-noise amplifiers around 94 GHz.

Center frequency (GHz)	Gain (dB)	Noise figure (dB)	Number of stages	Technology	Reference
90	7		1	750 nm PHEMT	[102]
92	14.8	4.5	3	150 nm GaAs PHEMT	[103]
92	17.3	3.3	3	150 nm InP HEMT	[103]
92	4.5		1	100 nm GaAs PHEMT	[104]
94	6.4		5	100 nm InP HEMT	[105]
90	8		2	100 nm InP HEMT	[106]
94	17.3	3.2	3	100 nm InP HEMT	[107]
94	11	4.7	2	100 nm GaAs PHEMT	[108]
93.4	16	3	2	150 nm InP HEMT	[109]
93	16.5	3	2	150 nm InP HEMT	[110]
90	8		2	100 nm InP HEMT	[111]
96	3.1	4.5	1	100 nm GaAs PHEMT	[112]
94	13.3	5.5	2	100 nm GaAs PHEMT	[113]
94	21	3.5	3	100 nm GaAs PHEMT	[114]
94	12	3.5	3	100 nm InP HEMT	[115]
94	20	6	4	100 nm GaAs PHEMT	[116]
94	12	4.5	2	100 nm GaAs PHEMT	[117]
94	20		4	100 nm GaAs PHEMT	[118]
90	27	5	4	100 nm InP HEMT	[119]
94	26.4	3.9	4	100 nm GaAs PHEMT	[120]
94	7	6	2	100 nm GaAs PHEMT	[121]
94	34	4	7	100 nm GaAs PHEMT	[122]
94	40	6.5	6	100 nm GaAs PHEMT	[123]
94	20	3.3	3	100 nm InP HEMT	[124]
94	5	2.3	1	100 nm InP HEMT	[125]
94	15.5		4	250 nm InP HEMT	[126]
94	20	5.5	4	150 nm GaAs PHEMT	[127]
94	5.9	4.2	1	100 nm InP HEMT	[128]
94	25		6	150 nm GaAs PHEMT	[129]
94	37	6	8	150 nm GaAs PHEMT	[130]
95	20	2.5	4	100 nm InP HEMT	[131]
94	12	3.3	2	100 nm InP HEMT	[132]
89	14	4.8	3	100 nm GaAs MHEMT	[133]
90	16	5.5	3	120 nm GaAs PHEMT	[134]
90	22		3	120 nm InP HEMT	[135]

90	21		4	100 nm InP HEMT	[136]
93	16	3	4	100 nm InP HEMT	[137]
95	20	3.7	4	100 nm InP HEMT	[138]
97	21		6	150 nm GaAs PHEMT	[139]
85	21	2.9	4	100 nm InP HEMT	[140]
90	17	2.8		MHEMT	[141]
105	22	4.5	3	120 nm GaAs MHEMT	[65]
92	25	3.3	4	100 nm InP HEMT	[142]
94	12	2.3	2	70 nm GaAs MHEMT	[143]
100	22	3.5	3	100 nm InP HEMT	[144]
94	20	2.5	4	70 nm GaAs MHEMT	[145]
94		2.2	3	100 nm InP HEMT	[146]
89	18.9	6.1	4	150 nm GaAs MHEMT	[147]
94	16	5.7	4	150 nm GaAs PHEMT	[148]
94	12.5	3.8	2	100 nm GaAs PHEMT	[149]
95	11.1	5.4	3	100 nm ABCS HEMT	[150]
94	20.5	3.9	5	200 nm ABCS HEMT	[151]
98	13		2	100 nm GaAs MHEMT	[152]
90	30	3	4	100 nm InP HEMT	[153]
90	5.6	2.5	1	200 nm ABCS HEMT	[154]
94	22	3.1	3	100 nm GaAs MHEMT	[101]
94	33	3.2		130 nm InP HEMT	[155]
94	35	4.5	7	130 nm InP HEMT	[156]
90	30	4.2	5	100 nm InP HEMT	[157]
94	20	1.8	4	50 nm GaAs MHEMT	[158]
93	19.5	3	3	100 nm InP HEMT	[159]
95	17	2.5	3	70 nm GaAs MHEMT	[160]
85	24.8	2.8	4	100 nm GaAs MHEMT	[161]
97	10.8		2	100 nm GaAs MHEMT	[162]
85	25	2.7	4	70 nm GaAs MHEMT	[163]
98	21.2		5	100 nm InP HEMT	[164]
95	18	2.1	2	35 nm InP HEMT	[165]
94	15	3	3	50 nm GaAs MHEMT	[166]
94	30	1.75	5	100 nm InP HEMT	[167]
90	11	5	2	100 nm GaAs PHEMT	[168]
85	25	2	3	50 nm GaAs MHEMT	[169]
85	18	3.8	3	70 nm GaAs MHEMT	[170]
94	19.5	3.0	3	100 nm GaAs MHEMT	[III]
94	23.0	3.5	4	100 nm GaAs MHEMT	[III]

At D-band (110-170 GHz), there is a local maximum in the atmospheric attenuation curve due to the oxygen molecular resonance line around 118.75 GHz. Measurements around the resonance line together with measurements at the closest window frequency range 125-170 GHz are used to characterize precipitation and snowfall as well as height and depth of the melting layer of clouds [13]. Two LNAs were designed to operate around 155 GHz with the 100 nm MHEMT technology [IV]. A micrograph of one of the amplifiers is presented in Figure 4.5. In addition to standard design library elements, one of the amplifiers includes an interdigital capacitor as an interstage matching element. The interdigital capacitors have lower capacitance per area than the MIM capacitors. When connected in series, this small capacitance will reduce the gain at frequencies below the operating range of the amplifier. The use of the interdigital capacitor also simplifies the design of the interstage matching network [IV], [171]. The amplifiers were tested both on-wafer and in a split-block module [IV]. The on-wafer measurement results are presented in Figure 4.6.

Two LNAs were designed to operate at 165 GHz transmission window frequency with both 50 nm and 100 nm MHEMT technologies [V], [VI]. Narrow band operation was targeted for 165 GHz LNAs. The amplifiers were tested both on-wafer and in a split-block module.

A comparison of published amplifiers in the 130-170 GHz window frequency range is presented in Table 4.3. The LNA demonstrated with the 50 nm MHEMT technology can reach noise figure of 5.2 dB, a feasible value in order to use the amplifier as the first stage of an Earth-observing radiometer.

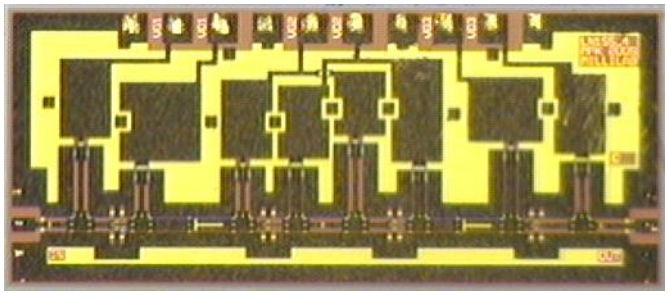

Figure 4.5. Micrograph of a 155 GHz low-noise amplifier [IV].

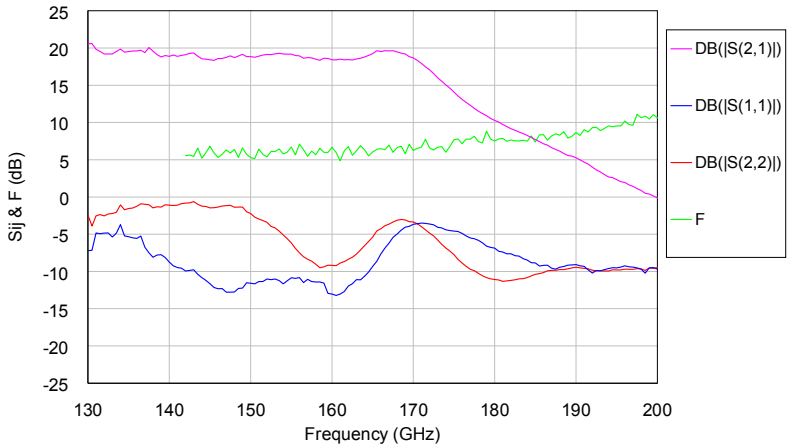

Figure 4.6. S-parameters and noise figure of a 155 GHz amplifier measured on-wafer. Data from [IV].

Table 4.3. Comparison of HEMT based MMIC low noise amplifiers for 130-170 GHz atmospheric window.

Center frequency (GHz)	Gain (dB)	Noise figure (dB)	Number of stages	Technology	Reference
142	9		2	100 nm InP HEMT	[172]
155	12		3	100 nm InP HEMT	[173]
130	14		6	100 nm InP PHEMT	[174]
154	10	5.1	3	100 nm InP PHEMT	[175]
153	7.5		3	120 nm InP HEMT	[176]
141	30		3	100 nm InP HEMT	[177]
155	8		4	70 nm InP PHEMT	[178]
160	6	6	4	80 nm InP PHEMT	[178]
160	26		6	80 nm InP PHEMT	[179]
140	14		4	100 nm InP HEMT	[180]
148	12		4	150 nm GaAs MHEMT	[181]
155	15	4	4	100 nm GaAs MHEMT	[182]
163	17		3	70 nm InP HEMT	[183]
152	8		2	70 nm InP HEMT	[184]
160	21	3.7	3	35 nm InP HEMT	[185]
150	19	4.5	4	70 nm GaAs MHEMT	[160]
130	27	3.8	4	100 nm GaAs MHEMT	[186]
140	20	4	4	50 nm GaAs MHEMT	[186]
155	24	6	4	70 nm GaAs MHEMT	[187]
135	23	3.5	4	20 nm GaAs MHEMT	[188]
160	15		3	75 nm InP HEMT	[190]
165	23		3	35 nm InP HEMT	[189]
130	23		4	50 nm GaAs MHEMT	[191]
140	25	6	4	50 nm GaAs MHEMT	[192]
151	30		4	20 nm GaAs MHEMT	[193]
142	19.0	6.0	4	100 nm GaAs MHEMT	[IV]
150	18.5	6.2	4	100 nm GaAs MHEMT	[IV]
165	25.0	5.2	4	50 nm GaAs MHEMT	[V]
153	20.6	5.2	4	100 nm GaAs MHEMT	[VI]

One amplifier was designed to operate around the 183 GHz water vapor line frequency [VI]. Radiometric measurements around this frequency can be utilized in characterization of water vapor profile and snowfall [13]. The amplifier was manufactured with the 100 nm MHEMT technology and wideband operation was targeted. The amplifier was tested on-wafer. Comparison with published amplifiers around 183 GHz is presented in Table 4.4. While the reported amplifier has 21.4 dB of gain, the noise figure of 7.5 dB is rather high when compared to the noise figures of the other reported amplifiers.

Table 4.4. Comparison of published HEMT based MMIC amplifiers for 183 GHz water vapor absorption peak frequency range.

Center frequency (GHz)	Gain (dB)	Noise figure (dB)	Number of stages	Technology	Reference
190	7.2		2	80 nm InP HEMT	[194]
188	9		2	70 nm InP PHEMT	[178]
189	9		2	80 nm InP PHEMT	[195]
185	18		6	80 nm InP PHEMT	[179]
180	17		8	100 nm InP HEMT	[180]
175	14	7	3	70 nm InP HEMT	[196]
186	15		6	100 nm InP HEMT	[197]
185	15		3	80 nm InP PHEMT	[198]
200	19		8	70 nm GaAs MHEMT	[145]
195	15		4	100 nm GaAs MHEMT	[100]
198	24		4	50 nm GaAs MHEMT	[199]
185	21		3	50 nm InP HEMT	[200]
200	17	4.8	4	50 nm GaAs MHEMT	[99]
180	14	4.2	3	35 nm InP HEMT	[185]
195	20		6	35 nm GaAs MHEMT	[202]
183	15.0	4.8	5	100 nm GaAs MHEMT	[201]
193	17		3	35 nm InP HEMT	[189]
190	23		4	35 nm InP HEMT	[203]
180	10		3	75 nm InP HEMT	[190]
192	23		4	35 nm GaAs MHEMT	[204]
183	20	6.7	5	50 nm GaAs MHEMT	[205]
180	24.5	3.5	5	50 nm GaAs MHEMT	[206]
183	21.4	7.5	5	100 nm GaAs MHEMT	[VI]

5. Passive millimeter-wave imaging

In passive millimeter-wave imaging, the noise temperature of the incoming signal is mapped over the desired area and an image is formed by comparing the incoming signal levels pixel by pixel. The noise temperature of incident radiation is measured by a radiometer. Imaging radiometers typically have high gain and narrow beam antennas to improve angular resolution. When the target fills the antenna beam completely the detected noise temperature is given by (1.12). Main sources of the incident radiation reflected from the object are natural objects (T_{refl} ~300 K) and the sky. At millimeter-wave frequencies, the sky noise is partly due to cosmic background noise and thermal noise caused by the atmospheric attenuation [17]. Thus, the brightness temperature of the sky noise depends on the angle of incidence due to the longer distance through the atmosphere at lover elevation angles. The brightness temperature of the sky as a function of antenna elevation angle at window channel between 70-110 GHz is presented in Figure 5.1. The noise temperature of the sky is more uniform versus incident angle at molecular absorption frequencies due to the increased attenuation of the atmosphere. Due to this increase in attenuation, passive millimeter-wave imaging is performed in window frequency ranges.

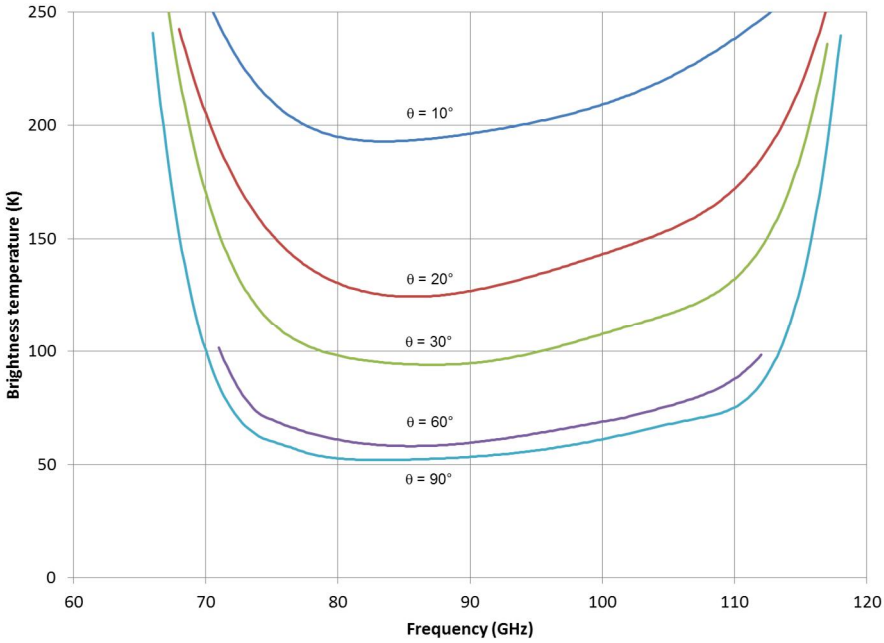

Figure 5.1. Brightness temperature of the sky at different elevation angles as a function of frequency. Adapted from [209]. T = 15°C, p = 1023 mbar, ρ_{water} = 7.5 g/m^3.

Different materials appear to be at different noise temperatures due to emissivity and reflectivity as given by (1.12). Examples of emissivity and reflectivity values of different materials at 94 GHz are presented in Table 5.1.

Table 5.1. Emissivity and reflectivity of different materials at 94 GHz [207], [208].

Material	Emissivity	Reflectivity
Metal	0.04	0.96
Metal under canvas	0.24	0.76
Dry gravel	0.92	0.08
Dry asphalt	0.91	0.09
Brick	0.90	0.10
Grass	0.95	0.05
Water, smooth surface	0.59	0.41
Human skin	0.90	0.10

5.1 Passive millimeter-wave imager

A passive millimeter-wave imager was built as a part of this work [VII], [210]. The focus of the system design was on the quality of images in terms of radiometric resolution ΔT by increasing the integration time. This results in a slow imaging speed. The targeted operational center frequency was around 94 GHz located in the atmospheric window frequency range. Other restrictions to the system were given by the movability and availability of the components.

The imaging system has a 300 mm diameter lens horn antenna with less than 1° beamwidth specified by the manufacturer. The far-field of the antenna, where radiation can be approximated as a plane wave and the antenna radiation pattern is well defined, is reached after 56 m. In order to use the antenna also for observing targets that are at a distance less than 56 m from the antenna, an additional focusing lens was manufactured from high density polyethylene (HDPE). The hyperboloid shaped focusing lens moves the focal point of the antenna from infinity to the distance of 2 m [210], [211].

The Dicke-radiometer used in the imaging system is presented in Figure 5.2. The first component of the radiometer is a PIN diode based single-pole-double-throw (SPDT) switch which connects either the antenna or reference load to the low-noise amplifier input. A waveguide termination is used as the reference load to reduce effects of gain variation. Complete noise temperature calibration would require two loads with different noise temperatures. The amplification chain consists of two low-noise amplifiers and the signal is detected by a wideband diode detector. Isolators have been utilized to reduce reflections due to mismatches between the amplifiers and the detector. The signal from the detector is amplified by a gain controlled video amplifier. The signal from the video amplifier is digitized by an AD-converter. The noise temperature and insertion gain of the radiometer chain from the switch input to the output of the second isolator measured with a noise figure measurement system are presented in Figure 5.3. The 3 dB bandwidth of the radiometer defined by the LNAs is roughly 90-96 GHz where a noise temperature of 900 K or better is achieved. Theoretical radiometric sensitivity ΔT calculated with (1.16) is 0.2 K with 20 ms integration time. In practice, additional noise coupling with the signal after the detector increase ΔT to 1 K [210].

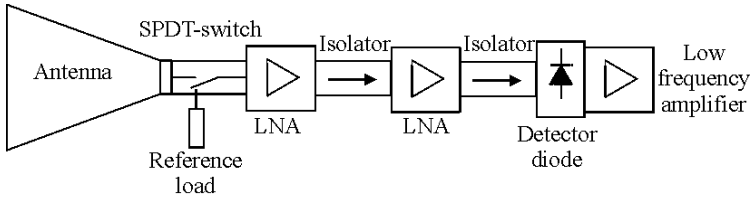

Figure 5.2. Realized Dicke-radiometer for the passive imaging system.

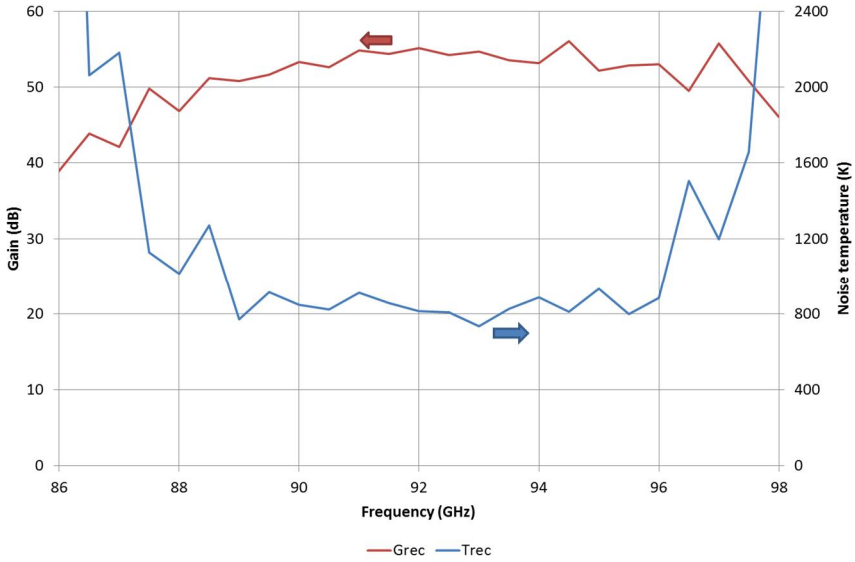

Figure 5.3. Gain and noise temperature of radiometer chain from the switch input to the output of the second isolator in the realized passive millimeter-wave imager.

The antenna and the radiometer are mounted on a structure where the antenna azimuth and elevation are controlled by stepper motors. The antenna elevation movement is continuous providing a so called line scan, while the azimuth movement is performed with discrete steps. The in-house written software controls the motors and produces the final millimeter-wave image. The millimeter-wave image is produced by sampling the line scan signal to discrete pixels. The scanning speed is set by integration time, 20 ms was selected as a trade-off between ΔT and imaging speed. A photograph of the imaging system is presented in Figure 5.4.

Figure 5.4. A photograph of the realized millimeter-wave imaging system.

5.2 Experimental results

Two main applications of passive millimeter-wave imaging, contraband detection and area surveillance, were studied with the realized imaging system. A photograph and an indoor taken millimeter-wave image of a contraband detection is presented in Figure 5.5. Higher noise temperatures are mapped with darker color and lower noise temperatures are mapped with lighter color in the grayscale image. The mapping is scaled within a single image, the lowest temperature is white and the highest temperature is black. Similar mapping is used in all millimeter-wave images presented in this thesis. The person in the photo is holding a metallic handgun silhouette under his shirt. The silhouette is seen as a lighter area in the millimeter-wave, while the person appears darker. A sharper image would require an even narrower antenna beam. The noise reflected by the metal silhouette is emitted by the walls, thus the silhouette is seen as grayscale color similar to the surroundings. Also, “a millimeter-wave shadow”, noise of the person reflected by the background wall is visible in the millimeter-wave image.

a)

b)

c)

Figure 5.5. a) A photograph b) an indoor taken millimeter-wave image of a person with c) a metal gun silhouette under his shirt. Data from [210].

Figure 5.6 shows a similar passive millimeter-wave image of contraband detection taken outdoors. The person on the right is hiding the metallic handgun silhouette under his jacket. Outdoors a significant part of the incident radiation to the target comes from the cold sky and the contrast is improved. The body parts that reflect the sky radiation towards the radiometer, such as the forehead, shoulders and arms appear lighter than the rest of the body. Also, keys and cellphone that are in the trouser pockets of the person on the left appear bright.

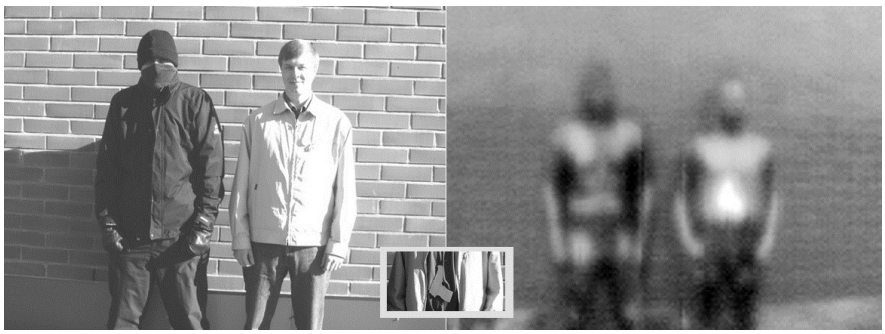

Figure 5.6. A photograph (*left*) and a millimeter-wave image (*right*) of two persons taken outdoors. The person on the right has a metal gun silhouette under his jacket. Data from [VII]

Millimeter waves penetrate dust, smoke, and fog much better than visible light or infrared light. Thus, millimeter-wave imaging can be used as an alternative for wide area surveillance under poor visibility conditions. A photograph and a millimeter-wave image over a wide area are presented in Figure 5.7. Different soil types, a walk path, trees, buildings and metallic objects can be distinguished from the image. The strongest reflections come from a car, roofs, a trash container, and street lamps. A cooling effect of the shadow on the grass can also be seen on the lower left part of the image. A similar image could be produced under the presence of fog.

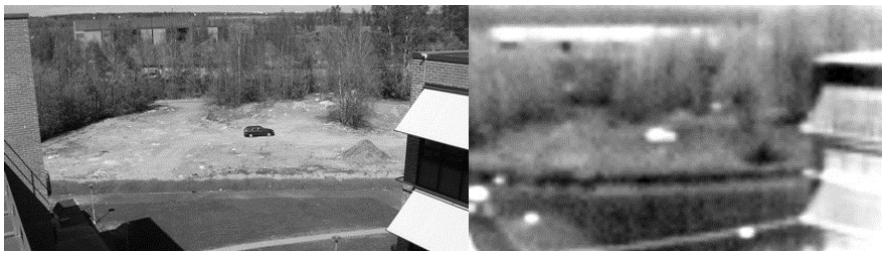

Figure 5.7. A photograph (*left*) and a millimeter-wave image (*right*) of a scenery. Data from [VII].

6. Summary of the appended publications

[I] “A wide-band on-wafer noise parameter measurement system at 50-75 GHz”

The design and performance verification of an automated on-wafer noise parameter system are presented in this publication. The motivation for the work was the ability to accurately characterize the noise performance of transistors over 50-75 GHz range for either modelling or verification purposes. The measurements are performed according to so called cold-source method and the operation of the test system is verified using both a passive and an active test device. The results and uncertainty analysis presented in the paper show that the measurement system can be used for transistor noise characterization with reasonable accuracy.

[II] “Active cold load MMICs for Ka-, V-, and W-bands”

The design and characterization of integrated active cold loads is presented in this publication. Motivation for the work is to use internal calibration loads to calibrate most parts of a radiometer without the need to use external loads, which usually require complex maneuvers of the radiometer or its platform. Additionally, the hybrid circuit realization of the ACLs that has successfully been used at lower frequencies becomes infeasible at millimeter-wave frequency range. Thus, the MMIC realization of ACLs was studied by designing three ACLs for selected frequencies within the 30-100 GHz range. The measured noise temperatures of the realized loads were 75, 141, and 170 K at 31.4, 52.0, and 89.0 GHz, respectively. While the achieved noise temperatures are useful for radiometer calibration in general, a careful case-by-case analysis for their use in an actual system is needed.

[III] “W-band low noise amplifiers”

The motivation for the work presented in this publication was to study the feasibility of 100 nm MHEMT process for realization of W-band low-noise amplifiers for radiometers. W-band radiometers are useful for instruments of weather forecasting satellites as well as for millimeter-imaging. Additionally, the W-band low-noise amplifiers are used in collision avoidance radars in cars as well as in high-speed data transfer communication systems. Multiple designs of W-band amplifiers are presented in the publication with 18-23 dB gain and 3.0-3.5 dB noise figure measured on-wafer. Also, the measurement results of amplifier

modules, both at room temperature and at cryogenic temperatures, are presented. The presented results demonstrated the feasibility of the 100 nm MHEMT technology for W-band low-noise amplifiers.

[IV] “Low noise amplifiers for D-band“

The motivation for the work presented in this publication was to study the feasibility of the 100 nm MHEMT process for realization of D-band low-noise amplifiers for radiometers. D-band radiometers are useful for instruments of weather forecasting satellites. Multiple designs of D-band amplifiers are presented in the publication with 17.6-22.7 dB gain and 5.5-7.0 dB noise figure measured on-wafer. Targeted gain values were achieved with the presented designs, but lower noise figures would be preferred for better sensitivity for D-band radiometers. Some amplifiers were packaged in split-block packages and the measurement results show only a slight decrease in performance.

[V] “MHEMT G-band low-noise amplifiers”

The motivation for the work presented in this publication was to study the feasibility of the 50 nm MHEMT process for realization of G-band low-noise amplifiers for radiometers, namely for 165 and 183 GHz. Combination of these frequencies is utilized for water vapor profiling for weather forecasting. Additionally, one of the aims was to compare performance of the LNAs manufactured with the 50 nm process against similar circuits manufactured with the 100 nm process. Multiple amplifier designs are presented for both frequencies in the publication. On-wafer measured performance show 25 dB of gain with 5.2 dB noise figure at 165 GHz and 20 dB of gain with 6.7 dB noise figure at 183 GHz.

[VI] “Low noise amplifiers for G-band radiometers”

The motivation for the work presented in this publication was to study the feasibility of the 100 nm MHEMT process for realization of G-band low-noise amplifiers for radiometers, namely for 165 and 183 GHz. Combination of these frequencies is utilized for water vapor profiling for weather forecasting. Multiple amplifier designs are presented for both frequencies in the publication. On-wafer measured performance show 19.2-27.4 dB peak gain and 4-8 dB noise figure. There is a frequency shift in the measured responses of the amplifiers compared to simulated ones.

[VII] “Passive millimeter-wave imager”

The motivation of this work was to demonstrate millimeter-wave imaging around 94 GHz by setting up a radiometer based imaging system and create images for different application scenarios. The design of the imaging system based on the Dicke-radiometer is presented in the publication. The operation of the imaging system is demonstrated by millimeter-wave images. The capabilities of the imaging system were demonstrated by the millimeter-wave images for security

screening both indoors and outdoors as well as for area surveillance are presented.

7. Conclusions

The research work presented in this thesis focused on design and characterization of low-noise circuits for radiometers. A measurement system for transistor noise parameter characterization was developed for 50-75 GHz range. The system can be used to provide data for device modeling or to verify existing models generated with data from lower frequency measurements. While the initial target was the modeling of III-V compound semiconductor devices, the recent developments with CMOS and SiGe technologies have increased the demand for transistor noise modeling at millimeter-wave range. The developed measurement system has been utilized in transistor measurements, both for in-house projects as well as a commercial service.

In some radiometric applications the internal calibration of the radiometer is required or the number of calibrations with measurements of external calibration loads could be reduced with internal calibration. The ACLs developed in this work demonstrate the capabilities of MMIC technology for ACL realization up to 100 GHz. Especially at the lower end of the millimeter-wave region, the realized cold load noise temperature is close to the boiling temperature of nitrogen which is a commonly used to cool absorber materials to provide a calibrated noise temperature.

A number of low-noise amplifiers for selected bands between 75-200 GHz range has been designed. The European Space Agency ordered a series of research projects to study the feasibility of MHEMT technology for radiometer applications. In the first projects the design work focused on the 100 nm MHEMT process. While these first design projects progressed, Fraunhofer IAF matured their 50 nm MHEMT process to the point that it could be used in the designs of the final projects. The work presented in this thesis partially demonstrated the maturity of the MHEMT technology for millimeter-wave low-noise amplifiers for space. Due to better noise performance, the 50 nm MHEMT process from Fraunhofer IAF, is the prime candidate to be used in the MetOp-SG, the next generation weather satellites, most likely up to 229 GHz.

In order to demonstrate terrestrial use of millimeter-wave radiometers a millimeter-wave imager was built. The quality of millimeter-wave images was emphasized in the imager design in expense of imaging time. The taken images demonstrate qualitatively the possibilities of millimeter-wave imaging in security

and surveillance applications. Quantitative assessment of the images as well as re-design of the entire system would be necessary for more practical use of millimeter-wave imaging.

References

[1] Jarosik, N., Bennett, C.L., Halpern, M., Hinshaw, G., Kogut, A., Limon, M., Meyer, S.S., Page, L., Pospieszalski, M., Spergel, D.N., Tucker, G. S., Wilkinson, D.T., Wollack, E., Wright, E.L., Zhang, Z., "Design, implementation, and testing of the microwave anisotropy probe radiometers," *The Astrophysical Journal Supplement Series*, vol. 145, pp. 413-436, Apr. 2003.

[2] Mennella, A., Bersanelli, M., Butler, R.C., Maino, D., Mandolesi, N., Morgante, G., Valenziano, L., Villa, F., Gaier, T., Seiffert, M., Levin, S., Lawrence, C., Meinhold, P., Lubin, P., Tuovinen, J., Varis, J., Karttaavi, T., Hughes, N., Jukkala, P., Sjöman, P., Kangaslahti, P., Roddis, N., Kettle, D., Winder, F., Blackhurst, E. , Davis, R., Wilkinson, A., Castelli, C., Aja, B., Artal, E., de la Fuente, L., Mediavilla, A., Pascual, J.P., Gallegos, J., Martinez-Gonzalez, E., de Paco, P., Pradell, L., "Advanced pseudo-correlation radiometers for the Planck-LFI instrument," in *Proceedings of 3rd ESA Workshop on Millimetre-Wave Technology and Applications*, Espoo, Finland, 2003, pp. 69-74.

[3] Lamarre, J.-M., Puget, J.-L., Ade, P.A.R., Bouchet, F., Guyot, G., Lange, A.E., Pajot, F., Arondel, A., Benabed, K., Beney, J.-L., Benoit, A., Bernard, J.-Ph., Bhatia, R., Blanc, Y., Bock, J.J., Bréelle, E., Bradshaw, T.W., Camus, P., Catalano, A., Charra, J., Charra, M., Church, S.E., Couchot, F., Coulais, A., Crill, B.P., Crook, M.R., Dassas, K., de Bernardis, P., Delabrouille, J., de Marcillac, P., Delouis, J.-M., Désert, F.-X., Dumesnil, C., Dupac, X., Efstathiou, G., Eng, P., Evesque, C., Fourmond, J.-J., Ganga, K., Giard, M., Gispert, R., Guglielmi, L., Haissinski, J., Henrot-Versillé, S., Hivon, E., Holmes, W.A., Jones, W.C., Koch, T.C., Lagardère, H., Lami, P., Landé, J., Leriche, B., Leroy, C., Longval, Y., Macías-Pérez, J.F., Maciaszek, T., Maffei, B., Mansoux, B., Marty,C., Masi, S., Mercier, C., Miville-Deschênes, M.-A., Moneti, A., Montier, L., Murphy, J.A., Narbonne, J., Nexon, M., Paine, C.G., Pahn, J., Perdereau, O., Piacentini, F., Piat, M., Plaszczynski, S., Pointecouteau, E., Pons, R., Ponthieu, N., Prunet, S., Rambaud, D., Recouvreur, G., Renault, C., Ristorcelli, I., Rosset, C., Santos, D., Savini, G., Serra, G., Stassi, P., Sudiwala, R.V., Sygnet , J.-F., Tauber, J.A., Torre, J.-P., Tristram, M., Vibert, L., Woodcraft, A., Yurchenko, V., Yvon, D., "Planck pre-launch status: The HFI instrument, from specification to actual performance," *Astronomy & Astrophysics*, vol. 520, no. A9, pp. 1-20, Sept. 2010.

[4] Peck, A.B., Beasley, A.J., “High resolution sub-millimeter imaging with ALMA,” *Journal of Physics: Conference Series*, vol. 131, no. 1, 012049, Oct. 2008.

[5] Rasshofer R.H., Naab K., “77 GHz long range radar systems status, ongoing developments and future challenges,” in *Proceedings of 2nd European Radar Conference 2005*, Paris, France, 2005, pp. 161-164.

[6] Klein, L.A., *Millimeter-Wave and Infrared Multisensor Design and Signal Processing*, Artech House, Norwood, MA, 1997.

[7] Mikkonen J., Corrado C., Evci C., Prögler M., “Emerging wireless broadband networks,” *IEEE Communications Magazine*, vol. 36, no. 2, pp. 112-117, 1998.

[8] Wang, P., Li, Y., Song, L., Vucetic, B., “Multi-gigabit millimeter wave wireless communications for 5G: From fixed access to cellular networks,” *IEEE Communications Magazine*, vol. 53, no. 1, pp. 168-178, Jan. 2015.

[9] Wang, C., Lin, C., Chen, Q., Lu, B., Deng, X., Zhang, J., “A 10-Gbit/s wireless communication link using 16-QAM modulation in 140-GHz band,” *IEEE Transactions on Microwave Theory and Techniques*, vol. 61, no. 7, pp. 2737-2746, July 2013.

[10] Kallfass, I., Antes, J., Schneider, T., Kurz, F., Lopez-Diaz, D., Diebold, S., Massler, H., Leuther, A., Tessmann, A., “All active MMIC-based wireless communication at 220 GHz,” *IEEE Transactions on Terahertz Science and Technology*, vol. 1, no. 2, pp. 477-487, Nov. 2011.

[11] Beas, J., Castanon, G., Aldaya, I., Aragon-Zavala, A., Campuzano, G., “Millimeter-wave frequency radio over fiber systems: A survey,” *IEEE Communications Surveys & Tutorials*, vol. 15, no. 4, pp. 1593-1619, Q4 2013.

[12] Pursula, P., Vähä-Heikkilä, T., Muller, A., Neculoiu, D., Konstantinidis, G., Oja, A., Tuovinen, J., “Millimeter-wave identification—A new short-range radio system for low-power high data-rate applications,” *IEEE Transactions on Microwave Theory and Techniques*, vol. 56, no. 10, pp. 2221-2228, Oct. 2008.

[13] Kangas, V., D'Addio, S., Betto, M., Barre, H., Loiselet, M., Mason, G., "MetOp second generation microwave sounding and microwave imaging missions," in *2012 EUMETSAT Meteorological Satellite Conference*, Sopot, Poland, 2012. Available: http://www.eumetsat.int/website/wcm/idc/idcplg?IdcService=GET_FILE&dDocName=PDF_CONF_P61_S1_09_KANGAS_V&RevisionSelectionMethod=LatestReleased&Rendition=Web. Accessed on 25.11.2016.

[14] Moradi, I., Ferraro, R.R., Eriksson, P., Weng, F., "Intercalibration and validation of observations from ATMS and SAPHIR microwave sounders," *IEEE Transactions on Geoscience and Remote Sensing*, vol. 53, no. 11, pp. 5915-5925, Nov. 2015.

[15] Friis, H.T, "Noise figure of radio receivers," *Proceedings of I.R.E.*, vol. 32, no. 7, pp. 419-422, July 1944.

[16] Miller, C.K.S., Daywitt, W.C., Arthur, M.G., "Noise standards, measurements, and receiver noise definitions," *Proceedings of IEEE*, vol. 55, no. 6, pp. 865-877, June 1967.

[17] Ulaby, F.T., Moore, R.K., Fung, A.K., *Microwave Remote Sensing: Active and Passive, Volume I: Microwave Remote Sensing Fundamentals and Radiometry*, Addison-Wesley Publishing Company, Reading, MA, 1981.

[18] Tiuri, M.E., Räisänen, A.V, "Radio-telescope receivers," Chapter 7 in Kraus, J.D., *Radio Astronomy, 2nd ed.*, Cygnus-Quasar, 1986.

[19] Dicke, R.H., "The measurement of thermal radiation at microwave frequencies," *Review of Scientific Instruments*, vol. 17, no. 7, pp. 268-275, July 1946.

[20] Adler, R., Haus, H.A., Engelbrecht, R.S., Lebenbaum, M.T., Harrison, S.W., Mumford, W.W., "Description of the noise performance of amplifiers and receiving systems," *Proceedings of the IEEE*, vol. 51, no. 3, pp. 436-442, Mar. 1963.

[21] ITU Recommendation, "Attenuation by atmospheric gases," Recommendation ITU-R P.676-10, Sept. 2013.

[22] Wang, H., Lin, K.-Y., Tsai, Z.-M., Lu, L.-H., Lu, H.-C., Wang, C.-H., Tsai, J.-H., Huang, T.-W., Lin, Y.-C., "MMICs in the millimeter-wave regime," *IEEE Microwave Magazine*, vol. 10, no. 1, pp. 99-117, Feb. 2009.

[23] Ali, F., Gupta, A. (eds.), *HEMTs & HBTs: Devices, Fabrication, and Circuits*, Artech House, Norwood, MA, 1991.

[24] Whelan, C.S., Marsh, P.F., Hoke, W.E., McTaggart, R.A., McCarrol, C.P., Kazior, T.E., "GaAs metamorphic HEMT (MHEMT): An attractive alternative to InP HEMTs for high performance low noise and power applications," in *2000 IEEE International Conference of Indium Phosphide and Related Materials Conference Proceedings*, Williamsburg, VA, 2000, pp. 337-340.

[25] Leuther, A., Tessmann, A., Kallfass, I., Massler, H., Loesch, R., Schlechtweg, M., Mikulla, M., Ambacher, O., "Metamorphic HEMT technology for submillimeter-wave MMIC applications," in *2010 IEEE International conference of Indium Phosphide and Related Materials Conference Proceedings*, Kagawa, Japan, 2010, pp. 1-6.

[26] Anholt, R., *Electrical and Thermal Characterization of MESFETs, HEMTs, and HBTs*, Artech House, Norwood, MA, 1995.

[27] Golio, J.M., *Microwave MESFETs and HEMTs*, Artech House, Norwood, MA, 1991.

[28] Pospieszalski, M.W., "Modeling of noise parameters of MESFETs and MODFETs and their frequency and temperature dependence," *IEEE Transactions on Microwave Theory and Techniques*, vol. 37, no. 9, pp. 1340-1350, Sept. 1989.

[29] Rothe, H., Dahlke, W., "Theory of noisy fourpoles," *Proceedings of the I.R.E.*, vol. 44, no. 6, pp. 811-818, June 1956.

[30] Rollett, J.M., "Stability and power-gain invariants of linear twoports," *IRE Transactions on Circuit Theory*, vol. 9, no. 1, pp. 29-32, Jan. 1962.

[31] Gonzales, G., *Microwave Transistor Amplifier Design,* Prentice Hall Inc., Upper saddle River, NJ, 1997.

[32] Edwards, M.L., Sinsky, J.H., "A new criterion for linear 2-port stability using geometrically derived parameters", *IEEE Transactions on Microwave Theory and Techniques*, vol. 40, no. 12, pp. 2303-2311, Dec. 1992.

[33] GGB [Online]. Available: http://ggb.com/. Accessed on 21.11.2016.

[34] Cascade Microtech [Online]. Available: http://www.cascademicrotech.com/. Accessed on 21.11.2016.

[35] Dominion DMPI [Online]. Available: http://dmprobes.com/indexM1.html. Accessed on 21.11.2016.

[36] Virginia Diodes [Online]. Available: http://www.vadiodes.com/en/. Accessed on 21.11.2016.

[37] Radiometer Physics [Online]. Available: http://www.radiometer-physics.de. Accessed on 21.11.2016.

[38] Keysight technologies [Online]. Available: http://www.keysight.com/main/home.jspx?cc=US&lc=eng. Accessed on 21.11.2016.

[39] Elva-1 [Online]. Available: http://www.elva-1.com/. Accessed on 21.11.2016.

[40] Dahlberg, K., "Development of on-wafer calibration methods and planar Schottky diode characterization at THz frequencies", *Doctoral Thesis*, Aalto University, Espoo, Finland, 2015.

[41] Engen, G.F., Hoer, C.A., "Thru-reflect-line: An improved technique for calibrating the dual six-port automatic network analyzer," *IEEE Transactions on Microwave Theory and Techniques*, vol. 27, no. 12, pp. 987-993, Apr. 1979.

[42] Davidson, A., Jones K., Strid, E., "LRM and LRRM calibrations with automatic determination of load conductance," in *36th ARTFG Conference Digest*, Monterrey, CA, 1990, pp. 57-63.

[43] Gaier, T., Samoska,, L., Fung, A., Deal, W.R., Radisic, V., Mei, X.B., Yoshida, W., Liu, P.H., Uyeda, J., Barsky, M., Lai, R., "Measurement of a 270 GHz low noise amplifier with 7.5 dB noise figure," *IEEE Microwave and Wireless Components Letters*, vol. 17, no. 7, pp. 546-548, July 2007.

[44] Dietlein, C., Popovic, Z., Grossman, E.N., "Aqueous blackbody calibration source for millimeter-wave/terahertz metrology," *Applied Optics*, vol. 47, no. 30, 5604-5615, Oct. 2008.

[45] Tasker, P.J., Reinert, W., Braunstein, J., Schlechtweg, M., "Transistor direct extraction of all four transistor noise parameters from a single noise figure measurement," in *Proceedings of the 22nd European Microwave Conference*, Helsinki, Finland, 1992, pp. 157-162.

[46] Dambrine, G., Happy, H., Danneville, F., Cappy, A., “A new method for on wafer noise measurement,” *IEEE Transactions on Microwave Theory and Techniques*, vol. 41, no. 3, pp. 375-380, Mar. 1993.

[47] Tasker, P.J., Reinert, W., Hughes, B., Braunstein, J., Schlechtweg, M., “Transistor noise parameter extraction using a 50 Ω measurement system,” in *1993 IEEE MTT Symposium Digest*, Atlanta, GA, 1993, pp. 1251-1254.

[48] Lázaro, A., Pradell, L., O’Callaghan, J.M., “FET noise-parameter determination using a novel technique based on 50-Ω noise-figure measurements,” *IEEE Transactions on Microwave Theory and Techniques*, vol. 47, no. 3, pp. 315-324, Mar. 1999.

[49] De Dominicis, M., Giannini, F., Limiti, E., Serino, A., “Direct noise characterization of microwave FET using 50Ω noise figure and Y-parameter measurements”, *Microwave and Optical Technology Letters*, vol. 44, no. 6, pp. 565-569, Mar. 2005.

[50] Ciccognani, W., Giannini, F., Limiti, E., Nanni, A., Serino, A., Lanzieri, C., Peroni, M., “Extraction of microwave FET noise parameters using frequency-dependent equivalent noise temperatures,” in *Proceedings of SBMO/IEEE MTT-S International Microwave and Optoelectronics Conference*, Salvador, Brazil, 2007, pp. 856-860.

[51] Strid, E., “Noise measurements of low-noise GaAs FET amplifiers,” *Microwave System News,* vol. 10, pp. 62-70, Nov. 1981.

[52] Meierer, R., Tsironis, C., “An on-wafer noise parameter measurement technique with automatic receiver calibration,” *Microwave Journal*, vol. 38, no. 3, pp. 22-37, Mar. 1995.

[53] Lane, R.Q., “The determination of device noise parameters,” *Proceedings of the IEEE*, vol. 57, no. 8, pp. 1461-1462, Aug. 1969.

[54] Vickes H. O., “*Microwave and millimeter-wave FETs and noise parameter measurements*,” Technical report no. 203, Gothenburg Chalmers University of Technology, 1990.

[55] O'Callaghan, J.M., Mondal, J.P., “A vector approach for noise parameter fitting and selection of source admittances,” *IEEE Transactions on Microwave Theory and Techniques*, vol. 39, no. 8, pp. 1376-1382, Aug. 1991.

[56] Mitama, M. Katoh, H., “An improved computational method for noise parameter measurement,” *IEEE Transactions on Microwave Theory and Techniques*, vol. 27, no. 6, pp.612-615, June 1979.

[57] Chen, H.-Y., Chen, K.-M., Huang, G.-W., Cho. M.-H., Chang, C.-Y., “Computation of noise parameters using genetic algorithms,” in *Proceedings of the 34th European Microwave Conference*, Amsterdam, The Netherlands, 2004, pp. 789-792.

[58] Vasilescu, G.I., Alquie, G., Krim, M., “Exact computation of two-port noise parameters,” *Electronics Letters*, vol. 25, no. 4, pp. 292-293, 1989.

[59] Escotte, L., Plana, R., Graffeuil, J., “Evaluation of noise parameter extraction methods,” *IEEE Transactions on Microwave Theory and Techniques*, vol. 41, no. 3, pp. 382-387, Mar. 1993.

[60] Press, W.H., Flannery, B.P., Teukolsky, S.A., Vetterling, W.T., *Numerical Recipies, The Art of Scientific Computing*, Cambridge University Press, Cambridge, UK, 1986.

[61] Taylor, B.N., Kuyatt, C.E., "*Guidelines for evaluating and expressing the uncertainty of NIST measurement results*." NIST Technical Note 1297, 1994 edition.

[62] Lahdes, M., “Uncertainty analysis of V-band on-wafer noise parameter measurement system,” in *Proceedings of the 28th European Microwave Conference*, Amsterdam, The Netherlands, 1998, pp. 445-450.

[63] Vähä-Heikkilä, T., Lahdes, M., Kantanen, M., Tuovinen, J., “On-wafer noise-parameter measurements at W-band,” *IEEE Transactions on Microwave Theory and Techniques*, vol. 51, no. 6, pp. 1621-1628, June 2003.

[64] Kantanen, M., Vähä-Heikkilä, T., Lahdes, M., Tuovinen, J., “Transistor noise characterisation at 50-94 GHz,” in *Proceedings of 3rd ESA Workshop on Millimetre-Wave Technology and Applications*, Espoo, Finland, 2003, pp. 529-533.

[65] Bessemoulin, A., Fellon, P., Gruenenpuett, J., Massler, H., Reinert, W., Kohn, E., Tessmann, A., “High gain 110GHz low noise amplifier MMICs using 120nm metamorphic HEMTs and coplanar waveguides,” in *Proceedings of 13th GAAS Symposium*, Paris, France, 2005, pp. 77-80.

[66] Niknejad, A.M., Emani, S., Doan, C., Heydari, B., Bohsali, M., “Design and modeling of active and passive devices,” Chapter 3 in *mm-Wave Silicon Technology 60 GHz and Beyond*, Niknejad, A.M., Hashemi, H. (eds.), Springer, 2008.

[67] Varonen, M., Kärkkäinen, M., Kantanen, M., Halonen, K.A.I., “Millimeter-wave integrated circuits in 65-nm CMOS,” *IEEE Journal of Solid-State Circuits*, vol. 43, no. 9, pp. 1991-2002, Sept. 2008.

[68] Karttaavi, T., Kantanen, M., Holmberg, J., “Transistor noise modeling for a 60 GHz CMOS LNA,” in *Proceedings of Global Symposium on Millimeter-Waves 2010*, Seoul, South Korea, 2010.

[69] Lahdes, M., Sipilä, M., Tuovinen, J., “60 GHz noise parameter measurements using cold-source method,” in *49th ARFTG Conference Digest*, Denver, CO, 1997, pp. 146-154.

[70] Lahdes, M., Tuovinen, J., “V-band on-wafer noise parameter measurements,” in *Proceedings of GaAs 1998, The European Gallium Arsenide & Related III-V Compounds Applications Symposium*, Amsterdam, The Netherlands, 1998, pp. 39-44.

[71] Béland, P., Roy, L., Labonté, Stubbs, M., “An enhanced on-wafer millimeter-wave noise parameter measurement system,” *IEEE Transactions on Instrumentation and Measurements*, vol. 48, no. 4, pp. 825-829, Aug. 1999.

[72] Webster, R.T., Slobodnik, A.J. Jr., Roberts, G.A., “Determination of InP HEMT noise parameters and S-parameters to 60 GHz,” *IEEE Transactions on Microwave Theory and Techniques*, vol. 43, no. 6, pp. 1216-1225, June 1995.

[73] Alam, T.A., Pollard, R.D., Snowden, C.M., “The determination of on-wafer noise parameters at W-band,” in *Proceedings of the 27th European Microwave Conference*, Jerusalem, Israel, 1997, pp. 687-691.

[74] Alam, T.A., Pollard, R.D., Snowden, C.M., “Determination of W-band noise parameters,” *Electronics Letters*, vol. 34, no. 3, pp. 288-289, Feb. 1998.

[75] Tagro, Y., Gloria, D., Boret, S., Morandini, Y., Dambrine, G., “In-situ silicon integrated tuner for automated on-wafer MMW noise parameter extraction of Si HBT and MOSFET in the range 60~110 GHz,“ in *72th ARFTG Conference Digest*, Portland, OR, 2008, pp. 119-122.

[76] Tagro, Y., Gloria, D., Boret, S., Morandini, Y., Dambrine, G., “In-situ silicon integrated tuner for automated on-wafer MMW noise parameters extraction using multi-impedance method for transistor characterization,” in *IEEE International Conference on Microelectronic Test Structures 2009*, Oxnard, CA, 2009, pp. 184-188.

[77] Tagro, Y., Gloria, D., Boret, S., Dambrine, G., “MMW lab in-situ to extract noise parameters of 65nm CMOS aiming 70~90 GHz applications,” in *2009 IEEE RFIC Symposium Digest*, Boston, MA, 2009, pp. 397-400.

[78] Tagro, Y., Waldhoff, N., Gloria, D., Boret, S., “In situ silicon-integrated tuner for automated on-wafer MMW noise parameters extraction using multi-impedance method for transistor characterization,” *IEEE Transactions on Semiconductor Manufacturing*, vol. 25, no. 2, pp. 170-177, May 2012.

[79] Yau, K.H.K., Chevalier, P., Chantre, A., Voinigescu, S.P., “Characterization of the noise parameters of SiGe HBTs in the 70–170-GHz range,” *IEEE Transactions on Microwave Theory and Techniques*, vol. 59, no. 8, pp. 1983-2000, Aug. 2011.

[80] Racette, P., “Radiometer design analysis based upon measurement uncertainty,” *Doctoral Thesis*, The George Washington University, Washington, D.C., 2005.

[81] Frater, R. H., Williams, D. R., “An active ‘cold’ noise source,” *IEEE Transactions on Microwave Theory and Techniques*, vol. 29, no. 4, pp. 344-347, Apr. 1981.

[82] Dunleavy, L. P., Smith, M. C., Lardizabal, S. M., “Design and characterization of FET based cold/hot noise sources,” in *IEEE MMT-S International Microwave Symposium Digest*, Denver, CO, 1997, pp. 1293-1296.

[83] Buhles, P. M., Lardizabal, S. M., “Design and characterization of MMIC active cold loads,” in *Radio Frequency Integrated Circuits Symposium Digest*, Boston, MA, 2000, pp. 221-225.

[84] Ciccognani, W., Giannini, F., Limit, E., Longhi, P. E., “Analysis, design and measurement of active low-noise terminations,” in *Proceedings of 14th Conference on Microwave Techniques (COMITE)*, Prague, Czech Republic, 2008, pp. 1-4.

[85] Sobjaerg, S. S., Skou, N., Barling, J. E., “Measurements on active cold loads for radiometer calibration,” *IEEE Transactions on Geoscience and Remote Sensing*, vol. 47, no. 9, pp. 3134-3139, Sept. 2009.

[86] Bredin, C., Sanson, D., Mohammed, N., Orlhac, J. C., Goutoule, J. M., Escotte, L., Piironen, P., “23.8 GHz and 36.5 GHz active cold loads for radiometer calibration,” in *Proceedings of ESA/ESTEC Workshop on Microwave Technology and Techniques*, Noordwijk, The Netherlands, 2010, p. 22.

[87] Scheeler, R., Popovic, Z., "A 1.4 GHz MMIC active cold noise source," in *Technical Digest of 2013 IEEE Compound Semiconductor Integrated Circuit Symposium*, Monterey, CA, 2013, pp.1-4.

[88] Weissbrodt, E., Tessmann, A., Schlechtweg, M., Kalfass, I., Ambacher, O., “Active load modules for W-band radiometer calibration,” in *Proceedings of 2012 IEEE International Geoscience and Remote Sensing Symposium*, Munich, Germany, 2012, pp. 2945-2948.

[89] Diebold, S.,Weissbrodt, E., Massler, H., Leuther, A., Tessmann, A., Kalfass, I., “A W-band monolithic integrated active hot and cold load noise source,” *IEEE Transactions on Microwave Theory and Techniques*, vol. 62, no. 3, pp. 623-630, Mar. 2014.

[90] Zirath, H., Winberg, E., “A novel millimeter-wave solid state noise source,” in *Proceedings of 15th European Microwave Conference*, Paris, France, 1984, pp. 297-302.

[91] Weatherspoon, M. H., Dunleavy, L. P., “Experimental validation of generalized equations for FET cold source design,” *IEEE Transactions on Microwave Theory and Techniques*, vol. 54, no. 2, pp. 608-614, Feb. 2006.

[92] Meys, R. P., “A wave approach to noise properties of linear microwave devices,” *IEEE Transactions on Microwave Theory and Techniques*, vol. 26, no. 1, pp 34-37, Jan. 1978.

[93] Penfield, P., “Wave representation of amplifier noise,” *IRE Transactions on Circuit Theory*, vol. 9, no. 1, pp.84-86, Mar. 1962.

[94] Haus, H.A., Adler, R.B., “Optimum noise performance of linear amplifiers”, *Proceedings of the IRE*, vol. 46, no. 8, pp. 1517-1533, Aug. 1958.

[95] Leong, K.M.K.H., Mei, X., Yoshida, W., Liu, P.-H., Zhou, Z., Lange, M., Lee, L.-S., Padilla, J.G., Zamora, A., Gorospe, B.S., Nguyen, K., Deal, W.R., “A 0.85 THz low noise amplifier using InP HEMT transistors,” *IEEE Microwave and Wireless Components Letters*, vol. 25, no. 6, pp. 397-399, June 2015.

[96] Tessmann, A., Leuther, A., Ohlrogge, M., Massler, H., “Submillimeter-wave amplifier circuits based on thin film microstrip line front-side technology,” in *Technical Digest of the IEEE Compound Semiconductor Integrated Circuit Symposium*, New Orleans, LA, 2015, pp. 1-4.

[97] Mei, X., Yoshida, W., Lange, M., Lee, J., Zhou, J., Liu, P.-H., Leong, K., Zamora, A., Padilla, J., Sarkozy, S., Lai, R., Deal, W.R., “First demonstration of amplification at 1 THz using 25-nm InP high electron mobility transistor process,” *IEEE Electron Device Letters*, vol. 36, no. 4, pp. 327-329, Apr. 2015.

[98] Leuther, A., Tessmann, A, Kalfass, I., Lösch, R., Seelmann-Eggebert, M., Wadefalk, N., Schäfer, F., Gallego Puyol, J.D., Schlechtweg, M., Mikulla, M., Ambacher, O., “Metamorphic HEMT technology for low-noise applications,” in *2009 IEEE International Conference on Indium Phosphide and Related Materials*, Newport Beach, CA, 2009, pp. 188-191.

[99] Tessmann, A., Kallfass, I., Leuther, A., Massler, H., Kuri, M., Riessle, M., Zink, M., Sommer, R., Wahlen, A., Essen, H., Hurm, V., Schlechtweg, M., Ambacher, O., ”Metamorphic HEMT MMICs and modules for use in a high-bandwidth 210 GHz radar,” *IEEE Journal of Solid-State Circuits*, vol. 43, no. 10, Oct. 2008.

[100] Tessmann, A., “220-GHz metamorphic HEMT amplifier MMICs for high-resolution imaging applications,” *IEEE Journal of Solid-State Circuits*, vol. 40, no. 10, Oct. 2005.

[101] Kärkkäinen, M., Varonen, M., Halonen, K.A.I., Kantanen, M., Karttaavi, T., Weber, R., Leuther, A., Seelmann-Eggebert, M., Närhi, T., “Coplanar 94 GHz metamorphic HEMT low noise amplifiers,” in *Technical Digest of the IEEE Compound Semiconductor IC Symposium*, San Antonio, TX, 2006, pp. 29-32.

[102] Camillier, N., Chye, P., Gregory, P., Lee, A., “A W-band monolithic amplifier,” in *IEEE MTT-S International Microwave Symposium Digest*, Dallas, TX, 1990, pp. 903-906.

[103] Duh, K.H.G, Chao, P.C., Ho, P., Tessmer, A., Liu, S.M.J, Kao, M.Y., Smith, P.M., Ballingall, J.M., "W-band InGaAs HEMT low noise amplifiers," in *IEEE MTT-S International Microwave Symposium Digest*, Dallas, TX, 1990, pp. 595-598.

[104] Sequeira, H.B., Duncan, S.W., Eskandrian, A., Golja, B.A., Martel, D.C., Southwick, S.B., Svensson, S.P., Trippe, M.W., Tu, D.W., Weinreb, S., Byer, N.E., "Monolithic GaAs W-band pseudomorphic MODFET amplifiers," in *12th Annual Gallium Arsenide Integrated Circuits Symposium Technical Digest*, New Orleans, LA, 1990, pp. 161-164.

[105] Majidi-Ahy, R., Riaziat, M., Nishimoto, C., Glenn, M., Silverman, S., Weng, S., Pao, Y.C., Zdasiuk, G., Bandy, S., Tan, Z., "94 GHz InP MMIC five-section distributed amplifier," *Electronic Letters*, vol. 26, no. 2, pp. 91-92, Jan. 1990.

[106] Majidi-Ahy, R., Nishimoto, C., Riaziat, M., Pao, Y.C., Weng, S., Silverman, S., Glenn, M., Zdasiuk, G., Bandy, S., Tan, Z., "100 GHz high-gain InP MMIC cascode amplifier," in *12th Annual Gallium Arsenide Integrated Circuits Symposium Technical Digest*, New Orleans, LA, 1990, pp. 173-176.

[107] Duh, K.H.G., Chao, P.C., Liu, S.M.J., Ho, P., Kao, M.Y., Ballingall, J.M., "A super low-noise 0.1 μm T-gate InAlAs-InGaAs-InP HEMT," *IEEE Microwave and Guided Wave Letters*, vol. 1, no. 5, pp. 114-116, May 1991.

[108] Wang, H., Tan, K., Dow, G.S ., Berenz, J., Garske, D., Rodgers, P., Hayashibara, G., "State-of-the-art low noise performance of 94 GHz monolithic amplifiers using 0.1 μm InGaAs/GaAs pseudomorphic HEMT technology," in *International Electron Devices Meeting Technical Digest*, Washington, DC, 1991, pp. 939-942.

[109] Streit, D.C., Tan, K.L., Liu, P.-H., Chow, P.D., "High gain W-band InGaAs-InAlAs-InP HEMTs for low noise W-band applications," in *Proceedings of IEEE/Cornell Conference on Advanced Concepts in High Speed Semiconductor Devices and Circuits*, Ithaca, NY, 1991, pp.455-460.

[110] Chow, P.D., Tan, K., Streit, D., Garske, D., Liu, P., Yen, H.C., "Ultra low noise high gain W-band InP-based HEMT downconverter," in *IEEE MTT-S International Microwave Symposium Digest*, Boston, MA, 1991, pp. 1041-1044.

[111] Majidi-Ahy, R., Nishimoto, C., Riaziat, M., Glenn, M., Silverman, S., Weng, S.L., Pao, Y.C., Zdasiuk, G., Bandy, S., Tan, Z., "100-GHz high-gain InP MMIC cascode amplifier," *IEEE Journal of Solid-State Circuits*, vol. 26, no. 10, pp. 1370-1378, Oct. 1991.

[112] Yoshinaga, H., Abe, B., Shibata, K., Kawasaki, H., Ohtomo, M., Tokaji, I., "Millimeter-wave monolithic gain block amplifiers using pseudomorphic HEMT," in *IEEE MTT-S International Microwave Symposium Digest*, Albuquerque, NM, 1992, pp. 583-586.

[113] Wang, H., Dow, G.S., Allen, B.R., Ton, T.-N., Tan, K.L., Chang, K.W., Chen, T., Berenz, J., Lin, T.S., Liu, P.-H., Streit, D. C., Bui, S.B., Raggio, J.J., Chow, P.D., "High-performance W-band monolithic pseudomorphic InGaAs HEMT LNA's and design/analysis methodology," *IEEE Transactions on Microwave Theory and Techniques*, vol. 40, no. 3, pp. 417-428, Mar. 1992.

[114] Wang, H., Ton, T.N., Tan, K.L., Dow, G.S., Chen, T.H., Chang, K.W., Berenz, J., Allen, B., Liu, P., Streit, D., Hayashibara, G., Liu, L.C.T., "An ultra low noise W-band monolithic three-stage amplifier using 0.1 μm pseudomorphic InGaAs/GaAs HEMT technology," in *IEEE MTT-S International Microwave Symposium Digest*, Albuquerque, NM, 1992, pp. 803-806.

[115] Duh, K.H.G, Liu, S.M.J, Kao, M.Y., Wang, S.C., Tang, O.S.A., Ho, P., Chao, P.C., Smith, P.M., "Advanced millimeter-wave InP HEMT MMICs," in *Proceedings of Fifth International Conference of Indium Phosphide and Related Materials*, Paris, France, 1993, pp.493-496.

[116] Liu, S.M.J., Duh, K.H.G., Wang, S.C., Tang, O.S.A., Smith, P.M., "75-110 GHz InGaAs/GaAs HEMT high gain MMIC amplifier," in *15th Annual Gallium Arsenide Integrated Circuits Symposium Technical Digest*, San Jose, CA, 1993, pp. 273-276.

[117] Ton, T.-N., Wang, H., Chen, S., Tan, K.L., Dow, G.S., Allen, B.R., Berenz, J., "W-band monolithic pseudomorphic AlGaAs/InGaAs/GaAs HEMT CBCPW LNA," *Electronics Letters*, vol. 29, no. 20, pp. 1804-1805, Sept. 1993.

[118] Wang, H., Lai, R., Chen, S.T., Berenz, J., "A monolithic 75-110 GHz balanced InP-based HEMT amplifier," *IEEE Microwave and Guided Wave Letters*, vol. 3, no. 10, pp. 381-383, Oct. 1993.

[119] Wang, H., Ton, T.N., Lai, R., Lo, D.C.W., Chen, S., Streit, D., Dow, G.S., Tan, K.L., Berenz, J., "Low noise and high gain 94 GHz monolithic InP-based HEMT amplifiers," in *International Electron Devices Meeting Technical Digest*, Washington, DC, 1993, pp. 239-242.

[120] Tu, D.-W., Duncan, S.W., Eskandarian, A., Golja, B., Kane, B.C., Svensson, S.P., Weinreb, S., Byer, N.E., "High gain monolithic W-Band low noise amplifiers based on pseudomorphic high electron mobility transistors," *IEEE Transactions on Microwave Theory and Techniques*, vol. 42, no. 12, pp. 2590-2097, Dec. 1994.

[121] Lo, D.C.W., Wang, H., Allen, B.R., Dow, G.S., Chen, S., Biedenbender, M., "A novel monolithic balanced switching low noise amplifier," in *IEEE 1994 Microwave and Millimeter-Wave Monolithic Circuits Symposium Digest*, San Diego, CA, 1994, pp. 245-248.

[122] Lo, D.C.W., Dow, G.S., Yujiri, L., Chen, S., Wang, H., Biedenbender, M., Mussetto, M., Allen, B.R., "Monolithic W-band seven-stage low noise amplifier/detector for radiometric imaging array application," *Electronics Letters*, vol. 30, no. 13, pp. 1075-1077, June 1994.

[123] Lo, D.C.W., Dow, G.S., Allen, B.R., Yujiri, L., Mussetto, M., Huang, T.W., Wang, H., Biedenbender, M., "A monolithic W-band high-gain LNA/detector for millimeter wave radiometric imaging applications," in *IEEE MTT-S International Microwave Symposium Digest*, Orlando, FL, 1995, pp. 1117-1120.

[124] Ng, G I., Lai, R., Hwang, Y., Wang, H., Lo, D.C.W., Block, T., Tan, K., Streit, D.C., Dia, R.M., Freudenthal, A., Chow, P.D., Berenz, J., "A fully passivated ultra low noise W-band monolithic InGaAs/InAlAs/InP HEMT amplifier," in *IEEE 1995 Microwave and Millimeter-Wave Monolithic Circuits Symposium Digest*, Orlando, FL, 1995, pp. 63-66.

[125] Wang, H., Ng, H., Lai, R., Hwang, Y., Lo, D.C.W., Dia, R., Freudenthal, A., Block, T., "Fully passivated W-band InAlAs/InGaAs/InP monolithic low noise amplifiers," *IEE Proceedings - Microwave, Antennas, and Propagation*, vol. 143, no. 5, pp. 361-366, Oct. 1996.

[126] Berg, M., Hackbarth, T., Dickmann, J., "80-100 GHz broadband amplifier MIMIC utilizing CPWs and quarter micron InP-based HEMTs," in *Proceedings of IEEE International Conference of Indium Phosphide and Related Materials*, Cape Cod, MA, 1997, pp. 245-248.

[127] Haydl, W.H., Verweyen, L., Jakobus, T., Neumann, M., Tessmann, A., Krems, T., Schlechtweg, M., Reinert, W., Massler, H., Rudiger, J., Bronner, W., Hulsmann, A., Fink, T., "Compact monolithic coplanar 94 GHz front ends," in *IEEE MTT-S International Microwave Symposium Digest*, Denver, CO, 1997, pp. 1281-1284.

[128] Kobayashi, K.W., Wang, H., Lai, R., Tran, L.T., Block, T.R., Liu, P.H., Cowles, J., Chen, Y.C., Huang, T.-W., Oki, A.K., Yen, H.C., Streit, D.C., "An InP HEMT W-band amplifier with monolithically integrated HBT bias regulation," *IEEE Microwave and Guided Wave Letters*, vol. 7, no. 8, pp. 222-224, Aug. 1997.

[129] Tessmann, A., Haydl, W.H., Hülsmann, A., Schlechtweg, M., "High-gain cascode MMIC's in coplanar technology at W-band frequencies," *IEEE Microwave and Guided Wave Letters*, vol. 8, no. 12, pp. 430-431, Dec. 1998.

[130] Tessmann, A., Haydl, W. H., Krems, T., Neumann, M., Massler, H., Verweyen, L., Hülsmann, A., Schlechtweg, M., "A compact coplanar W-band variable gain amplifier MMIC with wide control range using dual-gate HEMTs," *IEEE MTT-S International Microwave Symposium Digest*, Baltimore, MD, 1998, pp. 685-688.

[131] Matloubian, M., "Advances in millimeter-wave FET MMIC technology," in *IEEE Radio Frequency Integrated Circuits Symposium Digest*, Anaheim, CA, 1999, p. 141-144.

[132] Hoel, V., Boret S., Grimbert, B., Aperc, G., Bolaert, S., Happy, H., Wallart, X., Cappy, A., "94 GHz low noise amplifier on InP in coplanar technology," in *Proceedings of the European Gallium Arsenide and Related III-V Compound Applications Symposium*, Munich, Germany, 1999, pp. 257-262.

[133] Hwang, K.C., Chao, P.C., Creamer, C., Nichols, K.B., Wang, S., Tu, D., Kong, W., Dugas, D., Patton, G., "Very high gain millimeter-wave InAlAs/InGaAs/GaAs metamorphic HEMT's," *IEEE Electron Device Letters*, vol. 20, no 11, pp. 551-553, Nov. 1999.

[134] Werthof, A., Grave, T., Kellner, W., "W-band amplifier fabricated by optical stepper lithography," in *IEEE MTT-S International Microwave Symposium Digest*, Anaheim, CA, 1999, pp. 689-692.

[135] Edgar, D.L., McLelland, H., Ferguson, S., Cameron, N.I., Holland, M., Thayne, I.G., Taylor, M.R.S., Stanley, C.R., Beaumont, S.P., “94 and 150GHz coplanar waveguide MMIC amplifiers realised using InP technology,” in *IEEE MTT-S International Microwave Symposium Digest*, Anaheim, CA, 1999, pp. 247-250.

[136] Weinreb, S., Lai, R., Erickson, N., Gaier, T., Wielgus, J., “W-band InP Wideband MMIC LNA with 30K noise temperature,” in *IEEE MTT-S International Microwave Symposium Digest*, Anaheim, CA, 1999, pp. 101-104.

[137] Archer, J.W., Lai, R., Gough, R., “Ultra-low-noise Indium-Phosphide MMIC amplifiers for 85-115 GHz,” *IEEE Transactions on Microwave Theory and Techniques*, vol. 49, no. 11, pp. 2080-2085, Nov. 2001.

[138] Radisic, V., Pobanz, C., Hu, M., Micovic, M., Wetzel, M., Janke, P., Yu, M., Ngo, C., Dawson, D., Matloubian, M., “A high-performance 85-119 GHz GCPW MMIC low noise amplifier,” in *IEEE Radio Frequency Integrated Circuit Symposium Digest*, Boston, MA, 2000, pp. 43-46.

[139] Tessmann, A., Haydl, W.H., Neumann, M., Rüdiger, J., “W-Band cascode amplifier modules for passive imaging applications,” *IEEE Microwave and Guided Wave Letters*, vol. 10, no. 5, pp. 189-191, May 2000.

[140] Case, M. G., Pobanz, C., Weinreb, S., Matloubian, M., Hu, M., Wetzel, M., Janke, P., Ngo, C., “Low-cost, high-performance W-band LNA MMICs for millimeter-wave imaging,” in *Passive Millimeter-Wave Imaging Technology IV,* Smith, R.M., Appleby, R., (eds.), *Proceedings of SPIE*, vol. 4032, Orlando, FL, 2000, pp. 89-96.

[141] Smith, P.M., Nichols, K., Kong, W., MtPleasant, L., Pritchard, D., Lender, R., Fisher, J., Actis, R., Dugas, D., Meharry, D., Swanson, A.W., “Advances in InP HEMT technology for high frequency applications,” in *Proceedings of IEEE International Conference of Indium Phosphide and Related Materials*, Nara, Japan, 2001, pp. 9-13.

[142] Kangaslahti, P., Sjoman, P., Jukkala, P., Barnes, A.R., Munday, P., Jennings, R., Moore, M.T., Karttaavi, T., Lahdes, M., Tuovinen, J., “A W-band radar receiver for cloud observations,” in *Proceedings of 32nd European Microwave Conference*, Milan, Italy, 2002, pp. 1-4.

[143] Tessmann, A., Leuther, A., Schwoerer, C., Massler, H., Kudszus, S., Reinert, W., Schlechtweg, M., “A coplanar 94 GHz low-noise amplifier MMIC using 0.07 µm metamorphic cascade HEMTs,” in *IEEE MTT-S International Microwave Symposium Digest*, Philadelphia, PA, 2003, pp. 1581-1584.

[144] Barnes, A.R., Munday, P., Jennings, R., Moore, M., Black, M., Appleby, R., Anderton, R., Sinclair, G., Coward, P., “MMIC technology and its application in passive mm-wave imaging systems,” in *Proceedings of 3rd ESA Workshop on Millimetre Wave Technology and Applications*, Espoo, Finland, 2003, pp. 543-548.

[145] Tessmann, A., Leuther, A., Schwörer, C., Massler, H., Reinert, W., Walther, M., Lösch, R., Schlechtweg, M., “Millimeter-wave circuits based on advanced metamorphic HEMT technology,” in *Proceedings of Joint 29th International Conference on Infrared and Millimeter Waves and 12th International Conference on Terahertz Electronics*, Karlsruhe, Germany, 2004, pp. 165-166

[146] Grundbacher R., Uyeda, J., Lai, R., Umemoto, D., Liu, P.H., Barsky, M., Cavus, A., Lee, L.J., Chen, J., Gonzalez, J., Chen, S., Block, T., Oki, A., “High performance millimeter wave 0.1µm InP HEMT MMIC LNAs fabricated on 100 mm wafers”, in *Proceedings of IEEE International Indium Phosphide and Related Materials Conference*, Montpellier, France, 2004, pp. 284-287.

[147] Varonen, M., Kärkkäinen M., Kantanen, M., Karttaavi, T., Kangaslahti, P., Halonen, K., “Millimetre wave metamorphic HEMT amplifiers,” in *Proceedings of Norchip Conference*, Oslo, Norway, 2004, pp. 8-11.

[148] Kärkkäinen, M., Varonen, M., Kantanen, M., Karttaavi, T., Kangaslahti, P., Halonen, K., “Low noise amplifiers for 94 GHz cloud radar,” in *Proceedings of 38th European Microwave Conference*, Amsterdam, The Netherlands, 2004, pp. 33-36.

[149] Bessemoulin, A., Grunenputt, J., Fellon, P., Tessmann, A., Koh, E., “Coplanar W-band low noise amplifier MMIC using 100-nm gate-length GaAs PHEMTs,” in *Proceedings of 34th European Microwave Conference*, Amsterdam, The Netherlands, 2004, pp. 25-28.

[150] Deal, W.R., Tsai, R., Lange, M.D., Boos, J.B., Bennett, B.R., Gutierrez, A., “A W-band InAs/AlSb low-noise/low-power amplifier,” *IEEE Microwave and Wireless Components Letters*, vol. 15, no. 4, pp. 208-210, Apr. 2005.

[151] Hacker, J.B., Bergman, J., Nagy, G., Sullivan, G., Kadow, C., Lin, H.-K., Gossard, A.C., Rodwell, M., Brar, B., “An ultra-low power InAs/AlSb HEMT W-band low-noise amplifier,” in *IEEE MTT-S International Microwave Symposium Digest*, Long Beach, CA, 2005, pp. 1029-1032.

[152] An, D., Lee, B.-H., Lim, B.-O., Lee, M.-K., Park, H.-M., Rhee, J.-K., “W-band high gain MIMIC amplifier and low conversion loss MIMIC mixer using metamorphic HEMT,” in *Proceedings of International Joint Conference of the Seventh Topical Symposium on Millimeter Waves and the Sixth MINT Millimeter-wave International Symposium,* Seoul, South Korea 2005, pp. 27-30.

[153] Lynch, J.J., Schulman, J.N., Moyer, H.P., “Low noise direct detection sensors for millimeter wave imaging,” in *IEEE Compound Semiconductor Integrated Circuit Symposium Technical Digest*, San Antonio, TX, 2006 pp. 215-218.

[154] Riemer, P.J., Buhrow, B.R., Hacker, J.B., Bergman, J., Brar, B., Gilbert, B.K., Daniel, E.S., “Low-power W-band CPWG InAs/AlSb HEMT low-noise amplifier,” *IEEE Microwave and Wireless Components Letters*, vol. 16, no. 1, pp. 40-42, Jan. 2006.

[155] Sato, M., Hirose, T., Ohki, T., Sato, H., Sawaya, K., Mizuno, K., “94-GHz band high-gain and low-noise amplifier using InP-HEMTs for passive millimeter-wave imaging,” in *IEEE MTT-S International Microwave Symposium Digest*, Honolulu, HI, 2007, pp. 1775-1778.

[156] Sato, M., Hirose, T., Ohki, T., Takahashi, T., Makiyama, K., Hara, N., Sato, H., Sawaya, K., Mizuno, K., “InP-HEMT MMICs for passive millimeter-wave imaging sensors,” in *Proceedings of 20th IEEE International Conference of Indium Phosphide and Related Materials*, Versailles, France, 2008, pp. 1-4.

[157] Lynch, J.J., Schulman, J.N., Schaffner, J.H., Moyer, H.P., Y. Royter, Macdonald, P.A., Hughes, B., “Low noise radiometers for passive millimeter wave imaging,” in *Proceedings of 33rd International Conference on Infrared, Millimeter and Terahertz Waves*, Pasadena, CA, 2008, pp. 1-3.

[158] Tessmann, A., Leuther, A., Massler, H., Kuri, M., Lösch, R., Schlechtweg, M., Ambacher, O., “Millimeter-wave and submillimeter-wave mHEMT LNA MMICs,” in *Proceedings of ESA Microwave Technology and Techniques Workshop*, Noordwijk, The Netherlands, 2008.

[159] Mei, X.B., Lin, C.H., Lee, L.J., Kim Y.M., Liu, P.H., Lange, M., Cavus, A., To, R., Nishimoto, M., Lai, R., “A W-band InGaAs/InAlAs/InP HEMT low-noise amplifier MMIC with 2.5 dB noise figure and 19.4 dB gain at 94 GHz,” in *Proceedings of 20th IEEE International Conference of Indium Phosphide and Related Materials*, Versailles, France, 2008, pp. 1-3.

[160] Smith, D., Dambrine, G., Orlhac, J.-C., “Industrial MHEMT technologies for 80 - 220 GHz applications,” in *Proceedings of the 3rd European Microwave Integrated Circuits Conference*, Amsterdam, The Netherlands, 2008, pp. 214-217.

[161] Vassilev, V., Wadefalk, N., Kozhuharov, R., Abbasi, M., Zirath, H., Pellikka, T., Emrich, A., Kallfass, I., Leuther, A., ”MMIC-based receivers for mm-wave radiometry,” in *Proceedings of 35th International Conference on Infrared, Millimeter, and Terahertz Waves*, Rome, Italy, 2010, pp. 1-2.

[162] Moon, S.-W., Baek, Y.-H., Oh, J.-H., Han, M., Rhee, J.K., Kim, S.D., “New small-signal modelling method for W-band MHEMT-based amplifier design,” in *Proceedings of the 40th European Microwave Conference*, Paris, France, 2010, pp. 1146-1149.

[163] Ciccognani, W., Limiti, E., Longhi, P.E., Renvoisè, M., “MMIC LNAs for radioastronomy applications using advanced industrial 70 nm metamorphic technology,” *IEEE Journal of Solid-State Circuits*, vol. 45, no. 10, pp. 2008-2015 , Oct. 2010.

[164] Liu, L., Alt, A.R., Benedickter, H., Bolognesi, C.R., “Low power consumption millimeter-wave amplifiers using InP HEMT technology,” in *IEEE MTT-S International Microwave Workshop Series on Millimeter Wave Integration Technologies*, Sitges, Spain, 2011, pp. 9-12.

[165] Samoska, L.A., Church, S., Cleary, K., Fung, A., Gaier, T.C., Kangaslahti, P., Lai, R., Lau, J.M., Mei, G., Reeves, R., Sieth, M.M., Voll, P., “Cryogenic MMIC low noise amplifiers for W-band and beyond,” in *22nd International Symposium on Space Terahertz Technology*, Tucson, AZ, 2011, pp. 1-4.

[166] Thome, F., Massier, H., Wagner, S., Leuther, A., Kallfass, I., Schlechtweg, M., Ambacher, O., “Comparison of two W-band low-noise amplifier MMICs with ultra low power consumption based on 50 nm InGaAs mHEMT technology,” in *IEEE MTT-S International Microwave Symposium Digest*, Seattle, WA, 2013, pp. 1-4.

[167] Farkas, D.S., Sarkozy, S.J., Katz, R., “A W-band 100 nm InP HEMT ultra low noise amplifier,” in *Proceedings of Asia-Pacific Microwave Conference 2014*, Sendai, Japan, 2014, pp. 229-231.

[168] Bessemoulin, A., Tarazi, J., McCulloch, M.G., Mahon, S.J., “0.1-µm GaAs PHEMT W-band low noise amplifier MMIC using coplanar waveguide technology,” *Proceedings of 1st Australian Microwave Symposium (AMS)*, Melbourne, Australia, 2014, pp. 1-2.

[169] Smith, P.M., Ashman, M., Xu, D., Yang, X., Creamer, C., Chao, P.C., Chu, K., Duh, K.H., Koh, C., Schellenberg, J., “A 50nm MHEMT millimeter-wave MMIC LNA with wideband noise and gain performance,” in *IEEE MTT-S International Microwave Symposium Digest*, Tampa, FL, 2014, pp. 1-4.

[170] Reyaz, S., Gustafsson, A., Samuelsson, C., Malmqvist, R., Grandchamp, B., Rantakari, P., Vähä-Heikkilä, T., “A W-band RF-MEMS switched LNA in a 70 nm mHEMT process,” *International Journal of RF and Microwave Computer-Aided Engineering*, vol. 25, no. 7, pp. 639-646, Sept. 2015.

[171] Kantanen, M., Varonen, M., Kärkkäinen, M., Karttaavi, T., Weber, R., Leuther, A., Seelmann-Eggebert, M., Närhi, T., Halonen, K.A.I., “Coplanar 155 GHz MHEMT MMIC low noise amplifiers,” in *Asia-Pacific Microwave Conference Proceedings*, Yokohama, Japan, 2006, pp. 173-176.

[172] Wang, H., Lai, R., Lo, D.C.W., Streit, D.C., Liu, P.H., Dia, R.M., Pospieszalski, M.W., Berenz, J., “A 140-GHz monolithic low noise amplifier,” *IEEE Microwave and Guided Wave Letters*, vol. 5, no. 5, May 1995.

[173] Lai, R., Wang, H., Chen, Y.C., Block, T., Liu, P.H., Streit, D.C., Tran, D., Siegel, P., Barsky, M., Jones, W., Gaier, T., “D-band MMIC LNAs with 12 dB gain at 155 GHz fabricated on a high yield InP HEMT MMIC production process,” in *Proceedings of International Conference of Indium Phosphide and Related Materials*, Cape Cod, MA, 1997, pp. 241-244.

[174] Weinreb, S., Chao, P.C., Copp, W., “Full-waveguide band, 90 to 140 GHz, MMIC amplifier module,” in *IEEE MTT-S International Microwave Symposium Digest*, Denver, CO, 1997, pp. 1279-1280.

[175] Wang, H., Lai, R., Kok, Y.-L., Huang, T.-W., Aust, M.V., Chen, Y.C., Siegel, P.H., Gaier, T., Dengler, R.J., Allen, B.R., “A 155-GHz monolithic InP-based HEMT amplifier,” *IEEE Transactions on Microwave Theory and Techniques*, vol. 46, no. 11, pp. 1660-1666, Nov. 1998.

[176] Edgar, D.L., McLelland, H., Ferguson, S., Cameron, N.I., Holland, M., Thayne, I.G., Taylor, M.R.S., Stanley, C.R., Beaumont, S.P., “150GHz coplanar waveguide MMIC amplifier,” in *Proceedings of the 38th European Microwave Conference*, Munich, Germany, 1999, pp. 242-245.

[177] Pobanz, C.W., Matloubian, M., Lui, M., Sun, H.-C., Case, M., Ngo, C.M., Janke, P., Gaier, T., Samoska, L., “A high-gain monolithic D-band InP HEMT amplifier,” *IEEE Journal of Solid-State Circuits*, vol. 34, no. 9, Sept. 1999.

[178] Kok, Y.L., Wang, H., Huang, T.W., Lai, R., Barsky, M., Chen, Y.C., Sholley, M., Block, T., Streit, D.C., Liu, P.H., Allen, B.R., Samoska, L., Gaier, T., “160–190-GHz monolithic low-noise amplifiers,” *IEEE Microwave and Guided Wave Letters*, vol. 9, no. 8, Aug. 1999.

[179] Weinreb, S., Gaier, T., Lai, R., Barsky, M., Leong, Y.C., Samoska, L., “High-gain 150–215-GHz MMIC amplifier with integral waveguide transitions,” *IEEE Microwave and Guided Wave Letters*, vol. 9, no. 7, July 1999.

[180] Pobanz, C., Matloubian, M., Radisic, V., Raghavan, G., Case, M., Micovic, M., Hu, M., Nguyen, C., Weinreb, S., Samoska, L., “High performance MMICs with submillimeter wave InP-based HEMTs,” in *Proceedings of International Conference on Indium Phosphide and Related Materials*, Williamsburg, VA, 2000, pp. 67-70.

[181] Tessmann, A., Wohlgemuth, O., Reuter, R., Haydl, W.H., Massler, H., Hülsmann, A., “A coplanar 148 GHz cascade amplifier MMIC using 0.15 µm GaAs PHEMTs,” in *IEEE MTT-S International Microwave Symposium Digest*, Boston, MA, 2000, pp. 991-994.

[182] Schlechtweg, M., Leuther, A., Tessmann, A., Schwörer, C., Massler, H., Reinert, W., Lang, M., Nowotny, U., Kappeler, O., Wafther, M., Lösch, R., “Millimeter-wave and mixed-signal integrated circuits based on advanced metamorphic HEMT technology,” in *Proceedings of IEEE International Conference of Indium Phosphide and Related Materials*, Kagoshima, Japan, 2004, pp. 609-614.

[183] Grundbacher, R., Raja, R., Lai, R., Chou, Y.C., Nishimoto, M., Gaier, T., Dawson, D., Liu, P.W., Barsky, M., Oki, A., “A 150-215 GHz InP HEMT low noise amplifier with 12 dB gain,” in *Proceedings of International Conference of Indium Phosphide and Related Materials*, Glasgow, UK, 2005, pp. 613-616.

[184] Deal, W.R., Yujiri, L., Siddiqui, M., Lai, R., “Advanced MMIC for passive millimeter and submillimeter wave imaging,” in *International Solid-State Circuits Conference Digest*, San Francisco, CA, 2007, pp. 621-623.

[185] Kangaslahti, P., Pukala, D., Gaier, T., Deal, W., Mei, X., Lai, R., “Low noise amplifier for 180 GHz frequency band,” in *IEEE MTT-S International Microwave Symposium Digest*, Atlanta, GA, 2008, pp. 451-454.

[186] Weissbrodt, E., Kallfass, I., Weber, R., Tessmann, A., Massler, H., Leuther, A., “Low-noise amplifiers in D-band using 100 nm and 50 nm mHEMT technology,” in *German Microwave Conference Digest*, Berlin, Germany, 2010, pp. 55-58.

[187] Desruelles, G., Rolland, N., Rolland, P.-A., “G-band low noise amplifier and oscillator for synthetic aperture applications,” in *Proceedings of the 40th European Microwave Conference*, Paris, France, 2010, pp. 525-528.

[188] Leuther, A., Koch, S., Tessmann, A., Kallfass, I., Merkle, T., Massler, H., Lösch, R., Schlechtweg, M., Saito, S., Ambacher, O., “20 nm metamorphic HEMT with 660 GHz f_t,” in *Proceedings of International Conference on Indium Phosphide and Related Materials*, Berlin, Germany, 2011, pp. 1-4.

[189] Kangaslahti, P., Lim, B., Gaier, T., Tanner, A., Varonen, M., Samoska, L., Brown, S., Lambrigtsen, B., Reising, S., Tanabe, J., Montes, O., Dawson, D., Parashare, C., “Low noise amplifier receivers for millimeter wave atmospheric remote sensing,” in *IEEE MTT-S International Microwave Symposium Digest*, Montreal, Canada, 2012, pp. 1-3.

[190] Sato, M., Shiba, S., Matsumura, H., Takahashi, T., Suzuki, T., Nakasha, Y., Hara, N., “Submillimeter-wave InP HEMT amplifiers with current-reuse topology,” in *Proceedings of IEEE 13th Topical Meeting on Silicon Monolithic Integrated Circuits in RF Systems*, Austin, TX, 2013, pp. 150-152.

[191] Diebold, S., Pahl, P., Wagner, S., Massler, H., Tessmann, A., Leuther, A., Zwick, T., Kallfass, I., “A broadband amplifier MMIC with 105 to 140 GHz bandwidth,” in *Asia-Pacific Microwave Conference Proceedings*, Seoul, Republic of Korea, 2013, pp. 354-356.

[192] Merkle, T., Koch, S., Leuther, A., Seelmann-Eggebert, M., Massler, H., Kallfass, I., “Compact 110-170 GHz amplifier in 50 nm mHEMT technology with 25 dB gain,” in *Proceedings of the 8th European Microwave Integrated Circuits Conference*, Nuremberg, Germany, 2013, pp. 129-132.

[193] Merkle, T., Leuther, A., Koch, S., Kallfass, I., Tessmann, A., Wagner, S., Massler, H., Schlechtweg, M., Ambacher, O., “Backside process free broadband amplifier MMICs at D-band and H-band in 20 nm mHEMT technology,” in *IEEE Compound Semiconductor Integrated Circuit Symposium Technical Digest*, La Jolla, CA, 2014, pp. 1-4.

[194] Lai, R., Barsky, M., Huang, T., Sholley, M., Wang, H., Kok, Y.L., Streit, D.C., Block, T., Liu, P.H., Gaier, T., Samoska, L., “An InP HEMT MMIC LNA with 7.2-dB gain at 190 GHz,” *IEEE Microwave and Wireless Components Letters*, vol. 8, no. 11, pp. 393-395, Nov. 1998.

[195] Barsky, M., Lai, R., Kok, Y.L., Sholley, M., Streit, D.C., Block, T., Liu, P.H., Sabin, E., Rogers, H., Medvedev, V., Gaier, T., Samoska, L., “190 GHz InP HEMT MMIC LNA with dry etched backside vias,” in *Proceedings of International Conference on Indium Phosphide and Related Materials*, Davos, Switzerland, 1999, pp. 423-425.

[196] Lai, R., Barsky, M., Grundbacher, R., Liu, P.H., Chin, T.P., Nishimoto, M., Elmajarian, R., Rodriguez, R., Tran, L., Gutierrez, A., Oki, A., Streit, D., “InP HEMT amplifier development for G-band (1 40-220 GHz) applications,” in *International Electron Devices Meeting Digest*, San Francisco, CA, 2000, pp. 175-177.

[197] Archer, J.W., Lai, R., Grundbacher, R., Barsky, M., Tsai, R., Reid, P., “An indium phosphide MMIC amplifier for 180–205 GHz,” *IEEE Microwave and Wireless Components Letters*, vol. 11, no. 1, pp. 4-6, Jan. 2001.

[198] Raja, R., Nishimoto, Osgood, B., Barsky, M., Sholley, M., Quon, R., Barber, G., Liu, P., Lai, R., Hinte, F., Haviland, G., Vacek, B., “A 183 GHz low noise amplifier module with 5.5 dB noise figure for the conical-scanning microwave imager sounder (CMIS),” in *IEEE MTT-S International Microwave Symposium Digest*, Denver, CO, 2001, pp. 1275-1278.

[199] Leuther, A., Tessmann, A., Dammann, M., Schworer, C., Schlechtweg, M., Mikulla, M., Lösch, R., Weimann, G., “50 nm MHEMT technology for G- and H-band MMICs,” in *Proceedings of International Conference on Indium Phosphide and Related Materials*, Matsue, Japan, 2007, pp. 24-27.

[200] Liu, P.H., Yoshida, W., Lee, J., Dang, L., Wang, J., Liu, W., Uyeda, J., Li, D., Mei, X.B., Deal, W., Barsky, M., Kim, Y.M., Lange, M., Chin, T.P., Radisic, V., Gaier, T., Fung, A., Lai, R., “High gain G-band MMIC amplifiers based on sub-50 nm gate length InP HEMT,” *Proceedings of International Conference on Indium Phosphide and Related Materials*, Matsue, Japan, 2007, pp. 22-23.

[201] Vassilev, V., Wadefalk, N., Abbasi, M., Kozhuharov, R., Zirath, H., Gunnarsson, S.E., Pellikka, T., Emrich, A., Kallfass, I., Leuther, A., ” Integrated front-ends up to 200 GHz,” in *IEEE MTT-S International Microwave Workshop Series on Millimeter Wave Integration Technologies*, Sitges, Spain, 2011, pp. 57-60.

[202] Längst, J., Diebold, S., Massler, H., Tessmann, A., Leuther, A., Zwick, T., Kallfass, I., “A balanced 150-240 GHz amplifier MMIC using airbridge transmission lines,” in *Proceedings of Workshop on Integrated Nonlinear Microwave and Millimetre-wave Circuits*, Dublin, Ireland, 2012, pp. 1-3.

[203] Varonen, M., Larkoski, P., Fung, A., Samoska, L., Kangaslahti, P., Gaier, T., Lai, R., Sarkozy, S., “160-270-GHz InP HEMT MMIC low-noise amplifiers,” in *IEEE Compound Semiconductor Integrated Circuit Symposium Technical Digest*, La Jolla, CA, 2012, pp. 1-4.

[204] Campos-Roca, Y., Tessmann, A., Hurm, V., Massler, H., Seelmann-Eggebert, M., Leuther, A., “A G-band cascode MHEMT medium power amplifier,” in *Proceedings of 38th International Conference on Infrared, Millimeter, and Terahertz Waves*, Mainz, Germany, 2013, pp. 1-2.

[205] Kärkkäinen, M., Kantanen, M., Caujolle-Bert, S., Varonen, M., Weber, R., Leuther, A., Seelmann-Eggebert, M., Närhi, T., Halonen, K. A.I., “MHEMT G-Band low-noise amplifiers,” in *IEEE MTT-S International Microwave Symposium Digest*, Seattle, WA, 2013, pp. 1-4.

[206] Moschetti, G., Leuther, A., Massler, H., Aja, B., Rösch, M., Schlechtweg, M., Ambacher, O., Kangas, V., Perichaud, M.G., “A 183 GHz metamorphic HEMT low-noise amplifier with 3.5 dB noise figure,” *IEEE Microwave and Wireless Components Letters*, vol. 25, no. 9, Sept. 2015.

[207] Yujiri L., Shoucri M., Moffa P., “Passive millimeter-wave imaging,” *IEEE Microwave Magazine*, vol. 4 no. 3 s. 39-50, Sept. 2003.

[208] Appleby, R., Anderton, R.N., “Millimeter-wave and submillimeter-wave imaging for security and surveillance,” *Proceedings of the IEEE*, vol. 95, no. 8, pp. 1683-1690, Aug. 2007.

[209] ITU Recommendation, “Radio noise,” Recommendation ITU-R P.372-12, Jul. 2015.

[210] Kantanen, M., “Passiivinen millimetriaaltokuvaus (Passive millimeter-wave imaging)”, *Licenciate Thesis*, in Finnish, Helsinki University of Technology, Espoo, Finland, 2006.

[211] Tuovinen, J.J.A, ”Mm-alueen vapaan tilan keilojen mittausmenetelmien ja sovellusten kehittäminen (Development of free space beam measurement techniques and applications at millimeter waves)”, *Licenciate Thesis*, in Finnish, Helsinki University of Technology, Espoo, Finland, 1989.

Appendix A: Derivation of *kBG*-factor

Functional blocks of the noise parameter measurement system are presented in Figure A.1. When the noise source noise temperature is T_H, the noise power P_H measured over the load inside the receiver is given by

$$P_H = kBG_{t,TOT}(T_H + T_{SYS}) = kBG_{av,AD}G_{t,RCV}(T_H + T_{SYS}) \quad (A.1)$$

where $G_{t,TOT}$ is the total transducer power gain and T_{SYS} is the noise temperature of the system consisting of the network AD and the receiver, $G_{av,AD}$ is the available power gain of the network AD, and $G_{t,RCV}$ is the transducer power gain of the receiver. Respectively, for noise temperature T_C

$$P_C = kBG_{t,TOT}(T_C + T_{SYS}) = kBG_{av,AD}G_{t,RCV}(T_C + T_{SYS}). \quad (A.2)$$

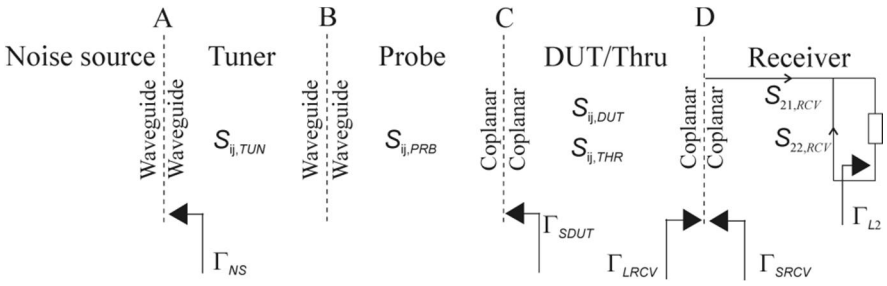

Figure A.1. Functional blocks of the noise parameter measurement system.

According to (1.27) and (1.28)

$$G_{t,RCV} = \frac{1-|\Gamma_{LRCV}|^2}{|1-\Gamma_{LRCV}\Gamma_{SRCV}|^2}\left|S_{21,RCV}\right|^2\frac{1-|\Gamma_{L2}|^2}{\left|1-S_{22,RCV}\Gamma_{L2}\right|^2} \quad (A.3)$$

where $S_{21,RCV}$ and $S_{22,RCV}$ are S-parameters of the receiver, and Γ_{L2} is reflection coefficient inside the receiver and

$$G_{av,AD} = \frac{1-|\Gamma_{NS}|^2}{\left|1-S_{11,AD}\Gamma_{NS}\right|^2}\left|S_{21,AD}\right|^2\frac{1}{1-|\Gamma_{LRCV}|^2}. \quad (A.4)$$

If the source impedance of the receiver is 50 Ω leading to $\Gamma_{LRCV} = 0$ we can write

$$G_{t,RCV,50} = \left|S_{21,RCV}\right|^2\frac{1-|\Gamma_{L2}|^2}{\left|1-S_{22,RCV}\Gamma_{L2}\right|^2} \quad (A.5)$$

and

$$G_{t,RCV} = \frac{1-|\Gamma_{LRCV}|^2}{|1-\Gamma_{LRCV}\Gamma_{SRCV}|^2} G_{t,RCV,50}. \quad \text{(A.6)}$$

Using (A.4) and (A.6) in (A.1) and (A.2) we obtain

$$P_H = kBG_{t,RCV,50} \frac{1}{|1-\Gamma_{LRCV}\Gamma_{SRCV}|^2} \frac{1-|\Gamma_{NS}|^2 |S_{21,AD}|^2}{|1-S_{11,AD}\Gamma_{NS}|^2} (T_H + T_{SYS}) \quad \text{(A.7)}$$

and

$$P_C = kBG_{t,RCV,50} \frac{1}{|1-\Gamma_{LRCV}\Gamma_{SRCV}|^2} \frac{1-|\Gamma_{NS}|^2 |S_{21,AD}|^2}{|1-S_{11,AD}\Gamma_{NS}|^2} (T_C + T_{SYS}). \quad \text{(A.8)}$$

$kBG_{t,RCV,50}$ can then be solved

$$kBG_{t,RCV,50} = \frac{P_H - P_C}{T_H - T_C} |1 - \Gamma_{LRCV}\Gamma_{SRCV}|^2 \frac{|1-S_{11,AD}\Gamma_{NS}|^2}{(1-|\Gamma_{NS}|^2)|S_{21,AD}|^2} \quad \text{(A.9)}$$

which is abbreviated as *kBG*-factor in (2.4).

Errata

In [IV], Fig. 5 and Fig. 13 are incorrect. The correct figures are shown below.

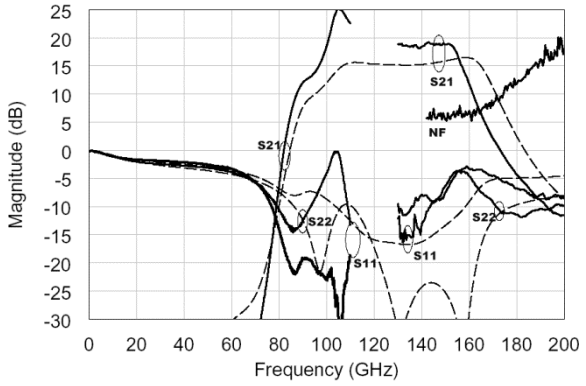

Fig. 5.

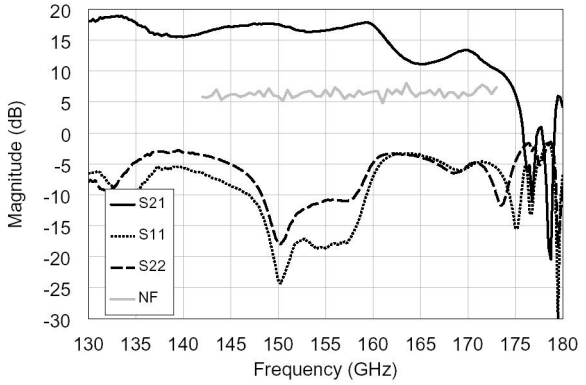

Fig. 13.

Publication I

Kantanen, M., Lahdes, M., Vähä-Heikkilä, T., Tuovinen, J., “A wide-band on-wafer noise parameter measurement system at 50-75 GHz,” *IEEE Transactions on Microwave Theory and Techniques*, vol. 51, no. 5, pp. 1489-1495, May 2003.

A Wide-Band On-Wafer Noise Parameter Measurement System at 50–75 GHz

Mikko Kantanen, Manu Lahdes, Tauno Vähä-Heikkilä, *Student Member, IEEE*, and Jussi Tuovinen, *Member, IEEE*

***Abstract*—A wide-band on-wafer noise parameter measurement system at 50–75 GHz is presented. This measurement system is based on the cold-source method with a computer-controlled waveguide tuner. Calibrations and measurement methods are discussed and measured results for passive and active on-wafer devices are shown over a 50–75-GHz range. An InP high electron-mobility transistor device is used as a test item for the active device. A Monte Carlo analysis to study measurement uncertainties is also shown. The measurement system is a useful tool in the development and verification of device noise models, as well as in device characterization.**

***Index Terms*—Noise-parameter measurements, on-wafer characterization, wide-band measurements.**

I. Introduction

COMMERCIAL exploitation of millimeter waves is currently becoming a reality with increasing intent. The main driving force has been the development in manufacturing monolithic integrated circuits, which can currently be produced up to approximately 220 GHz. Examples of commercial millimeter-wave applications are automotive collision-avoidance radars, radio links, and local area networks. Scientific millimeter-wave research is mainly related to radio astronomy and cosmology. Millimeter waves are also very attractive to be used in imaging systems for surveillance and contraband detection. Funding for this kind of application is coming from military and law enforcement agencies. Many applications mentioned above rely on the use of low-noise amplifiers (LNA). It is desirable to model noise behavior properly as early as possible during the LNA design process to avoid expensive and time-consuming iterations. The noise properties of LNAs are usually calculated during the design process using noise parameters of transistors.

In contrast to the microwave region, noise parameters of transistors at millimeter waves are usually not given by the manufacturer or they have been extrapolated from measurements made in the microwave region using device dependent noise models. These models themselves are commonly developed at microwave frequencies and applying them in a millimeter-wave region is risky. Thus, on-wafer noise parameter measurements at millimeter-wave frequencies are needed to characterize devices and to develop and verify device dependent noise models.

Thus far, wide-band on-wafer noise parameter measurements have been carried out up to 40 GHz [1]. At 50–75 GHz, measurements covering part of the band and using a manual input tuner have been reported [2]–[4]. A partial report about the measurement system described here has been presented in [5]. Above 75 GHz, results on single frequency and for a passive device have been presented [6]. Wide-band measurements are necessary in order to detect systematic errors that may not be detected in measurements over a narrow frequency band, even if the measurement system seems to work properly otherwise. Using the measurement system described here, noise parameters of a chip device can be measured over the entire 50–75-GHz range in an automated manner.

Manuscript received March 5, 2002; revised November 6, 2002. This work was supported by the European Space Agency under Contract 1655/95/NL/MV.

The authors are with the Millimeter Wave Laboratory of Finland–Millilab, VTT TECHNICAL RESEARCH CENTRE OF FINLAND, Espoo, FIN-02044 VTT, Finland (e-mail: mikko.kantanen@vtt.fi).

Digital Object Identifier 10.1109/TMTT.2003.810129

II. Noise Parameters

Noise parameters are not directly measurable quantities, which are determined indirectly by measuring the noise figure of a linear two-port with different source impedances connected to the device-under-test (DUT). The noise figure of a linear two-port varies as a function of the source reflection coefficient, as given by the commonly known equation [7]

$$F = F_{\min} + 4r_n \frac{|\Gamma_S - \Gamma_{\rm opt}|^2}{\left(1 - |\Gamma_S|^2\right)|1 + \Gamma_{\rm opt}|^2} \tag{1}$$

where $F_{\min}$ is the minimum noise figure of the two-port, r_n is the normalized noise resistance, $\Gamma_{\rm opt}$ is the optimum reflection coefficient, with which the minimum noise figure is achieved, and Γ_S is a reflection coefficient of a network connected to the input of the two-port. Parameters $F_{\min}$, r_n, and $\Gamma_{\rm opt}$ are called noise parameters. Since $\Gamma_{\rm opt}$ is a complex quantity, at least four noise-figure measurements using different source reflection coefficients Γ_S have to be made in order to solve the noise parameters of the DUT. To reduce the effect of measurement errors, more than four measurements are often made and noise parameters are solved using mathematical fitting routines.

III. Measurement Setup

The schematics and photograph of the automated measurement setup built are presented in Figs. 1 and 2, respectively. The reference planes used in the calibrations are also shown. The so-called cold-source method [8], [9] was selected to be used. In the developed setup, an automated noise-figure meter is used to perform the noise-figure measurements. Since the frequency range of the noise-figure meter is 10–1500 MHz, a receiver chain consisting of an LNA, a mixer, and a millimeter-wave signal generator is used to downconvert the noise power from millimeter waves to 30 MHz. The LNA is obtained through

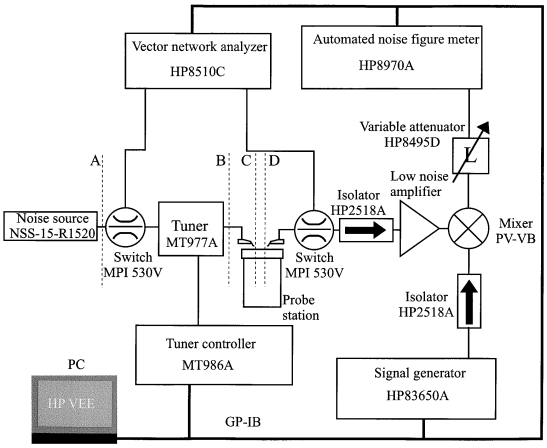

Fig. 1. Noise-parameter measurement setup.

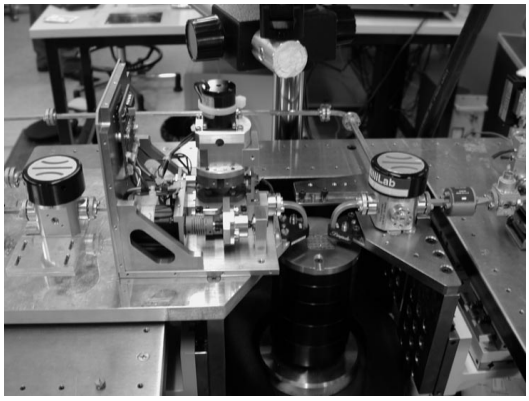

Fig. 2. Photograph of the measurement system.

Planck Surveyor collaboration [10]. A DUT is placed in a probe station and its source impedance is varied using the automated tuner. The tuner is a commercially available waveguide tuner in which the reflection coefficient at the reference plane B is controlled using a moveable probe. The magnitude of the reflection coefficient is controlled by changing probe insertion into the waveguide and the phase of the reflection coefficient is controlled moving the probe along the waveguide. The probe motions are automated by stepper motors. The probe's placement inside the waveguide can be characterized by two coordinates, which are step counts of the stepper motors. Thus, probe's placement will be referred to simply as *tuner position* below. Due to losses between the tuner and a DUT, the maximum realizable magnitude of a reflection coefficient at the DUT input is approximately 0.8. A solid-state noise source is connected to the tuner input. Bias for active devices is fed through internal bias tees of the probes. A vector network analyzer and waveguide switches are added to the measurement system in order to perform S-parameter measurements without a need of reconfiguration of the system. In-house written software is used to control measurement setup.

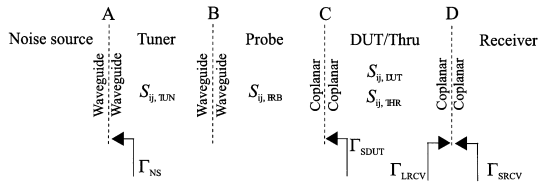

Fig. 3. Functional blocks, notations, and connection types of the measurement setup.

IV. Calibration and Measurement Procedures

From the operational point-of-view, the measurement setup can be divided into five functional blocks, which are the noise source, tuner, input probe, DUT, and noise receiver. These blocks, notation of their parameters, and connection types of the reference planes are shown in Fig. 3. The reference planes between different blocks are selected this way in order to make calibrations and calculations easier. Required measurements can be divided into three steps. The first two steps are related to the characterization of the measurement system and can be omitted if no change in the measurement system has been made. These three steps are described individually below.

A. S-Parameter and Reflection-Coefficient Measurements

In order to perform noise-parameter measurements, S-parameters of the tuner, the input probe, the DUT, and a thru calibration standard have to be known. S-parameters of one tuner position are needed in receiver calibration calculations and they are measured while the tuner probe is retracted from the waveguide and the tuner is essentially a normal waveguide. This measurement, as well as the S-parameter measurements for the DUT and the thru calibration standard, are done with a vector network analyzer in a straightforward manner. The line-reflect–reflect–match (LRRM) calibration [11] is used for the on-wafer components and waveguide thru-reflect-line (TRL) calibration [12] is used for the tuner. The calibration methods mentioned above were selected because they provided the best accuracy with existed calibration standards. Since the input probe is a noninsertable network, its S-parameters cannot be measured directly. Thus, two one-port calibrations are done, i.e., a waveguide short-offset short-load (SSL) calibration in reference plane B and a coplanar short-open-load (SOL) on-wafer calibration in reference plane C. S-parameters of the noninsertable network B–C can be calculated from the network analyzers' error correction coefficients obtained in these calibrations [13], [14].

The S-parameters of the thru standard, which are used in the calculations, are determined in the following manner. First, an LRRM calibration is done with a set of the calibration standards. S-parameters of a thru from a different set of calibration standards are then measured. These S-parameters are then used in the noise-parameter calculations. Usually, the magnitude of the S_{21} is approximately 0.99 over the entire V-band.

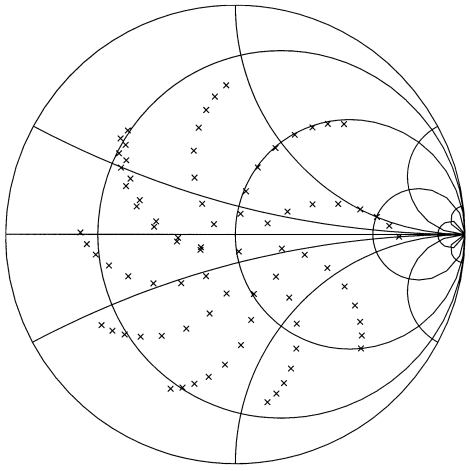

Fig. 4. Measured source reflection coefficients (Γ_{SDUT}) at 57 GHz during tuner characterization.

The reflection coefficient measurements include reflection coefficients of the cold noise source ($\Gamma_{\rm NS}$) and the receiver (Γ_{LRCV}), as well as source reflection coefficient (Γ_{SDUT}) measurements with different tuner positions. The latter two operations cannot be performed directly because the port to be measured is the coplanar probe tip in both cases. Thus, the thru calibration standard is used. Instead of measuring the reflection coefficient of the receiver at reference plane D, the reflection coefficient of a cascade of the thru and the receiver is measured at reference plane C. The reflection coefficient of the receiver can then be calculated from the measured value when S-parameters of the thru are known. A similar procedure is used when source reflection coefficients at the DUT input plane are measured using different tuner positions. During these measurements, the entire input network (noise source, tuner, and input probe) is assembled and the reflection coefficient is measured for a great number of tuner positions to allow device specific selection during the later measurements. As an example, measured source reflection coefficient values at 57 GHz are shown in Fig. 4. Measurement of $\Gamma_{\rm NS}$ is a simple waveguide operation.

The accurate characterization of these passive networks is a very important issue in noise-parameter measurements. The attenuation between the noise source and receiver decreases hot noise temperature at the receiver input and inaccuracies in the source reflection-coefficient measurements directly affects the noise parameter extraction accuracy. Thus, few unidealities and assumptions in calibration methods that degrade the accuracy of passive network characterization are outlined here [15], [16]. With waveguides, the two-port TRL and one-port SSL calibrations are considered to be very accurate with manufacturer provided standard definitions. The on-wafer coplanar SOL calibration is the most sensible for standard definition errors because all calibration standards used have to be fully characterized. With LRRM calibration, only the line standard needs to be fully known, reflect standards need not to be equal, and a load inductance present in the coplanar load is calculated during the calibration. Standard definitions for SOL standards and the LRRM line were provided by the calibration substrate manufacturer and their effects are taken into account in the calibration software used for the on-wafer calibrations. The differences between the actual standard used in the calibration and the standard definitions are the main source for inaccuracies in the calibrations. These differences can occur, for example, from wearing of the standards and probes, as well as from inaccurate probe placement. Thus, there will always be residual errors in measured S-parameters.

B. Noise Receiver Calibration

To carefully characterize the noise contribution of the receiver, its kBG-factor and noise parameters have to be known. The kBG-factor is a constant on each frequency and it includes the Boltzmann's constant k, the noise bandwidth of the measurement system B, and the transducer gain G of the receiver for a 50-Ω source. During these measurements, the thru calibration standard is placed in the probe station. A more detailed description about the measurement procedure can be found in [9]. Only the most important formulas are repeated here. The kBG-factor of the receiver is determined performing one noise power measurement with a hot and a cold noise source, respectively. The kBG-factor is calculated with the following:

$$kBG = \frac{P_H - P_C}{T_H - T_C} \left|1 - \Gamma_{LRCV}\Gamma_{SRCV}\right|^2 \cdot \frac{\left|1 - S_{11,\,AD}\Gamma_{\rm NS}\right|^2}{\left(1 - \left|\Gamma_{\rm NS}\right|^2\right)\left|S_{21,\,AD}\right|^2} \quad (2)$$

where P_H and P_C are noise powers measured with a hot and a cold noise source, respectively, T_H is the noise temperature of the hot noise source calculated from the excess noise ratio (ENR) and transformed into receiver input plane, T_C is the physical temperature of the measurement system, Γ_{SRCV} is the source reflection coefficient of the input network at the receiver input reference plane (the reference plane D), Γ_{LRCV} is the reflection coefficient of the receiver, and $S_{ij,\,AD}$ are overall S-parameters of the cascaded tuner, probe, and thru.

The noise parameters of the receiver are determined by measuring noise powers of the cold noise source using at least four different tuner positions. The noise figure is obtained using

$$F_i = \frac{P_{Ci}}{T_0 kBG}\frac{\left|1 - \Gamma_{LRCV}\Gamma_{SRCVi}\right|^2}{1 - \left|\Gamma_{SRCVi}\right|^2} - \frac{T_C}{T_0} + 1 \quad (3)$$

where P_{Ci} is the measured noise power for the ith source reflection coefficient Γ_{SRCVi}, T_0 is the standard temperature 290 K, and T_C is the physical temperature of the measurement system. Using obtained noise-figure–source reflection-coefficient pairs, noise parameters are calculated using the noise parameter extraction technique described in [17] with similar modifications as suggested in [18]. In brief, exact solutions of four $F_i - \Gamma_{SRCVi}$ pair subsets are calculated at first. Errors between values calculated using this solution and measured values are then derived. After all possible four pair subsets are investigated, solutions with which the error remained within predetermined boundaries are averaged to produce the final noise parameters. In these measurements, 20% of error was allowed for each value.

C. Noise-Parameter Measurements of the DUT

After the calibrations, the DUT is placed in the probe station. During this phase, only the cold noise source is used with different tuner positions. The total noise figure of the cascade of the DUT and receiver can be calculated using

$$F_{\mathrm{TOT}i} = \frac{P_{Ci}}{T_0 kBG} \cdot \frac{|1-S_{11,\mathrm{DUT}}\Gamma_{\mathrm{SDUT}i}|^2\,|1-\Gamma_{LRCV}\Gamma_{SRCVi}|^2}{\left(1-|\Gamma_{\mathrm{SDUT}i}|^2\right)|S_{21,\mathrm{DUT}}|^2} - \frac{T_C}{T_0}+1 \quad (4)$$

where P_{Ci} is the measured noise power for the ith source reflection coefficient $\Gamma_{\mathrm{SDUT}i}$ and Γ_{SRCVi} is the reflection coefficient of the network connected to the input of the receiver. With well-known Friis formula [19] for cascaded two-port, the DUT's noise figure can be calculated using

$$F_{\mathrm{DUT}i} = F_{\mathrm{TOT}i} - \frac{F_{RCVi}-1}{G_{\mathrm{DUT}i}} \quad (5)$$

where F_{RCVi} is the noise factor of the receiver calculated from the receiver's noise parameters for each source reflection coefficient and $G_{\mathrm{DUT}i}$ is the available gain of the DUT. Noise parameters of the DUT are determined using the same extraction procedure as with the receivers noise parameters.

V. Measurement Results

The operation of the measurement system was verified by measuring noise parameters of both passive and active on-wafer devices. Nine different source reflection-coefficient values were used during these measurements. The reflection-coefficient values used were distributed uniformly over the Smith chart. Minimum noise figure and normalized noise resistance of the receiver are shown in Figs. 5 and 6. The optimum source reflection coefficient was close to zero. The minimum noise figure shows uniform operation of the receiver over the entire 50–75-GHz band. With normalized noise resistance curve, there is a step in the curve after 66 GHz. Although the step remained in the results also after recalibration, this is suspected to be a fault. For a passive device, noise parameters can be calculated from measured S-parameters [20]–[22]. Comparison between the noise parameters determined using the developed measurement system and the values calculated from S-parameter measurements for passive device are shown in Figs. 7 and 8. The passive test item was nominally 40-Ω resistor connected in series between the probes. The resistor was measured from an old test wafer, where component characteristics differed from nominal values significantly. The resistor was selected because its S-parameters indicated a wide range for minimum noise figure. A good agreement between the measured and calculated data can be seen. There are only two significant deviations from calculated values in Fig. 8 at 73 and 74 GHz. Single origin for these errors can not be pointed out. Typical results obtained for an indium phosphide (InP) high electron-mobility transistor (HEMT) are shown in Figs. 9–12. Gate length and gatewidth of the HEMT device are 0.18 μm and 2 × 40 μm, respectively, and it was manufactured by DaimlerChrysler, Ulm, Germany. Drain voltage of 1.0 V and

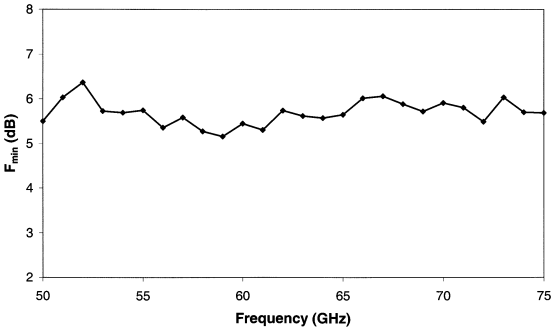

Fig. 5. Minimum noise figure of the receiver.

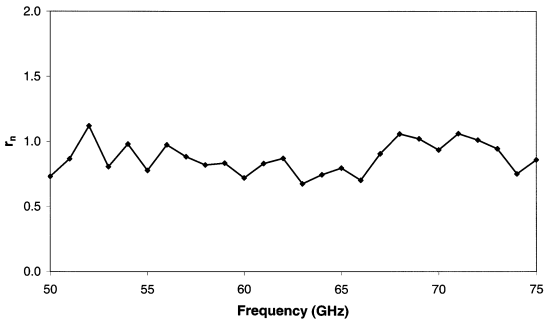

Fig. 6. Normalized noise resistance of the receiver.

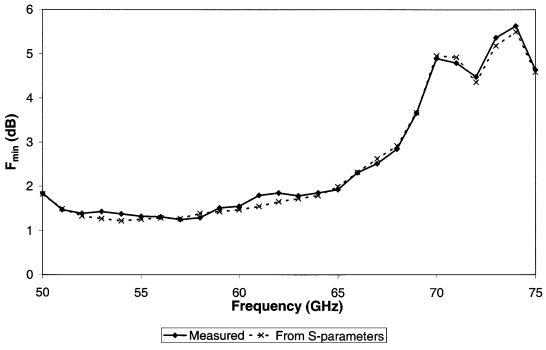

Fig. 7. Comparison of minimum noise figure between values measured using a wide-band measurement system and the value calculated from measured S-parameters for the passive on-wafer device.

drain current of 10 mA were used in the measurements. Values above 65 GHz have excess errors due to difficulties in the noise receiver calibration. Clear errors can be seen at the 66–68-GHz band, where the values of the minimum noise figure and noise resistance differ noticeably from the trend of preceding values. Similar behavior was seen on the normalized noise resistance of the receiver. The effect of the receiver noise resistance is greater with the HEMT device than with the resistor because receiver source reflection coefficient is further away from the center of the Smith chart with the HEMT device. Thus, the effect of some terms in (1) increases. These kinds of errors

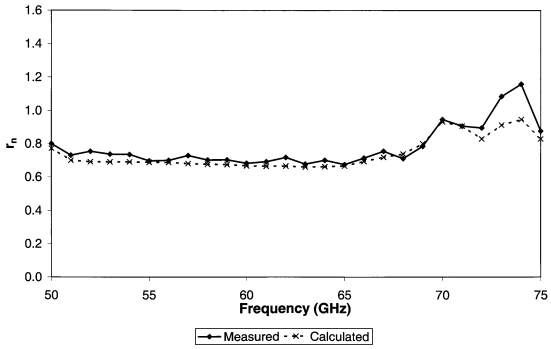

Fig. 8. Comparison of normalized noise resistance between values measured using a wide-band measurement system and the value calculated from measured S-parameters for the passive on-wafer device.

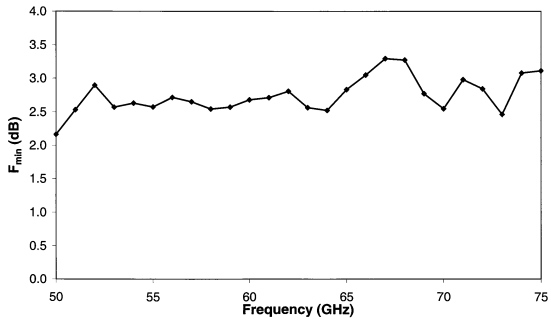

Fig. 9. Minimum noise figure measured for the InP HEMT device.

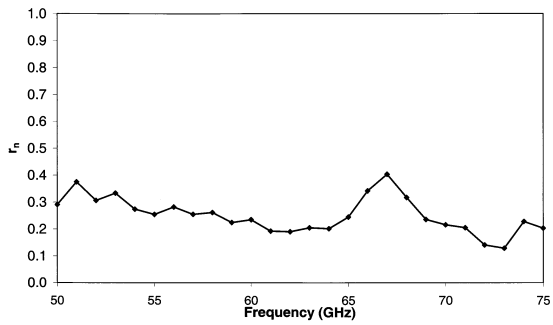

Fig. 10. Normalized noise resistance measured for the InP HEMT device.

can be clearly seen from the wide-band data, but may remain undiscovered when single-frequency measurements are done.

VI. Error Analysis

Almost 40 measured quantities affect the final values of the noise parameters. These include S-parameters, reflection coefficients, power measurements, ENR calibration of the noise source, and room temperature. To get an estimation of measurement accuracy, a Monte Carlo analysis [23] was carried out. In the analysis, random errors are added to the initial measured values and the noise parameters are calculated, e.g., 1000 times.

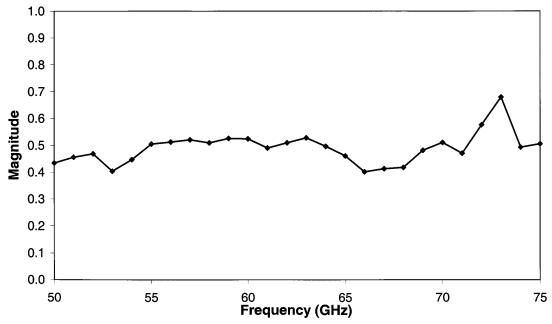

Fig. 11. Magnitude of optimum source reflection coefficient measured for the InP HEMT device.

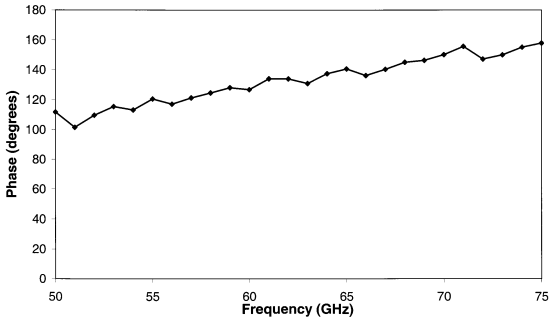

Fig. 12. Phase of optimum source reflection coefficient measured for the InP HEMT device.

TABLE I
Uncertainties for Measured Parameters

Parameter	Standard uncertainty	Uncertainty type
$S_{11,TUN}$, $S_{22,TUN}$	0.005	A, B
$S_{12,TUN}$, $S_{21,TUN}$	0.006	A, B
$S_{11,PRB}$, $S_{22,PRB}$	0.036	B
$S_{12,PRB}$, $S_{21,PRB}$	0.005	B
$S_{11,DUT}$, $S_{22,DUT}$	0.036	B
$S_{12,DUT}$, $S_{21,DUT}$	0.05	B
Γ_{LRCV}	0.036	B
Γ_{SDUT}	0.036	A, B
Γ_{NS}	0.005	B
ENR (dB)	0.06	B
P_H, P_C (dB)	0.04	B
T_C (K)	0.82	B

Statistical analysis is then performed to the obtained noise-parameter sets. To get values for random error distributions, uncertainties were divided into A- and B-type uncertainties, as suggested in [24]. A-type uncertainties are determined through statistical analysis and B-type uncertainties by any other means (i.e., from literature). Prior work with manual on-wafer measurement system provided most of the information [25]. Uncertainties used in the error analysis are listed in Table I. Rectangular distribution was used for S-parameter, reflection coefficient, and power measurement errors. Triangular distribution was used for ambient temperature. Deviations of the minimum noise figure and the optimum source reflection coeffi-

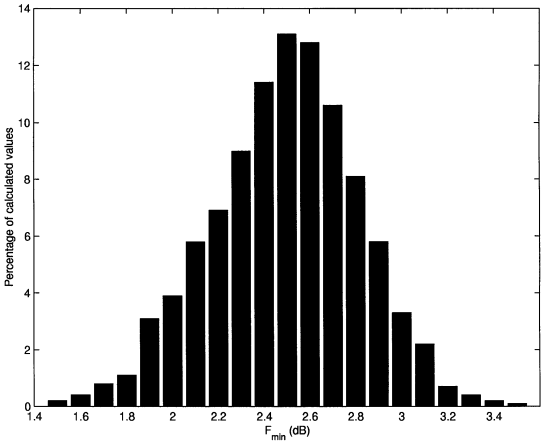

Fig. 13. Deviation of the minimum noise figure obtained in the Monte Carlo analysis with 1000 runs at 57 GHz.

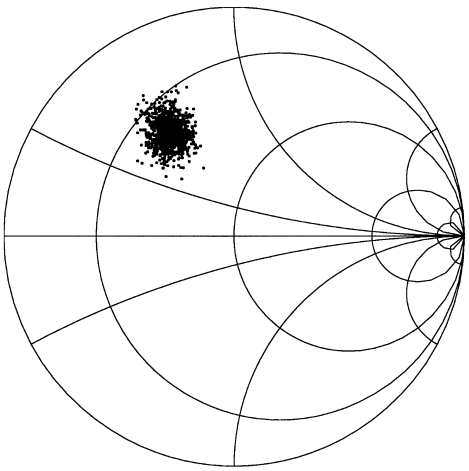

Fig. 14. Scattering of the optimum source reflection coefficient obtained in the Monte Carlo analysis with 1000 runs at 57 GHz.

TABLE II
MEASURED NOISE PARAMETERS AND CORRESPONDING CONFIDENCE BOUNDARIES FOR THE HEMT DEVICE AT 57 GHz

Parameter	F_{min}	r_n	$\lvert\Gamma_{opt}\rvert$	$\angle\Gamma_{opt}$
Measured value	2.65 dB	0.25	0.57	121°
2σ (95.5 %) confidence boundary	± 0.6 dB	± 0.06	± 0.1	± 9°

cient are presented in Figs. 13 and 14. S-parameters of the DUT and source reflection-coefficient measurement (Γ_{SDUT}) were found to be the main sources of errors. Confidence boundaries depend heavily on the test device. For example, the noise paraboloid defined by (1) for an HEMT device has a very flat bottom due to a low value of r_n. Thus, even a major displacement of the optimum source reflection coefficient has only a little effect on the shape of the noise paraboloid. This leads to a wide confidence boundary for the optimum reflection coefficient. As an example, the measured values for the HEMT device at 57 GHz with the corresponding 2σ confidence boundaries are given in Table II. Obtained boundaries correspond to observed ripple well when clearly erroneous values are discarded.

VII. CONCLUSIONS

A unique wide-band automated on-wafer noise parameter measurement setup has been built and its performance has been demonstrated by measuring noise parameters for both passive and active on-wafer devices. Wide-band noise-parameter measurements at millimeter-wave frequencies are important for accurate interpretation of the measured results. For example, if measurements had been made on a single frequency at 67 GHz, false results would have been obtained due to problems with the noise receiver calibration. These kinds of frequency-dependent systematic errors can be revealed only when wide-band measurements are performed. The wide-band on-wafer measurement system will also be an important tool in development and verification of device models, as well as in device characterization.

ACKNOWLEDGMENT

The authors would like to thank P. Kangaslahti, P. Jukkala, and N. Hughes, all of Ylinen Electronics Ltd., Kauniainen, Finland, for lending us the wide-band LNA. The authors would also like to recognize the invaluable support and comments of T. Närhi, European Space Agency (ESA), Noordwijk, The Netherlands, as well as T. Karttaavi, J. Varis, and H. Hakojärvi, all of the Millimeter Wave Laboratory of Finland–MilliLab, VTT TECHNICAL RESEARCH CENTRE OF FINLAND, Espoo, Finland.

REFERENCES

[1] J. Laskar, M. R. Murti, S. Y. Yoo, E. Gebera, and H. M. Harris, "Development of complete on-wafer cryogenic characterization: S-parameters, noise parameters and load-pull," in *Eur. GaAs and Related III–V Compounds, Application Symp. Dig.*, Amsterdam, The Netherlands, 1998, pp. 33–38.

[2] M. Lahdes, J. Tuovinen, and M. Sipilä, "60 GHz on-wafer noise measurements using cold-source method," in *49th ARFTG Conf. Dig.*, 1997, pp. 146–154.

[3] M. Lahdes and J. Tuovinen, "V-band on-wafer noise parameter measurements," in *Proc. GAAS*, 1998, pp. 39–44.

[4] J. Tuovinen, M. Lahdes, T. Karttaavi, and H. Hakojärvi, "Millimeter wave on-wafer testing at room and cryogenic temperatures," in *Proc. 7th Int. Recent Advances in Microwave Technology Symp.*, 1999, pp. 415–418.

[5] M. Kantanen, M. Lahdes, J. Tuovinen, T. Vähä-Heikkilä, P. Kangaslahti, P. Jukkala, and N. Hughes, "A wideband automated measurement system for on-wafer noise parameter measurements at 50–75 GHz," in *Proc. GAAS*, 2001, pp. 255–258.

[6] T. A. Alam, R. D. Polard, and C. M. Snowden, "The determination of on-wafer noise parameters in W-band," in *Proc. 27th Eur. Microwave Conf.*, 1997, pp. 687–691.

[7] H. Rothe and W. Dahlke, "Theory of noisy four poles," in *Proc. IRE*, vol. 44, 1956, pp. 811–818.

[8] V. Adamian and A. Uhlir, "A novel procedure for receiver noise characterization," *IEEE Trans. Instrum. Meas.*, vol. IM-22, pp. 181–182, June 1973.

[9] R. Meierer and C. Tsironis, "An on-wafer noise parameter measurement technique with automatic receiver calibration," *Microwave J.*, vol. 38, pp. 22–37, 1995.

[10] J. Tuovinen, P. Kangaslahti, P. Haapanen, N. Hughes, P. Jukkala, T. Karttaavi, O. Koistinen, M. Lahdes, H. Salminen, J. Tanskanen, and S. Urpo, "Development of 70 GHz receivers for the Planck LFI," *Astrophys. Lett. Commun.*, vol. 37, pp. 181–187, 2000.
[11] A. Davidson, K. Jones, and E. Strid, "LRM and LRRM calibrations with automatic determination of load inductance," in *36th ARFTG Conf. Dig.*, 1990, pp. 57–62.
[12] G. F. Engen and C. A. Hoer, "Thru-reflect-line: An improved technique for calibrating the dual six port automatic network analyzer," *IEEE Trans. Microwave Theory Tech.*, vol. 27, pp. 987–993, Dec. 1979.
[13] R. T. Webster, A. J. Slobodnik, and G. A. Roberts, "Determination of InP HEMT noise parameters and S-parameters to 60 GHz," *IEEE Trans. Microwave Theory Tech.*, vol. 43, pp. 1216–1225, June 1995.
[14] R. P. Meys, "A triple-through method for characterizing test fixtures," *IEEE Trans. Microwave Theory Tech.*, vol. 36, pp. 1043–1046, June 1988.
[15] C. L. Hammond and K. L. Virga, "Network analyzer calibration methods for high-density packaging characterization and validation of simulation methods," in *Proc. Electronic Components and Technology Conf.*, 2000, pp. 519–525.
[16] M. Nishimoto, M. Hamai, J. Laskar, and R. Lai, "On-wafer calibration techniques and applications at V-band," *IEEE Trans. Microwave Guided Wave Lett.*, vol. 4, pp. 370–372, Nov. 1994.
[17] G. I. Vasilescu, G. Alquie, and M. Krim, "Exact computation of two-port noise parameters," *Electron. Lett.*, vol. 25, pp. 292–293, 1989.
[18] L. Escotte, R. Plana, and J. Graffeuil, "Evaluation of noise parameter extraction methods," *IEEE Trans. Microwave Theory Tech.*, vol. 41, pp. 382–387, Mar. 1993.
[19] H. T. Friis, "Noise figure of radio receivers," in *Proc. IRE*, vol. 32, July 1944, pp. 419–422.
[20] A. Fraser, E. Strid, B. Leake, and T. Burcham, "Repeatability and verification of on-wafer noise parameter measurements," *Microwave J.*, vol. 31, no. 11, pp. 172–176, Nov. 1988.
[21] A. Boudiaf, C. Dubon-Chevallier, and D. Pasquet, "Verification of on-wafer noise parameter measurements," *IEEE Trans. Instrum. Meas.*, vol. 44, pp. 332–335, June–July 1995.
[22] E. Strid, "Noise measurements for low-noise GaAs FET amplifiers," *Microwave Syst. News*, vol. 10, pp. 62–70, 1981.
[23] W. H. Press, B. P. Flannery, S. A. Teukolsky, and W. T. Vetterling, *Numerical Recipes, The Art of Scientific Computing*. Cambridge, MA: Cambridge Univ. Press, 1986.
[24] B. N. Taylor and C. E. Kuyatt, "Guidelines for evaluating and expressing the uncertainty of NIST measurement results," NIST, Boulder, CO, Tech. Note 1297, 1994.
[25] M. Lahdes, "Uncertainty analysis of V-band on-wafer noise parameter measurement system," in *Proc. 28th Eur. Microwave Conf.*, 1998, pp. 445–450.

Mikko Kantanen received the Master of Science degree in electrical engineering degree from the Helsinki University of Technology (HUT), Espoo, Finland, in 2001.

Since 1999, he has been with the Millimeter Wave Laboratory of Finland–MilliLab, VTT TECHNICAL RESEARCH CENTRE OF FINLAND, Espoo, Finland, initially as a Trainee Research Scientist and, since 2001, as a Research Scientist involved with noise measurements at millimeter waves. He is currently also involved with other millimeter-wave activities including on-wafer measurement systems, monolithic microwave integrated circuit (MMIC) design, and passive imaging.

Manu Lahdes received the Master of Science degree in electrical engineering degree from the Helsinki University of Technology, Espoo, Finland, in 1996.

Since 1996, he has been with a Research Scientist the Millimeter Wave Laboratory of Finland–MilliLab, VTT TECHNICAL RESEARCH CENTRE OF FINLAND, Espoo, Finland. His research interests in the millimeter-wave area have been on-wafer noise parameter measurements, cryogenic on-wafer measurements, active device modeling, and MMIC design and testing. He has authored or coauthored several papers. His current activities also include passive millimeter imaging.

Tauno Vähä-Heikkilä (S'01) received the B.S. and M.S. degrees in physics from the University of Turku, Turku, Finland, in 2000 and 2001, respectively. His M.S. thesis concerned W-band on-wafer noise-parameter measurements.

He was a Trainee Research Scientist and, since 2002, he has been a Research Scientist with the Millimeter Wave Laboratory of Finland–MilliLab, VTT TECHNICAL RESEARCH CENTRE OF FINLAND, Espoo, Finland. He is also currently a Visiting Scholar with the Radiation Laboratory, The University of Michigan at Ann Arbor. His research interests include RF microelectromechanical systems (MEMS) and millimeter-wave on-wafer measurements.

Mr. Vähä-Heikkilä has been a secretary for the IEEE Antennas and Propagation (AP)/Electron Devices (ED)/Microwave Theory and Techniques (MTT) Finland Chapter since 2001.

Jussi Tuovinen (S'86–M'91) received the Dipl.Eng., Lic.Tech., and Dr.Tech. degrees in electrical engineering from the Helsinki University of Technology (HUT), Espoo, Finland, in 1986, 1989, and 1991, respectively.

From 1986 to 1991, he was a Research Engineer with the HUT Radio Laboratory, where he was involved with millimeter-wave antenna testing for the European Space Agency (ESA), quasi-optical measurements, and Gaussian beam theory. From 1991 to 1994, he was a Senior Post-Doctoral Fellow with the Five College Radio Astronomy Observatory, University of Massachusetts, Amherst, where he studied holographic testing methods and developed frequency multipliers up to 1 THz. From 1994 to 1995, he was a Project Manager with the HUT Radio Laboratory, where he was involved with hologram compact antenna test range (CATR) and 119-GHz receiver development for Odin-satellite. He is currently a co-investigator and heads development of 70-GHz receivers for the low-frequency instrument of the ESA Planck Surveyor. His research activities also includes development of methods for on-wafer testing of integrated circuits and components. He is currently a Research Professor with VTT TECHNICAL RESEARCH CENTRE OF FINLAND Information Technology and a Director of the Millimeter Wave Laboratory of Finland–MilliLab, ESA External Laboratory. From 2001 to 2002, he was a Visiting Researcher with the University of Hawaii at Manoa, where he developed communications methods using retrodirective antennas. He has authored or coauthored over 100 papers.

Dr. Tuovinen is a past secretary of the Finnish National Committee of the Committee on Space Research (COSPAR) and the IEEE Finland Section. He was also the executive secretary of the Local Organizing Committee of the 27th Plenary Meeting of COSPAR, held in 1988. In 1998, he was a co-chairman of the Second ESA Workshop on Millimeter Wave Technology and Applications. He has served as a chairman of the IEEE Microwave Theory and Techniques (MTT)/Antennas and Propagation (AP) Finland Chapter. He is the chairman of the Third ESA Workshop on Millimeter Wave Technology and Applications. He was the recipient of an ESA Fellowship for multiplier work at the University of Massachusetts in 1992 and again in 1993.

Publication II

Kantanen, M., Weissbrodt, E., Varis, J., Leuther, A., Seelmann-Eggebert, M., Rösch, M., Schlecthweg, M., Poutanen, T., Sundberg, I., Kaisti, M., Altti, M., Jukkala, P., Piironen, P., “Active cold load MMICs for Ka-, V-, and W-bands,” *IET Microwaves, Antennas & Propagation*, vol. 9, no. 8, pp. 742-747, May 2015.

IET Microwaves, Antennas & Propagation

Research Article

IET Journals
The Institution of Engineering and Technology

Active cold load MMICs for Ka-, V-, and W-bands

ISSN 1751-8725
Received on 17th April 2014
Accepted on 6th November 2014
doi: 10.1049/iet-map.2014.0243
www.ietdl.org

Mikko Kantanen[1] ✉, Ernst Weissbrodt[2], Jussi Varis[1], Arnulf Leuther[2], Matthias Seelmann-Eggebert[2], Markus Rösch[2], Michael Schlecthweg[2], Torsti Poutanen[3], Iiro Sundberg[3], Matti Kaisti[3], Miikka Altti[3], Petri Jukkala[3], Petri Piironen[4]

[1]*MilliLab, VTT Technical Research Centre of Finland, P.O. Box 1000, FI-02044 VTT, Espoo, Finland*
[2]*Fraunhofer Institute for Applied Solid-State Physics, Tullastrasse 27, D-79108 Freiburg, Germany*
[3]*DA-Design, Keskuskatu 29, FI-31600 Jokioinen, Finland*
[4]*European Space Agency (ESTEC), NL-2200 AG Noordwijk, The Netherlands*
✉ *E-mail: mikko.kantanen@vtt.fi*

Abstract: Three active cold load circuits operating at millimetre-wave frequencies are presented. The circuits have been manufactured using 100 nm metamorphic high electron mobility transistor technology. On-wafer measurements of noise temperature and match are presented. Measured noise temperatures are 75 K, 141 K, and 170 K at 31.4 GHz, 52 GHz, and 89 GHz, respectively. Measured reflection coefficients are better than −19 dB for all designs.

1 Introduction

Radiometers are widely used in several applications in the areas of earth atmosphere and surface observation, radio astronomy, spectroscopy as well as deep space astrophysics. Radiometers are calibrated by measuring at least two loads with known noise temperature. For the best accuracy noise temperatures of the loads should be outside the expected noise temperature of the target, that is, 'hot' and 'cold' load. The calibration loads can be either external or internal. External calibration loads are viewed by the entire radiometer system, including a target-looking antenna. This way the antenna and the associated feed network are also calibrated. An External calibration load can be a cold sky target or a heated microwave absorber. Internal calibration loads are connected between the antenna and the radiometer front-end. Thus, only the radiometer itself is calibrated by the internal calibration loads. The antenna and the feed network need to be calibrated by other means. Typical realisation of an internal calibration system includes a through path for the antenna and means to connect two loads to the radiometer input by switches or directional couplers. The losses of the through path worsen accuracy of the radiometer and should be minimised. Examples of internal calibration loads are noise diodes, matched loads, and active cold loads (ACL).

An ACL is a one port transistor circuit with noise temperature below the physical ambient temperature. Low noise temperature makes ACLs attractive calibration loads especially in earth observation radiometers. Typical target temperature for the earth observation radiometers is 100–300 K and ACLs can provide low temperature calibration point. Previously published ACL realisations include hybrid designs [1–5] and monolithic microwave integrated circuit (MMIC) designs [6–8] for RF and microwave regions. The first millimetre wave MMIC designs have been reported in [9]. A summary of published results is presented in Table 1.

This paper presents design and measurements for three ACL circuits operating at millimetre-wave frequencies. Nominal specifications for the operating frequencies are 31.4 ± 0.2 GHz, 52.0 ± 2.0 GHz, and 89.0 ± 2.0 GHz. The frequency ranges are selected to cover multiple channels in the planned MetOp-SG instruments [10]. The ACLs are realised as MMICs using 100 nm GaAs metamorphic high electron mobility transistor (MHEMT) technology. MMIC realisation offers advantages over hybrid realisation in performance and size at the lower frequency end of millimetre-wave frequencies. The GaAs MHEMT technology provides good low noise performance with lower costs compared to InP HEMT technology.

2 Theory

The theoretical foundations of cold transistor circuits were laid in 1981 [1], when it was shown that noise temperatures below ambient temperature could be achieved for FET based circuit by proper matching network design. Noise wave based analysis and generalised design flow have been presented in [11]. The most important formulas are repeated here. Notation of two-port noise analysis is presented in Fig. 1. The noise temperature incident at the input plane of the system is

$$T_{s1} = T_b + \left[\left(T_1\left(1-|\Gamma_1|^2\right)+T_a\right)G_{21,ti}|\Gamma_2|^2 + T_2\left(1-|\Gamma_2|^2\right)\right]G_{12,ti} \quad (1)$$

where T_a and T_b are alternate noise parameters [12], which are derived from the traditional noise parameters ($T_{e,\,\min}$, R_n, $Y_{\text{opt}} = G_{\text{opt}} + \text{j}B_{\text{opt}}$) by

$$T_a = T_{e,\min} + \frac{T_k\left|\Gamma'_{\text{opt}}\right|^2}{1-\left|\Gamma'_{\text{opt}}\right|^2} \quad (2)$$

and

$$T_b = \frac{T_k}{1-\left|\Gamma'_{\text{opt}}\right|^2} - T_{e,\min} \quad (3)$$

T_k is given by

$$T_k = 4T_0R_nG_{\text{opt}} \quad (4)$$

and

$$\Gamma'_{\text{opt}} = \frac{\Gamma^*_{\text{in}} - \Gamma_{\text{opt}}}{\Gamma_{\text{opt}}\Gamma_{\text{in}} - 1} \quad (5)$$

Table 1 Previously published transistor based cold loads

Frequency, GHz	Noise temperature, K	Technology	Reference
1.4	50	GaAs MESFET	[1]
18	105	InP HEMT	[2]
2–10	90	GaAs MHEMT	[6]
10–26	125	GaAs MHEMT	[6]
4–8	100	GaAs PHMET	[7]
10.69	56	GaAs PHEMT	[3]
1.4	65	SiGe HBT	[4]
23.8	72	GaAs MHEMT	[5]
1.4	90	GaAs PHEMT	[8]
94	155	GaAs MHEMT	[9]

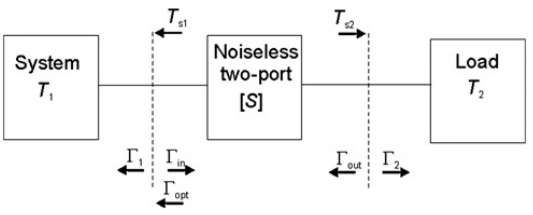

Fig. 1 *Notation for two-port noise analysis*

Here the T_0 is standard temperature of 290 K. The terminal invariant gains are derived from the circuit S-parameters and are given by

$$G_{12,ti} = \frac{|S_{12}|^2}{1 - |S_{11}|^2} \tag{6}$$

and

$$G_{21,ti} = \frac{|S_{21}|^2}{1 - |S_{22}|^2} \tag{7}$$

T_{s1} is minimised when $\Gamma_{in} = \Gamma^*_{opt}$. Input noise and power matching can be obtained simultaneously when

$$\Gamma_2 = \frac{\Gamma^*_{opt} - S_{11}}{S_{12}S_{21} + S_{22}(\Gamma^*_{opt} - S_{11})} \tag{8}$$

For a transistor alone, Γ_2 can have magnitude greater than unity. In this case a feedback network has to be designed to obtain a realisable value.

3 Designs

The manufacturing process used in this work is the 100 nm GaAs based MHEMT technology of the Fraunhofer IAF, Freiburg, Germany. The transistors have f_t of 220 GHz, and the process is suitable for grounded coplanar waveguide (GCPW) designs. The process features NiCr thin film resistors, metal-insulator-metal (MIM) capacitors and backside metallisation. Unwanted substrate modes are suppressed using ground via holes through the GaAs substrate. As a result of extensive modelling work the Fraunhofer IAF provides reliable models for CPW components and transistors [13].

The schematic of the realised ACL designs is presented in Fig. 2. The two port noise analysis can be utilised in a circuit simulator software by replacing the termination at the drain matching network by a 50 Ω simulation port. In principle, the ACL design work has three steps [11]:

1. Design of a feedback network to obtain a realisable value for the drain matching circuit reflection coefficient $\Gamma_L = \Gamma_2$.
2. Design of a drain matching circuit for Γ_L.
3. Design of a gate matching circuit for Γ^*_{opt}.

Inductive source feedback was utilised in the ACL circuits realised in this work.

The transistor size and the length of source transmission line have the largest effect on the overall noise temperature of an ACL. According to the design theory [11], the inductive feedback is adjusted to obtain the lowest noise temperature while satisfying the condition $|\Gamma_L| < 1$ for drain matching network. Additional restrictions for the source transmission line length arise from stability considerations. Fig. 3*a* shows the expected noise temperature at 31.4 GHz as a function of the source line length for four differently sized transistors. The expected noise temperature decreases as the source line length increases. However, the stability of the transistor above 100 GHz depends heavily on the source line length. Fig. 3*b* shows μ stability factor of a 4×20 μm transistor as a function of frequency for five source line lengths. With longer source transmission line μ stability factor becomes smaller at frequencies above 100 GHz indicating larger unstable area on a Smith's chart. The designer is forced to perform a trade-off between the expected noise temperature and the stability.

The drain matching networks are designed to provide optimum load impedance for the transistor. The drain matching networks are

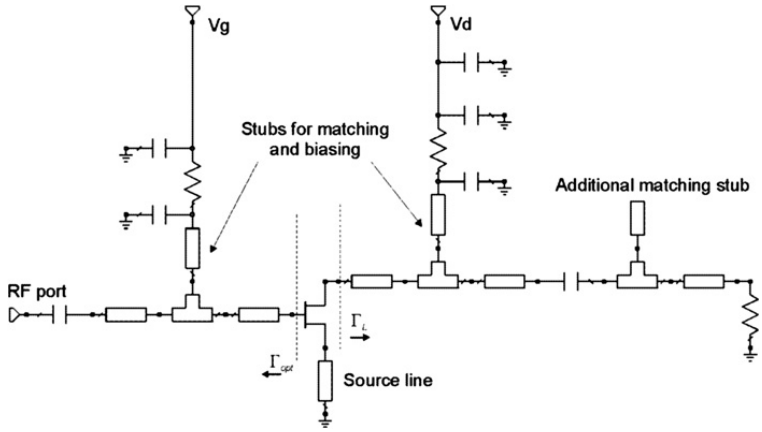

Fig. 2 *Schematic of realised ACL designs*

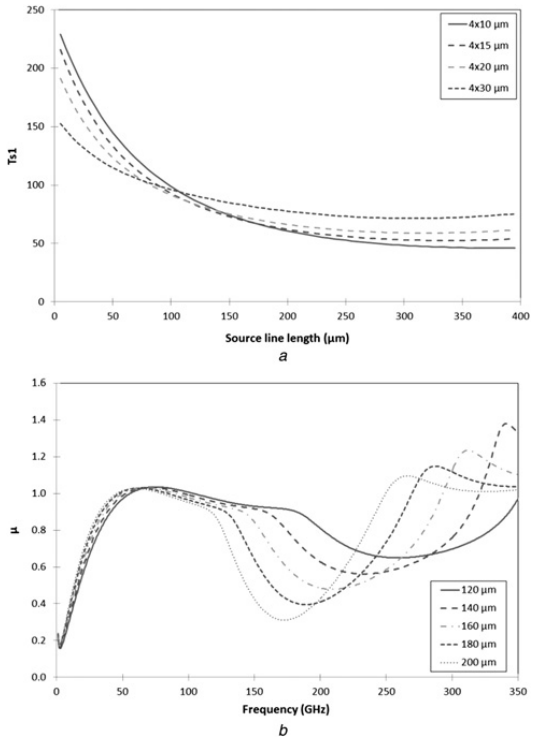

Fig. 3 *Expected noise temperature at 31.4 GHz as a function of the source line length or transistor size*

a Expected noise temperature as a function of source transmission line length for four transistor sizes at 31.4 GHz
b Stability factor µ of a 4 × 20 µm transistor as a function of frequency for five source transmission line lengths

realised using one open-ended stub and one RF-shorted stub. At 89 GHz, only a single RF-shorted stub is used. Other matching elements are a 50 Ω resistor and a DC-blocking capacitor which is also optimised for matching. The RF-short is realised by a capacitor. The transistor is biased through a RF-shorted stub, an additional stabilising resistor and large valued capacitors. An additional open-ended stub gives the designer one more degree of freedom in designing the matching network. It also improves the bandwidth of the RF port match. The reverse gain of the transistor is small and the noise contribution of the drain matching network is almost negligible. Thus, additional stabilising or matching elements can be added to the drain matching network without deteriorating the overall noise performance.

The gate matching networks provide simultaneous noise and conjugate match for the transistor. The losses of the gate matching network affect the overall noise performance greatly. The gate matching networks are realised using an RF-shorted stub, a series transmission line and a DC-blocking capacitor. Gate bias is fed through the RF-shorted stub. The resistor on the bias line was minimised or omitted to improve noise temperature while maintaining unconditionally stable operation. The simulated ACL results based on these design principles are presented in Section 5 together with measured results.

4 Measurements

Three test setups were used to characterise the noise temperatures of the realised ACLs. The setups are based on waveguide components at Ka-, V-, and W-bands. All measurement setups have similar functional blocks and a generic block diagram is shown in Fig. 4*a*. At Ka-band, the probe block includes a coaxial on-wafer probe and a short section of coaxial cable. Stainless steel waveguide is not used at Ka-band, but it is included in the V- and W-band setups. The noise calibration plane is at the coaxial port of the coaxial to waveguide transition connected to a waveguide full-band isolator input. A commercially available waveguide LNA and a fundamental mixer are used to amplify and downconvert the noise signal to fixed IF frequency. The isolator provides constant source impedance to the LNA. A microwave signal generator provides the LO-signal to the mixer. A noise figure analyser is utilised for noise power measurements. The Ka-band setup is calibrated by a noise diode with nominal excess noise ratio (ENR) of 12 dB. The calibration method is not optimal for the ACL measurement because the expected noise temperature is lower than the cold temperature of the calibration. Extrapolation of the calibration line increases measurement uncertainty because the setup behaviour is assumed to be linear, which may not always be the case. Also, the hot calibration temperature is very high compared to the expected ACL noise temperature.

At V- and W-band setups the waveguide on-wafer probes are followed by sections of stainless steel waveguides. A photograph of the V-band measurement setup is shown in Fig. 4*b*. Again, isolators are utilised to provide constant source impedance for the LNAs. The LNAs on both bands are developed in-house and they are housed in split-block waveguide packages. Fundamental mixers are again used and the LO-chain includes a microwave signal generator and a quadrupler at both bands. At both the V- and the W-band, the noise calibration is performed using heatable waveguide loads. Noise powers are measured with load temperatures of 298 K and 373 K. The stainless steel waveguide prevents heat flow from the load to the rest of the measurement setup. A temperature controller keeps the load temperature within ±1.5 K during the frequency sweeps. Again, the expected ACL noise temperatures on both bands are below calibration points and the extrapolation of the calibration line is required.

After calibration, the ACL under test and the on-wafer probe are connected to the measurement setup and the noise temperature at the probe output plane is measured. The probe loss is calculated from its S-parameters and the noise due to the probe is removed

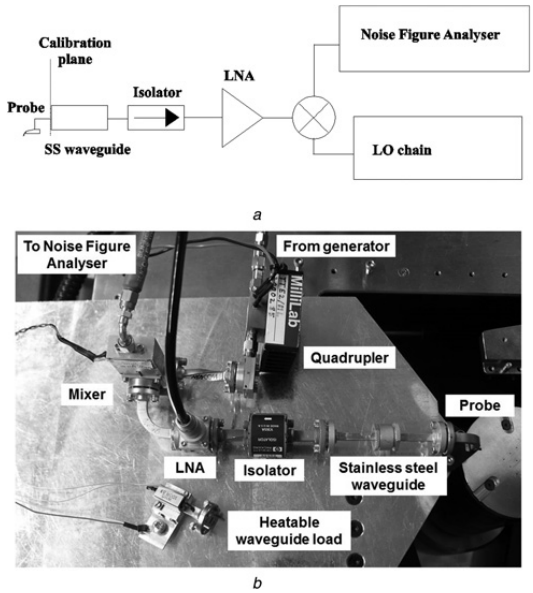

Fig. 4 *Measurement setup*

a Functional block diagram of the measurement setups
b Photograph of V-band measurement setup with heatable load

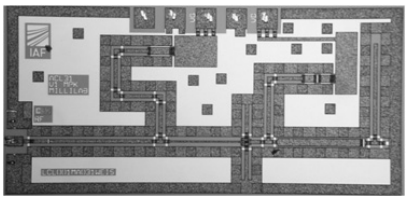

Fig. 5 *Micrograph of the 31.4 GHz ACL*
Chip size is 2.0 mm × 1.0 mm

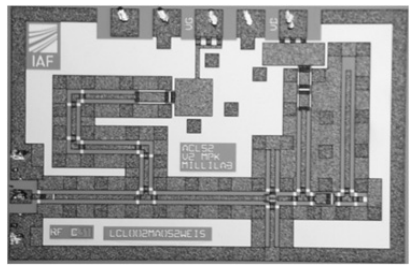

Fig. 7 *Micrograph of the 52 GHz ACL*
Chip size is 1.5 mm × 1.0 mm

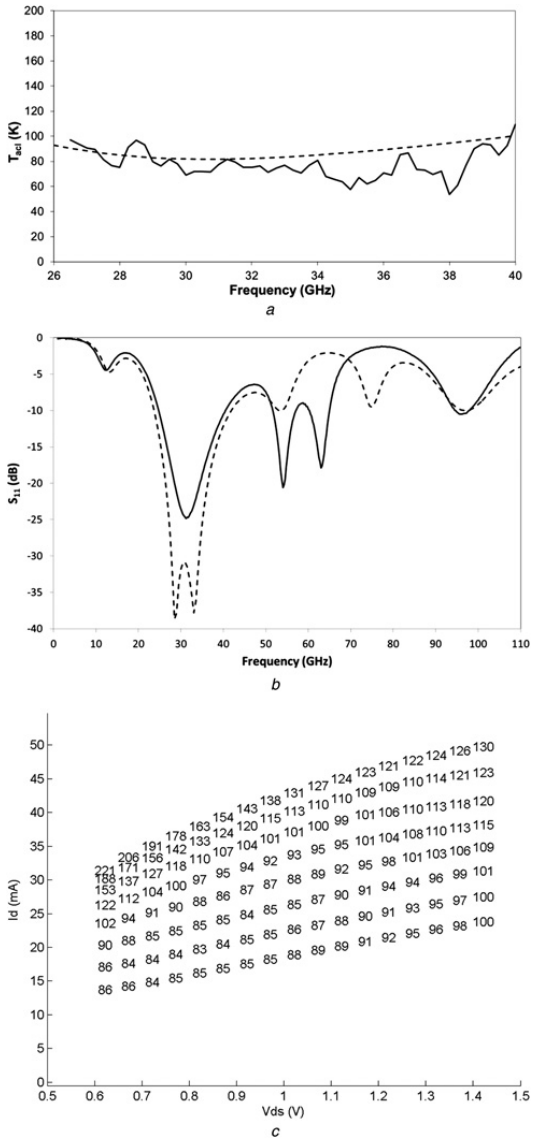

Fig. 6 *Performance of the 31.4 GHz ACL*

a Measured (solid) and simulated (dashed) noise temperature of the 31.4 GHz ACL at design bias $V_d = 1.0$ V, $I_d = 24$ mA
b Measured (solid) and simulated (dashed) RF port reflection of the 31.4 GHz ACL at design bias $V_d = 1.0$ V, $I_d = 24$ mA
c Variation of noise temperature over bias at 31.4 GHz

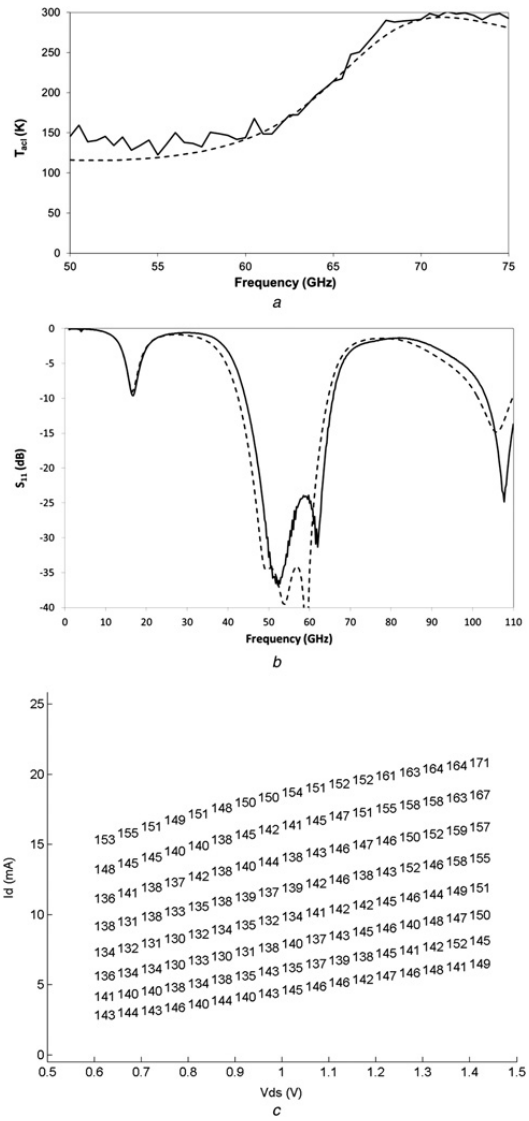

Fig. 8 *Performance of the 52 GHz ACL*

a Measured (solid) and simulated (dashed) noise temperature of the 52 GHz ACL at design bias $V_d = 1.0$ V, $I_d = 12$ mA
b Measured (solid) and simulated (dashed) RF port reflection coefficient of the 52 GHz ACL at design bias $V_d = 1.0$ V, $I_d = 12$ mA
c Variation of noise temperature over bias at 52 GHz

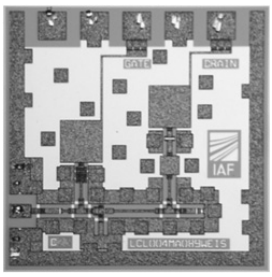

Fig. 9 *Micrograph of the 89 GHz ACL*
Chip size is 1.0 mm × 1.0 mm

from the measured noise temperature. The S-parameters of the probes are determined using a method described in [14]. The noise temperature values are not corrected due to mismatch in any measurement reported here. This introduces a systematic measurement error. However, ACLs have low reflection coefficient values especially over design band which reduces the mismatch effect.

A micrograph of a 31.4 GHz ACL is shown in Fig. 5. A transistor of size 4 × 20 μm with source transmission lines of 140 μm was selected for the design. A comparison between the measured and the simulated noise temperatures and the RF port reflection coefficient at the design bias of Vd = 1.0 V and Id = 24 mA are presented in Figs. 6*a* and *b*, respectively. The simulated noise temperature agrees with the measured noise temperature very well, the difference between the values is about 10 K around the design band. The average noise temperature over 30–32 GHz is 75 K. Assuming ±0.2 dB worst-case uncertainty [15] for ENR value during receiver calibration leads to ±15 K uncertainty in measured noise temperature value when calibration line is extrapolated. Also, the lowest reflection coefficient is achieved at the desired frequency range although even lower value was obtained in the simulations. However, the RF port reflection coefficient is better than −20 dB over 29–34 GHz. On our narrow design band of 31.4 ± 0.2 GHz the reflection coefficient is better than −24 dB. The effect of bias was studied at the 31.4 GHz frequency by measuring the noise temperature with different bias settings. Results are presented in Fig. 6*c*. The noise temperature of this ACL is rather insensitive to small changes in the drain voltage or current.

A micrograph of a 52 GHz ACL is shown in Fig. 7. The transistor size is 2 × 20 μm and the source transmission line length is 135 μm. A comparison between the measured and the simulated noise temperatures and the RF port reflection coefficient at design bias of Vd = 1.0 V and Id = 12 mA are presented in Figs. 8*a* and *b*, respectively. Again, the simulation agreed with the measured noise temperature very well. There is about 20 K difference between the measurement and the simulation at the lower frequency end of the measurement band. This could be partly due to the measurement system, because the operation of the LNA and the mixer in the measurement system are deteriorated at the band edges. The average noise temperature over 50–54 GHz is 141 K. Estimated worst-case noise temperature uncertainty due to calibration line extrapolation is ±10 K assuming 2 K deviation in calibration load temperatures. The RF port reflection coefficient over the design band of 50–54 GHz is better than −30 dB and the simulations correspond to the measurements extremely well. On a wider range, the reflection coefficient is better than −24 dB over a 49–63 GHz range. The effect of bias was investigated at 52 GHz frequency. Results are presented in Fig. 8*c*. Again, the ACL is rather insensitive to small changes in the drain voltage or current. Some improvement in noise temperature could be achieved by lowering the drain voltage and current.

A micrograph of an 89 GHz ACL is shown in Fig. 9. The transistor size is 2 × 15 μm and the source transmission line length is 47 μm. A comparison between the measured and the simulated noise temperatures and the RF port reflection coefficient at the design bias of Vd = 1.0 V and Id = 12 mA are presented in

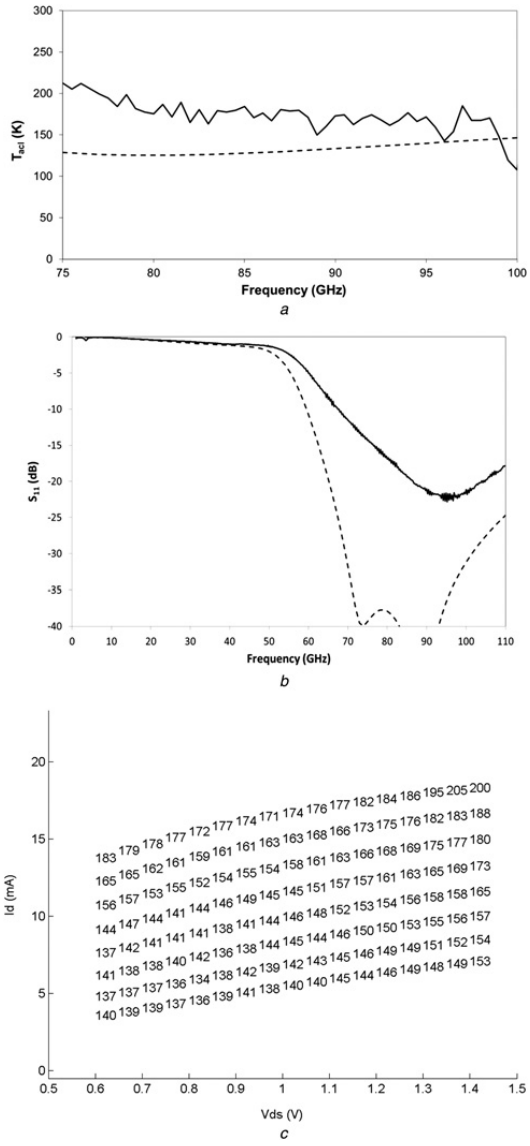

Fig. 10 *Performance of the 89 GHz ACL*
a Measured (solid) and simulated (dashed) noise temperature of the 89 GHz ACL at design bias $V_d = 1.0$ V, $I_d = 12$ mA
b Measured (solid) and simulated (dashed) RF port reflection coefficient of the 89 GHz ACL at design bias $V_d = 1.0$ V, $I_d = 12$ mA
c Variation of noise temperature over bias at 89 GHz

Figs. 10*a* and *b*, respectively. For this circuit the measured noise temperature is about 40 K higher than the simulated one. The frequency, where the minimum noise temperature occurs, has shifted towards higher frequencies, which explains a part of the

Table 2 Performance summary of realized MHEMT cold loads

Frequency, GHz	Noise temperature, K	Worst case match, dB	Power consumption, mW
31.4 ± 0.2	75	−24	24
52.0 ± 2.0	141	−30	12
89.0 ± 2.0	170	−19	12

noise temperature difference. The average noise temperature over 87–91 GHz is 170 K. Estimated worst-case noise temperature uncertainty due to calibration line extrapolation is ±8 K assuming 2 K deviation in calibration load temperatures. The RF port reflection coefficient over the design band of 87–91 GHz is better than −19 dB and the agreement between the measured and the simulated value is not as good as with the two ACLs operating at lower frequencies. On a wider range, the reflection coefficient is better than −15 dB over a 76–110 GHz range. The effect of bias at the 89 GHz frequency is presented in Fig. 10*c*. Also at the 89 GHz, the variation of the noise temperature is only a few Kelvins for small changes in the drain voltage or current. Again, some improvement in noise temperature could be achieved by lowering the drain voltage and current.

The performance values of the realised ACLs are summarised in Table 2. The measured performance compares well to the previously published ACL results.

5 Conclusion

Three active cold loads operating at millimetre-wave frequencies of 31.4, 52, and 89 GHz have been designed and characterised. MHEMT MMIC ACLs offer noise temperatures well below ambient up to at least 100 GHz. Simulation models predicted resulting noise temperature very well. Good RF port reflection coefficient levels of −20 dB were realised at 31.4 and 52 GHz. At 89 GHz RF port reflection coefficient is slightly worse due to frequency shift of 5 GHz towards higher frequencies.

Achieved noise temperatures are useful for Earth observation radiometers. For practical use with a radiometer, packaging and a switch are needed. Whether additional losses can be tolerated and usefulness of ACL assessed, careful system level calculations are needed for the specific radiometer and application.

6 Acknowledgment

This work has been supported by the European Space Agency under contract 4000101234/10/NL/GLC.

7 References

1 Frater, R.H., Williams, D.R.: 'An active 'cold' noise source', *IEEE Trans. Microw. Theory Tech.*, 1981, **MTT-29**, pp. 344–347
2 Dunleavy, L.P., Smith, M.C., Lardizabal, S.M.: 'Design and characterization of FET based cold/hot noise sources'. IEEE MMT-S Int. Microwave Symp. Digest, 1997, pp. 1293–1296
3 Sobjaerg, S.S., Skou, N., Barling, J.E.: 'Measurements on active cold loads for radiometer calibration', *IEEE MTT-S Int. Microw. Symp. Dig.*, 2009, **47**, pp. 3134–3139
4 de la Jarrige, E.L., Escotte, L., Goutoule, J.M., Gonneau, E., Rayssac, J.: 'SiGe HBT.based active cold load for radiometer calibration', *IEEE Microw. Wirel. Compon. Lett.*, 2010, **20**, pp. 238–240
5 Bredin, C., Sanson, D., Mohammed, N., *et al.*: '23.8 GHz and 36.5 GHz active cold loads for radiometer calibration'. Proc. of ESA/ESTEC Workshop on Microwave Technology and Techniques, 2010, p. 22
6 Buhles, P.M., Lardizabal, S.M.: 'Design and characterization of MMIC active cold loads'. Radio Frequency Integrated Circuits Symp. Digest, 2000, pp. 221–225
7 Ciccognani, W., Giannini, F., Limit, E., Longhi, P.E.: 'Analysis, design and measurement of active low-noise terminations'. Proc. of 14th Conf. on Microwave Techniques (COMITE), 2008, pp. 1–4
8 Scheeler, R., Popovic, Z.: 'A 1.4 GHz MMIC active cold noise source'. Technical Digest of IEEE Compound Semiconductor Integrated Circuit Symp. (CSICS), 2013, October 2013, pp. 1–4
9 Weissbrodt, E., Tessmann, A., Schlechtweg, M., Kalfass, I., Ambacher, O.: 'Active load modules for W-band radiometer calibration'. Proc. of IEEE Int. Geoscience and Remote Sensing Symp. (IGARSS), 2012, pp. 2945–2948
10 Kangas, V., D'Addio, S., Betto, M., Barre, H., Loiselet, M., Mason, G.: 'MetOp second generation microwave sounding and microwave imaging missions'. 2012 EUMETSAT Meteorological Satellite Conf., 2012. Available at http://www.eumetsat.int/Home/Main/AboutEUMETSAT/Publications/ConferenceandWorkshopProceedings/2012/groups/cps/documents/document/pdf_conf_p61_s1_09_kangas_v.pdf
11 Weatherspoon, M.H., Dunleavy, L.P.: 'Experimental validation of generalized equations for FET cold source design', *IEEE Trans. Microw. Theory Tech.*, 2006, **54**, pp. 608–614
12 Meys, R.P.: 'A wave approach to noise properties of linear microwave devices', *IEEE Trans. Microw. Theory Tech.*, 1978, **26**, (1), pp. 34–37
13 Leuther, A., Tessmann, A., Kallfass, I., *et al.*: 'Metamorphic HEMT technology for low-noise applications'. Proc. of IEEE Int. Conf. on Indium Phosphide and Related Materials, May 2009, pp. 188–191
14 Webster, R.T., Slobodnik, A.J., Roberts, G.A.: 'Determination of InP HEMT noise parameters and S-parameters to 60 GHz', *IEEE Trans. Microw. Theory Tecnhol.*, 1995, **43**, pp. 1216–1225
15 'Noise figure measurement accuracy – Y-factor method', Agilent Technologies Application Note 57-2, 2014

Publication III

Varonen, M., Kärkkäinen, M., Kantanen, M., Laaninen, M., Karttaavi, T., Weber, R., Leuther, A., Seelmann-Eggebert, M., Närhi, T., Lahtinen, J., Halonen, K.A.I, "W-band low noise amplifiers," *Proceedings of the European Microwave Association*, vol. 3, no. 4, pp. 358-366, Dec. 2007.

W-band low-noise amplifiers

Mikko Varonen[1], Mikko Kärkkäinen[1], Mikko Kantanen[2], Mikko Laaninen[3], Timo Karttaavi[2], Rainer Weber[4], Arnulf Leuther[4], Matthias Seelmann-Eggebert[4], Tapani Närhi[5], Janne Lahtinen[6] and Kari A. I. Halonen[1]

Abstract – We report low noise amplifiers for a 94-GHz cloud profiling radar. Four amplifiers were designed using coplanar waveguides and they were manufactured with a 100-nm metamorphic high electron mobility transistor technology. Selected chips were assembled in a split block package having WR-10 waveguide interfaces and alumina microstrip transitions. The scattering parameters and the noise figures of the amplifiers were measured on-wafer and in WR-10 waveguide environment at W-band. At room temperature, the on-wafer measured gain at 94 GHz was between 18 and 23 dB and the measured noise figure ranged from 3.0 to 3.5 dB. Packaged amplifiers exhibit more than 20 dB of gain and noise figures around 3.7 dB. One packaged amplifier was also measured at cryogenic temperature and the results are presented.

Index Terms – Low noise amplifiers, Metamorphic high electron mobility transistors, Microstrip transitions, MMIC amplifiers, packaging, W-band.

I. Introduction

In an effort to increase the accuracy of climate models one has to obtain more information on vertical profile characteristics of clouds. A 94-GHz cloud profiling radar (CPR) is an important element of the joint European-Japanese EarthCARE (Earth Clouds, Aerosols and Radiation Explorer) mission, currently under pre-development for the planned launch in 2012 [1].

The low noise amplifier (LNA) is one of the key components in a millimetre-wave receiver application, such as the cloud profiling radar. Millimetre-wave integrated circuits have traditionally been implemented using technologies, which are based on compound semiconductors such as gallium arsenide (GaAs) or indium phosphide (InP). The metamorphic high electron mobility transistor (MHEMT) has emerged as an attractive, low cost alternative to InP HEMTs. In MHEMT technology, the metamorphic buffer layer is grown on the GaAs, which enables the growth of a channel layer having 30-80 % indium content. This leads to a substantial cost reduction and manufacturability improvement over InP-substrate based devices [2]. Recently, the antimonide-based compound semiconductor (ABCS) InAs/AlSb HEMTs have become interesting because of their low dc-power dissipation.

A performance overview of state-of-the-art millimetre wave integrated amplifiers can be found in [3]. At W-band, GaAs pseudomorphic high electron mobility transistor (PHEMT) amplifiers have achieved noise figures (NF) of 3.6-4.0 dB [4], [5]. Previously, best noise results at W-band have been achieved with InP HEMT amplifiers [6]-[9]. The MHEMT amplifiers have recently shown performances comparable to InP HEMT amplifiers [10]-[12]. The InAs/AlSb HEMT amplifiers have demonstrated noise figures ranging from 3.9 to 5.4 dB at 94 GHz [13], [14].

At millimetre-waves the packaging of the monolithic microwave integrated circuits (MMIC) becomes more demanding than at lower frequencies. Typically, the MMIC can be mounted face-up on a housing and bonded to a transition to couple the MMIC to waveguide [10], [15], [16]. Another approach is the flip-chip technology [17].

The aim of our work was to find out how well the 100-nm metamorphic HEMT technology and an E-plane split-block package assembly suits to low noise amplification at W-band and, particularly, considering the cloud profiling radar operating at 94 GHz. In this paper, we present the design of the waveguide transitions of an E-plane split-block package and the measured results obtained from the packaged amplifiers. Because of the careful design of the mechanical package and the waveguide probes, the packaging degraded the noise figure only by a few tenths of decibels when compared to on-wafer results. In addition, one of the amplifier packages was measured at cryogenic temperatures.

This paper is organized as follows: The fabrication technology is presented in Section II. The detailed design of the MMIC LNAs was reported in [18]. Therefore, only a brief summary and measurement results of these circuits are presented in Section III. The design of the package and waveguide probes are presented in Section IV following the measurement results of the packaged LNAs. In that section, measurement results of one packaged amplifier at cryogenic temperature are also shown. Finally, we present conclusions in Section V.

II. Fabrication technology

The manufacturing process is a 100-nm GaAs based metamorphic HEMT technology from Fraunhofer

Received July 5th, 2007. Revised October 26th, 2007.

[1] MilliLab, SMARAD2 / Electronic Circuit Design Laboratory, Helsinki University of Technology, FI-02150 Espoo, Finland; E-mail: mva@ecdl.tkk.fi
[2] MilliLab, VTT Technical Research Centre of Finland, FI-02044 VTT Espoo, Finland.
[3] Elektrobit Ltd., FI-02150 Espoo, Finland.
[4] Fraunhofer Institute for Applied Solid-State Physics, D-79108 Freiburg, Germany.
[5] European Space Agency (ESTEC), NL-2200 AG Noordwijk, The Netherlands.
[6] Ylinen Electronics, FI-02700 Kauniainen, Finland.

IAF, Freiburg, Germany. The transistor f_T and f_{max} are 220 and 300 GHz, respectively, and the process features ground via holes through GaAs-substrate as well as backside metallization. The structure of the composite channel of the MHEMT is $In_{0.52}Al_{0.48}As/In_{0.80}Ga_{0.20}As/In_{0.53}Ga_{0.47}As$. A transmission electron microscope (TEM) picture of a cross-section of a 100-nm MHEMT is shown in Fig. 1. This technology achieves a maximum transconductance of 1300 mS/mm and a gate-to-drain breakdown voltage of 4 volts.

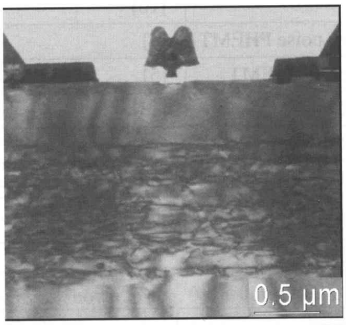

Fig. 1. A TEM cross-section of a 100-nm metamorphic HEMT.

III. MMIC low noise amplifier design

Four low noise amplifiers with different design targets were implemented using grounded coplanar waveguide (GCPW) topology. A 4x15-μm gate width MHEMT was chosen as a suitable low noise device for the amplifiers. The transistor is in a common source configuration. The simulation models were provided by the Fraunhofer IAF. The detailed design of the MMIC LNAs is presented in [18]. The first design (LNA1) is a narrowband three-stage amplifier while the second design (LNA2) is a wideband three-stage amplifier. All the stages are biased to optimum gain. A simplified schematic and a micrograph of the LNA2 is presented in Fig. 2 and 3, respectively.

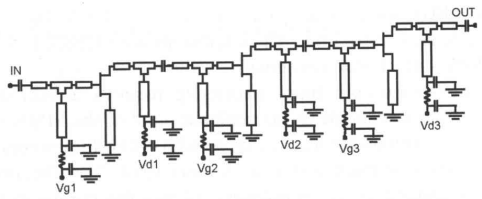

Fig. 2. Simplified schematic of the wideband LNA2.

The third design (LNA3) is also a three-stage amplifier. This design is optimised for low noise performance. The first stage is biased to low noise bias, while second and third stages are biased for peak gain. To increase gain and bandwidth of the LNA3, a four-stage version (LNA4) was designed.

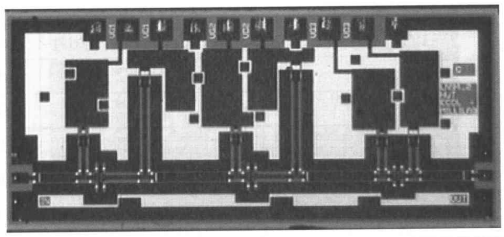

Fig. 3. Micrograph of the LNA2. The chip size is 2.25 mm × 1.00 mm.

The on-wafer noise measurement setup is described in [19]. The measured and simulated S-parameters and noise figures of the four amplifiers are presented in Figs. 4-7.

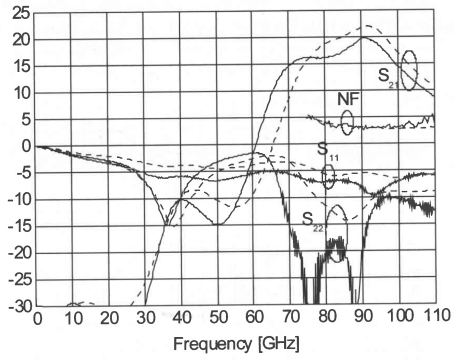

Fig. 4. Measured and simulated (dashed lines) S-parameters and noise figure of the narrowband LNA1. Data from [18]. The measured gain and noise figure are 18 dB and 3.1 dB at 94 GHz, respectively. $V_{supply} = 1.7$ V, $I_d = 54$ mA.

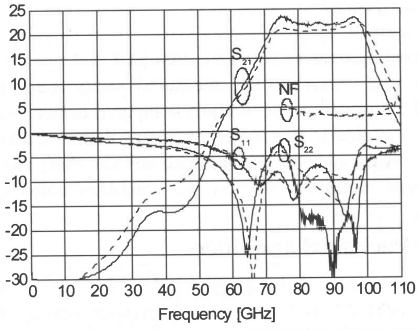

Fig. 5. Measured and simulated (dashed lines) S-parameters and noise figure of the wideband LNA2. Data from [18]. The measured gain and noise figure are 22.5 dB and 3.3 dB at 94 GHz, respectively. $V_{supply} = 1.34$ V, $I_d = 54$ mA.

Frequency [GHz]	Gain [dB]	NF [dB]	Technology	Ref.
95	20	2.5	InP	[6]
94	18	2.9	InP	[7]
94	16	3.2	100-nm InP	[8]
94	12	3.3	100-nm InP	[9]
90	17	2.8	MHEMT	[12]
89	14	4.8	100-nm MHEMT	[20]
80-100	12	2.3	70-nm MHEMT	[11]
70-105	20	2.5	70-nm MHEMT	[10]
94	31	4.0	100-nm GaAs low noise PHEMT	[4]
90-100	10.3	3.6	100-nm GaAs power PHEMT	[5]
94	11	5.4	100-nm InAs/AlSb HEMT	[13]
94	20	3.9	200-nm InAs/AlSb HEMT	[14]
94	18-23	3.0-3.5	100-nm MHEMT	This work, on-wafer

Table 1. Comparison of Published HEMT MMIC Amplifiers for W-band.

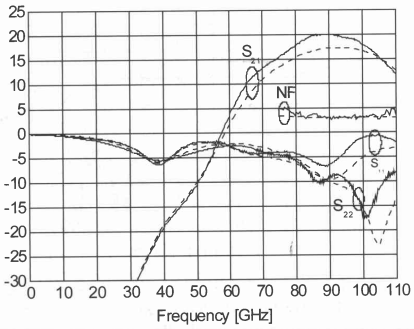

Fig. 6. Measured and simulated (dashed lines) S-parameters and noise figure of the LNA3. Data from [18]. The measured gain and noise figure are 19.5 dB and 3.0 dB at 94 GHz, respectively. $V_{supply} = 0.95$ V, $I_d = 45$ mA.

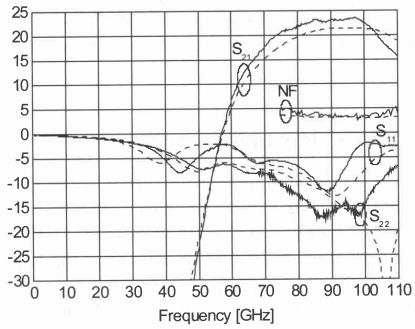

Fig. 7. Measured and simulated (dashed lines) S-parameters and noise figure of the LNA4. Data from [18]. The measured gain and noise figure are 23 dB and 3.5 dB at 94 GHz, respectively. $V_{supply} = 0.94$ V, $I_d = 63$ mA.

A good agreement between simulated and measured results was achieved. The measured performance of the MMIC low noise amplifiers is compared to published results in Table I. The presented results demonstrate excellent noise and gain performance and the designed chips compare well with the previously published amplifiers.

IV. Packaged amplifiers

Selected chips of the designs LNA1, LNA2, and LNA4 were assembled in a split block package having WR-10 waveguide interfaces.

A) Mechanical package and waveguide probes

The design of the package is based on an E-plane split-block [16]. The block has a space for a 5-pin micro connector and a small PCB for installing a bias network (low pass RC), and a small space adjacent to the LNA-chip for single layer capacitors. All components are attached to the block with conductive epoxy.

The E-plane split block packaging requires transitions from the waveguide to the coplanar input of the MMICs. The transitions are manufactured with a thin-film process on 100 μm thick polished alumina (99.6 %). The design method of the transitions follows the outline presented in [21]. By using Ansoft HFSS electromagnetic simulations, the transitions were designed by determining the length, metallization width and backshort distance of the waveguide probe to achieve nearly constant impedance over a wide bandwidth. A short inductive line and a quarter-wave transformer were then added as matching

elements to bring this impedance to 50 Ω. As shown in simulations in Fig. 8., the transition provides better than 20 dB return loss to the microstrip over almost 30-GHz bandwidth.

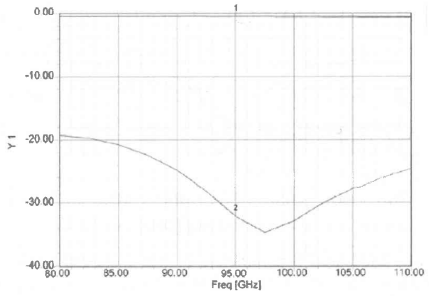

Fig. 8. Simulated transmission (1) and return loss (2) of the WR-10-to-microstrip transition.

Since the MMIC has a coplanar waveguide input, a transition from microstrip to CPW was added to the probe. The ground pads are connected to the backside metal by plated-through vias as shown in Fig. 9. In simulations, the effect of this transition is negligible on the overall performance of the waveguide probe.

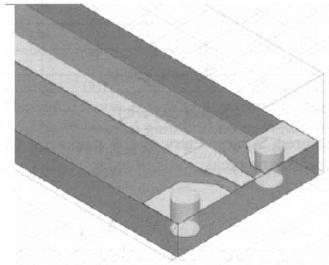

Fig. 9. Microstrip to CPW transition.

A micrograph of a low noise amplifier chip assembled in a housing is presented in Fig. 10 and a photograph of the package is shown in Fig. 11.

B) Measurement systems for LNA packages

The packaged amplifiers were measured in WR-10 waveguide environment. The s-parameters were measured using an HP8510C vector network analyser with the Agilent W85104A extension modules for W-band. Correction coefficients for the analyser were obtained through the TRL-calibration method [22]. An external attenuator was needed to reduce input power from port one to avoid compression of the LNAs. The attenuator reduces the dynamic range of the analyser and, thus, the quality of S11 calibration will deteriorate. However, despite the approximate 15 dB of additional attenuation, a successful calibration was achieved.

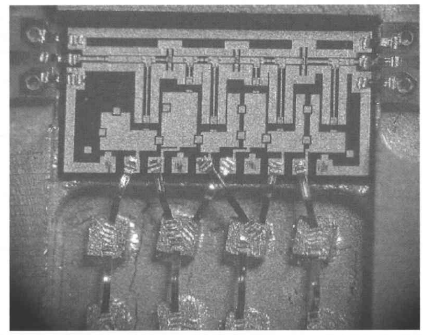

Fig. 10. A 94-GHz MMIC low noise amplifier assembled in the lower half of the split block package.

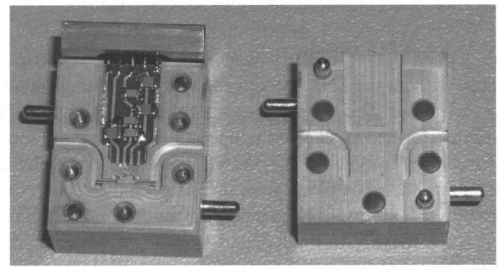

Fig. 11. A photograph of the split-block package. The dimensions of the package are 16 mm × 19 mm × 19 mm.

The noise figure and the insertion gain were measured using the Y-factor method. The block diagram of the room temperature measurement setup is shown in Fig. 12(a). The measurement system utilizes an Agilent N8973A Noise Figure Analyzer and a noise diode from ELVA-1 having an excess noise ratio (ENR) of about 15 dB. An in-house assembled noise downconverter, consisting of a mixer and a LO-multiplier, transforms the noise signal from the 75-110 GHz range to a 50-MHz signal, which is a suitable input frequency for the noise figure analyser. At frequencies above 105 GHz the noise figure of the downconverter increases rapidly, which leads to a higher measurement uncertainty.

The same setup was also used for noise figure (NF) and the insertion gain (G_{ins}) measurements at cryogenic temperatures. The setup is shown in Fig. 12(b). In this case, a cryogenic test chamber is connected between the noise diode and the noise downconverter. The input and output waveguide assemblies, which both consist of a stainless steel waveguide for thermal isolation and a short section of standard waveguide, are located inside the test chamber. The LNA block is connected between these assemblies. The entire assembly is presented in Fig. 13. A thermally conductive wire connects the LNA block to a cold finger of the cryogenic cooler. Temperature sensors are placed on the LNA block and on the waveguides to monitor cooling. At first, during the first cooling cycle, the insertion gain

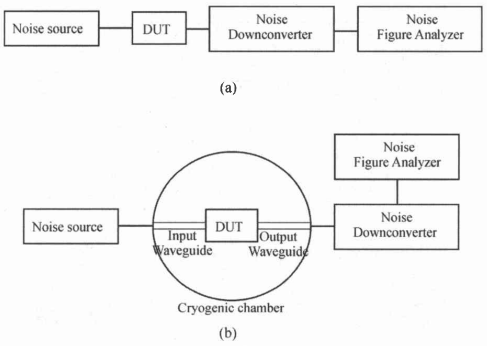

Fig. 12. Block diagrams of noise figure measurement setups. (a) Room temperature setup. (b) Cryogenic temperatures setup.

(G_{ins}) and the NF of the waveguide assembly were measured without the LNA by connecting the input and output to each other. The measurements of the G_{ins} and the NF were performed at selected temperatures. During the second cooling cycle the G_{ins} and the NF of the entire chain including the LNA block were measured at the same temperatures. The insertion gain G_{LNA} and the noise figure F_{LNA} of the LNA is calculated from the total insertion gain and noise figure using

$$F_{LNA} = \frac{F_{tot} - F_{in}}{L_{in}} + \frac{F_{out} - 1}{G_{LNA}} + 1, \quad (1)$$

where F_{tot} is the total noise figure of cascaded waveguides and the LNA, F_{in} and F_{out} are noise figures of the input and output waveguides, respectively, and L_{in} is the loss of the input waveguide.

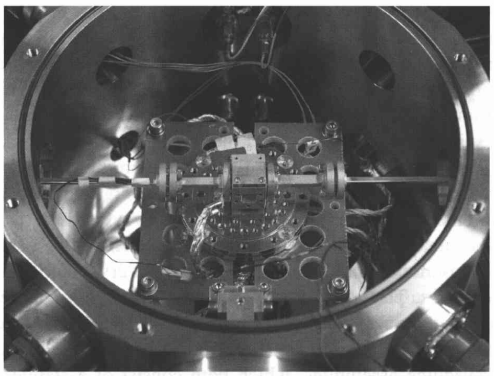

Fig. 13. Photograph of the cryogenic measurement setup.

C) Room temperature measurement results of the packaged LNAs

The measured S-parameters of the packaged LNA1, LNA2 and LNA4 are presented in Fig. 14, Fig. 15. and Fig. 16, respectively.

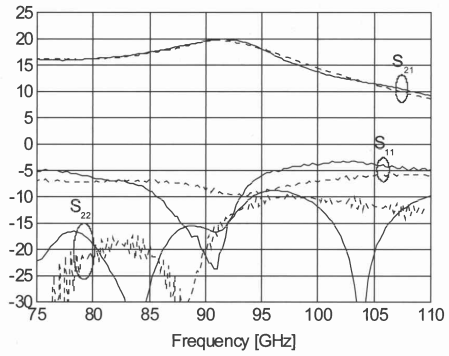

Fig. 14. Measured S-parameters of the packaged LNA1. The dashed lines represent measured on-wafer results. $V_{supply} = 1.7$ V, $I_d = 54$ mA.

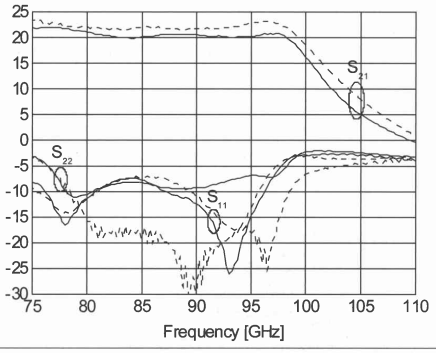

Fig. 15. Measured S-parameters of the packaged LNA2. The dashed lines represent measured on-wafer results. $V_{supply} = 1.34$ V, $I_d = 54$ mA.

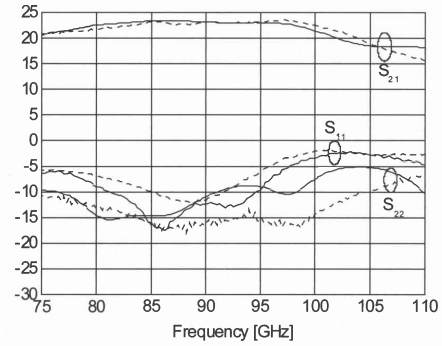

Fig. 16. Measured S-parameters of the packaged LNA4. The dashed lines represent measured on-wafer results. $V_{supply} = 0.94$ V, $I_d = 63$ mA.

The noise performances of the packaged amplifiers are shown in Fig. 17, Fig. 18. and Fig. 19. The measured on-wafer results are included in these figures for compari-

son. Although, the gain response of the packaged LNA1 has slightly shifted downwards in frequency, the measured gain and noise figure are 15 dB and 4.2 dB at 94 GHz, respectively. The packaged LNA2 exhibits a gain better than 18.5 dB from 75 to 100 GHz. It achieves a 3.7 dB noise figure at 94 GHz. The packaged LNA4 has more than 15 dB gain over the entire W-band. At 94 GHz, the measured noise figure is 3.7 dB.

As a conclusion, the measured results indicate that the packaging and the design of waveguide probes were realized successfully. The packaging has a minimal effect on the frequency responses of the LNA MMICs. Moreover, the packaging degraded the noise figure only by a few tenths of decibels when compared to the on-wafer results.

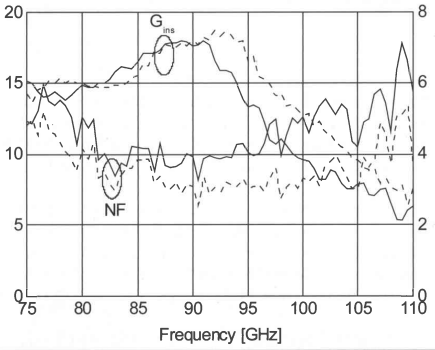

Fig. 17. Measured noise figure and insertion gain of the packaged LNA1. The measured gain and noise figure are 15 dB and 4.2 dB at 94 GHz, respectively. V_{supply} = 1.7 V, I_d = 54 mA. The dashed lines represent measured on-wafer results.

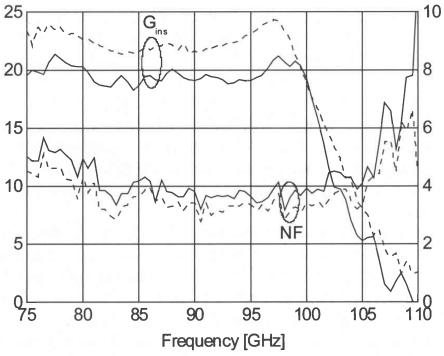

Fig. 18. Measured noise figure and insertion gain of the packaged LNA2. The measured gain and noise figure are 19 dB and 3.7 dB at 94 GHz, respectively. V_{supply} = 1.34 V, I_d = 54 mA. The dashed lines represent measured on-wafer results.

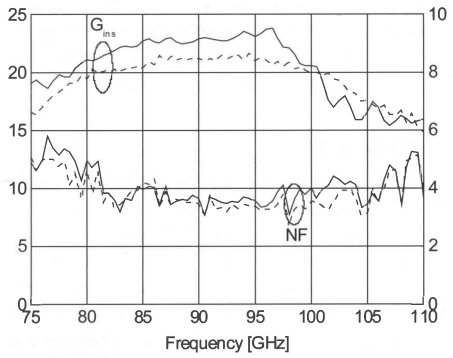

Fig. 19. Measured noise figure and insertion gain of the packaged LNA4. The measured gain and noise figure are 23.5 dB and 3.7 dB at 94 GHz, respectively. V_{supply} = 0.94 V, I_d =63 mA. The dashed lines represent measured on-wafer results.

D) Test results at cryogenic temperatures

Measured noise figure and insertion gain of the packaged LNA2 for various physical temperatures in cryogenic measurement setup are presented in Fig. 20. and Fig. 21, respectively.

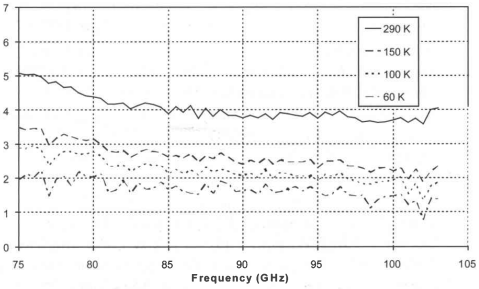

Fig. 20. Measured noise figure of the packaged LNA2 at various physical temperatures. V_{supply} = 1.1 V, V_g =0.1 V, I_d = 38, 32, 30, 28 mA.

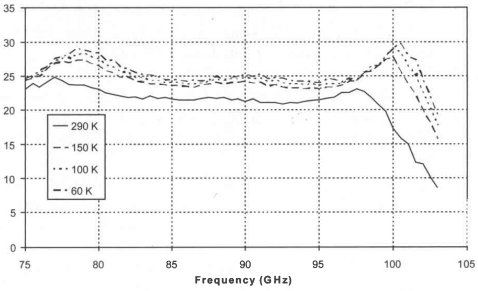

Fig. 21. Measured insertion gain of the packaged LNA2 at various physical temperatures. V_{supply} =1.1 V, V_g =0.1 V, I_d = 38, 32, 30, 28 mA.

The supply voltage and gate-to-source voltages were kept constant at different temperatures. About 3 dB improvement in insertion gain and 2.5 dB in noise figure can be observed over the tested temperature range.

V. Conclusions

This paper describes the design of MMIC amplifiers and their successful integration into waveguide packages. Measurement results of both LNA MMICs and packaged amplifiers are presented and the results are discussed. The presented results demonstrate excellent noise and gain performance and the designed chips compare well with the previously published amplifiers. Because of the careful design of the mechanical package and the waveguide probes, the packaging has a minimal effect on the frequency responses of the LNA MMICs. Moreover, the packaging degraded the noise figure only by a few tenths of decibels when compared to the on-wafer results. These design methods and the chosen manufacturing technologies look promising when considering the intended cloud radar application.

VI. Acknowledgment

This work was done under Contract 13521/99/NL/PB to the European Space Agency and was supported by the Academy of Finland under the Millimono Project. Ylinen Electronics (Finland, email: info@ylinen.fi) was the prime contractor of the work while Fraunhofer Institute for Applied Solid-State Physics and Millimetre Wave Laboratory of Finland-MilliLab acted as subcontractors.
The authors would like to thank Petri Jukkala from Elektrobit Ltd., Espoo, Finland, for advice.

References

[1] European Space Agency (ESA), EarthCARE (Earth Clouds, Aerosols, and Radiation Explorer). http://www.esa.int

[2] Whelan, C.S.; Marsh, P.F.; Hoke, W.E.; McTaggart, R.A.; McCarroll, C.P.; Kazior, T. E.: GaAs metamorphic HEMT (MHEMT): An attractive alternative to InP HEMTs for high performance low noise and power applications, in Proc. 2000 IEEE Int. Conf. Indium Phosphide and Related Materials, Williamsburg, VA, May 2000, 337-340.

[3] Samoska, L.: Towards terahertz MMIC amplifiers: present status and trends, in 2006 IEEE MTT-S Int. Microwave Symp. Dig., San Francisco, CA, June 2006, 333-336.

[4] Tu, D.W.; Berk, W. P.; Brown, S. E.; Byer, N.E.; Duncan, S.W.; Eskandarian, A.; Fischer, E.; Gill, D.M.; Golja, B.; Kane, B. C.; Svensson, S.P.; Weinreb, S.: High gain monolithic p-HEMT W-band four-stage low noise amplifiers, in 1994 IEEE Microwave and Millimeter-Wave Monolithic Circuit Symp. Dig., San Diego, CA, May 1994, 29-32.

[5] Bessemoulin, A.; Grunenputt, J.; Fellon, P.; Tessmann, A.; Kohn, E.: Coplanar W-band low noise amplifier MMIC using 100-nm gate-length GaAs PHEMTs, in Proc. 34th European Microwave Conference, Amsterdam, The Netherlands, October 2004, 25-28.

[6] Matloubian, M.: Advances in millimeter-wave FET MMIC technology, in 1999 IEEE Radio Frequency Integrated Symp. Dig., Anaheim, CA, June 1999, 141-144.

[7] Lai, R.; Barsky, M.; Huang, T.; Sholley, M.; Wang, H. Kok, Y.L.; Streit, D. C.; Block, T.; Liu, P. H.; Gaier, T.; Samoska, L.: An InP HEMT MMIC LNA with 7.2-dB gain at 190 GHz. IEEE Microwave and Guided Wave Letters, **8** (1998), 393-395.

[8] Archer, J.W.; Lai, R.: Ultra-low-noise InP-MMIC amplifiers for 85-115 GHz, in Proc. 2000 Asia-Pacific Microwave Conference, Sydney, Australia, December 2000, 173-176.

[9] Hoel, V.; Boret, S.; Grimbert, B.; Aperce, G.; Bollaert, S.; Happy, H.; Wallart, X.; Cappy, A.: 94-GHz low noise amplifier on InP in coplanar technology, in Proc. 1998 European Gallium Arsenide, and Related III-V Compounds, Application Symp., Munich, Germany, October 1999, 257-262.

[10] Schlechtweg, M.; Tessmann, A.; Leuther, A.; Schwörer, C.; Massler, H.; Mikulla, M.; Walther, M.; Riessle, M.: Advanced mm-wave ICs and applications, in Proc. 2005 IEEE Int. Workshop on Radio-Frequency Integration Tech., Singapore, November 2005, 46-49.

[11] Tessmann, A.; Leuther, A.; Schwoerer, C.; Massler, H; Kudszus, S.; Reinert, W.; Schlechtweg, M.: A coplanar 94 GHz low-noise amplifier MMIC using 0.07 mm metamorphic cascode HEMTs, in 2003 IEEE MTT-S Int. Microwave Symp. Dig., Philadelphia, PA, June 2003, 1581-1584.

[12] Smith, P.M.; Nichols, K.; Kong, W.; MtPleasant, L.; Pritchard, D.; Lender, R.; Fisher, J.; Actis, R.; Dugas, D.; Meharry,D.; Swanson, A.W. : Advances in InP HEMT technology for high frequency applications, in Proc. 2001 IEEE Int. Conf. Indium Phosphide and Related Materials, Nara, Japan, May 2001, 9-14.

[13] Deal, W.R.; Tsai, R.; Lange, M.D.; Boos, J.B.; Bennett, B.R.; Gutierrez, A.: A W-band InAs/AlSb low-noise/low-power amplifier. IEEE Microwave Wireless Compon. Lett., **15** (2005), 208-210.

[14] Hacker, J.B.; Bergman, J.; Nagy, G.; Sullivan, G.; Kadow, C.; Lin, H.K.; Gossard, A.C.; Rodwell, M.; Brar, B.: An ultra-low power InAs/AlSb HEMT W-band low-noise amplifier, in 2005 IEEE MTT-S Int. Microwave Symp. Dig., Long Beach, CA, June 2005, 1029-1032.

[15] Tessmann, A.; Kuri, M.; Riessle, M.; Massler, H.; Zink, M.; Reinert, W.; Bronner, W.; Leuther, A.: A compact W-band dual-channel receiver module, in 2006 IEEE MTT-S Int. Microwave Symp. Dig., San Francisco, CA, June 2006, 85-88.

[16] Weinreb, S.; Lai, R.; Erickson, N.; Gaier, T.; Wielgus, J.: W-band InP wideband MMIC LNA with 30K noise temperature, in 1999 IEEE MTT-S Int. Microwave Symp. Dig., Anaheim, CA, June 1999, 101-104.

[17] Song, S.; Kim, S.; Yeon, S.; Park, S.; Lee, J.Y.; Lee, S.; Choi, W.; Kwon, Y.; Seo, K.S.: The flip-chip mounted MMIC technology using the modified MCM-D substrate for compact and low-cost W-band transceiver, in 2005 IEEE MTT-S Int. Microwave Symp. Dig., Long Beach, CA, June 2005, 1011-1014.

[18] Kärkkäinen, M.; Varonen, M.; Kantanen, M.; Karttaavi, T.; Weber, R.; Leuther, A.; Seelmann-Eggebert, M.; Närhi, T.;

Halonen, K.A.I.: Coplanar 94 GHz metamorphic HEMT low noise amplifiers, in 2006 IEEE Compound Semiconductor Integrated Circuit Symp. Dig., San Antonio, TX, Nov. 2006, 29-32.

[19] Vähä-Heikkilä, T.; Lahdes, M.; Kantanen, M.; Karttaavi, T.; Tuovinen, J.: Very wideband automated on-wafer noise figure and gain measurements at 50-110 GHz, in Proc. 2002 European Gallium Arsenide, and Related III-V Compounds, Application Symp., Milan, Italy, September 2002, 233-236.

[20] Hwang, K.C.; Chao, P.C.; Creamer, C.; Nichols, K.B.; Wang, S.; Tu, D.; Kong, W.; Dugas, D.; Patton, G.: Very high gain millimeter-wave InAlAs/InGaAs/GaAs metamorphic HEMT's. IEEE Electron Device Letters, **20** (1999), 551-553.

[21] Leong, Y.C.; Weinreb, S.: Full band waveguide-to-microstrip probe transitions, in 1999 IEEE MTT-S Int. Microwave Symp. Dig., Anaheim, CA, June 1999, 1435-1438.

[22] Engen, G.F.; Hoer, C.A.: Thru-reflect-line: An improved technique for calibrating the dual six port automatic network analyzer. IEEE Trans. Microwave Theory Tech., **27** (1979), 987-993.

Mikko Varonen received the M.Sc. and Lic.Sc. degrees in electrical engineering from the Helsinki University of Technology (TKK), Espoo, Finland, in 2002 and 2005, respectively. He is currently working toward the D.Sc. degree in electrical engineering at the Electronic Circuit Design Laboratory, Helsinki University of Technology.

His research interests involve millimetre-wave integrated circuits. He is a member of the Finnish Graduate School of Electronics, Telecommunications and Automation (GETA). He was the co-recipient of the APMC 2006 Prize for the outstanding contribution to the Asia-Pacific Microwave Conference.

Mikko Kärkkäinen was born in 1975. He received the Lic. Sc. and the M. Sc. degrees in electrical engineering from the Helsinki University of Technology, Espoo, Finland, in 2005 and 2000, respectively. He is currently working towards the Ph.D. degree at the Helsinki University of Technology.

In 1998 he started working at the Electronic Circuit Design Laboratory, Helsinki University of Technology. His current research interests are in the field of CMOS millimetre-wave circuits for integrated radio front-ends. He is also a co-recipient of the APMC 2006 Prize for an outstanding contribution to the Asia-Pacific Microwave Conference held in Yokohama, Japan.

Mikko Kantanen received his M.Sc. and Lic.Sc. degrees in Electrical Engineering from the Helsinki University of Technology (TKK), Espoo, Finland 2001 and 2006, respectively.

Since 2001 he has worked as a Research Scientist in MilliLab, VTT Technical Research Centre of Finland, Espoo, Finland, in the areas of millimetre wave integrated circuit design, millimetre wave measurements, and millimetre wave systems. He is a recipient of an Asia-Pacific Microwave Conference 2006 Prize.

Mikko Laaninen received his M.Sc. from the Helsinki University of Technology in 2003, specializing in micro- and millimeter-wave measurements. In 2003-2006 he participated in the design and testing of the ESA Planck satellite's 70GHz cryogenic receivers at Ylinen Electronics. Currently he works on commercial telecommunications equipment at Elektrobit, Finland.

Timo Karttaavi received the degree of M. Sc. (EE) and Lic. Sc (EE) degrees from the Helsinki University of Technology in 1989 and 2000, respectively. He spent a year at the Swiss Federal Institute of Technology, Lausanne in 1990-91. From 1991 to 1993 he was with the University of Helsinki developing readout electronics for high energy physics experiments stationed at CERN in Geneva. Since 1993 he has been with VTT working on microwave and millimeter wave circuits and systems. During 2005-06 he spent a year with the Berkeley Wireless Research Centre in the USA working on millimeter wave CMOS circuits. He heads currently a millimeter wave research group at VTT.

Rainer Weber was born in Offenburg, Germany, in 1978. He received the Dipl.-Ing. (FH) degree in electrical engineering from the University of Applied Sciences Offenburg, Germany, in 2003.

He then joined the High Frequency Devices and Circuits Department of the Fraunhofer Institute for Applied Solid-State Physics (IAF), Freiburg, Germany, where he is involved in the MMIC design of oscillators and amplifiers up to 220 GHz.

Arnulf Leuther received the Dipl. Phys. degree and the PhD degree in physics from the Technical University of Aachen. He is with the Fraunhofer Institute for Applied Solid State Physics (IAF) since 1996. His research work was focused on the development of III/V-process technology for high frequency MMICs.

Matthias Seelmann-Eggebert received his Diploma and Ph.D. degree in physics from the University of Tübingen in 1980 and 1986, respectively. From 1980 to 1996 he was involved in R&D related to infrared detectors based on HgCdTe and developed electrochemical and surface physical methods for the characterization of compound semiconductor surfaces. From 1990 to 1991 he was a visiting scientist at Stanford University. From 1997 to 2000 he was engaged in the growth of CVD diamond. Since 2001 he is a member of the department of high frequency electronics of the IAF in Freiburg,Germany, and is concerned with the preparation and development of simulation models for active and passive III-V devices.

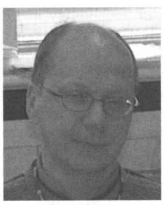

Tapani Närhi received the M.Sc. and D.Tech. degrees in electrical engineering from the Helsinki University of Technology, Espoo, Finland, in 1978 and 1993, respectively. From 1978 to 1981, he was a Research Engineer at the Telecommunications Laboratory, Technical Research Centre of Finland (VTT), where he was involved in the design and characterization of solid-state microwave circuits. From 1981 to 1984, he was a Communications Engineering Instructor at the Civil Aviation Training Centre, Dhaka, Bangladesh, for the International Civil Aviation Organization (ICAO). After returning to VTT in 1984, he was a Project Manager in several research and development projects dealing with communications applications of microwave technology, concentrating on mobile communications. In 1990, he joined the European Space Agency (ESA). Since then, he has been involved with space applications of microwave and millimetre-wave technology at the RF Payload Systems Division, European Space Research and Technology Centre (ESTEC), Noordwijk, The Netherlands. His research interests include linear and non-linear microwave and millimetre-wave circuits and computer-aided design (CAD) methods. Over the last few years, he has focussed more specifically to millimetre and sub-millimetre wave technology towards Earth Observation and Scientific applications. Dr. Närhi was the recipient of the 1998 Microwave Prize.

Janne Lahtinen received the M.Sc. (Tech.), Lic.Sc. (Tech.), and D.Sc. (Tech.) degrees from the Helsinki University of Technology (TKK), Finland, in 1996, 2001, and 2003, respectively.

Since 2007, he is the Managing Director of Harp Technologies Ltd, Espoo, Finland. From 2006 to 2007 he was the Director, Space at SF-Design Ltd, Jokioinen, Finland. From 2004 to 2006 he was with Elektrobit Microwave Ltd (Ylinen Electronics Ltd), Kauniainen, Finland serving in various positions, finally as the Manager, Space and Security. From 2002 to 2003 he was a Research Fellow at the ESA-ESTEC in Noordwijk, The Netherlands and from 1995 to 2002 with the TKK Laboratory of Space Technology. His research interests include microwave remote sensing systems and spacecraft hardware. He has authored or co-authored 50 publications.

Dr. Lahtinen served as a Secretary of the Finnish National Committee of COSPAR from 1997 to 2002. From 2006 to 2007, he was an advisor of the Finnish Space Committee. He was welcomed as a Burgen Scholar by Academia Europaea in 2004, he won the Young Scientist Award of the National Convention on Radio Science (URSI) in 2001, and he received the third place in the IEEE GRS-S Student Prize Paper Competition in 2000.

Kari A. I. Halonen received the M.Sc. degree in electrical engineering from Helsinki University of Technology, Finland, in 1982, and the Ph.D. degree in electrical engineering from the Katholieke Universiteit Leuven, Belgium, in 1987. Since 1988 he has been with the Electronic Circuit Design Laboratory, Helsinki University of Technology. From 1993 he has been an associate professor, and since 1997 a full professor at the Faculty of Electrical Engineering and Telecommunications. He became the Head of Electronic Circuit Design Laboratory year 1998. He has been an associate editor of IEEE Transactions on Circuits and Systems I, a guest editor for IEEE Journal of Solid-State Circuits and the Technical Program Committee Chairman for European Solid-State Circuits Conference year 2000. He has been awarded the Beatrice Winner Award in ISSCC'02 Conference year 2002. He is a TPC- member of ESSCIRC and ISSCC. He specializes in CMOS and BiCMOS analog integrated circuits, particularly for telecommunication applications. He is author or co-author over two hundred international and national conference and journal publications on analog integrated circuits.

Publication IV

Kantanen, M., Kärkkäinen, M., Varonen, M., Laaninen, M., Karttaavi, T., Weber, R., Leuther, A., Seelmann-Eggebert, M., Närhi, T., Lahtinen, J., Halonen, K.A.I, "Low noise amplifiers for D-band," *Proceedings of the European Microwave Association*, vol. 4, no. 4, pp. 268-275, Dec. 2008.

Low noise amplifiers for D-band

Mikko Kantanen[1], Mikko Kärkkäinen[2], Mikko Varonen[2], Mikko Laaninen[3], Timo Karttaavi[1], Rainer Weber[4], Arnulf Leuther[4], Matthias Seelmann-Eggebert[4], Tapani Närhi[5], Janne Lahtinen[6] and Kari A. I. Halonen[2]

Abstract – Four low noise amplifiers for D-band (110-170 GHz) operation are presented. The amplifier circuits have been manufactured using a 100-nm gate length metamorphic high electron mobility transistor technology. A good agreement between simulations and measurements is verified by on-wafer measurements. Selected amplifiers have been assembled into a split-block waveguide module. The design and performance of the amplifier modules are presented. The amplifier modules exhibit better than 15-20 dB small signal gain with 6.0-7.5 dB noise figure. The bandwidths range from 141-152 GHz to 130-170 GHz.

Index Terms – Millimeter wave amplifiers, MMIC amplifiers, Integrated circuit packaging, Metamorphic high electron mobility transistors (MHEMT).

I. Introduction

Advances in the manufacturing of millimeter-wave monolithic integrated circuits (MMICs) can open new possibilities to exploit large bandwidths available above 100 GHz. Low noise amplifiers have been developed up to 260 GHz and the first circuits exhibiting gain at 300 GHz have been reported [1]-[4]. Future applications above 100 GHz may include wideband communication, environmental monitoring and millimeter-wave imaging.

An example application is the atmospheric water vapor profiling using a radiometer for simultaneous measurements at the water vapor resonance frequency 183 GHz and at a window frequency within 140 to 165 GHz. In the current generation of atmospheric sounders, heterodyne radiometer architecture is used with Schottky mixers as the first component after the antenna. The sensitivity of these instruments could be improved with a low noise amplifier (LNA), and even direct detection architecture is possible.

Traditionally, the manufacturing of low noise millimeter-wave integrated circuits has relied on the use of high electron mobility transistors (HEMT) implemented with gallium arsenide (GaAs) or indium phosphide (InP). While best noise performance has been achieved using InP HEMT technology there are some drawbacks. These include higher manufacturing cost, lower breakdown voltage, more fragile structure, and device reliability when comparing to GaAs technology. Few InP HEMT based LNAs operating at D-band have been reported [5]-[10].

To overcome some of drawbacks with InP, the possibility to process indium channel devices on GaAs carrier wafer has been introduced in pseudomorphic (PHEMT) and MHEMT technologies. In MHEMT technology, a metamorphic buffer layer is grown on the GaAs substrate, to enable the growth of the channel layer having 30-80 % indium content. This leads to cost reduction and manufacturability improvement over pure InP technology [11], [12]. So far, few PHEMT and MHEMT LNAs operating at D-band have been reported [13]-[18].

Packaging of MMICs operating above 100 GHz is challenging. Typically, the MMIC is mounted inside a waveguide module and a transition is used to couple the signal from the rectangular waveguide to the MMIC. Transitions can be manufactured on a separate substrate, which are then connected to MMIC using wire bonding or flip-chip technique. As frequency increases, the wire bonding becomes more demanding and the length of the wire has to be minimized [19], [20]. The use of flip-chip technique has been demonstrated with MMICs up to 100 GHz [21]-[24]. In addition, the integration of the transition on MMIC has been studied in [6].

With the water vapor profiling as a background application, the aim of this work was to study the possibilities of using metamorphic high electron mobility transistors (MHEMTs) for low noise amplification in the D-band (110-170 GHz). Four low noise amplifiers were designed and selected chips were assembled in an E-plane split-block package. Package design including transitions from coplanar to rectangular waveguide is presented. Results on both on-wafer and packaged module measurement are shown.

II. Fabrication technology and modelling

The manufacturing process used in this work is the 100-nm GaAs based MHEMT technology of the Fraunhofer IAF, Freiburg, Germany. The process is suitable for coplanar waveguide (CPW) designs [3]. The process features NiCr thin film resistors, metal-insulator-metal (MIM) capacitors and backside metallization. Unwanted substrate modes are

Received January 16th, 2008. Revised May 6th, 2008.

[1]MilliLab, VTT Technical Research Centre of Finland, P.O. Box 1000, FI-02044 VTT, Finland Phone: +358 207226501; Fax: +358 207227012;
E-mail: mikko.kantanen@vtt.fi
[2] MilliLab, SMARAD2 / Electronic Circuit Design Laboratory TKK Helsinki University of Technology, P.O. Box 1000, FI-02015 TKK, Finland;
[3] Elektrobit Microwave Ltd., FI-02150 Espoo, Finland;
[4] Fraunhofer Institute for Applied Solid-State Physics, D-79108 Freiburg, Germany;
[5] European Space Agency (ESTEC), NL-2200 AG Noordwijk, The Netherlands;
[6] Ylinen Electronics, FI-31600 Jokioinen, Finland.

suppressed using ground via holes through the GaAs substrate. As a result of extensive modelling work the Fraunhofer IAF provided reliable models for CPW components and transistors. A transistor with a gate width of 2x15 μm was chosen as a suitable device for D-band operation. The ft of the transistor is about 200 GHz and it is used in common source configuration. All designs were optimized for high stable gain rather than low noise, because the noise model extracted from lower frequencies was considered unreliable at these frequencies.

III. Low noise amplifier designs

Four low noise amplifiers were designed using different design goals or design methodologies. More detailed description of LNA designs is presented in [25]. The basic schematic of the first design (LNA1) is shown in Fig. 1.

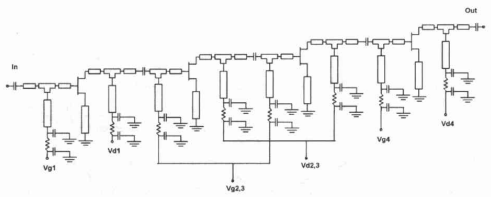

Fig. 1. Principal schematics of the LNA1.

LNA1 is a narrowband amplifier. Matching networks are designed using conventional reactive matching technique. Stability is improved using inductive source feedback. A micrograph of the LNA1 is presented in Fig. 2. The on-wafer measurement results and simulations are shown in Fig. 3. The measurements show peak gain of 22.7 dB at 152 GHz with a noise figure of 6.0 dB. The S-parameters were measured using two systems. The Agilent PNA series network analyzer was used over the range 1-110 GHz and the HP8510C network analyzer with G-band extension modules was applied for 130-200 GHz range. The noise figure measurement setup for the G-band consists of in-house assembled external downconverter and Agilent N8973A noise figure analyzer.

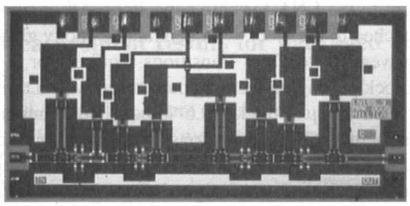

Fig. 2. Micrograph of the LNA1 MMIC. The chip size is 1.0 × 2.0 mm^2.

The second design (LNA2) is a narrowband four-stage amplifier. Input, output and interstage matching is based on series transmission lines. Bias voltage for the transistor is fed through λ/4 short circuited shunt stubs.

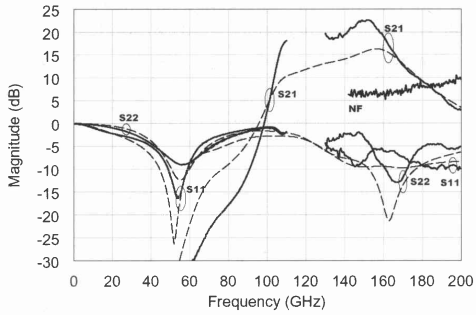

Fig. 3. Measured (solid) and simulated (dashed) S-parameters and noise figure (measurement only) for LNA1. The peak gain of 22.7 dB with the noise figure of 6.0 dB is achieved at 152 GHz. Vd = 1.09 V, Id = 36 mA. Data from [25].

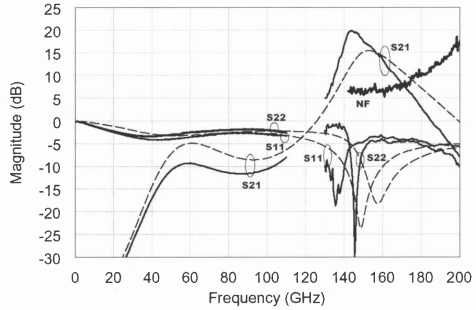

Fig. 4. Measured (solid) and simulated (dashed) S-parameters and noise figure (measurement only) for LNA2. The peak gain of 19.8 dB with the noise figure of 6.3 dB is achieved at 143 GHz. The applied bias values were Vd = 1.54 V, Id = 36 mA. Data from [25].

Stability is improved by using inductive source feedback and small series resistors in shunt stubs. The on-wafer measurement results and simulations are shown in Fig. 4. The measurements show a peak gain of 19.8 dB at 143 GHz with a noise figure of 6.3 dB.

The third design (LNA3) is a wideband amplifier. The input and output matching networks are designed using the reactive matching technique. The double resonant matching technique is used for interstage matching, in order to obtain wideband match. Stability is improved using inductive source feedback. The on-wafer measurement results and simulations are shown in Fig. 5. There is an unwanted gain peak with a poor output return loss at around 105 GHz, making the amplifier only conditionally stable. Otherwise, average gain of 18.0 dB is achieved over a wide bandwidth.

The fourth design (LNA4) is also a wideband amplifier. To suppress gain below 100 GHz, an interdigital capacitor is placed in two interstage networks. This capacitor provides smaller capacitance than MIM capacitors. Otherwise, the

Table 1. Comparison of reported HEMT MMIC LNAs at D-band.

Frequency (GHz)	Gain (dB)	NF (dB)	Number of Stages	Technology	Reference
150-215	12	N.A.	3	70-nm InP HEMT	[5]
150-215	20±6	8	6	80-nm InP HEMT	[6], [7]
150-205	17±2	N.A.	8	100-nm InP HEMT	[8]
140	30	N.A.	3	100-nm InP HEMT	[9]
90-140	15±3	N.A.	6	100-nm InP HEMT	[10]
150	5	N.A.	1	120-nm InP HEMT	[12]
164	6	N.A.	2	70-nm InP PHEMT	[13]
120-124	10-12	N.A.	2	100-nm InP PHEMT	[14]
142	9	N.A.	2	100-nm InP PHEMT	[15]
155	10.1	5.1	3	100-nm InP PHEMT	[16]
148	12	N.A.	2 cascode stages	150-nm GaAs PHEMT	[17]
155-160	15	N.A.	2 cascode stages	70-nm GaAs MHEMT	[18]
152	22.7	6.0	4	100-nm GaAs MHEMT	This work, on-wafer
143	19.8	6.3	4	100-nm GaAs MHEMT	This work, on-wafer
130-154	18.0-19.0	5.5-7.0	4	100-nm GaAs MHEMT	This work, on-wafer
130-171	17.6-20.6	5.5-7.0	4	100-nm GaAs MHEMT	This work, on-wafer

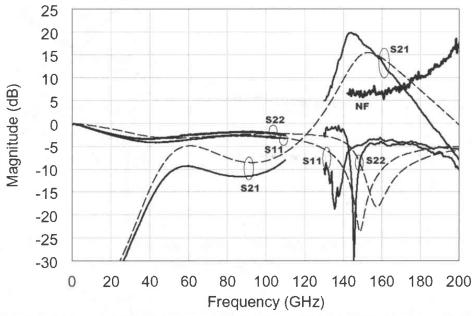

Fig. 5. Measured (solid) and simulated (dashed) S-parameters and noise figure (measurement only) for LNA3. A flat gain of 18 dB was achieved at D-band with noise figure of 5.5-7.0 dB. Vd = 1.36 V, Vg = 36 mA. Data from [25].

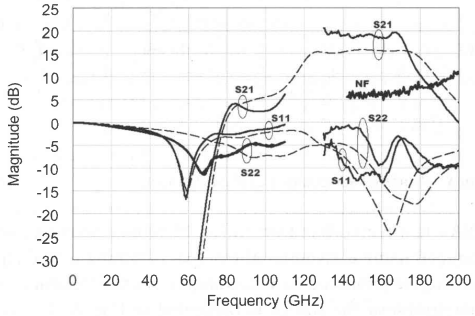

Fig. 6. Measured (solid) and simulated (dashed) S-parameters and noise figure (measurement only) for LNA4. The peak gain of 20.6 dB was achieved at 130 GHz. The 3 dB bandwidth is 130-171 GHz. The noise figure is less than 7.0 dB at 142-175 GHz range. Vd = 1.18 V, Id = 36 mA. Data from [25].

reactive matching technique was used for matching network design and inductive source feedback improves stability. The on-wafer measurement results and simulations are shown in Fig. 6. The maximum gain is 20.6 dB with a 3 dB bandwidth of 130-175 GHz. The measured noise figure is 5.5-7.0 dB between 142-175 GHz.

As a summary, the measured gain was found to be higher than simulated ones. The on-wafer performance of the designed amplifiers has been compared to previously reported MMIC LNAs at D-band in Tab. 1. The LNAs reported in this paper show comparable or better performance than the previously published amplifiers.

IV. Packaging

The mechanical design of the module used in this work is based on an E-plane split-block package, originally described in [26]. The concept is illustrated in Fig. 7, showing both halves of a WR-6 (110-170 GHz) block with the amplifier MMIC and two waveguide to CPW transitions. The outer dimensions of the block (excluding waveguide alignment pins) are 16x19x19 mm. The block has a space for a 5-pin micro connector and a small PCB for installing a bias network (lowpass RC), as well as a smaller cavity adjacent to the LNA for chip capacitors. All components are attached to the block with conductive epoxy glue.

The waveguide to CPW transitions required for E-plane split-block packaging were manufactured with a thin-film process on 100 μm thick, 99.6 % polished alumina. The design method of the transitions follows the outline presented in [27], where general transitions from waveguide to microstrip have been designed. The simulation model for the transition is illustrated in Fig. 8. The height and width of the microstrip channel were designed to result in cutoff above 200 GHz for the first waveguide-like mode in the channel. For the WR-6 antenna probe it was possible to find a combination of the width and length of the probe as well as the backshort distance that resulted directly in 50 Ω real impedance. A transition from microstrip to CPW

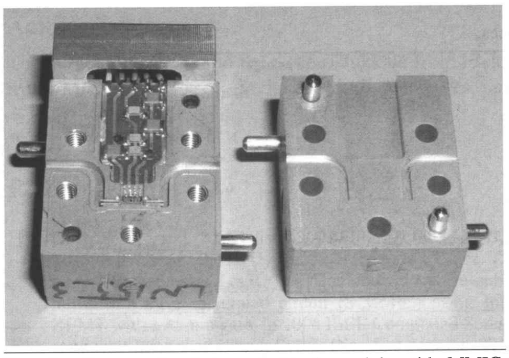

Fig. 7. Photograph of the split-block module with MMIC, waveguide to CPW transitions and DC-feeding network assembled.

is obtained with a short taper from the 50 Ω microstrip to the 47 μm wide center conductor of the CPW added to the transition. CPW structure is completed with two ground pads on the sides, which are connected to the backside metal by plated-through vias. For the transition, the simulations showed a transmission loss below 1 dB and the return loss above 20 dB over 20 GHz band around 150 GHz.

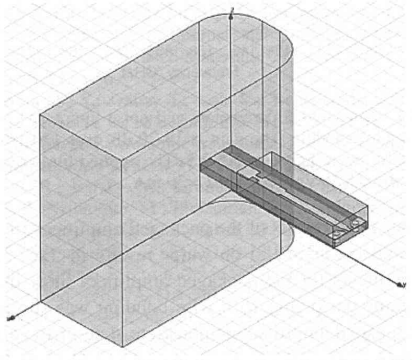

Fig. 8. Simulation model for waveguide to CPW transition.

V. Measurement results for packaged amplifiers

Selected amplifiers were packaged in a split-block waveguide package. The measurement range of packaged amplifiers was limited by the available test equipment. The S-parameters were measured using HP8510C with G-band extension modules, leading to a measurement range of 130-175 GHz. The upper frequency limit is due to the WR-6 package. The noise figures of the packaged amplifiers were measured using same measurement system as with the on-wafer measurements. It is noted that the meaningful noise measurement bandwidth depends on the gain of the amplifier.

First, the optimum bias conditions for each amplifier module were identified by sweeping the supply voltage and the drain current and measuring the noise figure and the insertion gain at a fixed frequency. As an example, the bias sweep for LNA3 is presented in Figs. 9 and 10 for noise figure and insertion gain, respectively.

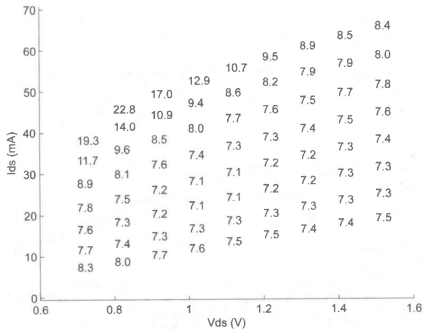

Fig. 9. Noise figure of the LNA3 in a waveguide module with different bias settings at 155 GHz. The gate voltage was swept from -0.1 V to 0.25 V with 0.5 V steps.

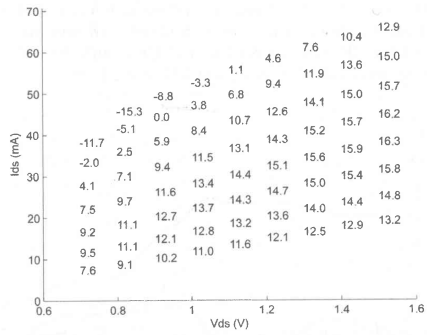

Fig. 10. Insertion gain of the LNA3 in a waveguide module with different bias settings at 155 GHz. The gate voltage was swept from -0.1 V to 0.25 V with 0.5 V steps.

The measurement results for a packaged LNA2 are presented in Fig. 11. With the tuned bias settings, the LNA2 exhibits a gain of 19.5 dB and a noise figure of 6.8 dB at 145 GHz. The values are not directly comparable to the on-wafer measurements due to different biasing conditions. Reasonable input and output match values (<-5 dB) are achieved over a wide bandwidth.

The measurement results for a packaged LNA3 are shown in Fig. 12. A peak gain of 18.9 dB and a noise figure of 6.7 dB are achieved at 151 GHz. Again, reasonable input and output match values are achieved up to 152 GHz. The gain is better than 15 dB at 130-140 GHz range.

Table 2. Comparison of on-wafer and packaged amplifier performances.

	On-wafer				Package			
Design	**Frequency (GHz)**	**Gain (dB)**	**NF (dB)**	**Bias**	**Frequency (GHz)**	**Gain (dB)**	**NF (dB)**	**Bias**
LNA1	152	22.7	6.0	V_d = 1.09 I_d = 36 mA	N.A.	N.A.	N.A.	N.A.
LNA2	143	19.8	6.3	V_d = 1.54 I_d = 36 mA	145	19.5	6.8	V_d = 1.1 I_d = 24 mA
LNA3	130-154	18.0-19.0	5.5-7.0	V_d = 1.36 I_d = 36 mA	130-154	15.0-18.9	5.5-7.5	V_d = 1.1 I_d = 30 mA
LNA4	130-171	17.6-20.6	5.5-7.0	V_d = 1.18 I_d = 36 mA	130-161	15.0-19.5	5.5-7.5	V_d = 0.8 I_d = 30 mA

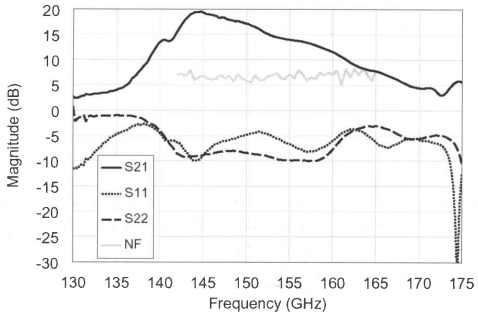

Fig. 11. Measured S-parameters and noise figure of LNA2 in a waveguide module. The peak gain of 19.5 dB with the noise figure of 6.8 dB was achieved at 145 GHz with the following bias conditions Vd = 1.1 V, Vg = 0.1 V, Id = 24 mA.

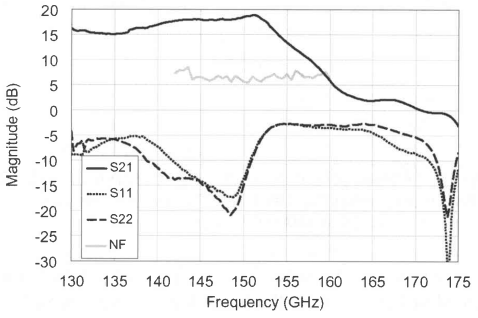

Fig. 12. Measured S-parameters and noise figure of LNA3 in a waveguide module. The peak gain of 18.9 dB with the noise figure of 6.7 dB was achieved at 151 GHz with the following bias conditions Vd = 1.1 V, Vg = 0.05 V, Id = 30 mA.

The measurement results of a packaged LNA4 are presented in Fig. 13. The gain is higher than 15 dB from 130 to 161 GHz and the noise figure values range from 5.5 to 7.5 dB at frequency range of 142-171 GHz.

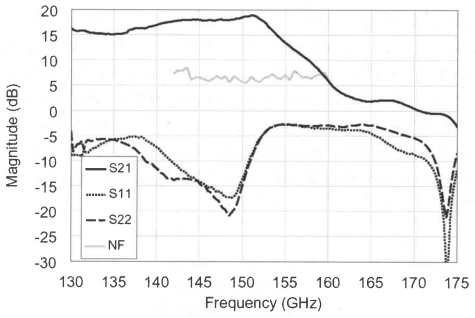

Fig. 13. Measured S-parameters and noise figure of LNA4 in a waveguide module. The gain is 14-20 dB over 130-161 GHz range with noise figure of 5.5-7.5. The applied bias conditions were Vd = 0.8 V, Vg = 0.0 V, Id = 30 mA.

The measured results of the packaged amplifiers are compiled and compared to on-wafer results in Tab. 2. The measurements for the packaged amplifiers show that the waveguide packaging with wire bonding was successful. The packaged amplifiers demonstrate state-of-the-art performance.

VI. Conclusion

Four amplifier designs for D-band operation and their performance have been presented. The on-wafer measurements showed larger gain than was predicted by the simulations. The measured results are comparable when compared to InP HEMT amplifiers. Selected amplifiers were packaged in a split-block waveguide package. The measurements for the packaged amplifier show that the waveguide packaging with wire bonding was successful. The MHEMT technology was found useful for D-band low noise applications. Using MMIC amplifiers the noise figure of D-band radiometers can be lowered, resulting better sensitivity compared to architectures with direct down conversion without preamplification.

Acknowledgment

The authors would like to thank Petri Jukkala from Elektrobit Microwave, Espoo, Finland, for his comments and Mr. Manu Lahdes from MilliLab, VTT for performing electromagnetic simulations for the interdigital capacitor.

References

[1] Deal, W. R.; Din, S.; Radisic, V.; Padilla, J.; Mei, X. B.; Yoshida, W.; Liu, P. H.; Uyeda, J.; Barsky, M.; Gaier, T.; Fung, A.; Samoska, L.; R. Lai: Demonstration of a submillimeter wave integrated circuit (S-MMIC) using InP HEMT with a 35-nm gate, in 2006 IEEE Compound Semiconductor Integrated Circuit Symp. Dig., San Antonio, TX, November 2006, 33-36.

[2] Dawson, D.; Samoska, L.; Fung, A. K.; Lee, K.; Lai, R.; Grundbacher, R.; Liu, P.-H.; Raja, R.: Beyond G-band: A 235 GHz InP MMIC amplifier. IEEE Microwave and Wireless Components Letters, **15** (2005), 874-876.

[3] Tessmann, A.: 220-GHz metamorphic HEMT amplifier MMICs for High-Resolution Imaging Applications. IEEE Journal of Solid-State Circuits, **40** (2005), 2070-2076.

[4] Streit, D.; Lai, R.; Oki, A.; Gutierrez-Aitken, A.: InP HEMT and HBT applications beyond 200 GHz, in Proceedings of 14th International Conference on Indium Phosphide and Related Materials, Stockholm, Sweden, May 2002, 11-14.

[5] Grundbacher, R.; Raja, R.; Lai, R.; Chou, Y. C.; Nishimoto, M.; Gaier, T.; Dawson, D.; Liu, P. H.; Barsky, M.; Oki, A.: A 150-215 GHz InP HEMT low noise amplifier with 12 dB gain, in 17th International Conference on Indium Phosphide and Related Materials, Glasgow, Scotland, May 2005, 613-616.

[6] Weinreb, S.; Gaier, T.; Lai, R.; Barsky, M.; Leong, Y. C.; Samoska, L.: High-gain 150-215-GHz MMIC amplifier with integral waveguide transitions. IEEE Microwave and Guided Wave Letters, **9** (1999), 282-284.

[7] Lai, R.; Barsky, M.; Grundbacher, R.; Liu, P. H.; Chin, T. P.; Nishimoto, M.; Elmajarian, R.; Rodriguez; Tran. L.; Gutierrez, A.; Oki, A.; Streit, D.: InP HEMT amplifier development for G-band (140-220 GHz) applications, in International Electron Devices Meeting Technical Digest, San Francisco, CA, December 2000, 175-177.

[8] Pobanz, C.; Matloubian, M.; Radisic, V.; Raghavan, G.; Case, M.; Misovic, M.; Hu, M.; Nguyen, C.; Weinreb, S.; Samoska, L.: High performance MMICs with submillimeter wave InP-based HEMTs, in Proceedings of 2000 International Conference on Indium Phosphide and Related Materials, Williamsburg, VA, May 2000, 67-70.

[9] Pobanz, C. W.; Matloubian, M.; Lui, M.; Sun, H.-C.; Case, M.; Ngo, C. M.; Janke, P.; Gaier, T.; Samoska, L.: A high-gain monolithic D-band InP HEMT amplifier. IEEE Journal of Solid-State Circuits, **34** (1999), 1219-1224.

[10] Weinreb, S.; Chao, P. C.; Copp, W.: Full-waveguide band, 90 to 140 GHz, MMIC amplifier module, in 1997 IEEE MTT-S International Symposium Digest, Denver, CO, June 1997, 1279-1280.

[11] Dambrine, G.; Parenty, T.; Bollaert, S.; Happy, H.; Cappy, A.; Mateos, J.; Narhi, T.; Orlhac, J. C.; Trier, M.; Baudet, P.; Landry, P.: An overview of low noise devices and associated circuits for 100-200 GHz space applications, in Proceedings of 11th GAAS Symposium, Munich, Germany, October 2003, 473-476.

[12] Edgar, D. L.; McLelland, H.; Ferguson, S.; Cameron, N. I.; Holland, M.; Thayne, I. G.; Taylor, M. R. S.; Stanley, C. R.; Beaumont, S. P.: 94 and 150GHz coplanar waveguide MMIC amplifiers realized using InP technology, in 1999 IEEE MTT-S International Microwave Symposium Digest, Anaheim, CA, June 1999, 247-250.

[13] Kok, Y. L.; Wang, H.; Huang, T. W.; Lai, R.; Barsky, M.; Chen, Y. C.; Sholley, M.; Block, T.; Streit, D. C.; Liu, P. H.; Allen, B. R.; Samoska, L.; Gaier, T.: 160-190-GHz monolithic low-noise amplifiers. IEEE Microwave and Guided Wave Letters, **9** (1999), 311-313.

[14] Lai, R.; Wang, H.; Tan, K. L.; Streit, D. C.; Liu, P. H.; Velebir Jr., J.; Chen, S.; Berenz, J.; Pospieszalski, M. W.: A monolithically integrated 120-GHz InGaAs/InAlAs/InP HEMT amplifier. IEEE Microwave and Guided Wave Letters,**4** (1994), 194-195.

[15] Wang, H.; Lai, R.; Lo, D. C. W.; Streit, D. C.; Liu, P. H.; Dia, R. M.; Pospieszalski, M. W.; Berenz, J.: A 140-GHz monolithic low noise amplifier. IEEE Microwave and Guided Wave Letters, **5** (1995), 150-152.

[16] Wang, H.; Lai, R.; Kok, Y.-L.; Huang, T.-W.; Aust, M. V.; Chen, Y. C.; Siegel, P. H.; Gaier, T.; Dengler, R. J.; Allen, B. R.: A 155-GHz monolithic low-noise amplifier. IEEE Transactions on Microwave Theory and Techniques, **46** (1998), 1660-1666.

[17] Tessmann, A.; Wohlgemuth, O.; Reuter, R.; Haydi, W. H.; Massler, H.; Hülsmann, A.: A coplanar 148 GHz cascode amplifier MMIC using 0.15 μm GaAs PHEMTs, in 2000 IEEE MTT-S International Microwave Symposium Digest, Boston, MA, June 2000, 991-994.

[18] Schlechtweg, M.; Leuther, A.; Tessmann, A.; Schwörer, C.; Massler, H.; Reinert, W.; Lang, M. ; Nowotny, U.; Kappeler, O.; Walther, M.; Lösch, R.: Millimeter-wave and mixed-signal integrated circuits based on advanced metamorphic HEMT technology, in Proceedings of 16th International Conference on Indium Phosphide and Related Materials, Kagoshima, Japan, May 2004, 609-614.

[19] Krems, T. ; Haydl, W.; Massler, H.; Rüdiger, J.: Millimeter-wave performance of chip interconnections using wire bonding and flip-chip, in 1996 IEEE MTT-S International Symposium Digest, San Francisco, CA, June 1996, 247-250.

[20] Heinrich, W.: The flip-chip approach for millimeter-wave packaging. IEEE Microwave Magazine, **6** (2005), 36-45.

[21] Hirose, T.; Makiyama, K.; Ono, K.; Shimura, T. M.; Aoki, S.; Ohashi, Y.; Yokokawa, S.; Watanabe, Y.: A flip-chip MMIC design with coplanar waveguide transmission line in the W-band. IEEE Transactions on Microwave Theory and Techniques, **46** (1998), 2276-2282.

[22] Schmückle, F. J.; Jentzsch, A.; Oppermann, H.; Riepe, K.; Heinrich, W.: W-band flip-chip interconnects on thin-film substrate, in 2002 IEEE MTT-S International Symposium Digest, Seattle, WA, June 2002, 1393-1396.

[23] Onodera, K.; Ishii, T.; Aoyama, S.; Sugitani, S.; Tokumitsu, M.: Novel flip-chip bonding technology for W-band interconnections using alternate lead-free solder bumps. IEEE Microwave and Wireless Components Letters, **12** (2002), 372-374.

[24] Kerssenbrock, T. V.; Heide, P.: Novel 77 GHz flip-chip sensor modules for automotive radar applications, in 1999 IEEE MTT-S International Symposium Digest, Anaheim, CA, June 1999, 289-292.

[25] Kantanen, M.; Varonen, M.; Kärkkäinen, M.; Karttaavi, T.;

Weber, R.; Leuther. A.; Seelmann-Eggebert, M.; Närhi, T.; Halonen, K. A. I.: Coplanar 155 GHz MHEMT MMIC Low Noise Amplifiers, in 2006 Asia-Pacific Microwave Conference Proceedings, Yokohama, Japan, December 2006, 173-176.

[26] Weinreb, S.; Lai, R.; Erickson, N.; Gaier, T.; Wielgus, J.: W-band InP wideband MMIC LNA with 30K noise temperature, in 1999 IEEE MTT-S International Microwave Symposium Digest, Anaheim, CA, June 1999, 101-104.

[27] Leong, Y.-C; Weinreb, S.: Full band waveguide-to-microstrip probe transitions, in 1999 IEEE MTT-S International Microwave Symposium Digest, Anaheim, CA, June 1999, 1435-1438.

Mikko Kantanen received his M.Sc. and Lic.Sc. degrees in Electrical Engineering from the Helsinki University of Technology (TKK), Espoo, Finland 2001 and 2006, respectively. Since 2001 he has worked as a Research Scientist in MilliLab, VTT Technical Research Centre of Finland, Espoo, Finland, in the areas of millimetre wave integrated circuit design, millimetre wave measurements, and millimetre wave systems. He is a co-recipient of an Asia-Pacific Microwave Conference 2006 Prize.

Mikko Kärkkäinen was born in 1975. He received the Lic. Sc. and the M. Sc. degrees in electrical engineering from the Hel-sinki University of Technology, Espoo, Finland, in 2005 and 2000, respectively. He is currently working towards the Ph.D. degree at the Helsinki University of Technology. In 1998 he started working at the Electronic Circuit Design Laboratory, Helsinki University of Technology. His current research interests are in the field of CMOS millimetre-wave circuits for integrated radio front-ends. He is also a co-recipient of the APMC 2006 Prize for an outstanding contribution to the Asia-Pacific Microwave Conference held in Yokohama, Japan.

Mikko Varonen received the M.Sc. and Lic.Sc. degrees in electrical engineering from the Helsinki University of Technology (TKK), Espoo, Finland, in 2002 and 2005, respectively. He is currently working toward the D.Sc. degree in electrical engineering at the Electronic Circuit Design Laboratory, Helsinki University of Technology.

His research interests involve millimetre-wave integrated circuits. He is a member of the Finnish Graduate School of Electronics, Telecommunications and Automation (GETA). He was the co-recipient of the APMC 2006 Prize for the outstanding contribution to the Asia-Pacific Microwave Conference.

Mikko Laaninen received his M.Sc. from the Helsinki University of Technology in 2003, specializing in micro- and millimeter-wave measurements.

In 2003-2006 he participated in the design and testing of the ESA Planck satellite's 70GHz cryogenic receivers at Ylinen Electronics. Currently he works on commercial telecommunications equipment at Elektrobit, Finland.

Timo Karttaavi received M. Sc. (EE) and Lic. Sc (EE) degrees from the Helsinki University of Technology in 1989 and 2000, respectively.

He spent a year at the Swiss Federal Institute of Technology, Lausanne in 1990-91. From 1991 to 1993 he was with the University of Helsinki developing readout electronics for high energy physics experiments stationed at CERN in Geneva. From 1993 to 2008 he has been with VTT working on microwave and millimeter wave circuits and systems. During 2005-06 he spent a year with the Berkeley Wireless Research Centre in the USA working on millimeter wave CMOS circuits. Since 2008 he has been with Nokia Research Center.

Rainer Weber was born in Offenburg, Germany, in 1978. He received the Dipl.-Ing. (FH) degree in electrical engineering from the University of Applied Sciences Offenburg, Germany, in 2003.

He then joined the High Frequency Devices and Circuits Department of the Fraunhofer Institute for Applied Solid-State Physics (IAF), Freiburg, Germany, where he is involved in the MMIC design of oscillators and amplifiers up to 220 GHz.

Arnulf Leuther received the Dipl. Phys. degree and the PhD degree in physics from the Technical University of Aachen.

He is with the Fraunhofer Institute for Applied Solid State Physics (IAF) since 1996. His research work was focused on the development of III/V-process technology for high frequency MMICs

Matthias Seelmann-Eggebert received his Diploma and Ph.D. degree in physics from the University of Tübingen in 1980 and 1986, respectively.

From 1980 to 1996 he was involved in R&D related to infrared detectors based on HgCdTe and developed electrochemical and surface physical methods for the characterization of compound semiconductor surfaces. From 1990 to 1991 he was a visiting scientist at Stanford University. From 1997 to 2000 he was engaged in the growth of CVD diamond. Since 2001 he is a member of the department of high frequency electronics of the IAF in Freiburg,Germany, and is concerned with the preparation and development of simulation models for active and passive III-V devices.

Tapani Närhi

Photograph of the Author not available at the time of printing.

Janne Lahtinen received the M.Sc. (Tech.), Lic.Sc. (Tech.), and D.Sc. (Tech.) degrees from the Helsinki University of Technology (TKK), Finland, in 1996, 2001, and 2003, respectively.

Since 2007, he is the Managing Director of Harp Technologies Ltd, Espoo, Finland. From 2006 to 2007 he was the Director, Space at SF-Design Ltd, Jokioinen, Finland. From 2004 to 2006 he was with Elektrobit Microwave Ltd (Ylinen Electronics Ltd), Kauniainen, Finland serving in various positions, finally as the Manager, Space and Security. From 2002 to 2003 he was a Research Fellow at the ESA-ESTEC in Noordwijk, The Netherlands and from 1995 to 2002 with the TKK Laboratory of Space Technology. His research interests include microwave remote sensing systems and spacecraft hardware. He has authored or co-authored over 50 publications.

Dr. Lahtinen served as a Secretary of the Finnish National Committee of COSPAR from 1997 to 2002. From 2006 to 2007, he was an advisor of the Finnish Space Committee. He was welcomed as a Burgen Scholar by Academia Europaea in 2004, he won the Young Scientist Award of the National Convention on Radio Science (URSI) in 2001, and he received the third place in the IEEE GRS-S Student Prize Paper Competition in 2000.

Kari A. I. Halonen received the M.Sc. degree in electrical engineering from Helsinki University of Technology, Finland, in 1982, and the Ph.D. degree in electrical engineering from the Katholieke Universiteit Leuven, Belgium, in 1987.

Since 1988 he has been with the Electronic Circuit Design Laboratory, Helsinki University of Technology. From 1993 he has been an associate professor, and since 1997 a full professor at the Faculty of Electrical Engineering and Telecommunications. He became the Head of Electronic Circuit Design Laboratory year 1998.

He has been an associate editor of IEEE Transactions on Circuits and Systems I, a guest editor for IEEE Journal of Solid-State Circuits and the Technical Program Committee Chairman for European Solid-State Circuits Conference year 2000. He has been awarded the Beatrice Winner Award in ISSCC'02 Conference year 2002. He is a TPC- member of ESSCIRC and ISSCC. He specializes in CMOS and BiCMOS analog integrated circuits, particularly for telecommunication applications. He is author or co-author over two hundred international and national conference and journal publications on analog integrated circuits.

Publication V

Kärkkäinen, M., Kantanen, M., Caujolle-Bert, S., Varonen, M., Weber, R., Leuther, A., Seelmann-Eggebert, M., Alanne, A., Jukkala, P., Närhi, T., Halonen, K.A.I., “MHEMT G-band low-noise amplifiers,” *IEEE Transactions on Terahertz Science and Technology*, vol. 4, no. 4, pp. 459-468, July 2014.

MHEMT G-Band Low-Noise Amplifiers

Mikko Kärkkäinen, Mikko Kantanen, Sylvain Caujolle-Bert, Mikko Varonen, Rainer Weber, Arnulf Leuther, Matthias Seelmann-Eggebert, Ari Alanne, Petri Jukkala, Tapani Närhi, and Kari A. I. Halonen

***Abstract*—To improve the performance of G-band equipment for humidity sounding of the atmosphere, a high-gain and low-noise amplifier is needed. Here, the performances of 165 and 183 GHz low-noise amplifier microchips intended for atmospheric water vapor profiling application are reported. The microchips are manufactured in metamorphic high-electron mobility transistor technology having a gate length of 50 nm. The on-wafer measured results show noise figures of 4.4–7.4 dB and 16–25 dB gain at the operating frequencies. In addition, two of the amplifiers were assembled in waveguide packages and the measured results show a gain of 19–20 dB and 7 dB noise figure at both 165 and 183 GHz.**

***Index Terms*—Low-noise amplifiers (LNAs), millimeter-wave integrated circuits, millimeter-wave transistors, MMICs, MODFETs.**

I. Introduction

ATMOSPHERIC sensing is becoming increasingly important when the climate is being studied at a global scale. For example, a high-resolution humidity profile of the atmosphere can be obtained by observing radiometer measurement results at around a window frequency and the water molecule resonances at 165 and 183 GHz, respectively [1]. The sensitivity of the humidity sounders could be improved by developing a high-performance low-noise amplifier (LNA) for the receiver.

Several amplifiers operating around the 180-GHz frequency have previously been reported [2]–[8]. Most of the state-of-the-art noise performance results are achieved with InP-HEMT-based devices. In the past, we have reported D-band amplifiers in 100-nm metamorphic high-electron mobility transistor (MHEMT) technology [9], and this work has been extended to higher frequencies using a 50-nm process [10]. The aim of this paper is to show that the metamorphic HEMT-based amplifiers are reaching performance levels that have previously been seen in results obtained from amplifiers based on indium phosphide devices exclusively. This paper presents the design of the amplifiers and the waveguide package in detail as well as explanation on the transistor model and measurement methods. Moreover, the paper is complemented with results from 165-GHz amplifiers.

This paper is organized as follows. In Section II, the manufacturing technology is briefly explained. The G-band low-noise amplifier (LNA) design, and both simulated and measured results are presented in Section III. In Section IV, the results for waveguide packaged 165- and 183-GHz LNAs are shown and compared with the corresponding on-wafer results. Finally, in Section V, a comparison with previously published results is presented, and conclusions are compiled.

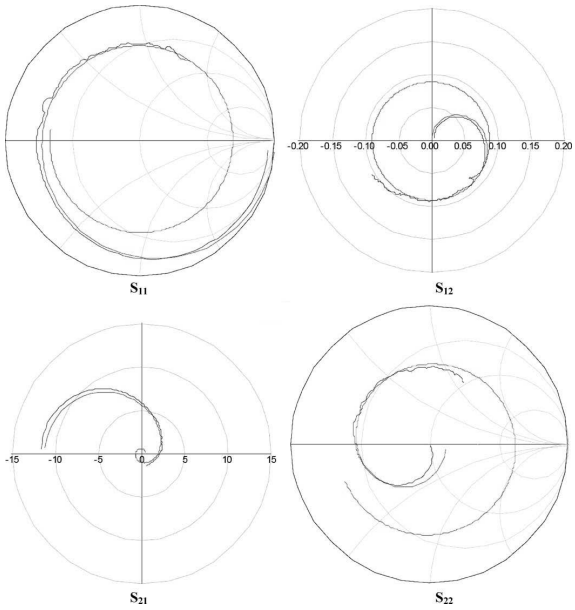

Fig. 1. Simulated small-signal 2×60 μm-sized mHEMT model. The current density is 400 mA/mm and the simulation range of the S-parameters is from 500 MHz to 300 GHz. The measured S-parameters are from 500 MHz to 110 GHz for comparison.

II. Manufacturing Technology and Transistor Model

The LNAs are manufactured in GaAs MHEMT technology from Fraunhofer IAF, Freiburg, Germany.

Manuscript received March 07, 2014; revised April 29, 2014; accepted May 16, 2014. Date of publication June 10, 2014; date of current version June 26, 2014. This work was supported in part by the European Space Research and Technology Centre (ESTEC), Noordwijk, the Netherlands under Contract AO 1-5619/08/NL/GLC and by the MilliLab, Millimetre wave Laboratory of Finland. The work of M. Varonen was supported by the Academy of Finland through the Postdoctoral Researcher post.

M. Kärkkäinen, M. Varonen, and K. A. I. Halonen are with the Department of Micro- and Nanosciences, School of Electrical Engineering, Aalto University, FI-00076 Aalto, Espoo, Finland (e-mail: mikko.m.karkkainen@aalto.fi).

M. Kantanen is with the VTT Technical Research Centre of Finland, FI-02044 VTT, Finland.

S. Caujolle-Bert was with the Department of Micro- and Nanosciences, School of Electrical Engineering, Aalto University, FI-00076 Aalto, Espoo, Finland. He is now with LATMOS-CNRS, 78280 Guyancourt, France.

R. Weber, A. Leuther and M. Seelmann-Eggebert are with the Fraunhofer Institute for Applied Physics (IAF), D-79108, Freiburg, Germany.

A. Alanne and P. Jukkala are with DA-Design Oy, FI-31600 Jokioinen, Finland.

T. Närhi is with the European Space Agency (ESTEC), NL-2200 AG, Noordwijk, The Netherlands.

Color versions of one or more of the figures in this paper are available online at http://ieeexplore.ieee.org.

Digital Object Identifier 10.1109/TTHZ.2014.2327383

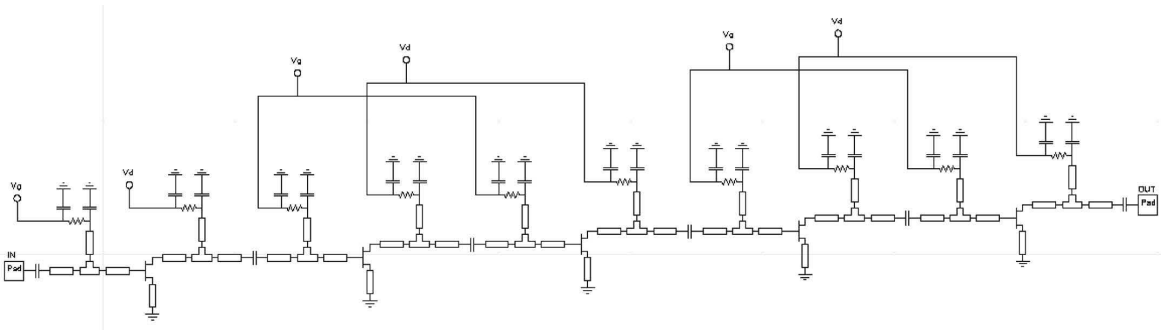

Fig. 2. Simplified schematic of a five-stage LNA.

This 50-nm gate-length technology features an $In_{0.52}Al_{0.48}As/In_{0.80}Ga_{0.20}As/In_{0.53}Ga_{0.47}As$ composite channel structure, resulting in an extrinsic transit frequency f_T of 370 GHz and a maximum extrinsic transconductance $g_{m,max}$ of 2100 mS/mm. The technology is suitable for grounded coplanar waveguide (GCPW) designs and features NiCr thin-film resistors, metal–insulator–metal (MIM) capacitors and both backside metallization and via holes through the substrate [11].

The small-signal transistor model is based on a large measurements database containing results from transistors having different sizes and different bias voltages. The database is generated from S-parameter measurements from 100 MHz to 110 GHz. The noise characteristics are modeled with Pospieszalski's method [12], although it proved to be sufficient to adjust the noise temperature of the output conductance only. The development and optimization of the fully scalable transistor model including the noise characteristics is presented in detail in [13]. The small-signal model was later verified by comparison to S-parameters, as shown in Fig. 1. In the beginning, we expected that the model would extrapolate up to the G-band and enable amplifier design.

III. Low-Noise Amplifiers

A. Design

A simplified schematic of a five-stage LNA is presented in Fig. 2. In each case, the designer chose transistor size and matching. All transistors are in common source configuration and the transistor sizes vary from 2×10 μm to 2×15 μm. The gate and drain bias voltages are fed through short-circuited shunt stubs. The use of inductive source feedback is mostly dictated by stability considerations and tolerable gain loss. The stability is checked for each amplifier stage separately and the feedback is tuned accordingly. A reasonable margin for stability was required for every stage. The amplifier design relied on the active and passive component models that were provided by the Fraunhofer IAF. Next, the design of a 183-GHz LNA is presented in more detail.

The decision on transistor size can be difficult as there are some tradeoffs between noise, gain, and stability. The selection of the amount of source feedback can be added to the list of difficult questions, especially, if the feedback line is modeled including its loss. To see how these issues are affecting the transistor characteristics, one can simulate the transistor performance and calculate, based on the simulations, the minimum noise figure of optimally matched cascaded chain of transistors, $F_{cas,min}$. This means that the transistors are matched to optimum noise measure [14]–[16]. As any ideal lossless passive network embedding the transistor does not affect this figure of merit [14], [17], one could neglect the feedback network from these simulations and still obtain the optimum solution concerning the selection of the transistor size. However, if one wants to see, how the actual lossy feedback network affects the $F_{cas,min}$, one can simulate it as a function of the feedback line length. In Fig. 3, the transistor layout is shown with the two-sided source lines connecting to the sources on the sides of the two-finger device. The length of the two parallel source feedback lines is equal, and they are swept simultaneously to find the optimum size. Although the effect is small, it is clearly visible, as shown in Fig. 4, for a selection of three different size unit fingers W_f at 183 GHz.

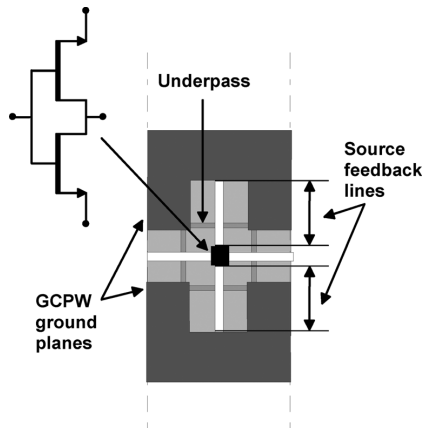

Fig. 3. Simplified layout of the connections of the two-finger MHEMT.

The second important issue is the related to the associated gain, when the input of the transistor is matched to the optimum noise measure and output to the corresponding conjugate. In some cases, as seen in Fig. 4, this results in a higher gain than

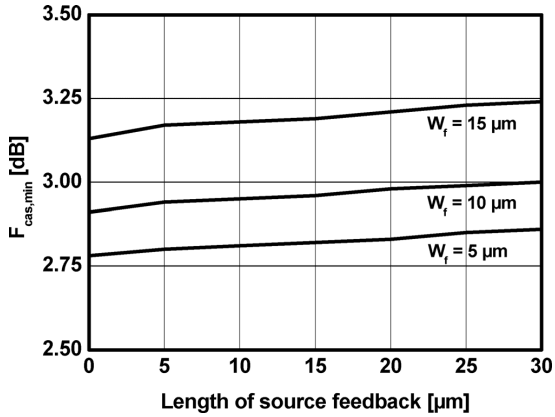

Fig. 4. Simulated $\mathrm{F_{cas,min}}$ of three different-size two-finger MHEMTs at 183 GHz and 400 mA/mm of drain current density.

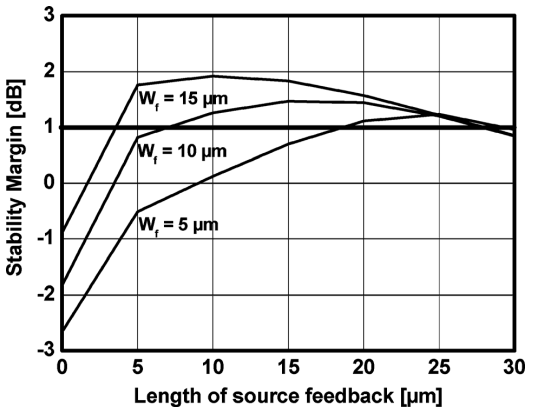

Fig. 5. Simulated stability margin of three different-size two-finger MHEMTs at 183 GHz and 400 mA/mm of drain current density. The margin is calculated as a difference between the optimally noise measure matched transistor gain and maximum stable gain (MSG).

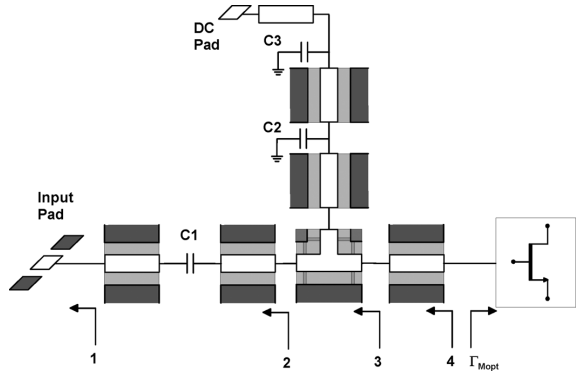

Fig. 6. LNA input matching.

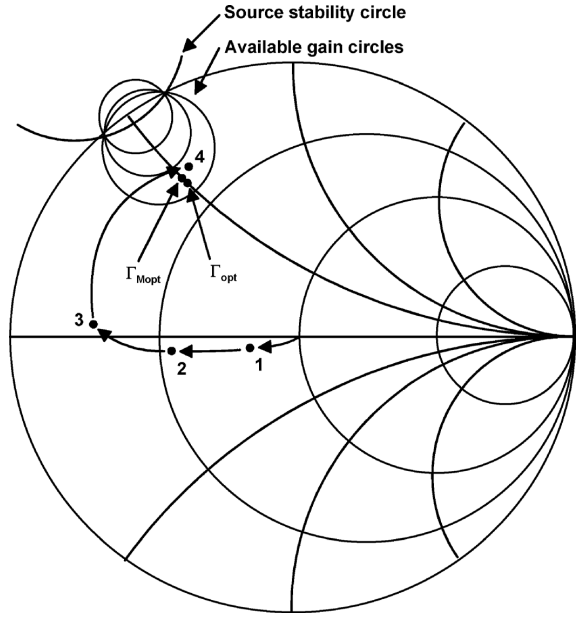

Fig. 7. LNA input matching showing the impedances at the different points of the network. Γ_{opt} shows the reflection coefficient for minimum noise figure and Γ_{Mopt} is for the corresponding reflection coefficient for the minimum noise measure.

the maximum stable gain is. This is an avoidable situation and one would like to have some margin for stability. In this case, the margin is set to 1 dB. From Fig. 5, it is seen that the 10-μm gate-width MHEMT exhibits a good margin with a source feedback length from 7 to 27 μm, whereas the 5-μm transistor is stable from 17 to 27 μm of feedback range only. This means that, with the $\mathrm{W_f} = 10$ μm, good stability should be achievable at the center frequency even if the source line has to be tuned to obtain good stability for out-of-band frequencies, as an example. Furthermore, as referring to Fig. 3, the $\mathrm{F_{cas,min}}$ of the 10-μm MHEMT is only 0.15 dB higher, when compared with the 5-μm transistor. For the 15-μm transistor the increase in $\mathrm{F_{cas,min}}$ is 0.37 dB.

In conclusion, the 10-μm unit finger width MHEMT has the best compromise between $\mathrm{F_{cas,min}}$ and stability margin over the range of source feedback line lengths varying from 7 to 27 μm at 183 GHz. The optimum noise measure bias would be around 300 mA/mm of current density, but it was noticed that, in practice, the peak transconductance bias of 400 mA/mm is better considering the gain requirement of 20 dB, bandwidth and only minor effect on total noise figure of a multistage amplifier and simplicity of the bias arrangements. However, the noise performance may be improved by a fraction of a decibel by biasing the first stage to the optimum noise bias. The design target for the 165-GHz amplifiers is a 5-GHz bandwidth and for the 183-GHz amplifiers it is 20 GHz.

The input matching consists of several parts as shown in Fig. 6, and the corresponding reflection coefficients are shown in Fig. 7. A wide-center-conductor GCPW having 30-Ω characteristic impedance helps in bringing the impedance closer to the optimum and it has lower loss, when compared to the other 50- and 70-Ω lines available in the design kit. The capacitors

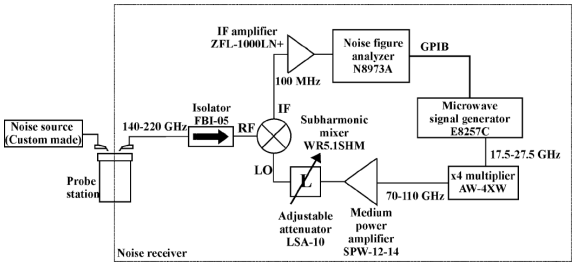

Fig. 8. Block diagram of the on-wafer noise figure and insertion gain measurement setup.

C1 and C2 have small capacitance to provide a good short at the center frequency, while C3 is used for stabilizing the amplifier and decoupling the dc bias network from the rest of the amplifier. In some designs, the series C1 is an essential part of the matching network as it effectively brings the phase of the reflection coefficient backwards as opposed to the effect of the connecting lines. In LNA5, there is an additional open stub at the input, which slightly improves the bandwidth.

B. Measurement Methods

The S-parameters in the range of 140–200 GHz have been tested using an HP8510B Network Analyzer with Oleson extension modules for G-band (140–220 GHz). The extension modules have been mounted on a Cascade Model 42 manual probe station and Picoprobe model 220 GSG-probes with 75-μm pitch were used. The measurement system is calibrated using Picoprobe calibration substrate and the LRRM calibration method [18], [19]. The calibration coefficients are calculated using WinCal-software from Cascade Microtech. Good calibration was achieved over the range of 140-200 GHz. Unfortunately, above 200 GHz, the calibration measurements suffer from poor dynamic range.

The noise figure and the insertion gain are measured using a well-known Y-factor method [20]. The measurement procedure is simple and requires only measurement of the relative power levels. The on-wafer noise measurement setup consists of two functional blocks, the noise source and the noise receiver. The block diagram of the measurement setup is presented in Fig. 8. A custom made solid-state noise source with two power levels, hot and cold, is used to generate noise with known noise temperature. An on-wafer probe is used to couple the noise to the device under test (DUT). The noise receiver consists of an input probe, an isolator, a subharmonic waveguide mixer, a sweepable microwave source, a frequency quadrupler, a 70–110-GHz (W-band) medium power amplifier (MPA), an adjustable attenuator, an IF-amplifier, and a noise figure analyzer.

The noise figure analyzer controls the output frequency of the microwave source via general purpose interface bus (GPIB) and sweeps the measurement frequency in selected steps over the entire G-band. The output frequency of the microwave source is quadrupled using the frequency multiplier to generate a millimeter wave signal in 70–110 GHz range. The signal is amplified in the MPA and fed to the LO-port of the harmonic mixer via the adjustable attenuator. The adjustable attenuator is used to fine tune the LO-power level to obtain as low noise temperature for the harmonic mixer as possible. Conversion loss of the mixer is in the range of 5-8 dB.

The wideband noise signal in the 140–220-GHz range is fed to the RF-port of the subharmonic mixer via the input probe and the isolator. The isolator is used to minimize effects of mismatch when the DUT is connected to the measurement setup. The IF signal is fed to the noise figure meter through the IF amplifier, and the noise power at single frequency is measured with 4-MHz bandwidth at 100 MHz. The measurement bandwidth is limited by noise figure analyzer's internal filter. The IF amplifier lowers overall noise temperature. Double side-band noise temperature of the receiver without the input probe is 3500–6500 K. Loss of a single probe is 2.5–3.5 dB over the G-band. For the packaged amplifier module measurements, the on-wafer probes and probe station are omitted from the setup.

C. Measured Results

1) 165-GHz LNAs: The LNA1 is a four-stage design with 2×15 μm-sized transistors. The micrograph of the chip and measured results are presented in Figs. 9 and 10, respectively. A gain of 20 dB and a noise figure of 4.4 dB are measured at 165 GHz. The power consumption of LNA1 is 44 mW.

After the first processing round, some of the possible problems related to the design kit models were considered. Reference plane uncertainty related to T-junctions and transistors were identified as most critical parameters for the designs. With refinements to reference planes a new low-noise amplifier was designed. The design is called LNA2. The measurement result for a second run chip is presented in Fig. 11. A gain of 25 dB and a noise figure of 5.2 dB are measured at 165 GHz. The power consumption of LNA2 is 36 mW.

2) 183-GHz LNAs: The LNA3 is a 4-stage design that has 2×10 μm –sized transistors. All the transistors are biased to peak transconductance of 400 mA/mm current density, which corresponds to 8 mA of drain current and 35 mW power consumption. The measured S-parameters and noise figure are presented in Fig. 12. A gain of 16 dB and a noise figure of 7.4 dB are measured at 183 GHz.

The LNA4 is a four-stage design, which has a varying transistor size from 2×10 μm to 2×12 μm. Again, all of the transistors are biased to peak transconductance. To obtain wideband matching open-ended stubs have been used and the series capacitors values have been tuned. The measured and simulated S-parameters and noise figure are presented in Fig. 13. A gain of 17 dB and a noise figure of 6.5 dB are measured at 183 GHz, while consuming 32 mW of dc power. Overall, frequency shifts of over 10 GHz are seen in the S_{11} and S_{22} in Figs. 10, 11, and 13 for the LNA1, LNA2, and LNA4, respectively. Furthermore, the LNA3 and LNA4 show decreasing gain at high frequencies that was not expected. It can be concluded that the original transistor model is too optimistic at G-band.

As with the 165-GHz amplifiers, a new version was designed for the second processing round to obtain better performance. The new five-stage amplifier is called LNA5. To ensure that sufficiently high gain and wide bandwidth would be obtained without compromising the stability, one stage was added to the original design in an effort to obtain 20 dB gain and to maintain

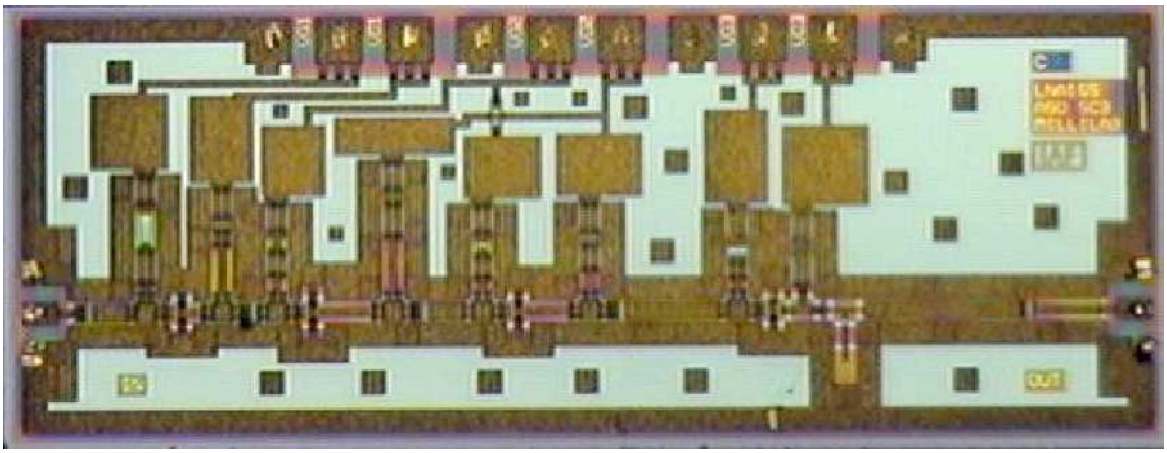

Fig. 9. Micrograph of LNA1. The chipsize is 2.5×1.0 mm^2 including pads.

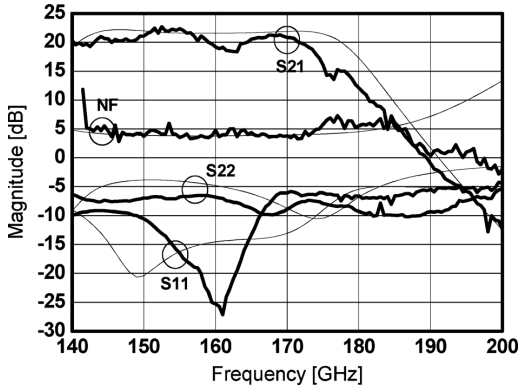

Fig. 10. Measured S-parameters and noise figure of LNA1. The thin lines represent the simulated results for comparison.

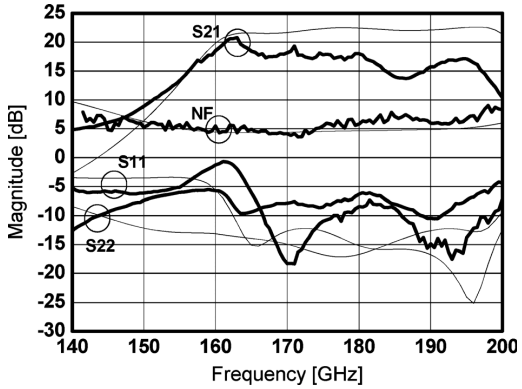

Fig. 12. Measured S-parameters and noise figure of LNA3. The thin lines represent the simulated results for comparison.

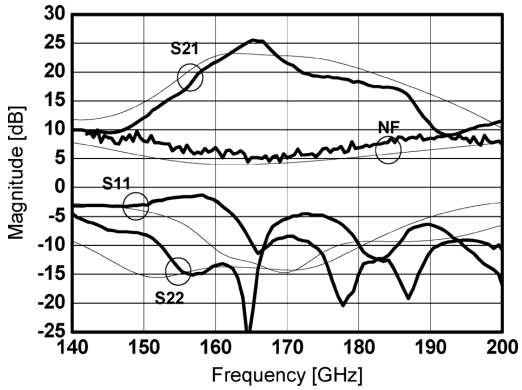

Fig. 11. Measured S-parameters and noise figure of LNA2. The thin lines represent the simulated results for comparison.

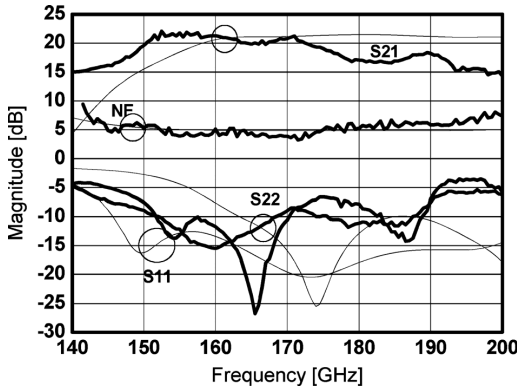

Fig. 13. Measured S-parameters and noise figure of LNA4. The thin lines represent the simulated results for comparison.

a good margin for stability. A microphotograph of the LNA5 is in Fig. 14, and both the simulated and measured results for the second processing round chip are presented in Fig. 15. A gain of 20 dB and a noise figure of 6.7 dB are obtained at 183 GHz.

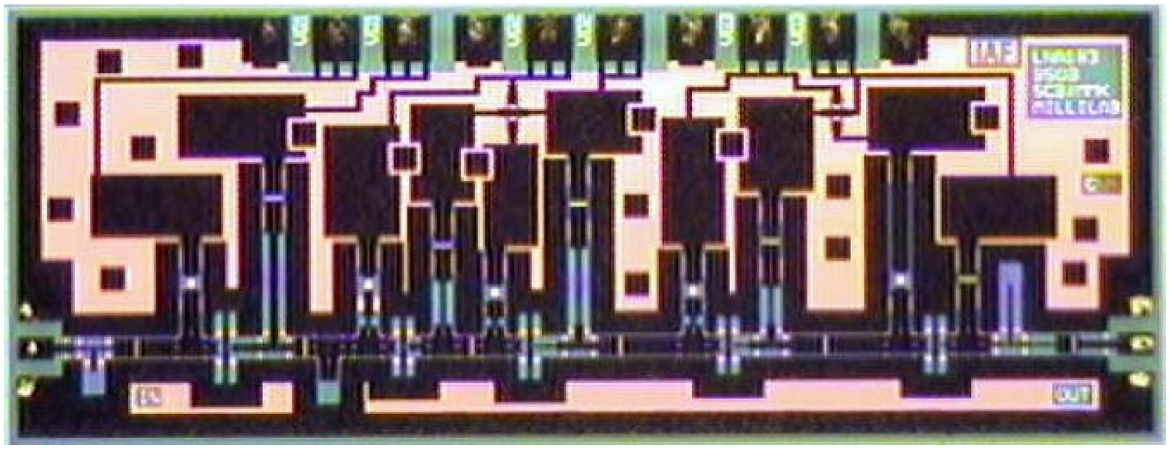

Fig. 14. Micrograph of LNA5. The chipsize is 2.5×1.0 mm^2 including pads.

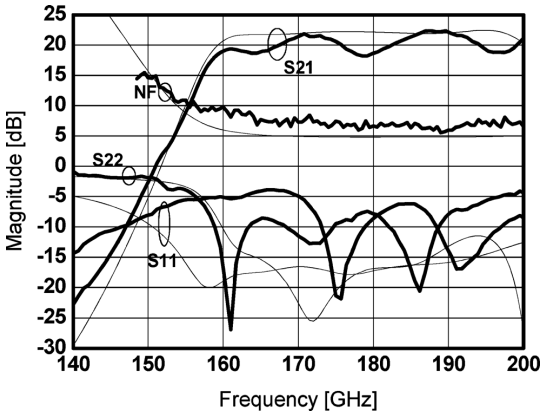

Fig. 15. Measured S-parameters and noise figure of LNA5. The thin lines represent the simulated results for comparison.

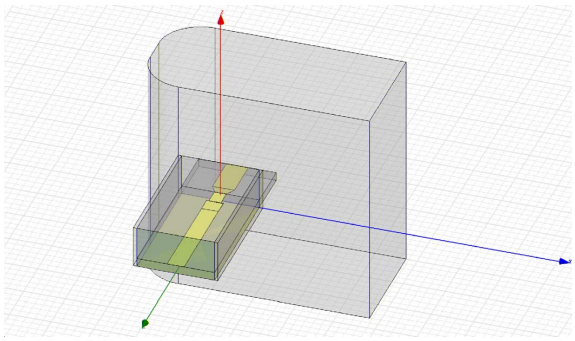

Fig. 16. Waveguide-to-microstrip transition design for the G-band split block package.

The power consumption of LNA5 is 41 mW, which is increased by 8 mW, because of the added fifth stage. For this design, the gain drop at high frequencies, which was observed in the earlier chips, has vanished.

IV. Packaged G-Band LNAs

A gold-plated brass G-band waveguide package was developed, which is similar to the one presented in [9] for lower frequencies. The original design method is presented in [21]. The E-plane split-block package requires transitions from the WR-5 waveguide interfaces to the coplanar input and output of the MMICs. Moreover, there is a small PC board for bias and supply voltages inside the package. The first design was made for alumina substrate that has been used before. However, sufficiently good full-band characteristics were difficult to achieve with this material and the alumina was replaced with quartz. According to the Ansoft HFSS EM-simulations, good full band characteristics were achieved. The design of the waveguide-to-microstrip transition substrate is shown in Fig. 16. The EM-simulation of the microstrip substrate channel was made to determine that the cutoff frequency of the waveguide modes is above 200 GHz. The impedance at the end of the waveguide probe in the window on the waveguide wall was simulated while the width and length of the probe and the back short distance were swept parametrically. The combination of the dimensions showing the minimum variation close to 50 Ω was selected for the subsequent simulations. The return loss at the end of the probe and the insertion loss between the waveguide input and the end of the probe were followed together with the impedance. Several sweeps were required to converge the dimension range and find the best dimension combination. The tapered section of the transmission line was added to improve the bandwidth.The parametric sweeps including the dimensions of the tapered section were computed to find the minimum impedance variation.

A separate WR-5 test module was designed and assembled in back-to-back configuration with two microstrip transitions bonded together without the additional length needed for the LNA chip. The S-parameters of the back-to-back module were measured to characterize the G-band package, as seen in Fig. 17. Between 150–165 GHz the loss is less than 1.3 dB with a return loss of around 20 dB. At higher frequencies, the loss in-

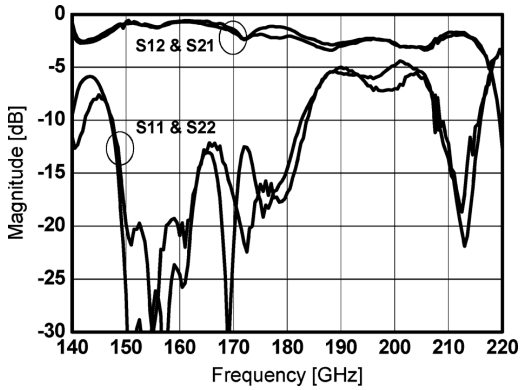

Fig. 17. Measured S-parameters of the G-band waveguide test module. Two transitions in back-to-back configuration are assembled inside the package.

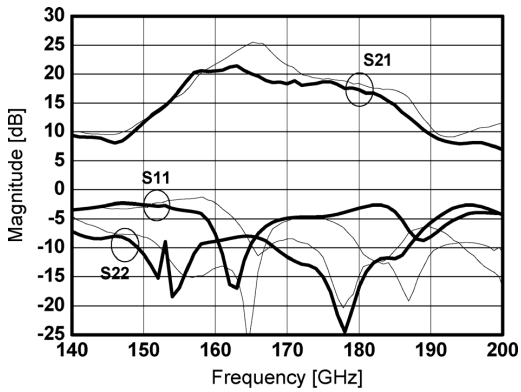

Fig. 18. Measured S-parameters of the waveguide packaged LNA2. The thin lines represent the on-wafer results for comparison.

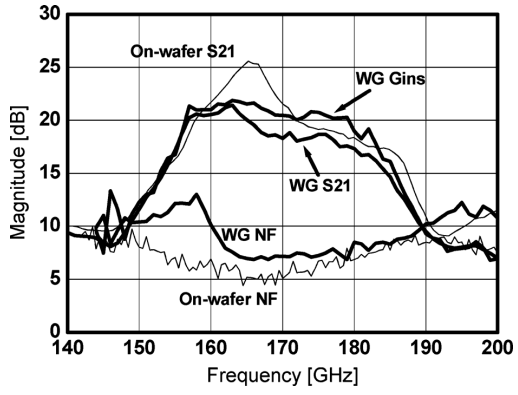

Fig. 19. Measured insertion gain (WG Gins) and noise figure (WG NF) of the waveguide packaged LNA2. The thin lines represent the on-wafer results for comparison.

creases up to around 2–3 dB and the matching deteriorates more significantly.

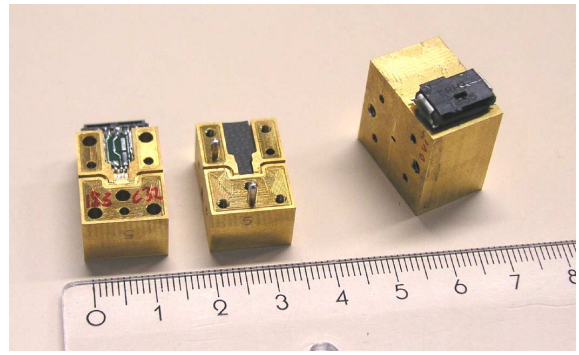

Fig. 20. Photograph of the manufactured split-block package with WR-5 waveguide input and output interfaces. The size of the package is approximately $10 \times 20 \times 20$ mm^3.

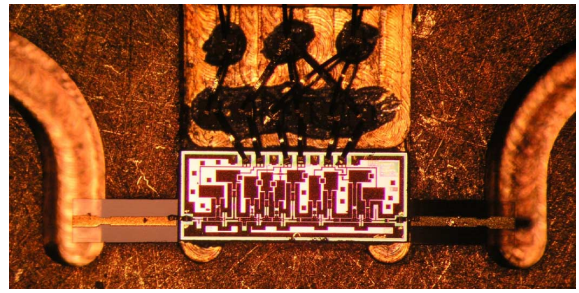

Fig. 21. Photograph of the LNA5 chip placed in the cavity inside the waveguide package. The input and output transitions are also visible on both sides of the chip.

The LNA2 of the 165-GHz designs and the LNA5 of the 183-GHz designs were mounted inside the packages. The S-parameter and noise measurement results for the 165-GHz packaged chip, and a comparison to on-wafer results are presented in Figs. 18 and 19, respectively. The insertion gain is computed from the noise figure measurement. Since the noise source does not present exact 50-Ω source impedance to the amplifier, the G_{ins} is not equal to the S_{21}. As shown in Figs. 18 and 19, gains of 20 and 7.0 dB noise figure were obtained for the 165-GHz LNA2 package.

The 183-GHz LNA5 package and the detailed picture of the chip-mounted inside the cavity are shown in Figs. 20 and 21, respectively. The measured results of the packaged LNA5 are compared to the on-wafer results in Figs. 22 and 23 The measured results show a gain of 19 dB and a noise figure of 7.1 dB at 183 GHz. Unfortunately, there was an unwanted resonance in the package cavity at around 165 GHz, which is visible in the measured curves. This resonance effect was minimized by placing absorbing material inside the cavity of the package. The average noise figure of the package is around 0-1 dB higher than the on-wafer result, which is in line with the measured back-to-back response and the simulated input transition loss of 0.68–0.80 dB for the package around a frequency range from

TABLE I
COMPARISON OF PUBLISHED G-BAND AMPLIFIERS

Frequency [GHz]	Gain [dB]	NF [dB]	Number of Stages	Technology	Ref.
183	16	3.4 *)	3	35-nm InP HEMT	[2]
150-220	18-26	-	3	50-nm InP HEMT	[4]
150-215	12	-	3	70-nm InP HEMT	[5]
150-215	20±6	8	6	80-nm InP HEMT	[6]
160-220	13-23	4.9-5.6 *)	3	35-nm InP HEMT	[7]
180-220	16	4.8	4	50-nm GaAs MHEMT	[8]
165	20	4.4	4	50-nm GaAs MHEMT	This work
165	20 *)	7.0 *)	4	50-nm GaAs MHEMT	This work
183	17	6.5	5	50-nm GaAs MHEMT	This work
183	19 *)	7.1 *)	5	50-nm GaAs MHEMT	This work

*) packaged chip

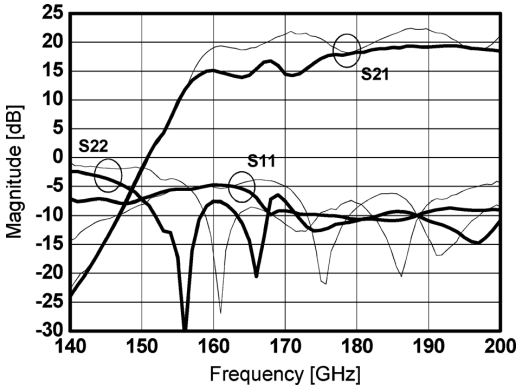

Fig. 22. Measured S-parameters of the waveguide packaged LNA5. The thin lines represent the on-wafer results for comparison.

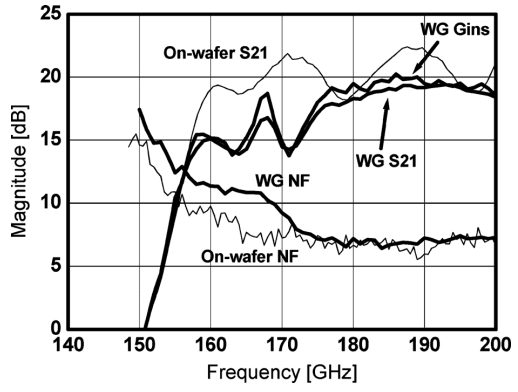

Fig. 23. Measured insertion gain (WG Gins) and noise figure (WG NF) of the waveguide packaged LNA5. The thin lines represent the on-wafer results for comparison.

170 to 200 GHz as well as taking into account the uncertainty of the on-wafer noise measurement.

V. CONCLUSION

This paper demonstrates the capability of a 50-nm metamorphic HEMT technology. The database extracted transistor model, including the noise characteristics, lends itself to G-band LNA design. Details regarding the transistor size selection and input matching were also discussed. In the measured results, two 165-GHz and three 183-GHz LNA designs were presented and the performance was improved for the second run circuits.

A WR-5 waveguide package was designed and manufactured for the LNAs. The packaged G-band amplifiers, LNA2 and LNA5, both achieve 19-20 dB gain and 7 dB noise figure at 165 and 183 GHz, respectively. Table I shows a comparison of the results to previously published 150-220–GHz amplifiers. The metamorphic HEMT-based amplifiers are reaching performance levels that have previously been seen in results obtained from amplifiers based on indium phosphide devices exclusively.

REFERENCES

[1] P. Ricaud, B. Gabard, S. Derrien, J.-P. Chaboureau, T. Rose, A. Mombauer, and H. Czekala, "HAMSTRAD-Tropo, A 183-GHz radiometer dedicated to sound tropospheric water vapor over Concordia Station Antarctica," *IEEE Trans. Geosci. Remote Sens.*, vol. 48, no. 3, pp. 1365–1380, Mar. 2010.

[2] P. Kangaslahti, L. Boon, T. Gaier, A. Tanner, M. Varonen, L. Samoska, S. Brown, B. Lambrigtsen, S. Reising, J. Tanabe, O. Montes, D. Dawson, and C. Parashare, "Low noise amplifier receivers for millimeter wave atmospheric remote sensing," in *IEEE MTT-S Int. Microw. Symp. Dig.*, Montreal, QC, Canada, Jun. 2012, pp. 1–3.

[3] P. Kangaslahti, "Recent developments in 180 GHz MMIC LNA and receiver technology," in *Proc. MicroRad*, 2010, pp. 272–275.

[4] P. H. Liu, W. Yoshida, J. Lee, L. Dang, J. Wang, W. Liu, J. Uyeda, D. Li, X. B. Mei, W. Deal, M. Barsky, Y. M. Kim, M. Lange, T. P. Chin, V. Radisic, T. Gaier, A. Fung, and R. Lai, "High gain G-band MMIC amplifiers based on sub-50 nm gate length InP HEMT," in *Proc. IEEE Int. Conf. Indium Phosphide and Related Mater.*, Matsue, Japan, May 2007, pp. 22–23.

[5] R. Grundbacher, R. Raja, R. Lai, Y. C. Chou, M. Nishimoto, T. Gaier, D. Dawson, P. H. Liu, M. Barsky, and A. Oki, "A 150–215 GHz InP HEMT low noise amplifier with 12 dB gain," in *Proc. IEEE Int. Conf. on Indium Phosphide and Related Mater.*, Glasgow, U.K., May 2005, pp. 613–616.

[6] S. Weinreb, T. Gaier, R. Lai, M. Barsky, Y. C. Leong, and L. Samoska, "High-gain 150–215-GHz MMIC amplifier with integral waveguide transitions," *IEEE Microw. Guided Wave Lett.*, vol. 9, no. 7, pp. 282–284, Jul. 1999.

[7] M. Varonen, P. Larkoski, A. Fung, L. Samoska, P. Kangaslahti, T. Gaier, R. Lai, and S. Sarkozy, "160–270-GHz InP HEMT MMIC low-noise amplifiers," in *Tech. Dig. IEEE Compound Semicond. Integr. Circuit Symp.*, La Jolla, CA, USA, Oct. 2012, pp. 1–4.
[8] A. Tessmann, I. Kallfass, A. Leuther, H. Massler, M. Kuri, M. Riessle, M. Zink, R. Sommer, A. Wahlen, H. Essen, V. Hurm, M. Schlechtweg, and O. Ambacher, "Metamorphic HEMT MMICs and modules for use in a high-bandwidth 210 GHz radar," *IEEE J. Solid-State Circuits*, vol. 43, no. 10, pp. 2194–2205, Oct. 2008.
[9] M. Kantanen, M. Kärkkäinen, M. Varonen, M. Laaninen, T. Karttaavi, R. Weber, A. Leuther, M. Seelman-Eggebert, T. Närhi, J. Lahtinen, and K. A. I. Halonen, "Low noise amplifiers for D-band," in *Proc. Eur. Microw. Assoc.*, Dec. 2008, vol. 4, pp. 268–275.
[10] M. Kärkkäinen, M. Kantanen, S. Caujolle-Bert, M. Varonen, R. Weber, A. Leuther, M. Seelmann-Eggebert, T. Närhi, and K. A. I. Halonen, "MHEMT *G*-band low-noise amplifiers," in *IEEE MTT-S Int. Microw. Symp. Dig.*, Seattle, WA, USA, Jun. 2–7, 2013, pp. 1–4.
[11] A. Leuther, A. Tessmann, M. Dammann, C. Schwörer, M. Schlechtweg, M. Mikulla, R. Lösch, and G. Weimann, "50 nm MHEMT technology for G-band and H-band MMICs," in *Proc. IEEE Int. Conf. Indium Phosphide and Related Mater.*, Matsue, Japan, 2007, pp. 24–27.
[12] M. W. Pospieszalski, "Modeling of noise parameters of MESFETs and MODFETs and their frequency and temperature dependence," *IEEE Trans. Microw. Theory Tech.*, vol. 37, no. 9, pp. 1340–1350, Sep. 1989.
[13] M. Seelmann-Eggebert, F. Schafer, A. Leuther, and H. Massler, "A versatile and cryogenic mHEMT-model including noise," in *IEEE MTT-S Int. Microw. Symp. Dig.*, May 2010, pp. 501–504.
[14] H. A. Haus and R. B. Adler, "Optimum noise performance of linear amplifiers," *Proc. IRE*, vol. 46, no. 8, pp. 1517–1533, Aug. 1958.
[15] H. Fukui, "Available power gain, noise figure and noise measure of two ports and their graphical representation," *IEEE Trans. Circuit Theory*, vol. CT-13, pp. 137–142, Jun. 1966.
[16] C. R. Poole and D. K. Paul, "Optimum noise measure terminations for microwave transistor amplifiers," *IEEE Trans. Microw. Theory Tech.*, vol. 33, no. 11, pp. 1254–1257, Nov. 1985.
[17] J. Engberg, "Simultaneous input power match and noise optimization using feedback," in *Dig. Tech. Papers 4th Eur. Microw. Conf.*, Sep. 1974, pp. 385–389.
[18] A. Davidson, K. Jones, and E. Strid, "LRM and LRRM calibrations with automatic determination of load inductance," in *36th ARTFG Conf. Dig.*, Nov. 1990, pp. 57–63.
[19] F. Purroy and L. Pradell, "New theoretical analysis of the LRRM calibration technique for vector network analysers," *IEEE Trans. Instrum. Meas.*, vol. 50, no. 5, pp. 1307–1314, Oct. 2001.
[20] "Fundamentals of RF and Microwave Noise Figure Measurements," Hewlett-Packard, Palo Alto, CA, USA, Application Note 57-1, 1983.
[21] Y.-C. Leong and S. Weinreb, "Full band waveguide-to-microstrip probe transitions," in *IEEE MTT-S Int. Microw. Symp. Dig.*, Jun. 1999, pp. 1435–1438.

Mikko Kärkkäinen received the M.Sc. and Lic.Sc. degrees in electrical engineering from the Aalto University (formerly Helsinki University of Technology), Espoo, Finland, in 2000 and 2005, respectively, where he is currently working toward the Ph.D. degree.

His current interests are in millimeter-wave circuits for integrated radio front-ends.

Mikko Kantanen received the M.S. and Lic.Sc. degrees in electrical engineering from Helsinki University of Technology (TKK), Espoo, Finland, in 2001 and 2006, respectively, where he is currently working toward the Ph.D. degree.

Since 2001, he has been with the MilliLab, VTT Technical Research Centre of Finland, Espoo, Finland, currently as a Senior Research Scientist. His research interests include millimeter-wave integrated circuit design, millimeter-wave measurements, and millimeter-wave systems.

Mr. Kantanen was a corecipient of an Asia–Pacific Microwave Conference 2006 Prize.

Sylvain Caujolle-Bert received the B.S. degree from Joseph Fourier University, Grenoble, France, in 2006, and the M.S. degree from Institut National des Sciences Appliquées, Lyon, France, in 2009, both in electrical engineering.

In 2007 and 2008, he was a Research Assistant with Electronic Circuit Design Laboratory, Aalto University, Helsinki, Finland. He is currently with CNRS, Guyancourt, France.

Mikko Varonen received the M.Sc., Lic.Sc., and D.Sc. (with distinction) degrees in electrical engineering from Aalto University (formerly Helsinki University of Technology), Espoo, Finland, in 2002, 2005, and 2010, respectively.

He is currently a Postdoctoral Researcher with the Academy of Finland, Department of Micro and Nanosciences, Aalto University, Espoo, Finland. During 2013, he was a Visiting Scientist both at the Jet Propulsion Laboratory (JPL) and the California Institute of Technology, and he is currently a Visiting Scientist with the Fraunhofer Institute of Applied Solid-State Physics. During 2011, he was a NASA Postdoctoral Program Fellow with JPL. His research interests involve the development of millimeter-wave integrated circuits using both silicon and compound semiconductor technologies for applications ranging from astrophysics and Earth remote sensing to millimeter-wave communications.

Rainer Weber was born in Offenburg, Germany, in 1978. He received the Dipl.-Ing. degree in electrical engineering from the University of Applied Sciences, Offenburg, Germany, in 2003.

He then joined the High Frequency Devices and Circuits Department, Fraunhofer-Institute for Applied Solid-State Physics, Freiburg, Germany, where he is involved with the MMIC design of amplifiers, oscillators, multipliers, and mixers up to 600 GHz.

Arnulf Leuther received the Dipl. Phys. degree and the PhD degree in physics from the Technical University of Aachen, Aachen, Germany.

He has been with the Fraunhofer Institute for Applied Solid State Physics, Freiburg, Germany, since 1996. His major area of interest is the development of HEMT technologies for sensor and communication systems up to 600 GHz.

Matthias Seelmann-Eggebert received the Diploma and Ph.D. degree in physics from the University of Tübingen, Tübingen, Germany, in 1980 and 1986, respectively.

From 1980 to 1996, he was involved in R&D related to infrared detectors based on HgCdTe and applied research in the field of electrochemistry and surface physics. From 1990 to 1991, he was a Visiting Scientist with Stanford University, Stanford, CA, USA. From 1997 to 2000, he was engaged in the growth of CVD diamonds. Since 2001, he has been a member of the Department of High Frequency Electronics, Fraunhofer Institute for Applied Solid State Physics, Freiburg, Germany. As a Leader of the modeling group, he is in charge of the development of linear and nonlinear compact models for III-V devices. He also coordinates an activity for the development of low-noise cryo-transistors and cryo-MMICs.

Ari Alanne received the M.Sc. degree in electrical engineering from Helsinki University of Technology (now Aalto University), Espoo, Finland, in 1999.

From 1999 to 2004, he worked in R&D of the telecommunications industry in Finland, developing radio communications and microwave circuits, devices, and systems. From 2005 to 2007, he was a Lecturer of telecommunications with Karelia University of Applied Science, Joensuu, Finland. He has been a Senior RF Design Engineer with DA-Design Oy, Jokioinen, Finland, since 2007. He has been involved in European Space Agency (ESA) space projects, such as the development of MDFE (Mission Dependent Frequency Equipment) and other radio-frequency harnesses for SAR subsystems and for ESA Sentinel 1-A and 1-B satellites. His current activity involves wireless communications, radar, and SAR products for space and military purposes.

Petri Jukkala received the M.Sc. and Lic.Tec. degrees from Aalto University, Espoo, Finland, in 1986 and 1991, respectively.

He is currently with DA-Design Oy, Jokioinen, Finland, as a Space Business Director.

Tapani Närhi received the M.Sc. and D.Sc. degrees in electrical engineering from the Helsinki University of Technology, Espoo, Finland, in 1978 and 1993, respectively.

In 1990, he joined the European Space Agency (ESA). He has been involved with space applications of microwave and millimeter-wave technology at the RF Payload Systems Division, European Space Research and Technology Centre (ESTEC), Noordwijk, The Netherlands.

Kari A. I. Halonen received the M.Sc. degree in electrical engineering from the Helsinki University of Technology (now Aalto University), Espoo, Finland, in 1982, and the Ph.D. degree in electrical engineering from the Katholieke Universiteit Leuven, Leuven, Belgium, in 1987.

Since 1988, he has been with the Electronic Circuit Design Laboratory, Helsinki University of Technology (now Aalto University), Espoo, Finland. Since 1993, he has been an Associate Professor, and since 1997 a Full Professor with the Faculty of Electrical Engineering and Telecommunications. He became the Head of Electronic Circuit Design Laboratory in 1998 and he was appointed as the Head of Department of Micro and Nano Sciences, Aalto University, in 2007–2013. He specializes in CMOS and BiCMOS analog and RF integrated circuits, particularly for telecommunication and sensor applications. He is the author or coauthor over 450 international and national conference and journal publications on analog and RF integrated circuits.

Prof. Kari Halonen has been an associate editor of the IEEE JOURNAL OF SOLID-STATE CIRCUITS and an associate editor of the IEEE TRANSACTIONS ON CIRCUITS AND SYSTEMS I—REGULAR PAPERS, a guest editor for the IEEE JOURNAL OF SOLID-STATE CIRCUITS, and the Technical Program Committee Chairman for European Solid-State Circuits Conference 2000 and 2011. He was the recipient of the Beatrice Winner Award at the 2002 ISSCC Conference. He has served as a TPC member of ESSCIRC and ISSCC.

Publication VI

Kantanen, M., Kärkkäinen, M., Caujolle-Bert, S., Varonen, M., Weber, R., Seelmann-Eggebert, M., Leuther, A., Jukkala, P., Närhi, T., Halonen, K.A.I., “Low noise amplifiers for G-band radiometers,” in *Proceedings of joint 6th ESA Workshop on Millimetre-Wave Technology and Applications and the 4 Global Symposium on Millimeter Waves (GSMM)*, Espoo, Finland, 2011, pp. 1-4.

Low noise amplifiers for G-band radiometers

M. Kantanen[1], M. Kärkkäinen[2], S. Caujolle-Bert[2], M. Varonen[2], R. Weber[3], M. Seelmann-Eggebert[3], A. Leuther[3], P. Jukkala[4], T. Närhi[5], K. A. I. Halonen[2]

[1]MilliLab, VTT Technical Research Centre of Finland, P.O. Box 1000, FI-02044 VTT, Espoo, Finland

[2]MilliLab, Aalto University, P.O. Box 13000, FI-00076 Aalto, Espoo, Finland

[3]Fraunhofer Institute for Applied Solid-State Physics, Tullastrasse 27, D-79108 Freiburg, Germany

[4]DA-Design Ltd., Keskuskatu 29, FI-31600 Jokioinen, Finland

[5]European Space Agency (ESTEC), Keplerlaan 1, NL-2200 AG Noordwijk, The Netherlands

***Abstract*-Six low noise amplifiers (LNAs) for three frequency ranges are presented. The amplifier circuits have been manufactured using a 100-nm gate length metamorphic high electron mobility transistor technology. Measured on-wafer performance shows 19-27 dB of gain and lowest noise figure values of 4 dB.**

I. Introduction

The advances in semiconductor technologies for millimeter-wave monolithic integrated circuits (MMICs) have made use low noise amplifier possible for higher frequency, namely up to 500 GHz [1]. For spaceborne radiometry above 140 GHz two main benefits of low noise amplifiers can be foreseen. First benefit is low-noise pre-amplification in front of currently used radiometers based on Schottky mixers improving receiver sensitivity. Secondly, low noise amplifiers enable the use of direct-detection radiometers.

II. Fabrication Technology

The manufacturing of low noise millimetre-wave integrated circuits has traditionally relied to use of high electron mobility transistors (HEMT) implemented with gallium arsenide (GaAs) or indium phosphide (InP). The best results have been achieved with InP technology. However, there are some drawbacks with the InP technology. These include higher manufacturing cost, lower breakdown voltage, more fragile structure, and device reliability when comparing to GaAs technology. To overcome some of these drawbacks, the possibility to process InP channel devices on the GaAs carrier wafer have been introduced in pseudomorphic (PHEMT) and metamorphic (MHEMT) technologies. In MHEMT technology, the metamorphic buffer layer is grown on the GaAs substrate, to enable the growth of the channel layer having 30-80 % indium content. This leads to cost reduction and manufacturability improvement over pure InP technology. The process can also be optimised for the intended purpose by controlling the indium content. The higher indium content provides more gain and less noise, whereas lower indium content is more suitable for applications requiring higher breakdown voltage [2].

The manufacturing process used in this work is the 100-nm GaAs based MHEMT technology of the Fraunhofer IAF, Freiburg, Germany. The process is suitable for coplanar waveguide (CPW) designs. The process features NiCr thin film resistors, metal-insulator-metal (MIM) capacitors and backside metallization. Unwanted substrate modes are suppressed using ground via holes through the GaAs substrate. As a result of extensive modelling work the Fraunhofer IAF provided reliable models for CPW components and transistors [3]. On-wafer G-band measurements of the test devices for the models suffered from serious systematic experimental errors, which were observed at the IAF as well as at Millilab. This phenomenon was attributed to an interference of the probe-tips with the neighboring on-wafer circuitry and is presently under detailed investigation. It impeded the extension of the model data base to G-band frequencies. Unfortunately, some parasitic and distributed effects become visible only at frequency above 100 GHz and lead to an unpredicted shift of up to 10 GHz to lower frequencies in the realized MMICs.

III. Designs and Measured Performance

Six low noise amplifiers were designed. LNA1 and LNA2 were targeted to narrowband operation at 165 ± 2 GHz, LNA3, LNA4, and LNA5 for a wide frequency range over 183 ± 10 GHz, and LNA6 for narrowband operation at 229 ± 2 GHz. Design goal was 20 dB of gain with -10 dB input and output match while achieving low noise performance.

All designs use coplanar waveguide (CPW) topology. Transistors with gate widths of 2x10 µm and 2x15 µm were chosen for the LNAs. Larger transistor was used for 165 GHz and smaller transistor for the two higher frequency ranges. Transistors achieve peak transconductance with 400 mA/mm drain current density and f_t is around 220 GHz. Availability of noise model enabled noise optimised designs.

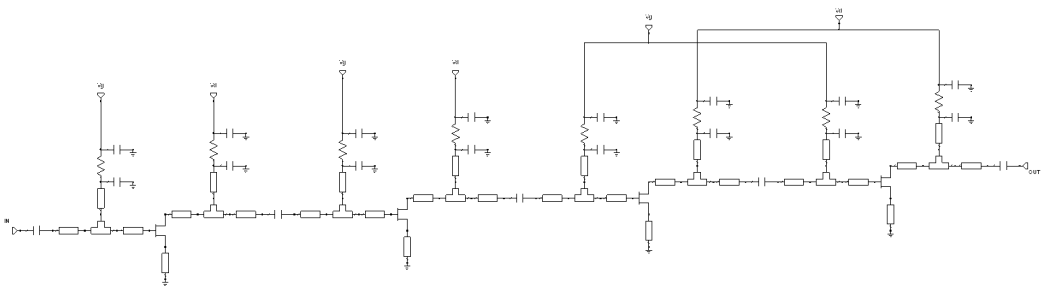

Figure 1. Schematics for baseline LNA design.

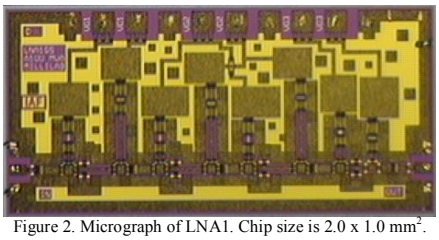

Figure 2. Micrograph of LNA1. Chip size is 2.0 x 1.0 mm^2.

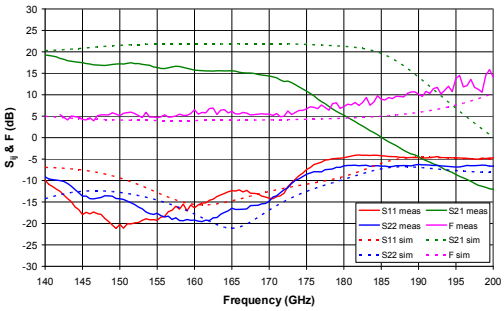

Figure 3. Measured (solid) and simulated (dashed) performance of LNA1.

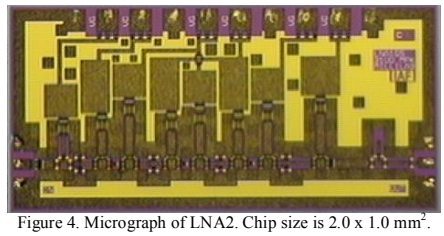

Figure 4. Micrograph of LNA2. Chip size is 2.0 x 1.0 mm^2.

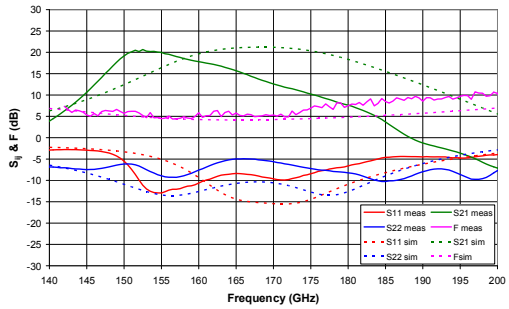

Figure 5. Measured (solid) and simulated (dashed) performance of LNA2.'

Schematics for a baseline LNA design is presented in Fig. 1. Matching networks are realised with conventional reactive matching networks, consisting of series transmission lines, series capacitors, and RF-short circuited shunt stubs. RF-short is realised using appropriately valued CPW-capacitor, typically 200-400 fF. Shunt stubs are used also for biasing. Low frequency stability is improved by small valued resistor and large MIM-capacitor following the RF-shorting capacitor on bias lines. Stability is further improved by using inductive source feedback.

A. LNA1

LNA1 is a 4-stage design using 2x15 µm transistors. Wideband approach to design was selected to mitigate possible frequency shifts. Micrograph of the circuits is shown in Fig. 2. The stages are biased below peak transconductance current density to improve stability. Second RF-shorting capacitor is added between series resistor and MIM-capacitor. Otherwise, design follows the baseline.

Comparison of measured and simulated S-parameters and noise figure is presented in Fig. 3. The measured gain and noise figure are 15.5 dB and 5.9 dB at 165 GHz, respectively. The best gain and noise performance is achieved around 140 GHz, where gain of 19.8 dB and noise figure of 5.0 dB are reached. The input and output matches are better than -10 dB over 136-174 GHz and 132-174 GHz, respectively.

B. LNA2

LNA2 is a narrowband 4-stage design using 2x15 µm transistors. The design was targeted for 165 GHz center frequency. Micrograph of LNA2 is shown in Fig. 4. The stages are biased below peak transconductance current density to improve stability. Design follows the baseline with an additional open ended stub that is added on output matching network to obtain wider bandwidth for matching.

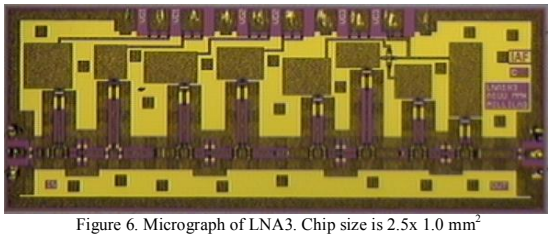

Figure 6. Micrograph of LNA3. Chip size is 2.5x 1.0 mm^2

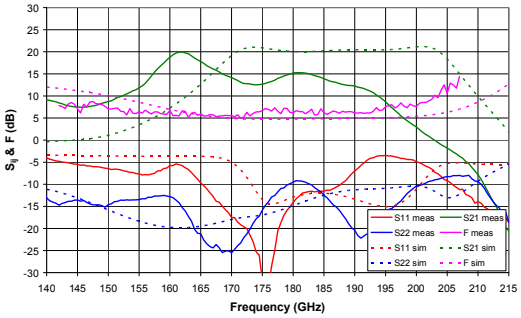

Figure 7. Measured (solid) and simulated (dashed) performance of LNA3.

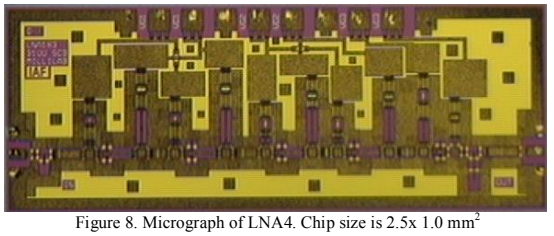

Figure 8. Micrograph of LNA4. Chip size is 2.5x 1.0 mm^2

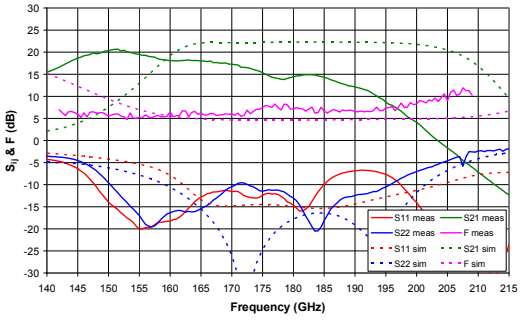

Figure 9. Measured (solid) and simulated (dashed) performance of LNA4.

Comparison of measured and simulated S-parameters and noise figure is presented in Fig. 5. The peak gain of 20.5 dB is achieved at 153 GHz and minimum noise of 4.3 dB at 156 GHz. The input and output matches are worse than simulated. The output match is better than -5 dB over 140-200 GHz and the input match reaches -10 dB level almost over 152-174 GHz.

C. LNA3

LNA3 is a wideband 4-stage design using 2x10 µm transistor. The stages are biased to peak transconductance current density. Realisation follows the baseline design. Micrograph of LNA3 is shown in Fig. 6.

The comparison of measured and simulated S-parameters and noise figure is presented in Fig. 7. The peak gain of 20 dB is achieved at 163 GHz and minimum noise of 5.3 dB at 172 GHz. The output match is better than -10 dB over 140-202 GHz and the input match is better than -10 dB level almost over 166-187 GHz.

D. LNA4

LNA4 is a wideband 5-stage design using transistors sizes in between 2x10 µm and 2x12 µm. Micrograph of LNA4 is shown in Fig. 8. Stages 1 and 2 are biased below peak transconductance current density, while stages 3, 4 and 5 are biased to peak transconductance current density. Main difference to design baseline is an additional 5th stage, which gives margin for gain per stage requirement. Also, open ended shunt stubs are added to input and output matching networks.

Comparison of simulated small-signal and noise performance is presented in Fig. 9. The best operation is achieved around 150 GHz, where gain of 20.2 dB and noise figure of 5.0 dB are measured. At 183 GHz are obtained 14.9 dB gain and 7.5 dB noise figure. Input and output matches remain below -10 dB over 148-184 GHz and 151-196 GHz, respectively.

E. LNA5

LNA5 is a five stage amplifier using 2x10µm transistors. Micrograph of the design is shown in Fig. 10. First three stages are biased below peak transconductance current density for better noise performance. Fourth and fifth stages are biased for peak transconductance current density. Additional fifth stage is added to the baseline design and capacitively loaded T-junctions are used in matching networks.

Comparison of measured and simulated S-parameters and noise figure at this bias point is presented in Fig. 11. This leads to gain peaking at 157 GHz where gain is reaching 29.0 dB. Also, input and output match are poor here and only conditional stability is achieved. Otherwise, the output match is better than -10 dB over 163-184 GHz and the input match reaches -10 dB over 180-187 GHz. Noise curve has quite nice and flat shape and values below 6 dB are reached between 166-173 GHz.

F. LNA6

LNA6 is a four stages design using 2x10 µm transistors. Micrograph of the design is shown in Fig. 12. All stages are biased to peak transconductance bias point and design follows the baseline design.

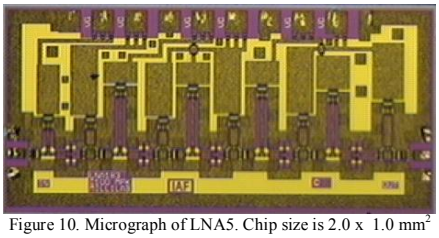

Figure 10. Micrograph of LNA5. Chip size is 2.0 x 1.0 mm^2

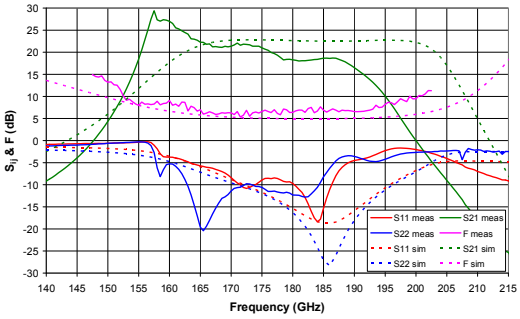

Figure 11. Measured (solid) and simulated (dashed) performance of LNA5.

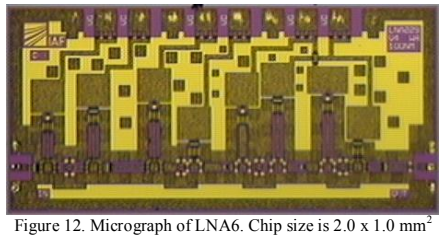

Figure 12. Micrograph of LNA6. Chip size is 2.0 x 1.0 mm^2

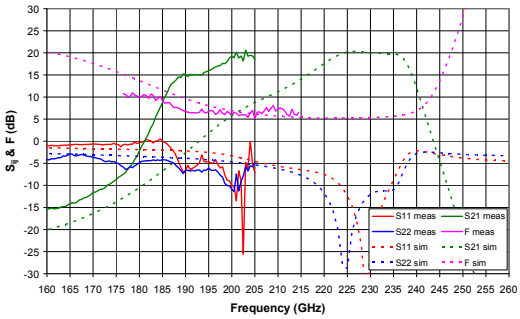

Figure 13. Measured (solid) and simulated (dashed) performance of LNA6.

TABLE I
MEASURED ON-WAFER PERFORMANCE OF THE DESIGNED AMPLIFIERS

Circuit	-3 dB Gain band (GHz)	Peak gain (dB)	< -10 dB Input match (GHz)	< -10 dB Output match (GHz)	Noise figure (dB)	Power consumption (mW)
LNA1	140-159	19.2	140-173	142-173	3.9-5.9	40
LNA2	149-160	20.6	152-161	N.A.	4.3-6.3	40
LNA3	158-166	19.9	165-188	140-179	5.4-6.8	35
LNA4	143-167	20.7	180-186	163-184	4.4-5.9	40
LNA5	157-161	27.4	171-174	163-184	8.2-9.5	37
LNA6	199-207	20.2	200-201	199-201	5.4-7.1	32

Comparison of measured and simulated S-parameters and noise figure at this bias point is presented in Fig. 13. Peak gain of 20 dB and minimum noise figure of 5.5 dB are achieved at 205 GHz. The input is very close to 0 dB at 183 GHz and reaches -10 dB on a narrow band around 201 GHz. The output match reaches also -10 dB on a narrow band near 200 GHz.

IV. CONCLUSIONS

Summary of measured performance is presented in Table I. Frequency shift in gain response was observed for all amplifier designs. Further investigations showed that the frequency shift could be attributed to the incomplete descriptions of the source line connection parasitics and a distributed effect in the parallel capacitors.

Gain values of 20 dB and noise figure values of 4-5 dB were achieved for the amplifiers, with one exception related to unstable operation. With the results from the first run amplifiers could be re-designed to obtain better performance over the targeted bands.

REFERENCES

[1] A. Tessmann, A. Leuther, R. Lösch, M. Seelmann-Eggebert, H. Massler, "A metamorphic HEMT S-MMIC amplifier with 16.1 dB gain at 460 GHz," *IEEE Compound Semiconductor Integrated Circuit Symposium*, Oct. 2010

[2] C. S. Whelan, P. F. Marsh, W. E. Hoke, R. A. McTaggart, C. P. McCarroll, T. E. Kazior, "GaAs metamorphic HEMT (MHEMT): An attractive alternative to InP HEMTs for high performance low noise and power applications," *IEEE International Conference on Indium Phosphide and Related Materials*, pp. 337-340, May 2000.

[3] A. Leuther, A. Tessmann, I. Kallfass, R. Lösch, M. Seelmann-Eggebert, N. Wadefalk, F. Schäfer, J. D. Gallego Puyol, M. Schlechtweg, M. Mikulla, O. Ambacher, "Metamorphic HEMT technology for low-noise applications," *IEEE International Conference on Indium Phosphide and Related Materials*, pp. 188-191, May 2009.

Publication VII

Kantanen, M., Lahdes, M., Tuovinen, J., “Passive millimeter-wave imager,” in *Proceedings of International Joint Conference of the Sixth MINT Millimeter-wave International Symposium and the Seventh Topical Symposium on Millimeter Waves,* Seoul, South Korea, 2005, pp. 240-243.

A millimeter wave imager

Mikko Kantanen, Manu Lahdes, Jussi Tuovinen
MilliLab, VTT Information Technology
P.O. Box 12021, FIN-02044 VTT, Finland
Tel: +358 9 456 6501 Fax: +358 9 456 7029
Email: mikko.kantanen@vtt.fi

Abstract

In this work a millimeter wave imager has been built to demonstrate millimeter wave imaging capabilities. Basic theory of millimeter wave imaging is presented and imaging system is described. Millimeter wave images taken with the system are shown.

1. Introduction

Progress in the manufacturing of the millimeter wave monolithic integrated circuits (MMICs) has increased the interest towards millimeter wave applications. The characteristic properties of millimeter waves enable some unique applications, one of which is the millimeter wave imaging. Millimeter wave imaging systems can be considered as an extension of imaging sensors working at visible light and infrared regions. Using millimeter waves, imaging can be performed when it is impossible to obtain images with visible light or infrared sensors. One great advantage of using millimeter waves is to be able to picture a scene under adverse weather conditions, for example through fog or dust. Possible applications for millimeter wave imaging sensors are automotive collision avoidance radars, enhanced vision systems, concealed weapon detection, and contraband detection.

In this paper, a 94 GHz single channel imaging demonstrator system is described. Millimeter wave images taken with the demonstrator are shown.

2. Theory

A millimeter wave image is created by measuring an antenna temperature map over the scene of interest using a very sensitive radiometer. The antenna temperature of the object depends on the noise radiated from the object. This noise has two components; part of the noise is related to the physical temperature of the object and the other part is surrounding noise reflected by the object. Mathematically this can be formulated

$$T_A = \varepsilon T_P + \rho T_r , \quad (1)$$

where T_A and T_P are the antenna temperature and the physical temperature of the object, respectively. T_r is the noise temperature of the reflected radiation. Material parameters emissivity ε and reflectivity ρ, describe how much radiation is coming from internal and external source. These two parameters are related by equation

$$\varepsilon + \rho = 1 . \quad (2)$$

Using (2), (1) can be re-written

$$T_A = T_r + \varepsilon(T_P - T_r) = T_r + (1-\rho)(T_P - T_r), \quad (3)$$

where it is seen that for two objects at same physical temperature, the difference in measured antenna temperatures depends only on the emissivity (or reflectivity) of the objects.

At millimeter wave region, the sky can be used as an external noise source for imaging. The antenna temperature of the sky is a function of the elevation angle and ranges between 30-290 K at 94 GHz. Thus, objects reflecting noise from the sky appear colder than their surroundings, in a sense of antenna temperature [1, 2].

3. Imager

3.1. Scanner

To obtain an informative image of the scene of interest large number of pixels is needed. In infrared imagers, full staring arrays with one detector for each pixel are used. In a millimeter wave imager, this kind of array is also possible but very expensive. Thus, imaging is normally performed using small number of receivers and scanning the main lobe of an antenna over the scene of interest.

Scanning can be mechanical or electrical. In mechanical scanning, entire antenna or focusing elements are moved step-by-step or continuously. Mechanical scanning is relatively easy to realize, but its drawback is slowness, which is present in mechanical movement. Also, antenna system may be quite heavy, which makes scanning system designing very challenging [3]. In electronic scanning, the main lobe of an antenna is moved by adjusting electrical properties of the antenna or a feed network. The main options for electronic scanning are multiplexing techniques, correlation radiometers and phased array antennas [4]. Electrical scanning systems require large amount of good quality components, such as switches and phase shifters. Also, quite complex signal processing algorithms are needed. For these reasons, millimeter wave imaging systems have so far mainly used mechanical scanning.

The purpose of this work has been to build a simple imager that demonstrates the capabilities of millimeter wave imaging. The main emphasis has been on the quality of images, while the imaging speed has been with less importance. Thus, a mechanical scanning has been used. In this scanner, the entire radiometer system is moved in azimuth and elevation planes using two computer controlled stepper motors. The scene of interest is scanned in a step-by-step fashion.

3.2. Radiometer

In addition to scanning, another main issue in creating an informative image is the ability to measure antenna temperature accurately. This is done using a very sensitive radiometer. The most well-known radiometer topologies are total power, Dicke and noise adding radiometers. In an ideal case, best antenna temperature resolution is achieved using a total power radiometer. However, gain instability of the radiometer degrades its performance. The gain instability issue is more important as the total imaging time is longer. The errors due the gain instability are reduced by calibrating the radiometer constantly, either by reference load as in Dicke radiometer or by added noise as in noise adding radiometer [5, 6].

In this work, a Dicke radiometer has been used. The block diagram and a photo of the radiometer are presented in Fig. 1 and Fig. 2, respectively. A 300 mm diameter horn antenna, with two focusing lenses is used to get a narrow main lobe. The beamwidth is 0.7°. Antenna is followed by a single pole double throw (SPDT) switch that connects either the antenna or the reference load to the first amplifier with 1 kHz frequency. The amplifier chain consists of two low noise amplifiers (LNA) and isolators to reduce possible mismatch problems. The millimeter wave signal is transformed directly to DC using a detector diode and a low frequency amplifier. The operational frequency of the radiometer is 94 GHz with 4 GHz bandwidth.

3.3. Data processing

The resulting two level 1 kHz signal from the detector diode is fed to 12-bit A/D-converter. The raw waveform data is read to the computer and reference and antenna signals are separated. Using the reference signal to track gain variations, a corrected antenna temperature reading is calculated. From the resulting data an appropriately scaled grayscale picture is created. The pictures can be further improved using commercial photo editing programs.

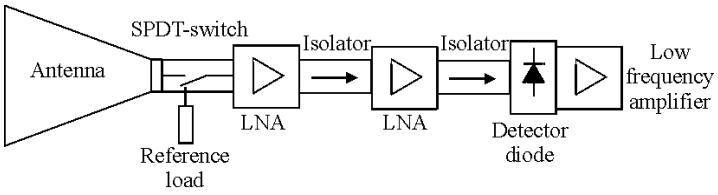

Fig. 1. The block diagram of the Dicke radiometer.

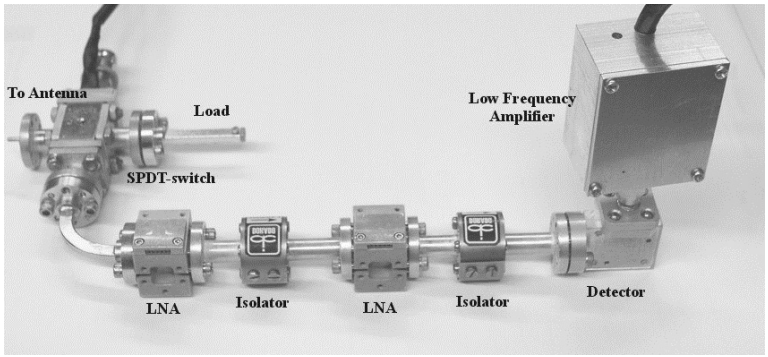

Fig. 2. A photo of the Dicke radiometer.

4. Millimeter wave images

In the following, some millimeter wave images taken with the imager described above are presented. In the images, colder objects appear brighter.

Fig. 3 shows two persons standing outdoors. The person on the right has a metallic handgun silhouette hidden inside his jacket. The cold sky is reflected from the metal producing a bright spot on the person. Reflections from shoulders, head, and arms can also been seen. A mobile phone and keys in the pockets of the left-side person produce also high reflections.

Fig. 4 presents similar situation indoors. In indoor imaging there is not as large contrast available, which is clearly seen in the picture. However, brighter area produced by the handgun silhouette can be detected also in indoors. For optimal indoor imaging performance some kind of illumination system is needed to produce more informative images.

Fig. 5 illustrates outdoors surveillance abilities. Different soil types, a walk path, trees, a building and a metallic object can be distinguished from the image. The strongest reflections come from the car, roofs, trash container, and street lamps. The cooling effect of the shadow on the grass can also been seen. Similar image could be produced in the presence of fog.

5. Conclusions

A millimeter wave imager at 94 GHz has been build. The capabilities of millimeter wave imaging are demonstrated for concealed weapons detection and surveillance applications.

6. Acknowledgment

This work has been supported by Finnish Defence Forces Technical Research Centre.

7. References

[1] L. Yujiri, M. Shoucri, and P. Moffa, "Passive millimeter wave imaging," *IEEE Microwave Magazine*, vol. 4, no. 3, pp. 39-50, 2003.

[2] R. M. Smith, K. D. Trott, B. M. Sundstrom, and D. Ewen, "The passive mm-wave scenario," *Microwave Journal*, vol. 39, no. 3, pp. 22-34, 1996.

[3] D. G. Gleed, R. Appleby, N. A. Salmon, S. Price, G. N. Sinclair, R. N. Anderton, J. R. Borrill, and M. R. M. Wasley, "Operational issues for passive millimeter wave imaging system," *Proc. of SPIE on Passive Millimeter-Wave Technology*, vol. 3064, Orlando, FL, 1997, pp. 23-33.

[4] A. R. Harvey, R. Appleby, P. M. Blanchard, and A. H. Greenaway, "Beam-steering technologies for real time passive millimeter wave imaging," *Proc. of SPIE on Passive Millimeter-Wave Technology II*, vol. 3378, Orlando, FL, 1998, pp. 63-72.

[5] L. A. Klein, *Millimeter Wave and Infrared Multisensor Design and Signal Processing*, Norwood, Artech House Inc., 1997.

[6] F. T. Ulaby, R. K. Moore, and A. K. Fung, *Microwave Remote Sensing*, Reading, Mass., Addison-Wesley Publishing Company, 1981.

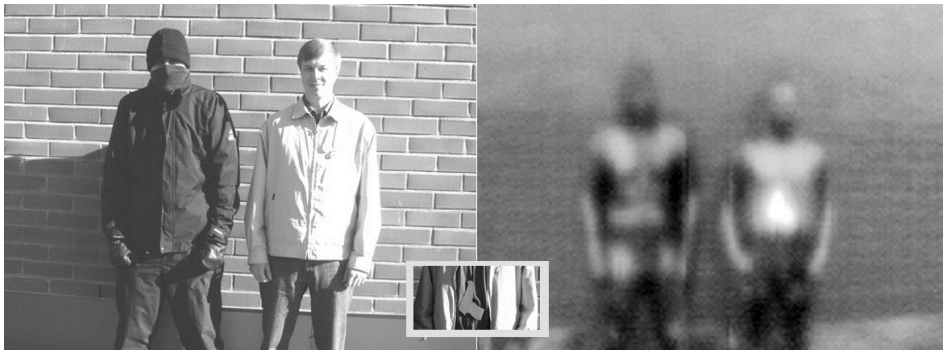

Fig. 3. A photo and a millimeter wave image of two persons outdoors. The person on the right has a handgun silhouette hidden inside his jacket.

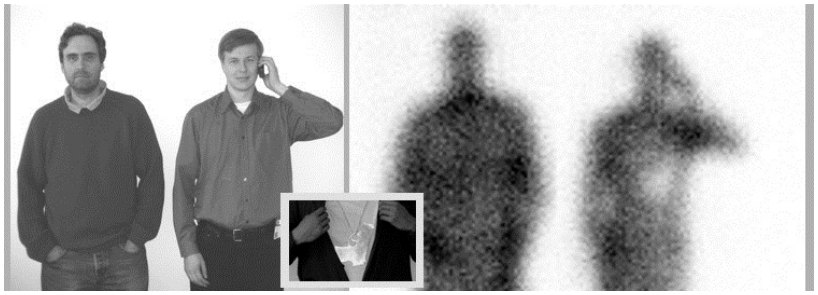

Fig. 4. A photo and a millimeter wave image of two persons indoors.

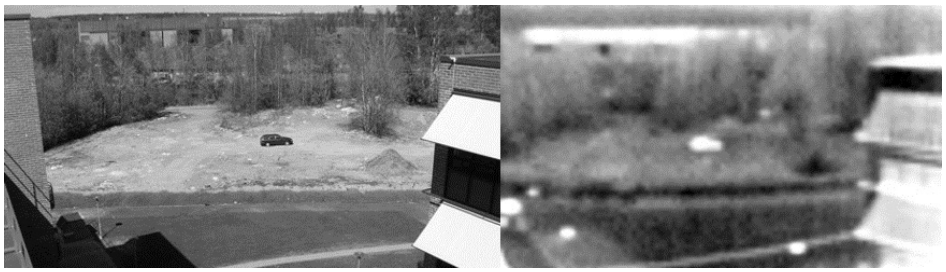

Fig. 5. A photo and a millimeter wave image of a scenery. Metallic objects such as a car, roofs and the street lamps are clearly visible.

Aalto-DD 270/2016
VTT SCIENCE 145

ISBN 978-952-60-7207-4 (printed)
ISBN 978-952-60-7206-7 (pdf)
ISSN-L 1799-4934
ISSN 1799-4934 (printed)
ISSN 1799-4942 (pdf)

978-951-38-8486-4 (printed)
978-951-38-8485-7 (pdf)
2242-119X
2242-119X (printed)
2242-1203 (pdf)

Aalto University
School of Electrical Engineering
Department of Radio Science and Engineering
www.aalto.fi

BUSINESS + ECONOMY

ART + DESIGN + ARCHITECTURE

SCIENCE + TECHNOLOGY

CROSSOVER

DOCTORAL DISSERTATIONS